Origin and pressure-temperature-time-fluid evolution of a subducted volcanoclastic sequence: the Theodul Glacier Unit (Western Alps, Switzerland)

Inaugural dissertation
of the Faculty of Science,
University of Bern

presented by

Thomas, Bovay

from Rougemont VD

Supervisor of the doctoral thesis:
Prof. Daniela Rubatto

Co-supervisor of the doctoral thesis:
Prof. Pierre Lanari

Institut für Geologie, University of Bern

Origin and pressure-temperature-time-fluid evolution of a subducted volcanoclastic sequence: the Theodul Glacier Unit (Western Alps, Switzerland)

Inaugural dissertation
of the Faculty of Science,
University of Bern

presented by

Thomas, Bovay

From Rougemont VD

Supervisor of the doctoral thesis:
Prof. Daniela Rubatto
Institut für Geologie, University of Bern

Co-supervisor of the doctoral thesis:
Prof. Pierre Lanari
Institut für Geologie, University of Bern

Accepted by the Faculty of Science.

Bern, 31.03.2021

The Dean
Prof. Dr. Zoltan Balogh

ABSTRACT

Ophiolites found within mountain belts testify the closure of oceanic basins at convergent margins and consists of variably hydrated exhumed fragments of oceanic lithosphere that may have undergone high-pressure metamorphism and deformation. This study investigates the Theodul Glacier Unit (TGU), a tectonic slice of volcanoclastic material within the Zermatt Saas meta-ophiolite (Western Alps) that was subducted during the closure of the Piemonte-Ligurian ocean. This well-exposed and preserved rock association offers the opportunity to gain insights into three crucial aspects of subduction, namely (1) the composition and variability of the input crustal material, (2) the variation of the geothermal gradient and (3) the generation and transfer of fluids within the slab.

The location of the TGU within the meta-ophiolites of the Zermatt-Saas Zone (ZSZ) and its unusual lithostratigraphy raises question about its origin. In **Chapter 1** it is shown that the preserved heterogeneous layering of the TGU is composed of lithologies with mafic (OIB) to felsic (UCC) composition that all contain a variable detrital input of Permian age. The internal structures and lithologies of the TGU are not directly comparable to the sedimentary cover of the ZSZ, or to the continental outliers embedded within the ZSZ, nor to crystalline basements. The TGU is thus interpreted as a volcanoclastic sequence and as a new type of allochthonous sedimentary cover of the Piemont-Ligurian oceanic crust in the Western Alps.

Collisional belts such as the Alps, necessarily include units with diverse origin and age and complex metamorphic evolutions. In the Western Alps, mono-metamorphic Alpine rocks record clockwise, high-pressure and low-temperature paths, where relatively small domains of UHP relicts are preserved. In contrast, pre-Alpine basement rocks evolved along hotter geotherms typical of collision and extension. In **Chapter 2**, garnet Lu-Hf ages from different lithologies of the TGU yield a restricted garnet crystallization time window between 50.3 and 48.8 Ma (± 0.5%, 2SD). The Alpine ages were measured even in garnet with complex 2-stages zoning observed in the schists, which further indicates an Alpine mono-metamorphic evolution for the TGU. Multiphase equilibrium thermodynamic modelling of garnet, phengite and rutile constrains a tight β-shape pressure-temperature (*P*–*T*) path with significant variation in pressure (26.5 ± 1.0 to 15.0 ± 1.0 kbar) in a very limited temperature range of ~30 °C. The older 50.3 ± 0.3 Ma Lu-Hf age is related to the high-*P* stage, whereas initial exhumation was rapid and led to isothermal decompression within 1 Myr prior to a reheating stage. Distinct stages of the β-shape metamorphic path correspond to different geotherms, where the reheating is best explained by upwelling of hot asthenospheric mantle material and transient storage of the unit at the crust–mantle boundary. Enigmatic garnet porphyroblasts from one type of schists have many similarities with those from other samples

(**Chapter 4**). However, this garnet type yields a Lu-Hf isochron date of 168.7 ± 1.8 Ma, which awaits confirmation before a scenario including a Jurassic stage can be fully evaluated.

In subduction zones, the aqueous fluids generated through hydrous phase breakdown have individual signatures, which equilibrated oxygen isotope composition is function of the bulk $\delta^{18}O$, rock chemistry and *P*–*T* conditions. Garnet from TGU lithologies show important intracrystalline drop of ~8 ‰ in $\delta^{18}O$, corresponding to sharp chemical zoning between a xenomorphic core and a euhedral rim (**Chapter 3**). Such variation in oxygen isotope is inconsistent with a closed system evolution and demand influx of external fluids in isotopic disequilibrium. Thermodynamic and $\delta^{18}O$ models constrain the interaction with external fluids at high–*P* and imply that the large amount of low $\delta^{18}O$ H_2O required for the isotopic shift was in isotopic equilibrium with the surrounding serpentinites. The calculated time-integrated fluid flux across the TGU rocks is above the open-system behaviour threshold and argues for pervasive flow across the unit. The transient rock volume variations caused by lawsonite breakdown in the TGU schist is identified as the possible trigger for the pervasive fluid influx. This process can eventually form a transient water-filled porosity network with sufficient connection to allow fluid mobilization and promote pervasive infiltration of external fluids. Thus, a sustained fluid income can prevent the newly formed porous network to collapse and efficiently modify bulk $\delta^{18}O$.

The work conducted in this thesis showed the importance and challenges of applying a multidisciplinary approach that takes into account field geology, petrology, modelling, geochronology and geochemistry in order to gather accurate information for reconstructing the geological evolutions of metamorphic units. This detailed record can then inform our understanding of processes such as crustal formation and recycling, as well as dynamics of subduction.

TABLE OF CONTENTS

INTRODUCTION

I. GENERAL INTRODUCTION

Subduction zones are the tectonic setting where crustal material sinks into the Earth's interior (Fig. 1). They are found at convergent plate boundaries in active margins and have a primary role in the formation of new continental crust (Tatsumi 2005). As the lower plate moves down the subducting channel, the pressure and the temperature increases leading to changes in mineral assemblages (Schmidt and Poli 2003). Prograde subduction metamorphism is associated to dehydration reactions through breakdown of hydrous phases and fluid release is in turn responsible for element transfer between subducting crust and the overriding mantle wedge (Poli and Schmidt 2002). Volatile recycling in subduction plays an important role in arc magmatism, geochemical

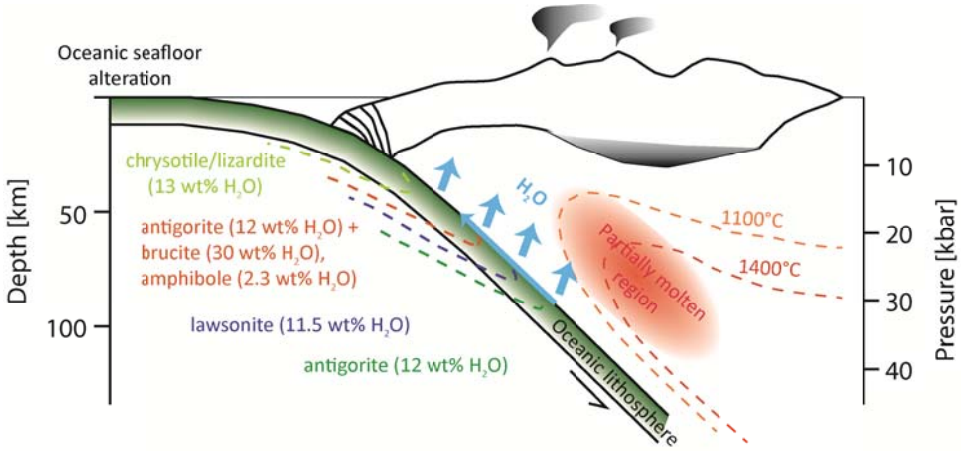

Figure 1: Representative sketch of a subduction zone structure. The main mineral dehydration reactions that occurs at different P–T conditions along the slab are indicated. These fluids are released within the different lithologies (sediment, mafic, ultramafic) composing the downgoing oceanic lithosphere. Modified after Früh-Green et al. (2001), Schmidt and Poli (2013), and Vitale Brovarone and Beyssac (2014).

cycles, energy budget, mantle composition and seismicity (Sorensen and Barton 1987; Bebout 1991a; Philippot and Selverstone 1991; Selverstone et al. 1992; Nadeau et al. 1993; Spandler et al. 2011). For the accurate reconstruction of subduction processes it is important to understand (1) the composition and variability of the input crustal material; (2) the distribution of the geothermal gradient, as reflected in the pressure–temperature–time (*P–T–t*) path of the subducted rocks; and (3) how dehydration fluids are generated and how they transfer within the slab. These are the three main topics that this thesis deals with, using as field laboratory the rock association of the Theodul Glacier Unit (TGU).

A. Ophiolites and oceanic lithosphere

The oceanic lithosphere forms in extensional tectonic settings at mid-ocean ridges. The internal structure, geochemical characteristics, and thickness of the oceanic crust vary with spreading rate, proximity to plumes or trenches, mantle temperature, mantle fertility, and the availability of fluids (Dilek and Furnes 2011). The lithostratigraphy of oceanic crust is composed of

ultramafic and mafic igneous rock topped by sediments, with two main end-members. Fast spreading ridges (>100 mm·a^{-1}) show high volcanic activity resulting in a well-developed layered sequence (Fig. 2). Typical actual equivalent are found in the Pacific ocean. At slow spreading ridges (<50 mm·a^{-1}) the lithostratigraphic sequence is heterogeneous and fragmented with little magmatic activity. Extensional tectonic results in the formation of deep rift valley and deep normal faulting (6-8 km), which can lead to the exposure of mantle peridotite at the seafloor (Fig. 2). This type of oceanic crust is actually composing the Atlantic, the Arctic and the Indian ocean (Bougault 1993; Alt 1995; Müller et al. 2008). The thickness and composition of the sediments constituting the top layer of the oceanic crust is dependent two, non-mutually exclusive processes: the erosion of the continents or continental ribbons and deposition of biological material on the seafloor (McLennan 1989; Plank 2014). Hydrothermal alteration at seafloor affects heterogeneously the oceanic crust, which depth and intensity is controlled by faulting and heating (Alt 1995). Such fluid-rock interaction process leads to hydration of a significant amount of the oceanic lithosphere, and to major chemical and isotopic variations of its original rock composition (Fig. 3) (Gregory and Taylor 1981; Dickin and Jones 1983; Gillis and Thompson 1993; Cartwright and Barnicoat 1999; Miller et al. 2001; Bach et al. 2003).

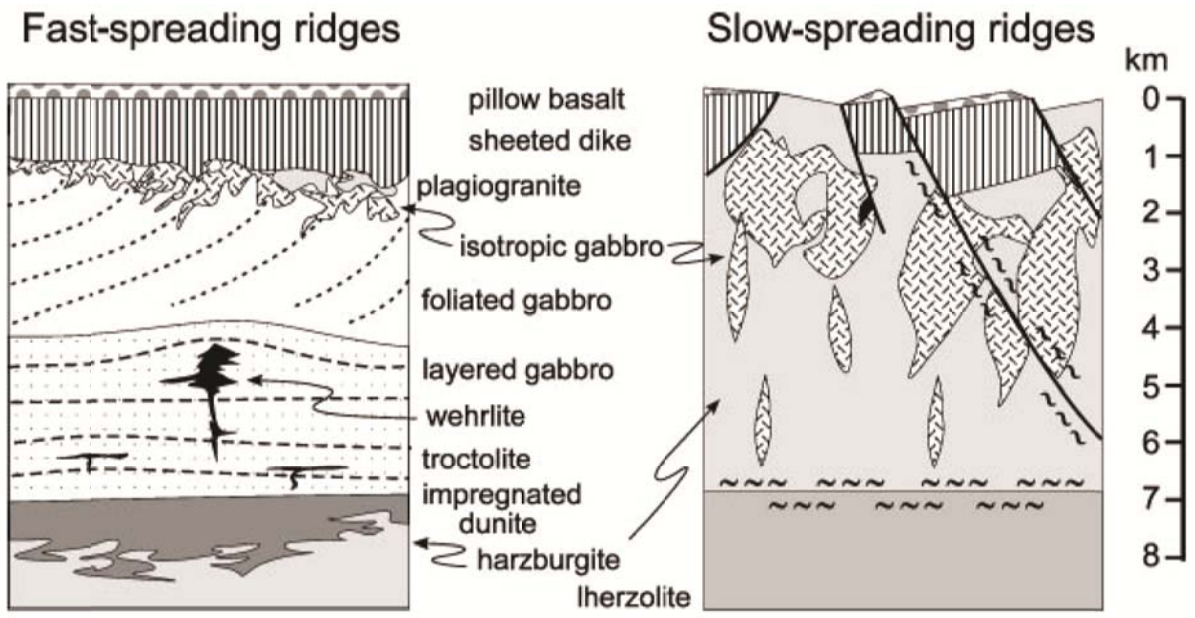

Figure 2: Schematic sections of the oceanic crust in fast- and slow-spreading ridges environment. Sketch from Poli and Schmidt (2002).

Ophiolites found within mountain belts are witnesses of oceanic closure at convergent margins, where they represent exhumed fragments of upper mantle and oceanic crust that are sometimes deformed and have possibly undergone (high pressure) metamorphism (Dilek and Furnes 2011, 2014). The origin of highly deformed meta-ophiolites and their heterogeneous rock associations, can be difficult to reconstruct because the original lithological contacts are reworked

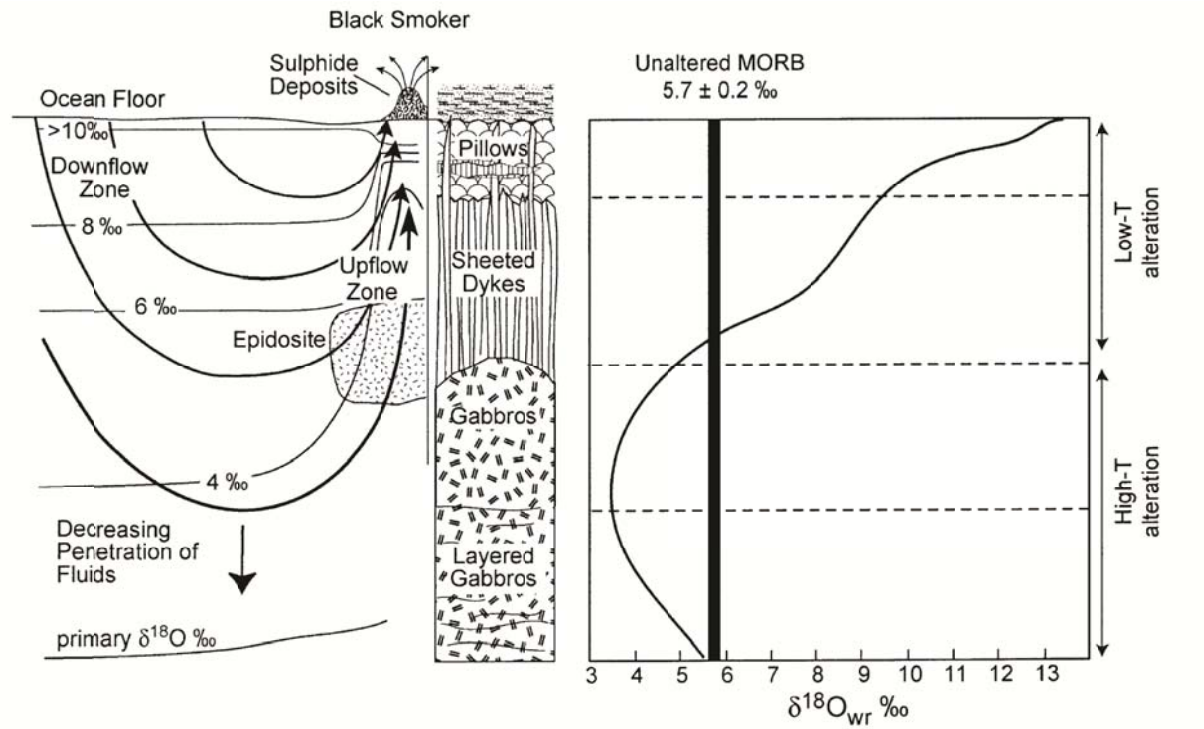

Figure 3: Sketch of seafloor hydrothermal alteration leading to major bulk chemical variation. Low-temperature alteration occurs in downflow zones accompanied by increase of $\delta^{18}O$ values and enrichment in Mg and depletion in Ca. The downgoing fluid is progressively heated by a plutonic heating source at depth and is focused in a narrow upflow zone with a higher permeability than the surrounding host rocks. The hydrothermal alteration is produced at higher-temperature leading to Ca- and Mn enrichment, and Mg- and Na depletion, with relatively low $\delta^{18}O$ values. Black smokers, sometimes associated to sulphide mineralisation, may develop on the seafloor where the hydrothermal system vent. Sketch from Miller et al. (2001) after Gregory and Taylor (1981) and Cartwright and Barnicoat (1999)

and original mineral assemblages might be overprinted (Spalla et al. 1996; Beltrando et al. 2014). Major and trace element geochemistry are commonly used to categorize end members oceanic crust materials, where sedimentary and magmatic rocks have characteristic signatures (McLennan 2001; Pearce 2014; Plank 2014). However determining rock provenance can still be challenging, because hydrothermal alteration at seafloor and metamorphism may overprint the original chemical and isotope bulk rock composition (Pfeifer et al. 1989; Dinelli et al. 1999; Li et al. 2004; Mahlen et al. 2005). The wide diversity of meta-ophiolites outcropping in mountain belts attests for the variability of oceanic crust involved in subduction zones. The study of this exhumed material is key to reconstruct the processes that occurred at depth, such as high-pressure fluid-rock interaction and metamorphism.

B. Metamorphism and timing

When entering the subduction zone, the slab is significantly cooler than the surrounding ambient mantle. As the slab is progressively buried, this contrast in temperature causes perturbation in the geotherm and lead to progressive increase of the *P–T* conditions within the oceanic

lithosphere. Mineral assemblage in the subducted crust transform in response to *P–T* variations and these changes affect rock textures and compositions. The stability of mineral assemblages and their re-equilibration through metamorphic reactions will strongly depend on the evolution of the geothermal gradient, the bulk rock chemistry and the presence of fluid (Syracuse et al. 2010). However, the transformation is rarely complete and mineral relics are key to decipher *P–T* evolution. Various mechanisms can affect the earth thermal structure and be recorded in metamorphic minerals, such as radiogenic heat production of additionally accreted continental blocks (Wiederkehr *et al.*, 2008), slab breakoff (Kurz *et al.*, 1998a; Brouwer *et al.*, 2002), continental collision after the end of oceanic lithosphere subduction (Borghi *et al.*, 1996), mantle delamination (Henk *et al.,* 2000), slowing exhumation rate (e.g. Wilke *et al.*, 2010), asthenospheric inflow ahead of the spreading ridge (Abers *et al.,* 2016), multiple short-lived burial-exhumation cycles associated to the alternation of shortening and extensional deformation (Beltrando *et al.* 2007), advective and conductive heating from the mantle (Sizova et al. 2019). In this study (Chapter 2 and 4) the *P–T* evolution of subducted and exhumed rocks is investigated with equilibrium phase diagram using thermodynamic databases, based on observed equilibrium assemblages coupled with chemical zoning of mineral known for their resistance to re-equilibration, such as garnet and zircon.

The same robust minerals are used for geochronology to time pre- or syn-metamorphic events underwent by the host rock. Thus, the use of garnet and zircon as geochronometers requires a good knowledge of their origin, growth conditions, and chemical zoning. Garnet is a typical metamorphic mineral, which major element composition is controlled by the *P–T* conditions of growth and makes it an ideal thermobarometer. Moreover, garnet geochronology enables time constraints through Sm-Nd and Lu-Hf systematics, providing a key tool to date metamorphic events and eventually distinguish between mono- and poly-metamorphic growth. On the other hand, zircon is well-known for its capacity to grow in magmatic and metamorphic environments and to record the successive events that affected its host rock (Beltrando et al. 2010). Its robustness to re-equilibration and ability to survive sedimentary as well as metamorphic cycles makes it a suitable candidate to unravel complex geological histories. Coupled with thermodynamic modelling and/or stable isotope geochemistry, either performed on the mineral used as geochronometer itself or based on a multi-mineral approach, geochronology provides unique information on the duration and absolute timing of a geological events.

C. High-pressure fluid-rock interaction

Dehydration of mafic oceanic crust and associated hydrated oceanic lithospheric mantle in subduction zone liberates large amounts of aqueous fluids (Fig. 1) (Ito et al. 1983; Peacock 1990;

Ulmer and Trommsdorff 1995; Poli and Schmidt 2002; Spandler et al. 2003; Angiboust and Agard 2010), causing major changes in rock density, volume and permeability (Connolly 2010). Propagation of fluids at depth may occur by interconnected vein networks and channelization (Philippot and Selverstone 1991; Miller and Cartwright 2000; Hacker et al. 2003; Miller et al. 2003; John et al. 2008; Spandler et al. 2011; Angiboust et al. 2014; Taetz et al. 2016) or by pervasive fluid flow (Bebout 1991b; Bebout and Barton 1993; Konrad-Schmolke et al. 2011). The fluid flow mechanisms may have different dynamics in the downgoing slab, at the slab mantle interface or in the hanging-wall mantle wedge (Konrad-Schmolke et al. 2011). Aqueous fluids released from the lower layers of the subducting slab necessarily infiltrate upper layers of the subducting oceanic plate and eventually infiltrate the overriding mantle wedge (Sorensen and Barton 1987; Zack and John 2007). Notably, the interface between subducting oceanic slabs and the hanging-wall is a complex area composed of chemically distinct lithologies. This zone has large potential for mass transfer and metasomatism through fluid mobilization (e.g. Bebout and Penniston-Dorland 2016). The fluid that is transferred from the subducting slab to the mantle wedge lowers the solidus of the peridotite and triggers melting. Thus, the generation of arc magmatism and associated formation of continental crust is only possible with subduction of hydrothermally altered oceanic lithosphere. Through the successive dehydration reaction the slab becomes increasingly anhydrous and dense with depth, which ultimately creates the slab-pull force needed for a long-lasting subduction process.

Many tracers show the mixed imprint of sediments, mafic crust and serpentinites in the supply of fluid and chemical components to arc volcanoes (e.g. Bebout 1991a, 2013). These signatures are distinguishable because the devolatilising lithologies composing the subducting oceanic crust have specific stable isotope signatures and chemical compositions that are significantly different than the upper mantle (Plank and Langmuir 1998; Plank 2014). The transfer of fluid of different origin further suggests open system fluid-rock interaction at depth. Stable isotopes are particularly suited to constrain the origin of subduction fluids and to describe fluid-rock and fluid-rock-melt interaction in subducting slabs (Bebout and Barton 1989; Sharp et al. 1993; Barnicoat and Cartwright 1997; Putlitz et al. 2000; Baumgartner and Valley 2001; Barnes et al. 2014). Distinct rock types are each characterized by a limited range of bulk $\delta^{18}O$ values, and thus the $\delta^{18}O$ composition of the derived fluids (water) at equilibrium can be estimated at a given temperature. Mineral-fluid interaction affecting refractive metamorphic minerals that are robust to successive re-equilibration, such as garnet, will results in intra-crystalline $\delta^{18}O$ variations when the reactive fluid is out of isotopic equilibrium with the bulk rock. Such variations in mineral oxygen isotope composition are a key tool to evaluate fluid-rock interaction with externally-derived fluids and its relative timing during *P–T* evolutions (e.g. Nadeau et al. 1993; Putlitz et al. 2000; Rubatto and Hermann 2003; Errico et al.

2013; Russell et al. 2013; Martin et al. 2014; Page et al. 2014, 2019; Rubatto and Angiboust 2015; Gauthiez-Putallaz et al. 2016; Engi et al. 2018).

D. The Western Alps and the Theodul Glacier Unit

The Western Alps are the product of the closure of the the Piemonte-Ligurian ocean, which formed between continental Europe in the north and continental Adria in the south during the Middle Jurassic (Trümpy 1975; Stampfli et al. 2002). Meta-ophiolites interpreted as relicts of the Piemonte-Ligurian ocean occur in two tectonic units, the structurally higher Combin unit and the lower Zermatt Saas Zone (ZSZ), see Figure 4 (Pleuger et al. 2007). Both tectonic units are now sandwiched between underlying units from the Middle Penninic domain (Briançonnais microcontinent) and overlying units from the Austroalpine domain (Adriatic microcontinent) (Escher et al. 1997). The ZSZ represents a dismembered ophiolitic sequence with mid-ocean ridge (MORB)

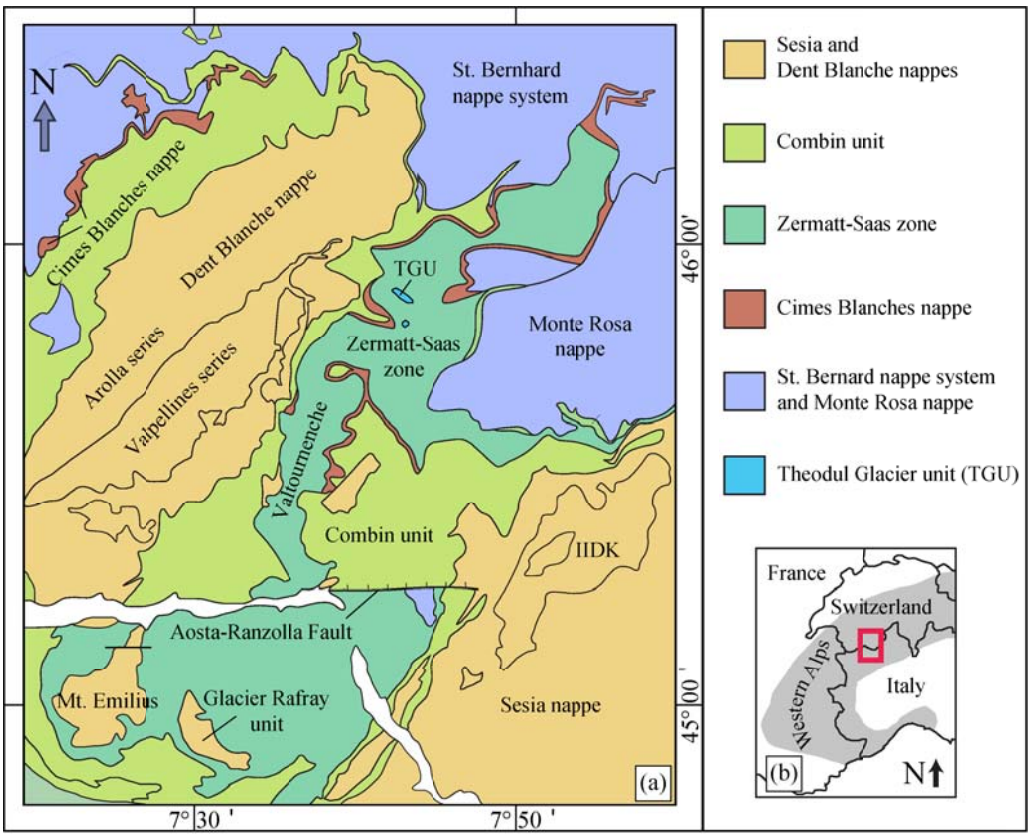

Figure 4: (a) Tectonic map of the Penninic units in the Swiss-Italian Western Alps. Modified after Steck et al. (1999), Pleuger et al. (2007), and Kirst and Leiss (2016). (b) Inset showing the position of the tectonic map within the Western Alps.

affinity (Bearth 1967; Beccaluva et al. 1984; Pfeifer et al. 1989) that has experienced HP to ultra-HP metamorphism (Bearth 1967; Dal Piaz and Ernst 1978; Reinecke 1998; Bucher et al. 2005; Angiboust et al. 2009; Groppo et al. 2009) during Eocene (Duchêne et al. 1997; Rubatto et al. 1998; Amato et al. 1999; Lapen et al. 2003; De Meyer et al. 2014). The overall stratigraphic sequence show slow

spreading ridge affinity (Dilek and Furnes 2014), usually characterized by abundant faulting and limited magma supply (Cannat et al. 1995; Dick et al. 2006). Hydrothermal oceanic alteration affected the ZSZ ophiolite prior to subduction as testified by numerous evidences (Dal Piaz 1979; Cartwright and Barnicoat 1999; Widmer et al. 2000).

The TGU is located SW of the village of Zermatt in Switzerland, close to the Trockener Steg cable car station. The outcropping rocks show little weathering as the retreat of the "Oberer Theodulgletscher" occurred only during the last three decades. The TGU is an association of metasedimentary and metamafic rocks embedded within the ZSZ unit (Fig. 4). The preservation of high-pressure mineral assemblages and the variety of the rock association make this area particularly suitable to investigate oceanic crust lithostratigraphy, *P–T* rock evolutions and fluid-rock interaction in high-pressure environments.

II. THESIS STRUCTURE

The thesis is subdivided in four Chapters, that deals with the geology, origin, metamorphic evolution, and geochemistry of samples from the TGU and the nearby ZSZ in the area of Trockener Steg (south-west Switzerland).

In the **first Chapter,** the geometry and the origin of the metasedimentary sequence (TGU) is defined on the basis of field mapping, bulk rock chemistry and U-Pb dating of zircon.

In the **second Chapter,** the *P–T–t* metamorphic evolution of the unit is unravelled using complex garnet textures, multi-mineral equilibrium thermodynamics and Lu-Hf garnet geochronology.

In the **third Chapter,** open system fluid-rock interaction during subduction is quantified based on oxygen isotope zoning in garnet and simulations using internally consistent thermodynamic and isotopic databases. The origin of the fluid is tracked and the potential mechanism of pervasive fluid flow is explored.

The **fourth Chapter** is an attempt to contextualize the growth stages of the iconic garnet porphyroblasts from the TGU, which yield unexpected and puzzling Lu-Hf date and challenging textures.

BIBLIOGRAPHY

Abers GA, Eilon Z, Gaherty JB, et al (2016) Southeast Papuan crustal tectonics: Imaging extension and buoyancy of an active rift. J Geophys Res Solid Earth 951–971. https://doi.org/10.1002/2015JB012621

Alt JC (1995) Subseafloor processes in mid-ocean ridge hydrothermal systems. Geophys Monogr 91:85–114

Amato JM, Johnson CM, Baumgartner LP, Beard BL (1999) Rapid exhumation of the Zermatt-Saas ophiolite deduced from. Earth Planet Sci Lett 171:425–438

Angiboust S, Agard P (2010) Lithos Initial water budget : The key to detaching large volumes of eclogitized oceanic crust along the subduction channel ? LITHOS 120:453–474. https://doi.org/10.1016/j.lithos.2010.09.007

Angiboust S, Agard P, Jolivet L, Beyssac O (2009) The Zermatt-Saas ophiolite: The largest (60-km wide) and deepest (c. 70-80km) continuous slice of oceanic lithosphere detached from a subduction zone? Terra Nov. https://doi.org/10.1111/j.1365-3121.2009.00870.x

Angiboust S, Pettke T, De Hoog JCM, et al (2014) Channelized fluid flow and eclogite-facies metasomatism along the subduction shear zone. J Petrol 55:883–916. https://doi.org/10.1093/petrology/egu010

Bach W, Bernhard PE, Hart SR, Blusztajn JS (2003) Geochemistry of hydrothermally altered oceanic crust: DSDP/ODP Hole 504B-Implications for seawater-crust exchange budgets and Sr-and Pb-isotopic evolution of the mantle. Geochemistry, Geophys Geosystems 4:40–55. https://doi.org/10.1029/2002GC000419

Barnes JD, Beltrando M, Lee CTA, et al (2014) Geochemistry of Alpine serpentinites from rifting to subduction: A view across paleogeographic domains and metamorphic grade. Chem Geol 389:29–47. https://doi.org/10.1016/j.chemgeo.2014.09.012

Barnicoat AC, Cartwright I (1997) The gabbro-eclogite transformation: An oxygen isotope and petrographic study of west Alpine ophiolites. J Metamorph Geol 15:93–104. https://doi.org/10.1111/j.1525-1314.1997.00058.x

Baumgartner LP, Valley JW (2001) Stable isotope transport and contact metamorphic fluid flow. Rev Mineral Geochemistry 43:414–467

Bearth P (1967) Die ophiolite der Zone von Zermatt-Saas Fee. Beiträge Geol Karte Schweitz 132:1–130

Bebout GE (1991a) Field-Based Evidence for Devolatilization in Subduction Zones: Implications for Arc Magmatism. Science (80-) 251:413–416

Bebout GE (1991b) Geometry and mechanisms of fluid flow at 15 to 45 kilometer depths in an early Cretaceous accretionary complex. Geophys Res Lett 18:923–926. https://doi.org/10.1017/CBO9781107415324.004

Bebout GE (2013) Chemical and Isotopic Cycling in Subduction Zones. Elsevier Ltd.

Bebout GE, Barton MD (1993) Metasomatism during subduction: products and possible paths in the Catalina Schist, California. Chem Geol 108:61–92. https://doi.org/10.1016/0009-2541(93)90318-D

Bebout GE, Barton MD (1989) Fluid flow and Metasomatism in a subduction zone hydrothermal system: Catalina Schist Terrane, California. Geology Vol. 17:976–980

Bebout GE, Penniston-Dorland SC (2016) Fluid and mass transfer at subduction interfaces-The field

metamorphic record. Lithos 240–243:228–258. https://doi.org/10.1016/j.lithos.2015.10.007

Beccaluva L, Macciotta G, Piccardo GB, Zeda O (1984) Petrology of lherzolitic rocks from the Northern Apennine ophiolites. Lithos 17:299–316

Beltrando M, Hermann J, Lister G, Compagnoni R (2007) On the evolution of orogens: Pressure cycles and deformation mode switches. Earth Planet Sci Lett 256:372–388. https://doi.org/10.1016/j.epsl.2007.01.022

Beltrando M, Manatschal G, Mohn G, et al (2014) Recognizing remnants of magma-poor rifted margins in high-pressure orogenic belts: The Alpine case study. Earth-Science Rev 131:88–115. https://doi.org/10.1016/j.earscirev.2014.01.001

Beltrando M, Rubatto D, Manatschal G (2010) From passive margins to orogens: The link between ocean-continent transition zones and (ultra)high-pressure metamorphism. Geology 38:559–562. https://doi.org/10.1130/G30768.1

Borghi A, Compagnoni R, Sandrone R (1996) Composite P-T paths in the Internal Penninic Massifs of the Western Alps: Petrological constraints to their thermo-mechanical evolution. Eclogae Geol Helv 89:345–367

Bougault H (1993) Fast and slow spreading ridges: structure and hydrothermal activity, ultramafic topographic highs, and CH4 output. J Geophys Res 98:9643–9651. https://doi.org/10.1029/93JB00508

Brouwer FM, Vissers RLM, Lamb WM (2002) Structure and metamorphism of the Gran Paradiso massif, western Alps, Italy. Contrib to Mineral Petrol 143:450–470. https://doi.org/10.1007/s00410-002-0357-6

Bucher K, Fazis Y, de Capitani C, Grapes R (2005) Blueschists, eclogites, and decompression assemblages of the Zermatt-Saas ophiolite: High-pressure metamorphism of subducted Tethys lithosphere. Am Mineral 90:821–835. https://doi.org/10.2138/am.2005.1718

Cannat M, Mécel C, Maia M, et al (1995) Thin crust, ultramafic exposures, and rugged faulting patterns at the Mid-Atlantic Ridge (22°-24°N). Geology 23:49–52. https://doi.org/10.1130/0091-7613(1995)023<0049:TCUEAR>2.3.CO;2

Cartwright I, Barnicoat AC (1999) Stable isotope geochemistry of Alpine ophiolites: A window to ocean-floor hydrothermal alteration and constraints on fluid-rock interaction during high-pressure metamorphism. Int J Earth Sci 88:219–235. https://doi.org/10.1007/s005310050261

Connolly JAD (2010) The mechanics of metamorphic fluid expulsion. Elements 6:165–172. https://doi.org/10.2113/gselements.6.3.165

Dal Piaz GV (1979) Manganiferous quartzitic schists of the piemonte ophiolite Nappe-in the Valsesia-valtournach arc, Italian Western Alps. Mem Sci Geol Gia Mom degli Ist Geol Miner dell Univ di Padova 24:

Dal Piaz GV, Ernst WG (1978) Areal geology and petrology of eclogites and associated metabasites of the Piemonte ophiolite nappe, breuil-st. Jacques area, Italian Western Alps. Tectonophysics 51:99–126. https://doi.org/10.1016/0040-1951(78)90053-7

De Meyer CMC, Baumgartner LP, Beard BL, Johnson CM (2014) Rb-Sr ages from phengite inclusions in garnets from high pressure rocks of the swiss western alps. Earth Planet Sci Lett 395:205–216. https://doi.org/10.1016/j.epsl.2014.03.050

Dick HJB, Natland JH, Ildefonse B (2006) Past and future impact of deep drilling in the oceanic crust and mantle. Oceanography 19:72–80. https://doi.org/10.5670/oceanog.2006.06

Dickin AP, Jones NW (1983) Relative elemental mobility during hydrothermal alteration of a basic sill, Isle of Skye, N.W. Scotland. Contrib to Mineral Petrol 82:147–153. https://doi.org/10.1007/BF01166609

Dilek Y, Furnes H (2011) Ophiolite genesis and global tectonics: Geochemical and tectonic fingerprinting of ancient oceanic lithosphere. Bull Geol Soc Am 123:387–411. https://doi.org/10.1130/B30446.1

Dilek Y, Furnes H (2014) Ophiolites and their origins. Elements 10:93–100. https://doi.org/10.2113/gselements.10.2.93

Dinelli E, Lucchini F, Mordenti A, Paganelli L (1999) Geochemistry of Oligocene-Miocene sandstones of the northern Apennines (Italy) and evolution of chemical features in relation to provenance changes. Sediment Geol 127:193–207. https://doi.org/10.1016/S0037-0738(99)00049-4

Duchêne S, Blichert-Toft J, Luais B, et al (1997) The Lu-Hf dating of garnets and the ages of the Alpine high-pressure metamorphism. Nature 387:586–589. https://doi.org/10.1038/42446

Engi M, Giuntoli F, Lanari P, et al (2018) Pervasive Eclogitization Due to Brittle Deformation and Rehydration of Subducted Basement: Effects on Continental Recycling? Geochemistry, Geophys Geosystems 19:865–881. https://doi.org/10.1002/2017GC007215

Errico JC, Barnes JD, Strickland A, Valley JW (2013) Oxygen isotope zoning in garnets from Franciscan eclogite blocks: Evidence for rock-buffered fluid interaction in the mantle wedge. Contrib to Mineral Petrol 166:1161–1176. https://doi.org/10.1007/s00410-013-0915-0

Escher A, Hunziker J-C, Marthaler M, et al (1997) Geologic framework and structural evolution of the western Swiss-Italian Alps

Früh-Green GL, Scambelluri M, Vallis F (2001) O-H isotope ratios of high pressure ultramafic rocks: Implications for fluid sources and mobility in the subducted hydrous mantle. Contrib to Mineral Petrol 141:145–159. https://doi.org/10.1007/s004100000228

Gauthiez-Putallaz L, Rubatto D, Hermann J (2016) Dating prograde fluid pulses during subduction by in situ U–Pb and oxygen isotope analysis. Contrib to Mineral Petrol 171:1–20. https://doi.org/10.1007/s00410-015-1226-4

Gillis KM, Thompson G (1993) Metabasalts from the Mid-Atlantic Ridge: new insights into hydrothermal systems in slow-spreading crust. Contrib to Mineral Petrol 113:502–523. https://doi.org/10.1007/BF00698319

Gregory RT, Taylor HP (1981) An oxygen isotope profile in a section of Cretaceous oceanic crust, Samail Ophiolite, Oman: Evidence for δ 18 O buffering of the oceans by deep (>5 km) seawater-hydrothermal circulation at mid-ocean ridges . J Geophys Res Solid Earth 86:2737–2755. https://doi.org/10.1029/jb086ib04p02737

Groppo C, Beltrando M, Compagnoni R (2009) The P-T path of the ultra-high pressure Lago Di Cignana and adjoining high-pressure meta-ophiolitic units: Insights into the evolution of the subducting Tethyan slab. J Metamorph Geol 27:207–231. https://doi.org/10.1111/j.1525-1314.2009.00814.x

Hacker BR, Peacock SM, Abers GA, Holloway SD (2003) Subduction factory 2. Are intermediate-depth

earthquakes in subducting slabs linked to metamorphic dehydration reactions? J Geophys Res Solid Earth 108:. https://doi.org/10.1029/2001jb001129

Henk A, von Blanckenburg F, Finger F, et al (2000) Syn-convergent high-temperature metamorphism and magmatism in the Variscides: A discussion of potential heat sources. Geol Soc Spec Publ 179:387–399. https://doi.org/10.1144/GSL.SP.2000.179.01.23

Ito E, Harris DM, Anderson AT (1983) Alteration of oceanic crust and geologic cycling of chlorine and water. Geochim Cosmochim Acta 47:1613–1624. https://doi.org/10.1016/0016-7037(83)90188-6

John T, Klemd R, Gao J, Garbe-Schönberg CD (2008) Trace-element mobilization in slabs due to non steady-state fluid-rock interaction: Constraints from an eclogite-facies transport vein in blueschist (Tianshan, China). Lithos 103:1–24. https://doi.org/10.1016/j.lithos.2007.09.005

Kirst F, Leiss B (2016) Kinematics of syn- and post-exhumational shear zones at Lago di Cignana (Western Alps, Italy): constraints on the exhumation of Zermatt–Saas (ultra)high‐pressure rocks and deformation along the Combin Fault and Dent Blanche Basal Thrust. Int J Earth SciGeol Rundsch). https://doi.org/10.1007/s00531-016-1316-1

Konrad-Schmolke M, O'Brien PJ, Zack T (2011) Fluid migration above a subducted slab-constraints on amount, pathways and major element mobility from partially overprinted eclogite-facies rocks (Sesia Zone, Western Alps). J Petrol 52:457–486. https://doi.org/10.1093/petrology/egq087

Kurz W, Neubauer F, Dachs E (1998) Eclogite meso- and microfabrics: implications for the burial and exhumation history of eclogites in the Tauern Window (Eastern Alps) from P - T - d paths. Tectonophysics 285:183–209

Lapen TJ, Johnson CM, Baumgartner LP, et al (2003) Burial rates during prograde metamorphism of an ultra-high-pressure terrane: An example from Lago di Cignana, western Alps, Italy. Earth Planet Sci Lett 215:57–72. https://doi.org/10.1016/S0012-821X(03)00455-2

Li XP, Rahn M, Bucher K (2004) Serpentinites of the Zermatt-Saas ophiolite complex and their texture evolution. J Metamorph Geol 22:159–177. https://doi.org/10.1111/j.1525-1314.2004.00503.x

Mahlen NJ, Johnson CM, Baumgartner LP, Beard BL (2005) Provenance of Jurassic Tethyan sediments in the HP/UHP Zermatt-Saas ophiolite, western Alps. Bull Geol Soc Am 117:530–544. https://doi.org/10.1130/B25545.1

Martin LAJ, Hermann J, Gauthiez-Putallaz L, et al (2014) Lawsonite geochemistry and stability - implication for trace element and water cycles in subduction zones. J Metamorph Geol 32:455–478. https://doi.org/10.1111/jmg.12093

McLennan SM (1989) Rare earth elements in sedimentary rocks: influence of provenance and sedimentary processes. Rev Mineral Geochemistry 21:169–200

McLennan SM (2001) Relationships between the trace element composition of sedimentary rocks and upper continental crust. Geochemistry, Geophys Geosystems 2:. https://doi.org/10.1029/2000GC000109

Miller JA, Cartwright I (2000) Distinguishing between seafloor alteration and fluid flow during subduction using stable isotope geochemistry: Examples from Tethyan ophiolites in the Western Alps. J Metamorph Geol. https://doi.org/10.1046/j.1525-1314.2000.00274.x

Miller JA, Cartwright I, Buick IS, Barnicoat AC (2001) An O-isotope profile through the HP-LT Corsican ophiolite, France and its implications for fluid flow during subduction. Chem Geol. https://doi.org/10.1016/S0009-2541(00)00428-9

Miller SA, Van der Zee W, Olgaard DL, Connolly JAD (2003) A fluid-pressure feedback model of dehydration reactions: Experiments, modelling, and application to subduction zones. Tectonophysics 370:241–251. https://doi.org/10.1016/S0040-1951(03)00189-6

Müller RD, Sdrolias M, Gaina C, Roest WR (2008) Age, spreading rates, and spreading asymmetry of the world's ocean crust. Geochemistry, Geophys Geosystems 9:1–19. https://doi.org/10.1029/2007GC001743

Nadeau S, Philippot P, Pineau F (1993) Fluid inclusion and mineral isotopic compositions (HCO) in eclogitic rocks as tracers of local fluid migration during high-pressure metamorphism. Earth Planet Sci Lett 114:431–448. https://doi.org/10.1016/0012-821X(93)90074-J

Page FZ, Cameron EM, Flood CM, et al (2019) Extreme oxygen isotope zoning in garnet and zircon from a metachert block in mélange reveals metasomatism at the peak of subduction metamorphism. Geology 47:655–658. https://doi.org/10.1130/G46135.1

Page FZ, Essene EJ, Mukasa SB, Valley JW (2014) A garnet-zircon oxygen isotope record of subduction and exhumation fluids from the Franciscan complex, California. J Petrol 55:103–131. https://doi.org/10.1093/petrology/egt062

Peacock SM (1990) Fluid processes in subduction zones. Science (80-) 248:329–337. https://doi.org/10.1126/science.248.4953.329

Pearce JA (2014) Immobile element fingerprinting of ophiolites. Elements 10:101–108. https://doi.org/10.2113/gselements.10.2.101

Pfeifer H, Colombi A, Ganguin J (1989) Zermatt-Saas and Antrona Zone: a petrographic and geochemical comparison of polyphase metamorphic ophiolites of the West-Central Alps. Schweizerische Mineral und Petrogr Mitteilungen 69:217–236. https://doi.org/10.5169/seals-52790

Philippot P, Selverstone J (1991) Trace-element-rich brines in eclogitic veins: implications for fluid composition and transport during subduction. Contrib to Mineral Petrol 106:417–430. https://doi.org/10.1007/BF00321985

Plank T (2014) The Chemical Composition of Subducting Sediments, 2nd edn. Elsevier Ltd.

Plank T, Langmuir CH (1998) The chemical composition of subducting sediment and its consequences for the crust and mantle. Chem Geol 145:325–394. https://doi.org/10.1016/S0009-2541(97)00150-2

Pleuger J, Roller S, Walter JM, et al (2007) Structural evolution of the contact between two Penninic nappes (Zermatt-Saas zone and Combin zone, Western Alps) and implications for the exhumation mechanism and palaeogeography. Int J Earth Sci 96:229–252. https://doi.org/10.1007/s00531-006-0106-6

Poli S, Schmidt MW (2002) Petrology of Subducted Slabs. Annu Rev Earth Planet Sci 30:207–235. https://doi.org/10.1146/annurev.earth.30.091201.140550

Putlitz B, Matthews A, Valley JW (2000) Oxygen and hydrogen isotope study of high-pressure metagabbros and metabasalts (Cyclades, Greece): Implications for the subduction of oceanic crust. Contrib to Mineral Petrol 138:114–126. https://doi.org/10.1007/s004100050012

Reinecke T (1998) Prograde high- to ultrahigh-pressure metamorphism and exhumation of oceanic sediments at Lago di Cignana, Zermatt-Saas Zone, western Alps. Lithos 42:147–189. https://doi.org/10.1016/s0024-4937(97)00041-8

Rubatto D, Angiboust S (2015) Oxygen isotope record of oceanic and high-pressure metasomatism: a P-T-time-fluid path for the Monviso eclogites (Italy). Contrib to Mineral Petrol. https://doi.org/10.1007/s00410-015-1198-4

Rubatto D, Gebauer D, Fanning M (1998) Jurassic formation and Eocene subduction of the Zermatt-Saas-Fee ophiolites: Implications for the geodynamic evolution of the Central and Western Alps. Contrib to Mineral Petrol 132:269–287. https://doi.org/10.1007/s004100050421

Rubatto D, Hermann J (2003) Zircon formation during fluid circulation in eclogites (Monviso, Western Alps): Implications for Zr and Hf budget in subduction zones. Geochim Cosmochim Acta 67:2173–2187. https://doi.org/10.1016/S0016-7037(02)01321-2

Russell AK, Kitajima K, Strickland A, et al (2013) Eclogite-facies fluid infiltration: Constraints from δ18O zoning in garnet. Contrib to Mineral Petrol 165:103–116. https://doi.org/10.1007/s00410-012-0794-9

Schmidt MW, Poli S (2003) Generation of Mobile Components during Subduction of Oceanic Crust. In: Treatise on Geochemistry. pp 567–591

Schmidt MW, Poli S (2013) Devolatilization During Subduction. In: Treatise on Geochemistry: Second Edition, 2nd edn. Elsevier Ltd., pp 669–701

Selverstone J, Franz G, Thomas S, Getty S (1992) Fluid variability in 2 GPa eclogites as an indicator of fluid behavior during subduction. Contrib to Mineral Petrol 112:341–357. https://doi.org/10.1007/BF00310465

Sharp ZD, Essene EJ, Hunziker J-C (1993) Stable isotope geochemistry and phase equilibria of coesite-bearing whiteschists, Dora Maira Massif, western Alps. Contrib to Mineral Petrol 114:1–12. https://doi.org/10.1007/BF00307861

Sizova E, Hauzenberger C, Fritz H, et al (2019) Late orogenic heating of (Ultra)high pressure rocks: Slab Rollback vs. Slab breakoff. Geosci 9:1–28. https://doi.org/10.3390/geosciences9120499

Sorensen SS, Barton MD (1987) Metasomatism and partial melting in a subduction complex: Catalina schist, southern California. Geology 15:115–118. https://doi.org/10.1130/0091-7613(1987)15<115:MAPMIA>2.0.CO;2

Spalla MI, Lardeaux JM, Dal Piaz GV, et al (1996) Tectonic significance of Alpine eclogites. J Geodyn 21:257–285. https://doi.org/10.1016/0264-3707(95)00033-X

Spandler C, Hermann J, Arculus RJ, Mavrogenes J (2003) Redistribution of trace elements during prograde metamorphism from lawsonite blueschist to eclogite facies; implications for deep subduction-zone processes. Contrib to Mineral Petrol 146:205–222. https://doi.org/10.1007/s00410-003-0495-5

Spandler C, Pettke T, Rubatto D (2011) Internal and external fluid sources for eclogite-facies veins in the Monviso Meta-ophiolite, Western Alps: Implications for fluid flow in subduction zones. J Petrol 52:1207–1236. https://doi.org/10.1093/petrology/egr025

Stampfli GM, Borel GD, Marchant R, Mosar J (2002) Western Alps geological constraints on western Tethyan

reconstructions. J Virtual Explor 8:75–104. https://doi.org/10.3809/jvirtex.2002.00057

Steck A, Bigioggero B, Dal Piaz GV, et al (1999) Carte tectonique des Alpes de Suisse occidentale et des régions avoisinantes 1:100000 (Tectonic map of the western Swiss Alps and neighbouring regions). Spec Geol map 123:

Syracuse EM, van Keken PE, Abers GA, et al (2010) The global range of subduction zone thermal models. Phys Earth Planet Inter 183:73–90. https://doi.org/10.1016/j.pepi.2010.02.004

Taetz S, John T, Bröcker M, Spandler C (2016) Fluid–rock interaction and evolution of a high-pressure/low-temperature vein system in eclogite from New Caledonia: insights into intraslab fluid flow processes. Contrib to Mineral Petrol 171:. https://doi.org/10.1007/s00410-016-1295-z

Tatsumi Y (2005) The subduction factory: How it operates in the evolving Earth. GSA Today 15:4–10. https://doi.org/10.1130/1052-5173(2005)015[4:TSFHIO]2.0.CO;2

Trümpy R (1975) Penninic-Austroalpine boundary in the Swiss Alps: a presumed former continental margin and its problems. Am J Sci 275-A:209–238

Ulmer P, Trommsdorff V (1995) Serpentine stability to mantle depths and subduction-related magmatism. Science (80-) 268:858–861. https://doi.org/10.1126/science.268.5212.858

Vitale Brovarone A, Beyssac O (2014) Lawsonite metasomatism: A new route for water to the deep Earth. Earth Planet Sci Lett 393:275–284. https://doi.org/10.1016/j.epsl.2014.03.001

Widmer T, Ganguin J, Thompson AB (2000) Ocean floor hydrothermal veins in eclogite facies rocks of the Zermatt-Saas Zone, Switzerland. Schweizerische Mineral und Petrogr Mitteilungen 80:63–73

Wiederkehr M, Bousquet R, Schmid SM, Berger A (2008) From subduction to collision: Thermal overprint of HP/LT meta-sediments in the north-eastern Lepontine Dome (Swiss Alps) and consequences regarding the tectono-metamorphic evolution of the Alpine orogenic wedge. Swiss J Geosci 101:. https://doi.org/10.1007/s00015-008-1289-6

Wilke FDH, O'Brien PJ, Altenberger U, et al (2010) Multi-stage reaction history in different eclogite types from the Pakistan Himalaya and implications for exhumation processes. Lithos 114:70–85. https://doi.org/10.1016/j.lithos.2009.07.015

Zack T, John T (2007) An evaluation of reactive fluid flow and trace element mobility in subducting slabs. Chem Geol 239:199–216. https://doi.org/10.1016/j.chemgeo.2006.10.020

CHAPTER 1

Origin and deformation of a metasedimentary sliver embedded within the Zermatt-Saas meta-ophiolite: The Theodul Glacier Unit

KEYWORDS

Oceanic crust; U-Pb zircon geochronology; Field mapping;

Volcanoclastic sequence; Bulk rock chemistry

In preparation for submission to *Swiss Journal of Geosciences*

ABSTRACT

The Theodul Glacier Unit outcrops within the Zermatt Saas ophiolite in the Western Alps. The tectonic unit consists of an association of mafic schist, chloritoid-schist, garnet-schist and mafic fels. The sequence reached eclogite facies metamorphism during Alpine orogeny (2.7 GPa and 580 °C). Our mapping reveals that the Theodul Glacier Unit forms a double anticline with an axial plane strikiinig N-S and dipping westwards.

Bulk rock chemistry allows identifying different protolith compositions. Mafic $fels_{TGU1}$ show a bulk composition close to that of OIB and is fundamentally different from the typical MORB signature of the Zermatt-Saas ophiolite. Mafic $fels_{TGU2}$ resembles mafic $fels_{TGU1}$ in major and immobile trace elements, but shows anomalies in mobile elements. This lithology is consequently interpreted as the hydrothermally altered product of the mafic $fels_{TGU1}$. Cld-schist and Grt-schist have a trace element composition comparable to that of the upper continental crust. Finally, mafic schist has a bulk chemistry that is intermediate between the mafic $fels_{TGU1}$ and the Chl- and Grt-schists, in line with its fine layering. The metre-scale intercalation of mafic and felsic components and the widespread occurrence of sulphides suggests sedimentation in a rifted margin associated to hydrothermal activity. The youngest population of zircons from multiple samples of schists and mafic felses returns Permian ages ranging from 230 to 280 Ma. The dated zircon crystals in the schists have variable REE patterns and $\delta^{18}O$ values. Based on similar ages, textures and shapes, the zircon grains from all lithologies are interpreted as detrital, originated from a restricted range of Permian crustal rocks. Zircons found in the underlying gabbro yield an age of 166.7 ± 2.8 Ma, and confirm the gabbro formation during the opening of the Piemont-Ligurian ocean.

The Theodul Glacier Unit is interpreted as a volcanoclastic sequence that was altered at the oceanic floor in the Jurassic. The unit was then subducted to high-pressure conditions together with the Zermatt-Saas ophiolites and was subsequently folded within the ophiolites during exhumation.

1. INTRODUCTION

Ophiolites found within mountain belts are witnesses of oceanic closure at convergent margins, where they represent exhumed fragments of oceanic lithosphere that were deformed and have possibly undergone (high pressure) metamorphism (Dilek and Furnes, 2011, 2014). The origin of highly deformed ophiolites and their heterogeneous rock associations, can be difficult to reconstruct because the original lithological contacts are reworked and pristine mineral assemblages might be overprinted (Spalla *et al.*, 1996; Beltrando *et al.*, 2014).

Numerous studies have used major and trace element geochemistry to categorize and end members oceanic crust material, where sedimentary and magmatic rocks have characteristic signatures (McLennan, 2001; Pearce, 2014; Plank, 2014). Despite possible hydrothermal alteration at seafloor and later metamorphism, meta-ophiolites can partly preserve their pristine bulk rock composition from which their provenance can be constrained (Pfeifer *et al.*, 1989; Dinelli *et al.*, 1999; Li *et al.*, 2004; Mahlen *et al.*, 2005). In order to validate rock origin, elements suspected to represent original signature have to be wisely evaluated prior to comparison with known reservoirs. In the case of an area where hydrothermal alteration is suspected, the use of specific trace element known for their resistance to mobilisation is preferred (McLennan *et al.*, 1993; Spandler *et al.*, 2004). Rare earth elements (REE) are commonly used to classify rocks, because they are relatively immobile through sedimentation processes, such as diagenesis, weathering and erosion, as well as during metamorphism (Green *et al.*, 1969; Taylor and McLennan, 1985; McLennan, 1989; Taylor and Mclennan, 1995; Spandler *et al.*, 2004; Mahlen *et al.*, 2005) and seafloor hydrothermal alteration (Hellman *et al.*, 1979; Dickin and Jones, 1983; Dungan *et al.*, 1983; Staudigel and Hart, 1983; Bach *et al.*, 2003; Pearce, 2014). High field strength elements (HFSE) are also relatively immobile and incompatible (Staudigel *et al.*, 1996; Paulick *et al.*, 2006) and their combination with specific REE can help to infer magma origin and evaluate crustal contamination (Pearce, 2008, 2014).

Together with investigation of bulk rock chemistry, the origin of the material that underwent metamorphism at convergent margins can be tracked through mineral resistant to re-equilibration (e.g. Manzotti and Ballèvre, 2013; Manzotti *et al.*, 2015). Zircon is well-known for its capacity to grow in magmatic and metamorphic environment and record the successive events that affected its host rock. Zircon does not only to have the ability to provide accurate absolute age constraints (Rubatto, 2017), but can also yield information on the mineral assemblage in which it grew through its REE composition (e.g. Rubatto, 2002), or retain the $\delta^{18}O$ composition of the growth environment (e.g. Valley, 2003). In the Alps, zircon studies have set important time constraints on the overall geodynamic evolution, deciphering events such as detrital provenance of sediments, and the main

stages of pre- and post-Alpine magmatism, as well as Variscan and Alpine metamorphism (e.g. Rubatto *et al.*, 1998, 1999; Liati *et al.*, 2000, 2003; Manzotti *et al.*, 2015; Kunz *et al.*, 2018).

This study aims to characterize the Theodul Glacier Unit (TGU), a metasedimentary slice embedded within the Zermatt-Saas (ZSZ) meta-ophiolite in the Western Alps. There has been disagreement whether the tectonic unit is a poly-metamorphic continental allochton (Bucher *et al.*, 2019, 2020) or a mono-metamorphic sedimentary sequence (Chap. 2). In the course of this study it has been established that the TGU underwent a mono-metamorphic history through Alpine deformation (Chap. 2). In this Chapter the origin of the protoliths and the timing of sedimentation is investigated through field mapping, bulk rock chemistry and zircon investigation.

2. GEOLOGICAL AND TECTONIC BACKGROUND

The Western Alps are the product of the closure of the Piemonte-Ligurian ocean, which formed between continental Europe in the north and continental Adria in the south during the Middle Jurassic (Trümpy, 1975; Stampfli *et al.*, 2002). The plate convergence leading to Alpine collision began during late Cretaceous with a SE-directed subduction of the Piemonte-Ligurian ocean beneath the Apulian plate (Duchêne *et al.*, 1997; Rubatto *et al.*, 1999, 2011). The closure of the oceanic basin occurred when the European margin reached the subduction zone in the late Eocene and continent-continent collision started (Lapen *et al.*, 2003; Brouwer *et al.*, 2005; Sandmann *et al.*, 2014). The composing tectonic units of the Western Alps belong to different paleogeographic realms with components from (Lower Penninic) the European margin and Valais ocean (a minor basin close to the European margin), the Briançonnais microcontinent (Middle Penninic), the Piemonte-Ligurian ocean (Upper Penninic) and the Adriatic microcontinent (Austroalpine domain) (Escher *et al.*, 1997; Stampfli *et al.*, 2002; Dal Piaz *et al.*, 2003; Schmid *et al.*, 2004). These groups of nappes were diachronously subducted to various depth and finally juxtaposed during their later exhumation, where the structurally highest unit were subducted first and are derived from a more southerly paleogeographic origin (Dal Piaz *et al.*, 2003).

Studies have shown that the structural history of the Western Alps are associated to three main deformation stages (Sartori, 1987; Steck, 1990; Pleuger *et al.*, 2005, 2007). The oldest structures were formed by north-west-vergent shearing (D_1). The second deformation event (D_2), which partially or totally overprinted the D_1 structures, is characterised by west- to southwest-vergent shearing. Deformation events D_1 and D_2 lead to the formation of isoclinal folds, which axes are parallel to their respective stretching direction. The third deformation stage (D_3) is related to east- to southeast-vergent shearing and might have affected D_1 and D_2. D_3 is associated to formation of isoclinal folds parallel to the stretching direction in the south and oblique to perpendicular in the

north. The resulting nappe stack has a dominant SE dip except in its internal part where backfolding and backthrusting caused important NW and N dips (Escher *et al.*, 1997).

In the Western Alps, ophiolites interpreted as relicts of the Piemonte-Ligurian ocean occur in two tectonic units, the structurally higher Combin unit (CBU) and the lower ZSZ (Pleuger *et al.*, 2007). Both tectonic units are now sandwiched between underlying units from the Middle Penninic domain and overlying units from the Austroalpine domain (Escher *et al.*, 1997). The ZSZ represents a dismembered ophiolitic sequence with mid-ocean ridge (MORB) affinity (Bearth, 1967; Beccaluva *et al.*, 1984; Pfeifer *et al.*, 1989) that has experienced HP to ultra-HP metamorphism (Bearth, 1967; Dal Piaz and Ernst, 1978; Reinecke, 1998; Bucher *et al.*, 2005; Angiboust *et al.*, 2009; Groppo *et al.*, 2009) during Eocene (Duchêne *et al.*, 1997; Rubatto *et al.*, 1998; Amato *et al.*, 1999; Lapen *et al.*, 2003; De Meyer *et al.*, 2014). It is composed of an association of metabasalts and metagabbros with a Jurassic protolith age (Rubatto *et al.*, 1998; Rubatto and Hermann, 2003; Pleuger *et al.*, 2007; Beltrando *et al.*, 2010) situated on top of a thick section of serpentinite (Bearth, 1967; Li *et al.*, 2004; Pleuger *et al.*, 2007; Angiboust and Agard, 2010; Fassmer *et al.*, 2016; Kirst and Leiss, 2016). The oceanic sedimentary cover of the oceanic basement also called “Schist Lustrés” or “Bündnerschiefer”, is mainly composed by marbles, schists, calcschists, metaradiolarites and Mn-bearing metacherts of Jurassic to Cretaceous protolith age (Bearth, 1967). The sediments discontinuously overlay the mafic to ultramafic rocks forming a thin continuous cover of the oceanic crust (Dal Piaz, 1979). The overall stratigraphic sequence show slow spreading ridge affinity (Dilek and Furnes, 2014), usually characterized by abundant faulting and limited magma supply (Cannat *et al.*, 1995; Dick *et al.*, 2006). Hydrothermal oceanic alteration affected the ZSZ ophiolite prior to subduction as testified by (a) occurrences of Fe–Cu sulphide in metabasalts and Mn ore deposits in siliceous sediments (Dal Piaz, 1979), (b) enrichment or depletion in major elements such as Mg, Ca, and Na in metabasalts (Widmer *et al.*, 2000), and (c) scattering of bulk rock $\delta^{18}O$ values of mafic and ultramafic rock types (Cartwright and Barnicoat, 1999).

Several slices of continental material are found at high structural level of the ZSZ, or along the tectonic contact between the CBU and ZSZ (Ballèvre *et al.*, 1986; Dal Piaz *et al.*, 2001) and are: the Etirol-Levaz, the Glacier Rafray and the Monte Emilius tectonic units (Pennacchioni, 1996; Dal Piaz *et al.*, 2001; Beltrando *et al.*, 2010; Fassmer *et al.*, 2016; Angiboust *et al.*, 2017). They consist of pre-Alpine basement rocks (Compagnoni, 1977; Spalla *et al.*, 1996; Dal Piaz *et al.*, 2001) that were partially overprinted by Alpine eclogite-facies metamorphism at similar conditions to those of the ZSZ (Fassmer *et al.*, 2016; Angiboust *et al.*, 2017) It has been proposed that the continental slivers were either incorporated into the ZSZ during Alpine deformation (Pleuger *et al.*, 2007; Kirst and Leiss, 2016), or that they became part on the Piemonte-Ligurian oceanic domain during early

Mesozoic rifting (Dal Piaz *et al.*, 2001; Beltrando *et al.*, 2010). In the latter case they would form a paleogeographic entity with the ZSZ zone (Fassmer et al., 2016), where juxtaposition of continental basement on top of serpentinites is typically found along OCT zones (Péron-Pinvidic and Manatschal, 2009; Beltrando *et al.*, 2010).

The TGU is a complex lithological association with felsic components embedded within the ZSZ unit. Bucher *et al.* (2019, 2020) interpreted the TGU as an extensional allochton, i.e a sliver of Permian continental crust, and a polymetamorphic history was deduced. Evidence in support of this hypothesis are (i) the proposed high-T granulitic core of the garnet in the schists (Weber an Bucher 2015 (Bucher *et al.*, 2019) and (ii) ID-TIMS dilution U-Pb dating of zircon from the mafic fels that returned an age of 295 ± 16 Ma (Bucher *et al.*, 2020). Lu-Hf dating of garnet from the mafic fels constrains the overprinting Alpine HP metamorphism at ~57 Ma (Weber and Bucher, 2015; Weber *et al.*, 2015), whereas garnet rim equilibria from the schist only recorded decompression (Bucher *et al.*, 2019). As detailed in Chapter 2 and based on multi-mineral approach, I propose a mono-metamorphic Alpine evolution for the TGU with a high-*P* peak at 26.5 kbar and 580 °C, at ~50 Ma (Lu-Hf bulk rock-garnet geochronology). The TGU complex garnet textures in the schist are interpreted as a result of intense pervasive fluid-rock interaction during HP metamorphism (Chap. 3). This latter interpretation is supported by a significant drop in $\delta^{18}O$ from garnet core to rim (Chap. 3) that can be reconciled with ingress of fluids sourcing from dehydration reaction from ZSZ serpentinites (Chap. 3).

In this Chapter, a new interpretation of TGU geometry and rock nomenclature is proposed based on field mapping and structural data analysis. Investigation of zircon (in situ U-Pb dating, $\delta^{18}O$ and trace element analysis) and bulk rock chemistry on a large spectrum of TGU lithologies allow further constraining the detrital origin of the sequence and the timing of sedimentation, as well as to make comparisons with the rocks of the ZSZ meta-ophiolite.

3. MAPPING AND LITHOLOGIES

The investigated field area is located SW from Trockener Steg cable car stop nearby Zermatt in Switzerland. Due to discrepancies between field observations made in the course of this study and what reported Weber and Bucher (2015), a mapping re-evaluation of the area and a new rock nomenclature is proposed for the TGU. The mapping was performed at 1:2,500 scale for an area of 1,500 x 400 m (Fig. 1). The outcropping rocks show little weathering thanks to the retreat of the "Oberer Theodulgletscher" glacier in the last decades. Active superficial weathering of sulphides gives a typical rusty tint to the rock outcrop. This weathering phenomenon affects pervasively and heterogeneously all rock types within the TGU (Fig. 2) and creates a marked colour contrast with the

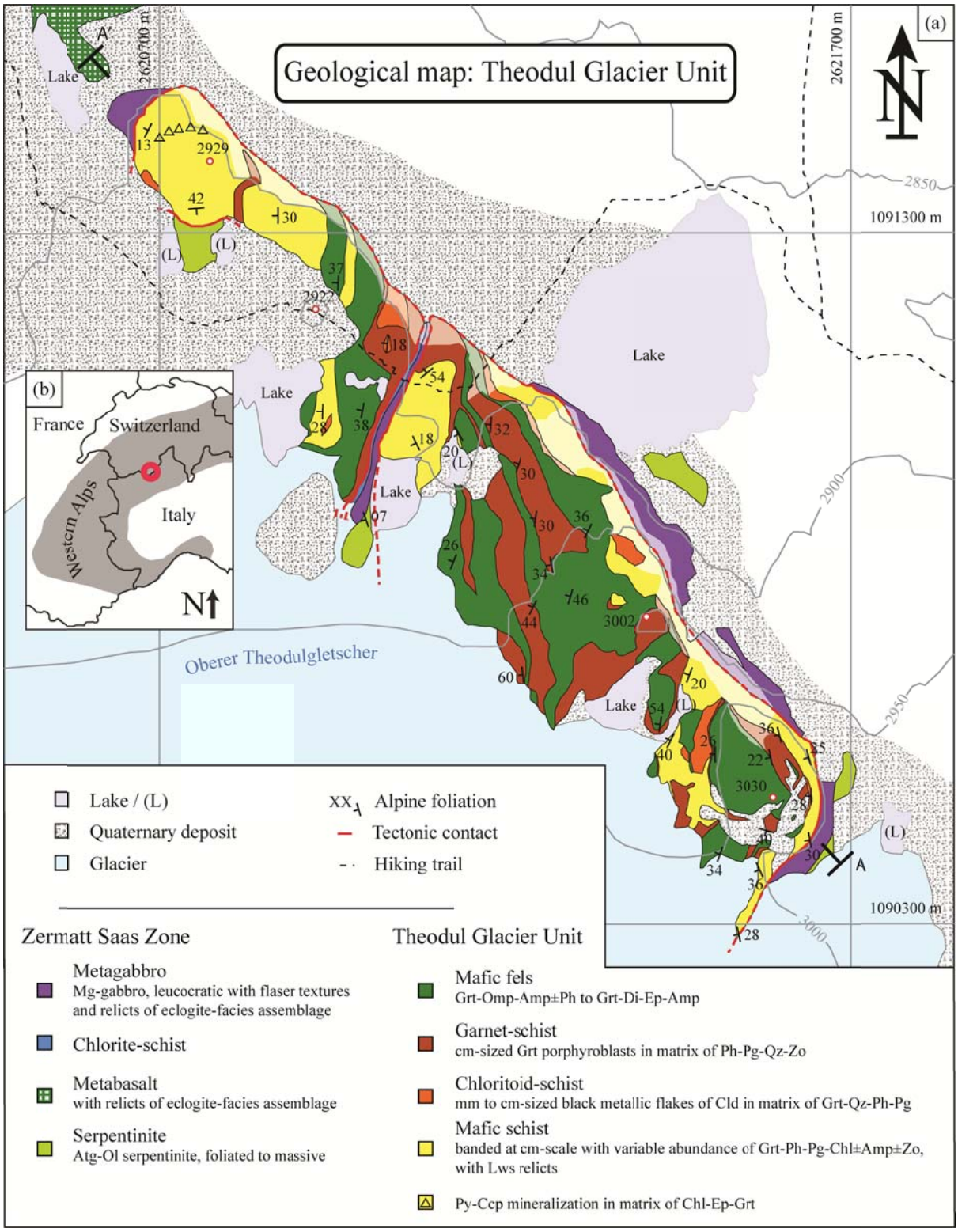

Figure 1: (a) Geological map of the Theodul Glacier Unit. A-A' specifies the location of the cross section. (b) Inset showing the position of TGU within the Western Alps.

surrounding ZSZ rocks. Field observation permit to make a connection between the TGU main outcrop at Trockener Steg and a smaller isolated outcrop located nearby the Theodul pass (Fig. 2a). At this specific place, the outcrop shows a fold hinge highlighted by contrasting colours (Fig. 2b,c),

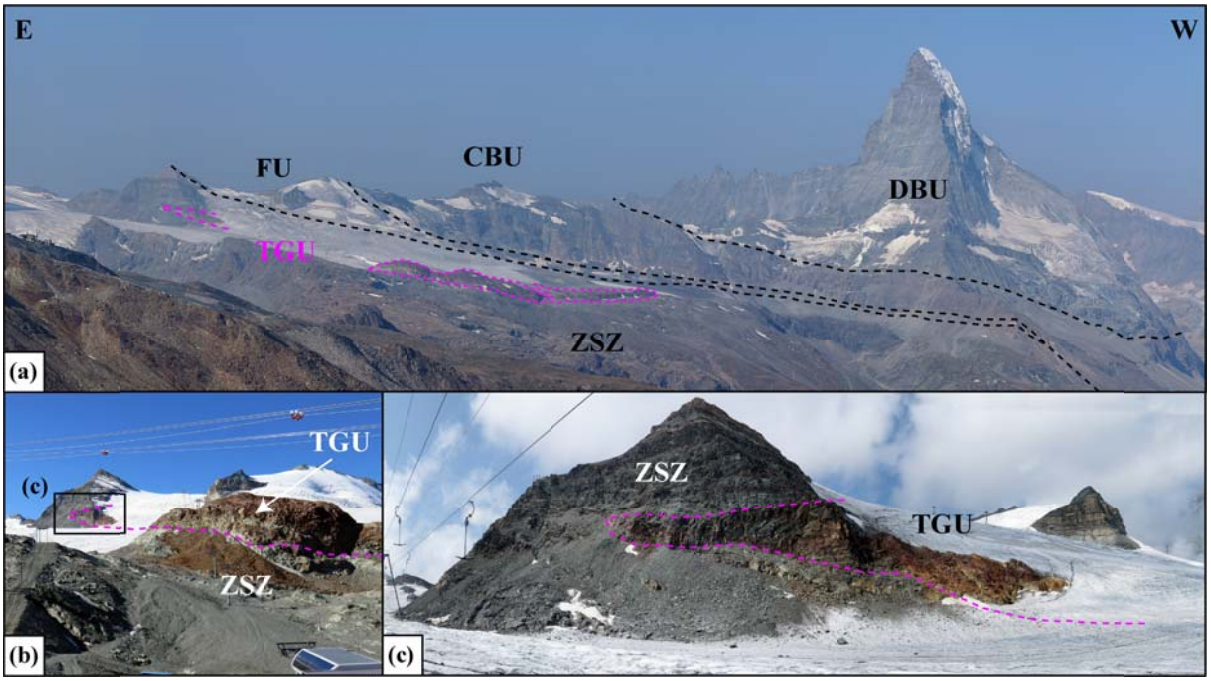

Figure 2: Landscape view of the field area. ZSZ: Zermatt-Saas Zone, TGU: Theodul Glacier Unit, FU: Frilihorn Unit, CBU: Combin Unit, DBU: Dent Blanche Unit. (a) Panorama taken from the Pfulwe pass. The different tectonic units and their spatial organization are highlighted with dashed lines. (b) The main outcrop of the TGU (right side) and the outcrop near the Theodul pass (left side) are linked with a pink dashed line. (c) View of the TGU fold hinge near the Theodul pass, showing that the TGU is embedded within the ZSZ.

composed by the rusty TGU lithologies at its core surrounded by ZSZ serpentinites. Notably, representative Grt-schists were observed, which were closely associated with mafic fels and mafic schist. Foliation measurements were collected on the field (Fig. S1) and analysed stereographically (Fig. 3) to investigate the TGU geometry. Two main foliation populations can be distinguished: the first and main foliation is striking N-S slightly dipping towards the West, whereas the second foliation group is dipping southwards with E-W strike.

Four main lithologies are recognised within the TGU (Fig. 1): the mafic schist, the chloritoid-schist (Cld-schist), the mafic fels and the garnet-schist (Grt-schist). Only a brief description of these rock types is given here, because the Grt-schist is carefully described in Chapter 4, whereas the other rock types are described in detail in Chapter 2. Eclogites and metagabbro from the ZSZ, sampled at Trockener Steg, were investigated in order to make comparison with the different TGU lithologies. TableS1 lists the 24 samples investigated with coordinates and mineral assemblage determined by optical microscopy and Raman spectroscopy.

3.1. Lithologies of the TGU

The mafic schist is the most abundant and widespread lithology of the TGU (Fig. 1). This lithology is found along the basal contact between the TGU and the ZSZ. It is well-foliated and composed of layers ranging from 1 cm to a few metres in thickness (Fig. 4a). The transition between each layer can be either sharp or gradual. The mineral assemblage garnet-phengite-paragonite-

quartz-chlorite±amphibole±zoisite is common to every layer but with a strong variation in mineral abundance, where zoisite can reach up to 70 vol%. Three garnet populations are observed that are differentiated regarding their chemical zoning and $\delta^{18}O$ composition variation, where garnet size is a good first order indicator to discriminate each garnet type (Chap. 2). Milky, diamond-shaped areas composed of a fine-grained association of zoisite-quartz-paragonite±garnet are interpreted as lawsonite pseudomorphs (Fig. 4b). In the western part of the TGU, the mafic shist is hosting a highly mineralized layer of around 2 m thickness (Fig. 1,4c). The mineralization is pervasive with association of anhedral pyrite-chalcopyrite within a chlorite-epidote-garnet matrix. Inhomogeneous retrogression is manifested by occurrence of chlorite+paragonite as a result of garnet alteration, titanite surrounding rutile and poikiloblastic albite.

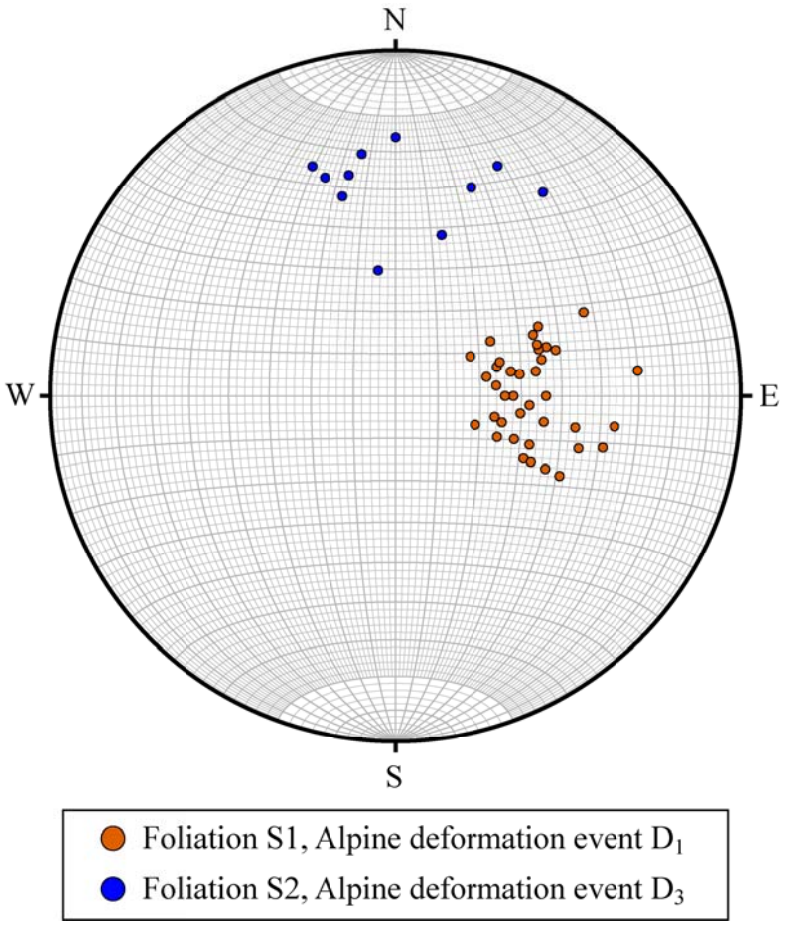

Figure 3: Lower-hemisphere projection plot of foliation represented as poles.

Cld-schist is a well-foliated lithology characterized by the occurrence of dark metallic chloritoid flakes. These minerals can reach up to 1 cm in diameter and are oriented parallel to the rock foliation made of quartz-phengite-paragonite (Fig. 4d). Euhedral garnet (0.2-0.4 mm diameter) and sporadic relicts of amphibole porphyroblasts complete the mineral assemblage. Rare crosscutting vein of chloritoid-quartz-garnet are observed.

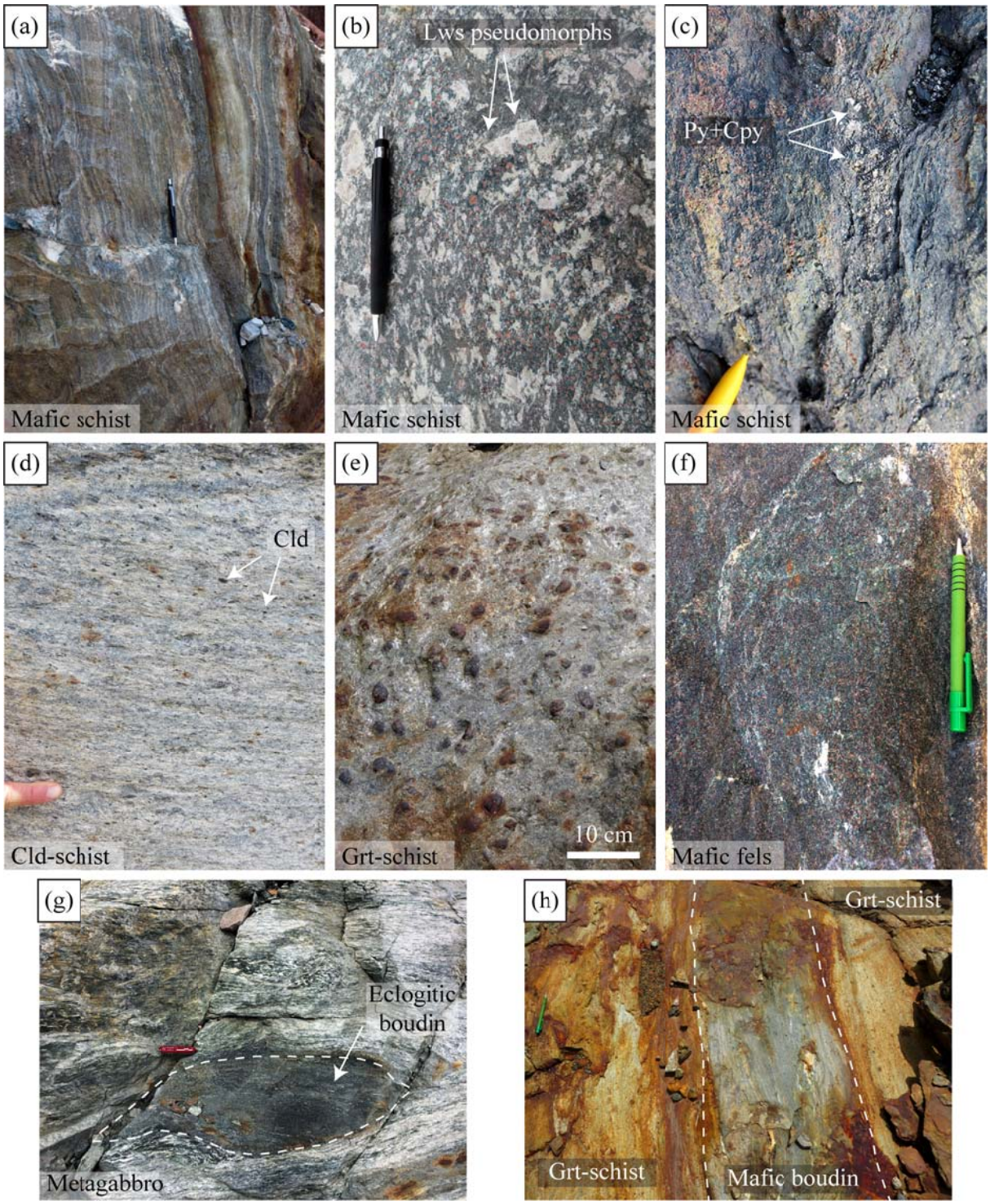

Figure 4: Field photographs of the representative lithologies of the TGU (a-f) and ZSZ (g). Mineral abbreviations follow Whitney and Evans (2010). (a) Banded mafic fels with layering parallel to the foliation. (b) Mafic schist with diamonds-shaped domains interpreted as pseudomorphs after lawsonite. (c) Pervasive mineralization within the mafic schist. (d) Cld-schist with dark flaky chloritoid. (e) Grt-schist with cm-sized garnet porphyroblasts and the typical patchy rusty weathering. (f) Mafic fels where the lighter areas are predominantly Omp-rich, whereas darker areas are Amp-rich. (g) Basal metagabbro layer with typical flaser texture and containing an eclogitic boudin. The metagabbro belongs to ZSZ and crops out along the tectonic contact between the TGU and the ZSZ. (h) Mafic fels boudin embedded in Grt-schist.

Layers of **Grt-schist** occur close and/or around the layers and boudins of mafic fels (Fig. 1,4h). The schist shows a pervasive foliation and contains a mineral assemblage of quartz-phengite-paragonite-zoisite. Garnet has a bimodal size distribution. The first population is characterized by spectacular rounded euhedral garnet porphyroblasts that are pluri-centimetric in diameter (Fig. 4e). The smaller garnets found as single grain in the matrix have a varying size ranging from few hundreds µm to mm in diameter and can be rounded or euhedral. Accessory phases are apatite, zircon, graphite, rutile and titanite. Rutile grains are aligned along the main foliation. Retrogression occurs locally and is marked by chlorite that usually rims garnet, and titanite around rutile.

Mafic fels occurs either as large coherent bodies of up to 10 m thick or as stretched boudins that are cm to m in size. These boudins are found within the mafic schist and Grt-schist (Fig. 4h) and elongated along to the main foliation. The largest bodies of mafic fels are observed in the highest topographic zone of the TGU outcrop (Fig. 1) as opposed to the north-western flank of the south-eastern hill, which shows a complex imbrication of Grt-schist and mafic boudins. The mafic fels is characterized by two main mineral assemblages, garnet-omphacite-amphibole±phengite±quartz on one side (Mafic fels$_{TGU1}$, Fig. 4f), as described by Bucher *et al.* (2020), and garnet-zoisite-epidote-diopside-amphibole (Mafic fels$_{TGU2}$, Fig. 2c in Chap. 2) on the other side. Both types contains an unexpected high amount of zircon, as described for the mafic fels$_{TGU1}$ (Weber and Bucher, 2015; Bucher *et al.*, 2020). Layering is due to mineral modal assemblage variation, which transition can be either sharp (Fig. 2b in Chap. 2) or gradual (Fig. 2c in Chap. 2). Fine layering and sulphide weathering can hamper the distinction between mafic fels and mafic schist in the field. Undeformed veinlets of garnet-diopside-amphibole-quartz-calcite are observed in some mafic boudins (Fig. 1b in Chap. 3). Inhomogeneous retrogression is characterized by chlorite, amphibole, albite and titanite together with crosscutting albite-epidote veins.

3.2. Lithologies of the ZSZ

The **eclogites** of the ZSZ that are in contact with the TGU unit in the areas of Trockener Steg contain the mineral assemblage garnet-omphacite-amphibole-zoisite-epidote-white mica with variable mineral modal assemblage. On the north-western part of the field area (Fig. 1) the rocks are outcropping as large and massive bodies with a weak foliation. Diamond-shaped areas are interpreted as pseudomorphs after lawsonite. The large area facing the cliff on the north-eastern part of the field area is more chaotic, showing a complex imbrication of foliated ultramafic lenses (serpentinite and ophicarbonates) of various sizes (dm to 40m) embedded within calcsilicates, calcschists, epidosites and banded metabasalts.

Leucocratic metagabbro (Fig. 4g) is observed at the contact with the mafic schist along the basal contact between the TGU and the ZSZ (Fig. 1,5a). The layers of metagabbro vary in thickness from dm to metre. This rock types outcrops: (i) in the south-eastern side of the mapped area, at the bottom of the cliff, (ii) at the extreme north-western part of the area and (iii) on a north-south striking band separating the schists approximatively in the centre of the mapped area. Mylonitic flaser texture, folded foliation and eclogitic boudins stretched along the foliation are evidence of intense deformation (Fig. 4g).

Chlorite schist (Chl-schist) is observed at the contact between the metagabbro and the mafic schist, or at the contact between the serpentinite and the mafic schist (Fig. 1,5). The level of chlorite-schist is variable in thickness, but generally below a meter. At the outcrop scale, this lithology shows intense foliation and development of pinch and swell structure (Fig. 5a).

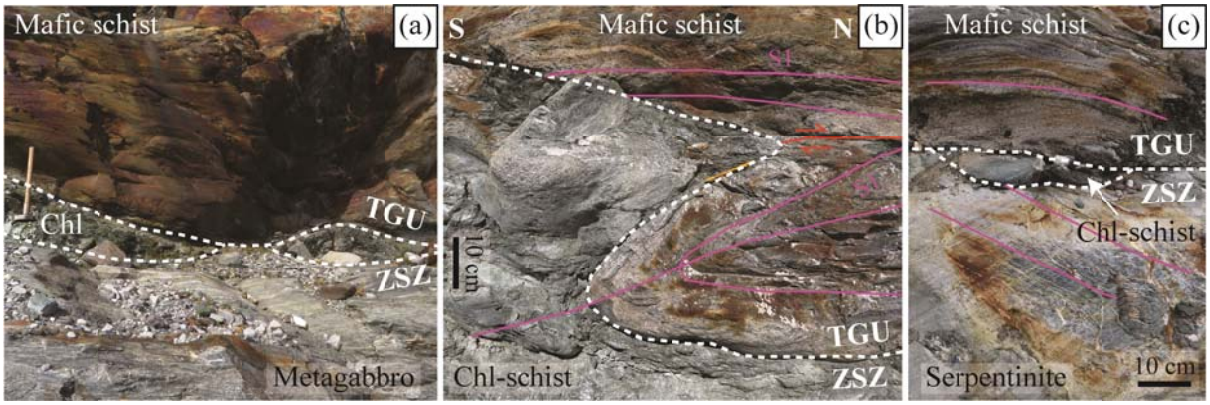

Figure 5: Field photographs of the contact between the ZSZ and the TGU. (a) Contact between the mafic schist from the TGU and the underlying metagabbro from the ZSZ. Note the pinch and swell of the Chl-schist, which locally marks the contact. The colour contrast is between the rusty pattern of the TGU metasediment due to sluphide weathering and the milky colour of the flaser metagabbro of the ZSZ. (b) Secondary Z-folding in the mafic schist (axial plane: 286/20) at the tectonic contact between the two antiforms. The deformation is overprinted by top to the NW shearing (see text for contextualisation). (c) Upper contact between serpentinites (ZSZ) and the mafic schist (TGU), with discordant foliation (foliation marked by the pink lines). A lens of Chl-schists marks the contact.

4. ANALYTICAL METHODS

4.1. Bulk rock chemistry on pressed powder pellets

Bulk rock chemical analyses were conducted at the Institute of Geological Sciences, University of Bern (Switzerland). Weathered material was first removed from rock samples, the rocks were subsequently crushed by using a stainless steel mortar and pestle. The samples were then dry milled in an agate mill ring for 30 min. Each run of sample was bracketed by sand quartz milling for 15min in order to clean the receptacle. Nanoparticulate pressed powder pellets (PPP) were created following the procedure described in Peters and Pettke (2017) by using microcrystalline cellulose as a binder. The PPP were analysed using a laser ablation inductively coupled plasma mass

spectrometer (LA-ICP-MS) consisting of a GeoLas-Pro 193 nm ArF Excimer laser system (Lambda Physik, Göttingen, Germany) in combination with an ELAN DRC-e quadrupole mass spectrometer (Perkin Elmer, Waltham, MA, USA). Calibration was based on GSD-1G (Jochum *et al.*, 2011) reference material. BRP-1 (Cotta *et al.*, 2007) was used as a secondary standard (Peters and Pettke, 2017) and accuracy was always better than 10%. PPP were measured in single spot mode with and energy density of 6 Jcm^{-2} at a repetition rate of 10 Hz and a beam size of 90 µm. Six analyses were measured for each PPP. The surface area was cleaned by pre-ablation using a larger spot size and for each analysis the signal was integrated over a 50-60 s. Data reduction was performed offline by using the software SILLS (Guillong *et al.*, 2008) and limits of detection were calculated after Pettke *et al.* (2012). Internal standardization was done by assuming (i) a fixed total of 100 wt% for major and trace elements, minus volatiles determined by loss on ignition; (ii) all Fe is present as Fe_2O_3.

4.2. Zircons investigation

Sample preparation was done at the Institute of Geological Sciences, University Bern. Samples were disaggregated using a SelFrag Lab system by high-voltage discharge, and sieved to select the grain fraction between 64 and 250 µm. Zircon grains were recovered using conventional magnetic and heavy liquid mineral separation. The grains were handpicked under a binocular microscope, mounted in an epoxy mount and polished to equatorial section. Zircon charge contrast (CC) images were acquired using a scanning electron microscope (SEM) ZEISS EVO50 operating at 10 keV accelerating voltage, 10 mm working distance, 1 nA beam current, and at variable pressure (VP) conditions. It has been previously demonstrated that CC images correlate exactly to cathodoluminescence (Watt *et al.*, 2000), as also confirmed by checks in the Bern laboratory.

4.2.1. U-Pb dating

Zircon U-Pb geochronology was performed using the SwissSIMS Cameca IMS 1280-HR ion probe at the University of Lausanne, during two sessions. Basic instrument set up parameters follow those described by Whitehouse and Kamber (2005) and included a O_2 primary beam of 5-7 nA, mass resolution M/ΔM ~5000, energy window = 40 eV, and spot size 20-25 µm. TEM zircon (reference 417 Ma, Black *et al.* 2003) was used as primary standard to correct for instrumental mass fractionation. Two secondary standards each ran during different analytical session reproduced average $^{206}Pb/^{238}U$ ages within reference values: 91500 zircon 1053 ± 15 Ma (session1, reference 1065 Ma, Wiedenbeck *et al.* 1995) and Pleisovice zircon 337 ± 4 Ma (session2, reference 337 Ma, Sláma *et al.* 2008). Uncertainty on standard $^{206}Pb/^{238}U$ – UO_2/U calibration were 1.5% (session1) and 2.0% (session2), which were propagated to the data as external error. Common Pb correction was based on the

measured ^{204}Pb signal (when significant relative to background) assuming the present day model terrestrial Pb composition of Stacey and Kramers (1975). Data evaluation and age calculation were done using the software Squid 2 and Isoplot/Ex (Ludwig, 2003), respectively. Age calculations use the decay constant recommendations of Steiger and Jäger (1977). The Isoplot Ex 4.15 (Ludwig, 2012) was employed to plot the diagrams and calculate concordia and weighted average ages. Individual uncertainties are quoted at 1σ level, the confidence level for weighted average and Concordia ages is 95% if not otherwise stated.

4.2.2. Oxygen isotope

In situ oxygen isotope analyses of zircon was performed using a CAMECA SIMS 1280HR ion probe at the Institute of Earth Sciences (University of Lausanne). The analyses were carried out following the protocol detailed in Seitz *et al.* (2018). A 10 kV $^{133}Cs^{+}$ primary Gaussian ion beam was used with a 1.8-2.0 nA current, which ended up with a typical spot size of 10 – 15 µm. A pre-sputtering time of 30 s was applied to remove gold coating, followed by automated secondary beam centering and 20 cycles of 5 s data acquisition. Data standardization was made using TEM200 zircon ($\delta^{18}O$ = 8.2 ‰, Valley (2003)). Count rates on the ^{16}O peak were between 1.8 and 1.9x10^{9} counts per second. Additionally, secondary zircon reference material 91500 (Valley, 2003; Wiedenbeck *et al.*, 2004) was analysed to confirm the matrix bias calibration (TableS2). In every case the $\delta^{18}O$ value obtained for the secondary reference material was within uncertainty of the reference values reported in Valley (2003). The internal uncertainty on individual oxygen isotopic analyses ranges between 0.12 and 0.27 ‰ (2σ), whereas the total uncertainty that includes the repeatability of the primary standard is 0.21 to 0.37 ‰ (2σ).

4.2.3. Trace elements

LA-ICP-MS mineral analyses of zircon were conducted using a Resonetics RESOlutionSE 193nm excimer laser system equipped with a S-155 large volume constant geometry chamber (Laurin Technic, Australia). The laser system was coupled to an Agilent 7900 quadrupole ICP-MS instrument. Zircon was ablated at 5 Hz and a fluence of 4 J·cm^{-2}. Calibration was performed using reference material NIST 612 (Jochum *et al.*, 2011), whereas GSD-1G (Jochum *et al.*, 2005) was used as secondary standard. The reference material was analysed every eight unknowns. Data were reduced offline employing Iolite v7.08 (Paton *et al.*, 2011). Drift was linearly corrected by bracketing the unknowns with the calibration material and LODs were calculated according to Pettke *et al.* (2012). Spot size was set at 30 µm according to grain size. During post acquisition quantification

processing ^{29}Si (14.76 wt%) was used as internal standard. Accuracy on secondary standard GSD-1G was within 10% for all elements and 30% for Y and 40% for Zr.

5. MAJOR AND TRACE ELEMENT BULK ROCK GEOCHEMISTRY

The major- and trace-element bulk rock composition of 22 samples form TGU and ZSZ was measured (TableS3). In samples with fine interlayering or banding, a representative piece was selected and the analysed bulk rock chemistry is an average of the variation within the sample. REE element pattern normalized to Chondrite are presented in Fig. 6, whereas major and trace element normalized to chondrite are presented in Fig. 7.

Among the TGU lithologies, the Chondrite normalized REE plot for the mafic $fels_{TGU1}$ (Fig. 6a,b) shows a particularly restricted range. The pattern decreases linearly from LREE (~100) to HREE (~10) and is comparable to average OIB from Sun and McDonough (1989). The REE pattern for different samples of mafic $fels_{TGU2}$ is more variable, with an overall trend decreasing from La (~60-100) to Dy (~10-20), whereas HREE shows a flat pattern (Fig. 6a,b). Three of the samples classified as mafic $fels_{TGU2}$ show a minor Eu negative anomaly.

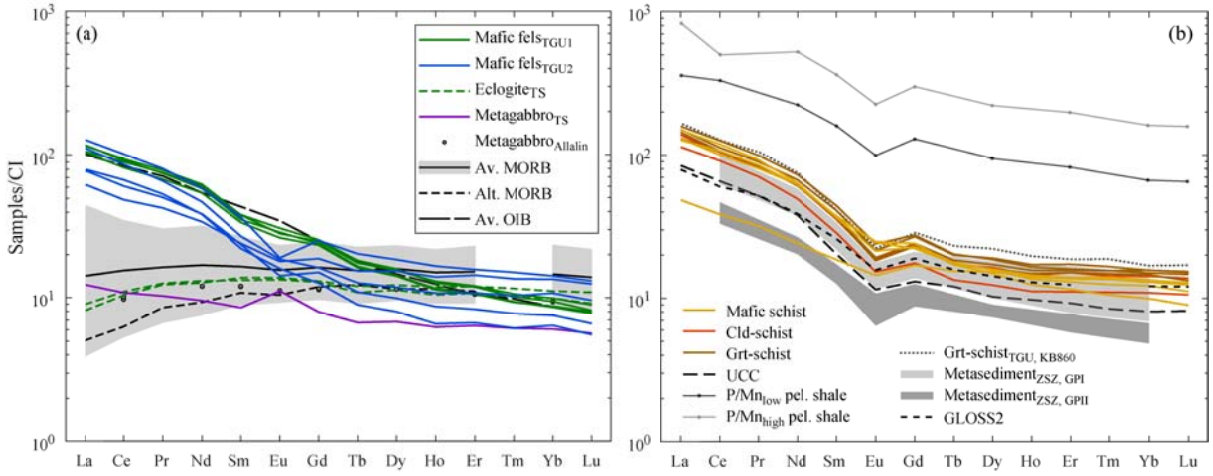

Figure 6: Chondrite-normalized REE patterns of bulk rock analyses. Normalization after Taylor and McLennan (1985). (a) Composition of mafic fels and metabasites from TGU together with eclogite and metagabbro from ZSZ. Average-, upper bound- and lower bound-MORB are after Gale et al. (2013); altered basaltic oceanic crust after Staudigel et al. (1996); Metagabbro from Allalin after Mahlen et al. (2005); Average OIB (Av. OIB) after Sun and McDonough (1989). (b) Compositions of schists from TGU from this study. Other reference plotted are: Grt-schist sample KB60 after Bucher et al. (2020); ZSZ metasediments after Mahlen et al. (2005); GLOSS2 after Plank (2014); UCC (Upper continental crust average) after Rudnick and Gao (2003); High P/Mn pelagic shale (sample 596-13.7) and High Mn/P pelagic shale (sample 596-22) after Plank and Langmuir (1998).

The REE pattern of the schist samples (Grt-schist, mafic schist and Cld-schist) is remarkably uniform (Fig. 6b), except for one mafic schist sample that is more depleted in LREE (Z17TB10). As for the mafic $fels_{TGU2}$, the REE pattern of the schists decreases linearly from La (~100-200) to Tb (~10-20) with a minor Eu negative anomaly and follows a flat trend for the HREE (Ho-Lu). REE pattern

observed for the mafic fels follows the one of the schist, except for the Eu anomaly not present for the mafic fels$_{TGU1}$. The TGU schists also have a comparable trend in REE to both GLOSS2 (Plank, 2014) and upper continental crust average (UCC, Rudnick and Gao, 2003) although at slightly higher concentration, with both showing a negative Eu anomaly. The two groups of ZSZ metasediment determined by Mahlen *et al.* (2005) also resemble the REE trend of the TGU schists, where GPI metasediments are the closest in REE content (Fig. 6b). Samples in GPII are richer in quartz than samples in GPI and compared to the TGU schist, both groups contains a variable amount of carbonate-bearing samples. The REE pattern discrepancy between GPI and GPII is attributed to contrasts in source material. REE pattern of pelagic clays with slow sedimentation rate show overall higher REE concentration (Plank and Langmuir, 1998). The schist sample from the TGU presented in Bucher *et al. (*2020) represents an upper end member among the variation observed in the TGU schists in this study (Fig. 6b).

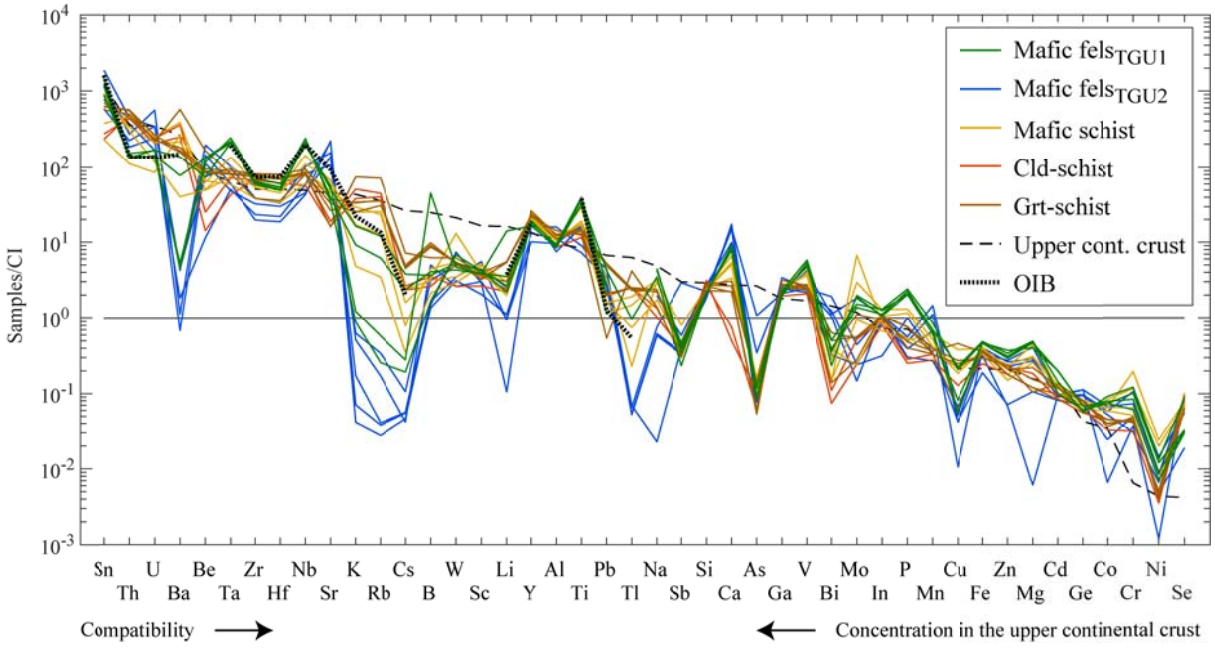

Figure 7: Trace element chondrite normalized concentrations of bulk rock analyses. Normalization after Palme et al. (2010). Upper crust after Rudnick and Gao (2003) and OIB after Sun and McDonough (1989). The sequence of elements is determined by the order of decreasing concentrations in the upper continental crust average after Rudnick and Gao (2003) normalized to Chondrites (Palme et al., 2010).

The Chondrite-normalized REE pattern from the ZSZ eclogites (Fig. 6a) lies within the MORB variation range defined by Gale *et al.* (2013). More specifically the signal is situated in between the average MORB from Gale *et al.* (2013) and the altered MORB defined by Staudigel *et al.* (1996). The LREE shows a moderate enrichment (La-Sm), whereas the pattern is flat from MREE to HREE. The metagabbro of the ZSZ that marks the contact with the TGU at Trockener Steg presents a weakly sloping pattern from LREE to HREE with a minor positive Eu anomaly (Fig. 6a). The pattern is similar

to that of the metagabbro from Allalin (Fig. 6a, Mahlen *et al.*, 2005), although at lower REE concentrations.

Major and trace element normalized to Chondrite (Fig. 7) show that the mafic $fels_{TGU1}$ closely mimic the average OIB composition, as observed for the REE. The affinity to OIB of mafic $fels_{TGU1}$ is further highlighted in the Th/Yb–Nb/Yb binary plot of Pearce (2008), where ZSZ eclogite samples plot further down in the MORB-OIB array within the typical N-MORB field (Fig. 8). In general, mafic $fels_{TGU1}$ has higher concentrations of most elements compared to mafic $fels_{TGU2}$, except for U, Sr, Sb, Ca, As and Bi. Compared to the OIB trend, the TGU mafic felses show significantly lower Ba, and depletion is also seen for K, Rb, Cs, Li and Tl, at least in some samples (Fig. 7).

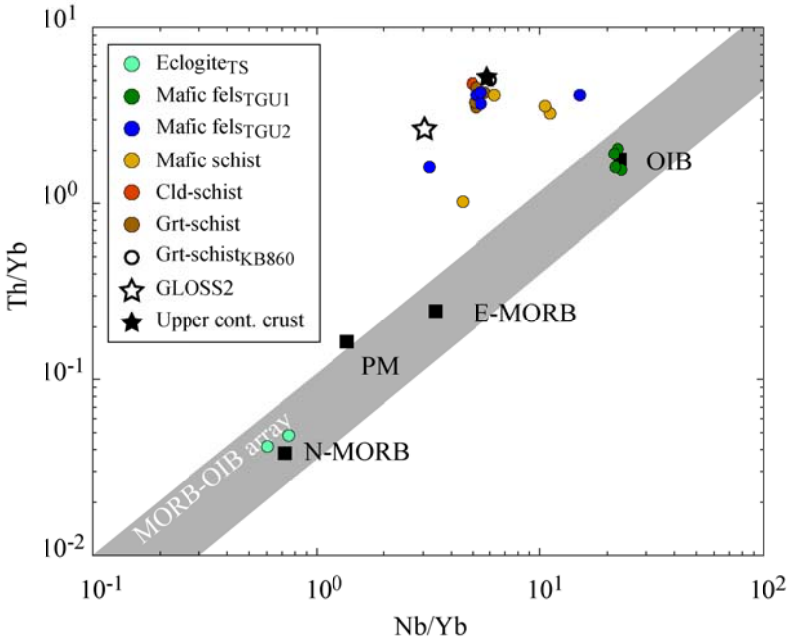

Figure 8: Th/Yb–Nb/Yb binary plot after Pearce (2008) for the investigated TGU and ZSZ samples. Additionally Grt-schist sample KB60 is after Bucher et al. (2020); GLOSS2 after Plank (2014); UCC (Upper continental crust average) after Rudnick and Gao (2003). For N-MORB, E-MORB, OIB: Oceanic intraplate basalt, PM: Primitive Mantle, see Pearce (2008) and references therein.

The different types of schists in the TGU generally follow the concentration of UCC (Fig. 9) in major and trace element normalized to Chondrite. The TGU schists however have lower concentration than UCC in Cs, B, W, Sc, Li, Tl, Na, Sb, As, Bi, and Mo, and higher in Cr and Se. More specifically, the Cld-schist shows similar trends than the Grt-schist with depletion in Be, Pb, Na, Ca and Cu. The mafic schist have the most variable trace element composition among the schists, the variation of each element concentration usually plots between the Grt-schist and the mafic $fels_{TGU1}$ values. In the Th/Yb–Nb/Yb binary plot (Fig. 8), the mafic schist, Grt-schist, Cld-schist and mafic $fels_{TGU2}$ are outside the area forming the MORB-OIB array and clusters around the GLOSS2 and the UCC references.

6. ZIRCON GEOCHRONOLOGY AND GEOCHEMISTRY

6.1. Zircon textures

The zircons from the Grt-schist (sample Z16TB31), mafic schist (sample Z16TB04, Z16TB11, Z16TB28) and mafic $fels_{TGU1}$ (sample Z18TB06, Z18TB13, Z18TB15, Z18TB27) from TGU were investigated, together with a ZSZ metagabbro (sample Z18TB26). In general, samples of Grt-schist and the mafic schist contain abundant zircon grains, whereas the amount of grains in the mafic $fels_{TGU1}$ is less abundant and only few grains were found in the metagabbro. Representative CC-images for the investigated samples are shown in Figure 9. The variable shape, texture and size of grains observed among the Grt-schist, the mafic schist and the mafic $fels_{TGU1}$ present similarities. The grain size varies between 200 and 400 µm and the grain shape is from rounded (Fig. 9a,b) to elongated and prismatic (Fig. 9c-j). The internal zoning of the zircon grains shows significant morphological variations with either sector (Fig. 9b) or oscillatory zoning (Fig. 9d,g,i), whereas others have a detrital core, which can be partially resorbed, with multiple overgrowths (Fig. 9a,c,e,f,h,j).

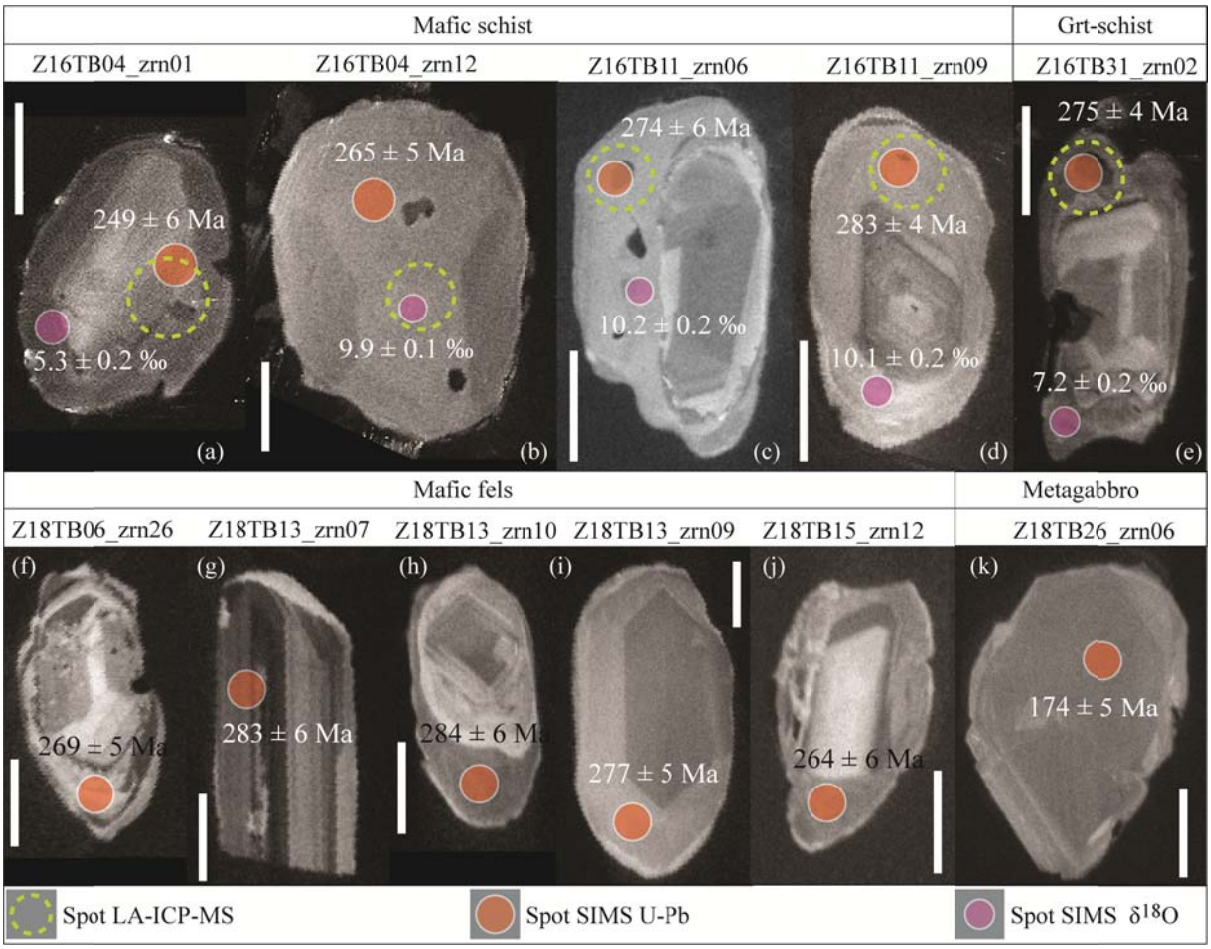

Figure 9: Representative charge contrast (CC) images of zircons with the location of spot analyses for U-Pb, $\delta^{18}O$ and trace elements. The scale bar present on each picture corresponds to 100 µm. (a-d) mafic schist, (e) Grt-schist, (f-j) mafic $fels_{TGU1}$, (k) metagabbro.

The transition between zones is often sharp and the core usually shows more complex textures. The rim of crystals sometimes shows weak oscillatory zoning or is uniform. Occasionally, a discordant rim of <10 µm is visible (Fig. 9d,f,g,i), but this external rim could not be analysed because of its small size. The zircon grains from the metagabbro are euhedral and range between 300 and 400 µm in diameter (Fig. 9k). They show weak oscillatory or sector zoning and, unlike in the TGU schists and felses, they lack any discordant core.

6.2. U-Pb geochronology

Zircon grains from the nine samples mentioned above were analysed for U-Pb and results are presented in TableS4, whereas representative zone analysed are reported in Figure 9. In the Grt-schist, the mafic schist and the mafic $fels_{TGU1}$, the rim of the grains (between 10 and 27 analyses) was targeted in order to investigate the youngest event recorded. Overall, the dates obtained vary from 171.6 ± 7.4 to 2129 ± 37 Ma (TableS4). For each sample, the youngest consistent group of analyses (between 5 and 15 analyses) were used to calculate both Concordia and weighted $^{206}Pb/^{238}U$ mean ages (Fig. 10,11). MSWD of average ages are between 0.8 and 1.8 indicating statistically valid groups. For each samples, the Concordia and the average ages are identical within uncertainty, and hereafter the Concordia age is reported. Mafic schist sample Z16TB04 is an exception, as in this sample no consistent group of dates exists and dates range from 229.6 ± 8.9 to 276.9 ± 8.4 Ma. In the two samples of mafic schist, the Concordia ages of the youngest zircon rim population is 277.5 ± 4.3 Ma (sample Z16TB11) and 276.8 ± 7.0 Ma (sample Z16TB28). The Grt-schist returned a similar youngest age of 279.2 ± 5.2 Ma (sample Z16TB31). Zircons from the four samples of mafic fels have a youngest population at 258.6 ± 5.4 Ma (sample Z18TB06), 276.7 ± 4.1 Ma (sample Z18TB13), 278.0 ± 3.4 Ma (sample Z18TB15) and 271.8 ± 3.1 Ma (sample Z18TB27). For the ZSZ metagabbro (sample Z18TB26) 16 grains were analysed and, independently of core or rim location, the Concordia age of all analyses is 166.7 ± 2.8 Ma (Fig. 12).

6.3. Zircon $\delta^{18}O$ composition

The oxygen isotope composition of zircon rims from the Grt-schist (sample Z16TB31) and the mafic schist (sample Z16TB04, Z16TB11, Z16TB28) were investigated. The analyses were performed on some of the zircon domains that define the youngest consistent group of U-Pb dates. The analyses are available in TableS2 and presented on Figure 13a. Representative spot locations are indicated on Figure 9. In each sample the isotope composition of the zircon rim scatters significantly. All samples contain Permian zircon rims with $\delta^{18}O$ value around 10 – 11 ‰. Lower $\delta^{18}O$ values around 7 – 8 ‰ are found in Permian zircon rims of three samples (Z16TB04, Z16TB28 and Z16TB31).

In mafic schist Z16TB04 and Grt-schists Z16TB31 a single analysis returned the oxygen isotope composition that is typical of mantle melts (5.3 ± 0.3 ‰; Valley, 2003).

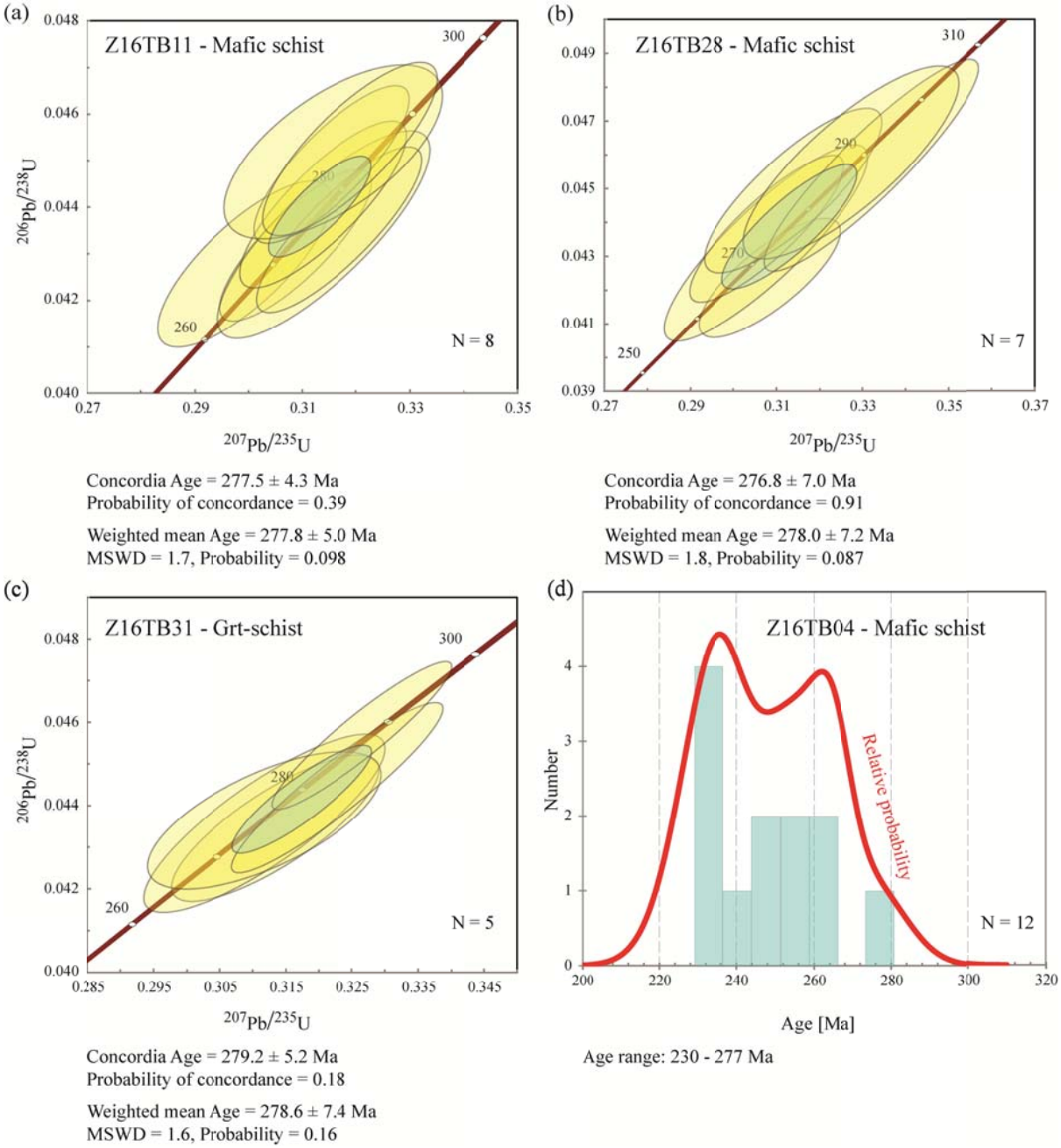

Figure 10: Concordia diagrams for U-Pb analyses of zircon from the schists. Only the youngest consistent group of U-Pb date is considered (see text). The Concordia age and the mean age are reported for each sample. See Figure 9 for representative spot location. (d) Sample Z16TB04 has no consistent group of dates and the age range is specified with the relative probability.

6.4. Zircon rim trace element composition

The zircon domains that yielded the youngest ages were also characterised for trace element in the Grt-schist (sample Z16TB31) and the mafic schists (sample Z16TB04, Z16TB11, Z16TB28). The analyses are available in TableS5 and presented on Figure 13b and Figure 14,

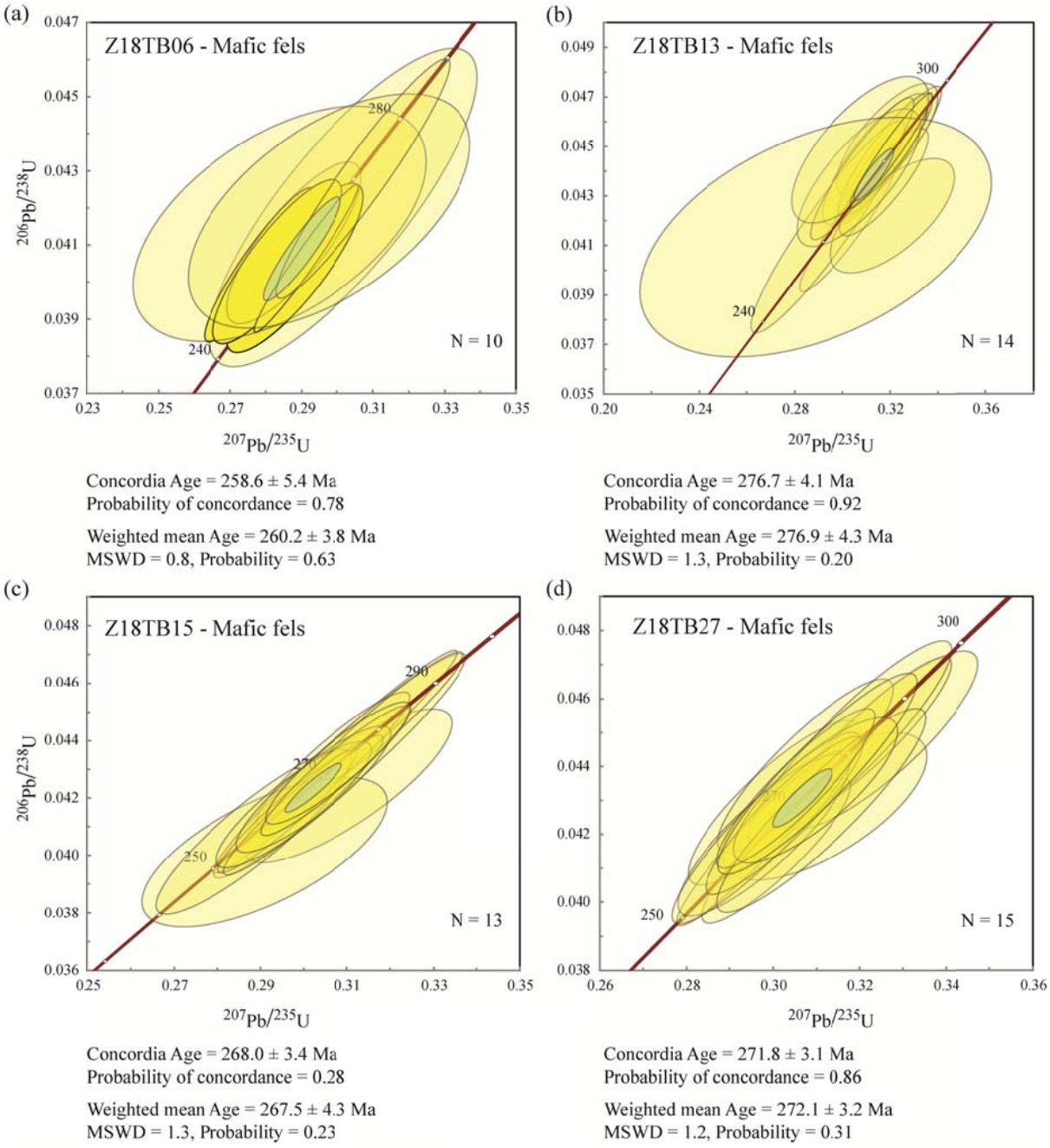

Figure 11: Concordia diagrams for U-Pb analyses of zircon from the mafic felses. Only the youngest consistent group of U-Pb date is considered (see text) The Concordia age and the mean age are reported for each sample. See Figure 9 for representative spot location.

representative spot zones are indicated on Figure 9. Th/U values vary from 0.001 to 0.8. All the mafic schist samples show Th/U values that are both below and above the 0.1 threshold commonly used to distinguish magmatic from metamorphic zircon (Fig. 13b; Rubatto, 2017). In the Grt-schist the Th/U of Permian zircon domains is consistently below 0.1, typical for metamorphic signature. The REE pattern of the zircons analysed in each sample is generally comparable across samples, but internally inconsistent within sample, in that patterns cross cut each other. The slope for the HREE pattern (Gd to Lu) is variable, and within a same sample, some Permian zircon domains have a flat

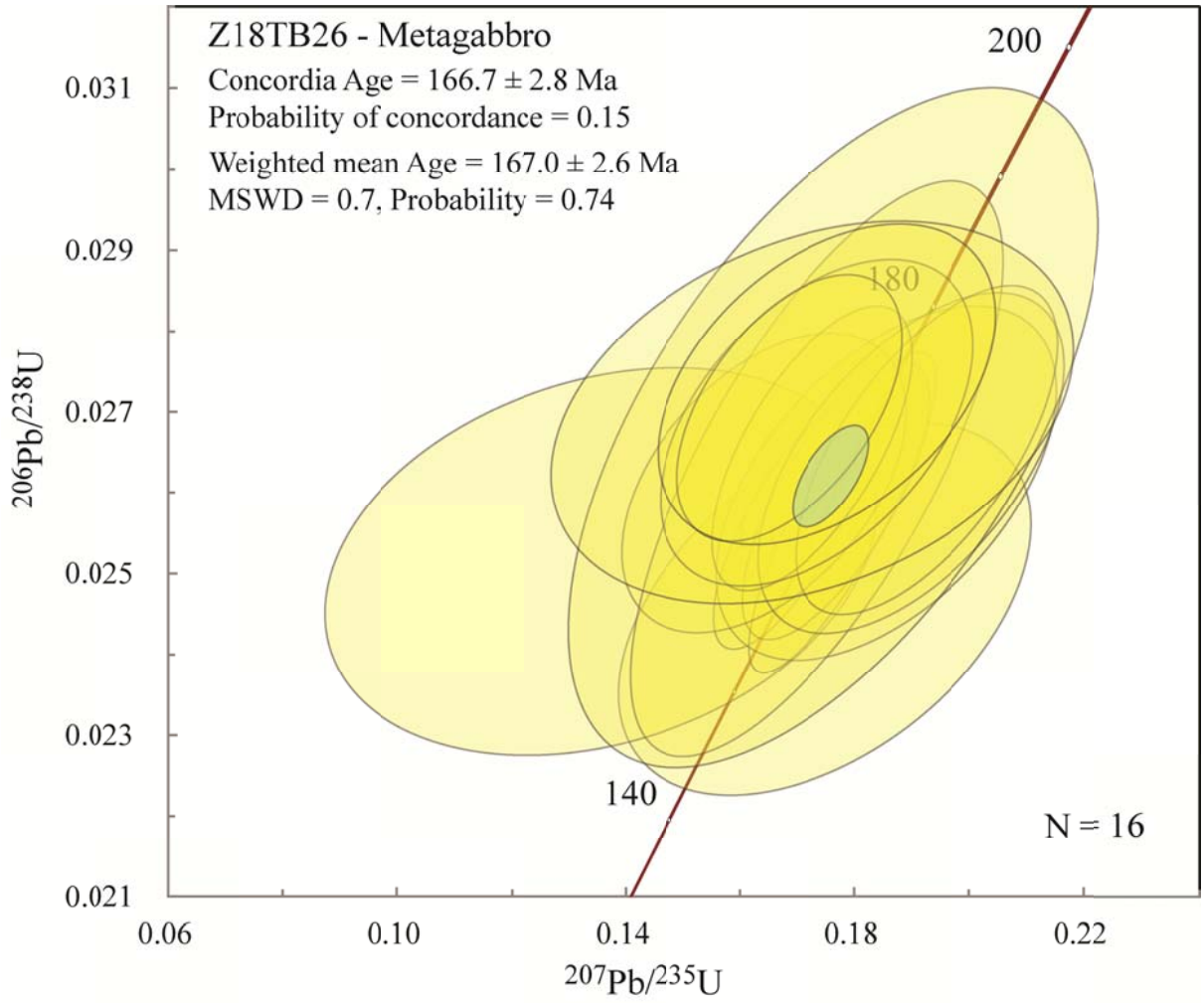

Figure 12: Concordia diagrams for U-Pb analyses of zircon from the metagabbro. See Figure 9 for representative spot location.

pattern and others are characterized by steep enrichment of HREE over the MREE. A common feature is the Eu anomaly observed in each pattern.

7. DISCUSSION

7.1. General structure of the TGU and kinematic evolution

The two foliation populations distinguished on the stereonet (Fig. 3) can be associated to Alpine deformation events. The rocks of the TGU commonly show a dominant and pervasive planar fabric, parallel to the rock banding, striking N-S slightly dipping towards the West. These data are in concordance with the surrounding ZSZ, which shows a similar overall W-NW foliation in the area (Steck, 1990; Pleuger *et al.*, 2007). The second foliation group is dipping southwards with E-W strike and is probably associated to the Alpine backfolding deformation event D_3, which lead to nappe backfolding in the SE side of the Western Alps (Steck, 1990; Escher *et al.*, 1993; Pleuger *et al.*, 2007). Both deformation events were observed in quartzite textures within rocks from the surrounding area, as for example in the Cimes Blanches and CBU (Pleuger *et al.*, 2007).

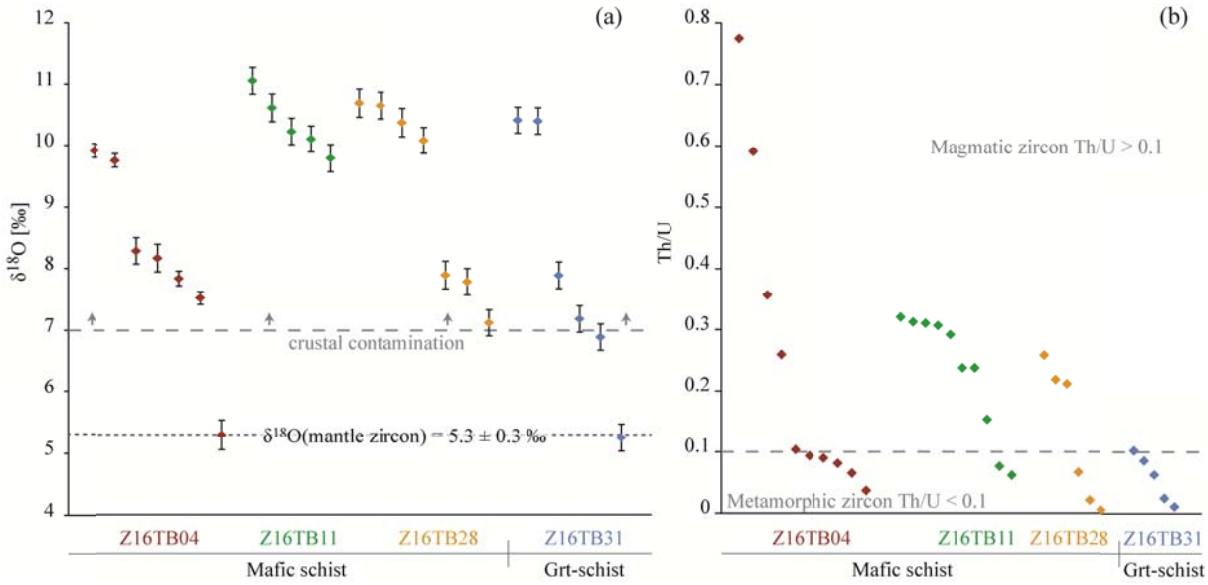

Figure 13: Geochemical analyses of the zircon from the schists. (a) δ18O composition of zircon rims. Mantle value from Valley et al. (1998). (b) Th/U ratio of zircon rims calculated from LA-ICP-MS data.

Nearby the Theodul pass an outcrop was interpreted to belong to the TGU (Fig. 2a). This outcrop shows a fold hinge composed by the TGU lithologies at its core surrounded by ZSZ serpentinites. These field relationships are further supported by geochemical and geochronological evidence. Among the studied mafic $fels_{TGU1}$ samples, sample Z18TB06 was sampled in the upper outcrop close to the Theodul pass (Fig. 2). U-Pb dating of zircon in this sample returned minimum ages and trace element signature that are comparable to the other mafic $fels_{TGU1}$ samples from the main TGU outcrop (Fig. 6,7,8 and 11).

These relationships allow drawing a double antiform syncline closing southwards in the cross section (Fig. 15). The measured main foliation is consistent over the whole field area, and thus both antiforms are drawn as recumbent isoclinal folds with a foliation parallel to the to the axial plane. Secondary Z-shaped folding (axial plane: 286/20) accompanied by top to the NW shearing (Fig. 5b) was observed in the mafic schist on the south-eastern limb of the north-western antiform and supports this interpretation.

In summary, the lithostratigraphy deduced from the cross section of the TGU, assuming a syncline structure, shows from bottom to top: (1) A basal layer of mafic schist with variable thickness ranging from 20 to 120 m; an increasing amount of lenses of Cld-schist and Grt-schist are observed upwards the layer. (2) A transition zone showing a close imbrication of Grt-schist and mafic fels. (3) The tectonic unit is topped by a massive body of mafic fels, up to 15 m thick.

7.2. Sedimentary origin for the TGU sequence

The lithostratigraphic sequence of the TGU is interpreted as a basal layer composed of schist topped by mafic fels. Within the schist, the banding is omnipresent with intercalation of more felsic

and mafic layers having variable thickness. The overall layering is parallel to the rock main foliation in accordance with the surrounding regional Alpine structures. The association of mafic and felsic rocks raises questions regarding the origin of the TGU prior to Alpine deformation.

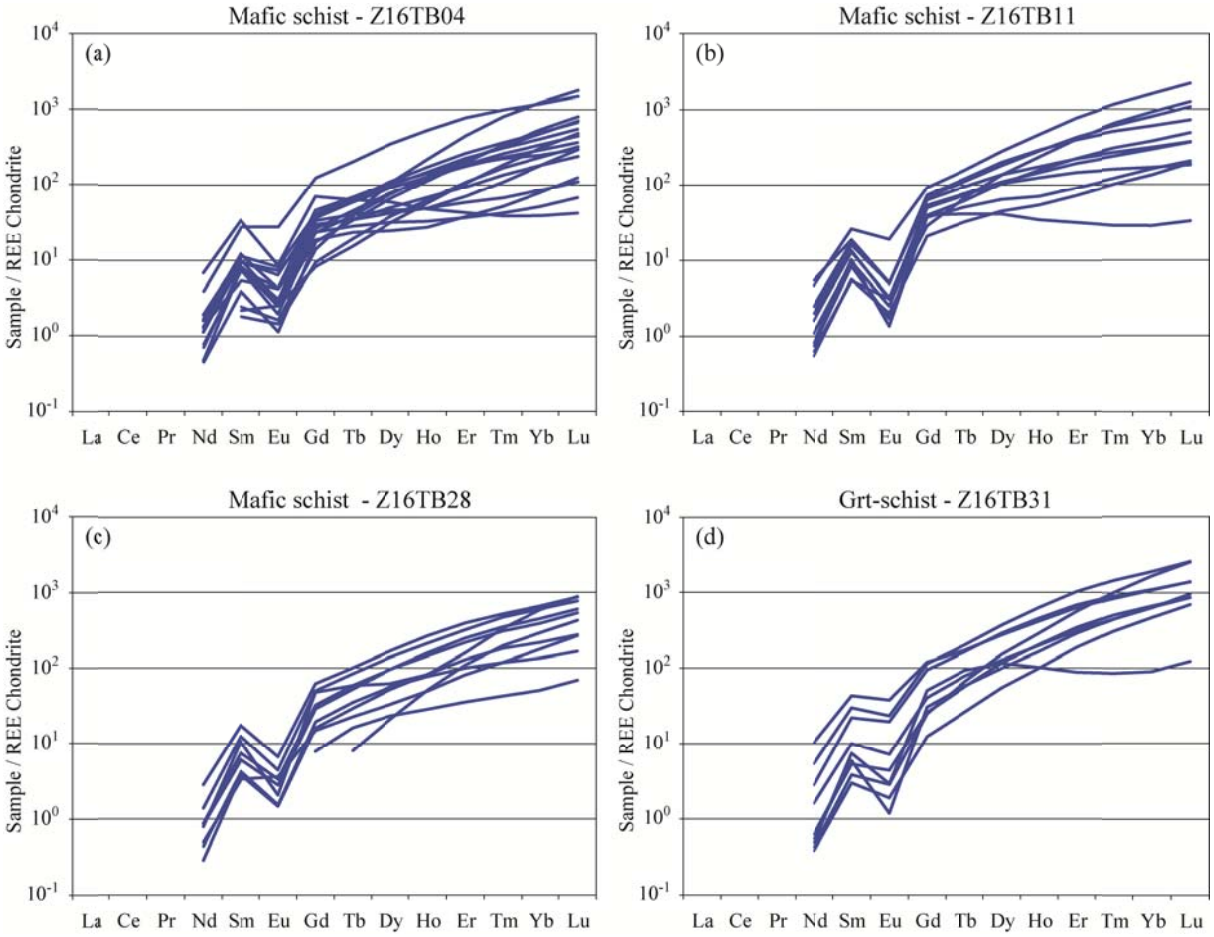

Figure 14: Chondrite-normalized REE patterns of zircon analyses. Normalization after Taylor and McLennan (1985). See Figure 9 for representative spot location.

Continental basement units in the Western Alps are by definition composed of pre-Alpine material. The main lithologies described in these crystalline massifs and derived continental allochtons are an association of para- and orthogneisses intruded by plutonic bodies (e.g. Bearth, 1952; Dal Piaz, 1964; Compagnoni *et al.*, 1974; Ballèvre *et al.*, 1986; Massonne and Chopin, 1989; Beltrando *et al.*, 2010). The superimposition of the Alpine deformation may have partially or totally overprinted the pre-Alpine features in these rocks (e.g. Dal Piaz and Lombardo, 1986). Thus, components such as meta-plutonic body and/or relict of high-T metamorphism assemblage are usually considered as representative for pre-Alpine inheritance. These elements were never observed within the TGU and their absence makes the architecture of the TGU compatible with a deformed sedimentary sequence.

The uppermost layers of the oceanic crust in slow-spreading ridge environments, such as the Piemonte-Ligurian ocean, are typically made of an association of mafic igneous and sedimentary

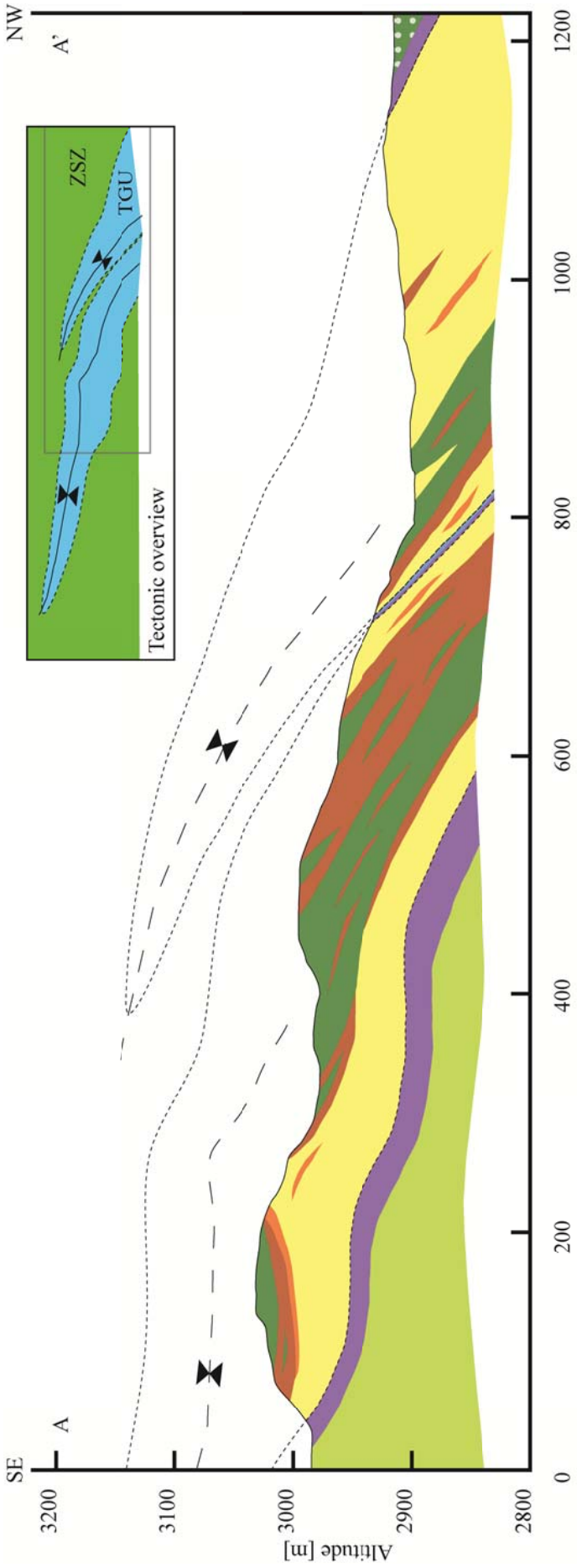

Figure 15: SE-NW cross-section from the studied area. The profile A-A' and the main structural data are indicated in Figure 1.

material (Dilek and Furnes, 2011, 2014) and a similar rock association was observed in the TGU. The actual proximity of the TGU with the ZSZ could suggest that the TGU belongs to the top of the ZSZ meta-ophiolitic sequence. The sedimentary cover of the ZSZ that outcrop elsewhere has been described as composed of marbles, schists, calcschists, metaradiolarites and Mn-bearing metacherts (Bearth, 1967), whereas the underlying mafic rock show a typical MORB signature (Bearth, 1967; Beccaluva *et al.*, 1984; Pfeifer *et al.*, 1989). Ultramafic and mafic clasts of various sizes belonging to the underlying oceanic crust are sometimes mixed together with the metasediments (Vannay and Allemann, 1990; Manzotti *et al.*, 2017). The TGU sequence is lacking key elements typically found in the Bündnerschiefer and underlying mafic rocks, such as: (1) Sediments rich in carbonate; (2) Mafic rocks with MORB-like signature and associated pillow structures; (3) Ultramafic clasts. The lack of these peculiar characteristics in the TGU indicates that this sequence is not corresponding to any previously described metasedimentary sequence associated to the ZSZ.

An important constraint on the sedimentary nature of the TGU rocks is obtained from zircon. Despite different chemistry and mineral assemblages, the shape and the internal textures of the zircons are similar among all lithologies from the TGU (Fig. 9). All samples contain zircon grains with a variety of shapes and a mix of euhedral and rounded crystals; this diversity in shape is a common feature for detrital zircon populations (Manzotti *et al.*, 2015; Kunz *et al.*, 2018). Notably, the youngest zircon population found in each of the metasediments as in the mafic fels are comparable. These young components yield a Permian to Triassic minimum age ranging between ~ 280 and 260 Ma (Fig. 10,11), which is in general agreement with zircon U-Pb dating of the mafic fels by Bucher *et al.* (2020) at 295 ± 16 Ma. The age coherence among all TGU lithologies means that the rock layout in TGU cannot represent a basement associated with late mafic intrusions, as it is expected for the Permian crust (e.g. Beltrando *et al.*, 2010). Moreover, within each mafic fels sample, zircon domains with similar texture yield a diversity of ages (TableS3). This chronology is in line with a sedimentary, origin rather than a magmatic origin.

The U-Pb analyses in the mafic schist and the Grt-schist were coupled to oxygen isotope and trace element investigation. In three samples, zircon shows significant $\delta^{18}O$ variation between grains of up to 6 ‰ (Fig. 13a). Oxygen isotopic fractionation among mineral growing in equilibrium within a rock is temperature dependant (Zheng, 1993). Thus, cogenetic zircon grains, i.e. those that yield similar ages within a sample, are expected to be in isotopic equilibrium, which is not the case in the investigated samples. The detrital nature of the TGU shists is further supported by the trace element investigation of zircon rims. The REE patterns of different zircon crystals from each sample show a relatively large variability (HREE vary over 1 or 1.5 orders of magnitude) and, importantly, different patterns that intersect each other (Fig. 14). Moreover, the same zircon domains have a large

variation in Th/U within most samples (Fig. 13b). Despite the prevalence of Permain ages, the geochemical variability of the zircon grains within each sample is hard to reconcile with a single magmatic or metamorphic zircon population. As a result, the zircons are interpreted as detrital grains from various sources, both magmatic and metamorphic. It has to be however kept in mind that any detrital zircon population likely over represents felsic versus mafic sources and plutonic versus volcanic sources. Indeed, the mafic fels is the lithology that contains the least zircon.

Each rock type of the TGU investigated show evidences for detrital input on the basis of the zircon and thus the whole TGU is considered as a metasedimentary sequence. In sedimentary rocks, the age of the youngest detrital zircon gives a maximum depositional age. The youngest coherent ages of zircon rims retrieved by each sample range between 260 and 280 Ma, except sample Z16TB04 that did not yield a statistically consistent group of dates. For each sample, the ages were calculated with most of the analysis, and only a minor amount of older dates were obtained (TableS4), suggesting a significant input from detrital material of Permian age. In the Western Alps, the Early Permian corresponds to the post Variscan high-*T* metamorphism recorded in the continental basement associated to the onset of extensional rifting (Engi *et al.*, 2001; Zucali *et al.*, 2011; Manzotti *et al.*, 2012; Pesenti *et al.*, 2012; Ewing *et al.*, 2013; Kunz *et al.*, 2018). The extensional dynamic was associated to magmatism, represented by gabbro and granitoids intrusions, dated at 270–290 Ma (Paquette *et al.*, 1989; Bussy and Cadoppi, 1996; Bussy *et al.*, 1998; Rubatto *et al.*, 1999; Bertrand *et al.*, 2005; Monjoie *et al.*, 2007; Cenki-Tok *et al.*, 2011). This continental material formerly composed either the Briançonnais or the Adriatic continent bordering the Piemonte-Ligurian prior to Alpine metamorphism. At the time of sedimentation, the source of TGU sediments possibly originated from one or more of these paleogeographic domains. The preservation of some euhedral zircon grains indicates a short transport prior to deposition (Rubatto *et al.*, 1998), which argues for a sedimentation basin close to one of the two continental margin, or in the vicinity of a continental outlier. This suggests that the TGU is either the allochtonous sedimentary cover of a yet non-identified crystalline basement, or a new type of sedimentary sequence deposited on the Piemont-Ligurian oceanic floor.

7.3. TGU: a volcanoclastic sequence

The frequent intercalation of mafic and felsic layers in the TGU is interpreted as reflecting relict of sedimentary stratification, where the high ratio of mafic schist over the other lithologies testifies for strong material inflow of mafic origin. This mafic input could either be of sedimentary origin or volcanic; particularly mafic volcanism would contain little or no zircon. The complex strata imbrication within the mafic schist further suggests random and irregular alternance among the

sources of the sedimentary material. Additionally, the omnipresence of zircon with comparable features across each lithology argues for a rather constant input from Permian material. The preferred scenario is that of a volcanoclastic sequence where the felsic component is detrital and the mafic is, at least in part, produce in situ by volcanic activity. In the mafic sediments, it is however impossible to infer the relative proportions of primary (in situ volcanic) or detrital (sedimentary) material.

Because the sedimentary origin of the TGU is not yet fully unravelled, it is complicated to evaluate if the measured bulk rock compositions are representative of the rock pristine composition. A rather low bulk $\delta^{18}O$ composition of TGU lithologies was reconstructed from the composition of the prograde garnet minerals (Chap. 3). This low signature is interpreted to be the result of seafloor hydrothermal alteration and suggests that the sedimentary sequence was probably underwater during or after sedimentation. Hydrothermal activity commonly affects the pristine bulk rock chemistry at the oceanic seafloor (e.g. Widmer *et al.*, 2000; Bach *et al.*, 2003) and sometimes leads to ore formation, such as black-smokers type deposits (Staudigel *et al.*, 1996; Cartwright and Barnicoat, 1999; Widmer *et al.*, 2000), that could explain the occurrence of a mineralized zone on the NW part of the main outcrop (Fig. 1,4c). Despite these hints, it is however challenging to quantitatively investigate the effect of oceanic hydrothermal alteration on the TGU bulk rock geochemistry, because the evaluation of element mobility is only possible in the presence of a known protolith. A qualitative effect of hydrothermal alteration that affected TGU lithologies is observed in the Chondrite normalized trace element plot (Fig. 6), where the mafic $fels_{TGU2}$ follows the mafic $fels_{TGU1}$ trend with additional and inhomogeneous anomalies. Most of the elements concerned by these variations corresponds to elements prone to be mobilized during seafloor alteration (Staudigel *et al.*, 1995, 1996; Plank and Langmuir, 1998; Manatschal *et al.*, 2000; Widmer *et al.*, 2000; Bach *et al.*, 2003; Kelley *et al.*, 2003; Spandler *et al.*, 2004; Paulick *et al.*, 2006). This suggests heterogeneous metasomatism through hydrothermal activity within the mafic fels and that these lithologies probably had a similar rock protolith.

The Chondrite normalized REE and trace element plots (Fig. 6a, 7) show that the mafic $fels_{TGU1}$ from TGU has OIB affinity. In the latter the match with OIB reference of Sun and McDonough (1989) is nearly perfect, except for Ba. This is in line with trace element bulk chemistry evaluated with ternary diagrams based on HFSE+Y, that showed within plate basalt affinities for TGU mafic $fels_{TGU1}$ (Fig. 12 in Weber and Bucher, 2015). On the other hand, zircon investigation showed that the mafic $fels_{TGU1}$ have a detrital component, at least for the rare zircon grains. Th and Nb are used as proxies to evaluate crustal contamination in oceanic basalts, which will eventually displace contaminated oceanic basaltic material above the diagonal MORB–OIB array in a Th/Yb–Nb/Yb

binary plot (Pearce, 2008). The mafic $fels_{TGU1}$ plots in the MORB–OIB array indicating minor continental contamination (Fig. 8). This set of chemical characteristics indicates that the major and REE chemistry of the mafic fels is dominated by OIB-like material, either reworked in the sedimentary cycle or erupted in situ. Unlike mafic $fels_{TGU1}$, the composition of mafic $fels_{TGU2}$ in a Th/Yb–Nb/Yb binary diagram, falls outside the MORB–OIB mixing and is closer to the GLOSS2 and the UCC references (Fig. 8), suggesting a stronger detrital continental input.

The Grt-schist and the Cld-schist represent the felsic detrital end-member of the TGU metasediments. Both lithologies broadly follows the UCC geochemical trend with some exceptions (Fig. 6b,7,8). The bulk rock composition of the mafic schist is between that of the mafic $fels_{TGU1}$ and the Grt-schist/Cld-schist (Fig. 6b,7). Therefore, the mafic schist is interpreted as a hybrid lithology made of variable amount of OIB volcanic material and detrital continental material. This argument is supported by field observation with fine layering imbrication within the mafic schist (Fig. 4a).

The complex lithostratigraphy of the TGU is best explained as a volcanoclastic sequence, resulting either from in situ eruption and deposition of volcanic material mixed with eroded Permian material from the vicinity, or from the full erosion and short transport of detrital material from various nearby sources. The detrital material composing the TGU sequence is made of at least two end-members: (1) OIB, and (2) continental material having a composition close to UCC. Even though good match of TGU lithologies with bulk geochemistry reservoirs is observed and allow successful categorization, low bulk $\delta^{18}O$ (Chap. 3), mineralization and geochemical alteration of some of the major and trace element in every rock type argues for hydrothermal alteration overprinting heterogeneously the original rock composition.

7.4. Contact and comparison between the TGU and the ZSZ

At the lithological contact between the ultramafic rocks and the metasediments, a Chl-schist layer is sometimes present (Fig. 5) and evidences of intense shearing, such as mylonitic fabric, folded foliation and boudinage are observed. Moreover, at the transition between the mafic schist and either the metagabbro or the serpentinite the foliation of these lithologies is subparallel to the lithological contact in some places (Fig. 5a), but discordant in other localities (Fig. 5b,c). Based on this information the transition between the metagabbro or the serpentinites and the mafic schist is interpreted to be the basal tectonic contact between the ZSZ and the TGU (Fig. 1). Chl-schist is an unusual lithology that is generally associated to fluid circulation between mafic and ultramafic rocks (Jöns *et al.*, 2009). Fluids usually migrate along pressure gradients and preferentially along weak zones such as lithological contacts (Ague, 2003), here the TGU–ZSZ contact. Moreover, a significant amount of fluid is expected to interact with TGU lithologies during retrogression and exhumation

(Weber and Bucher, 2015). Fluid that propagated at the contact between TGU and ZSZ during greenschist facies metamorphism would have promoted chemical exchange between lithologies of contrasting bulk chemistry and the Chl-schist could be the product of such a reaction zone.

The zircons found in the metagabbro show homogeneous textures and high Th/U ratios that support a magmatic origin (Rubatto *et al.*, 1998). The bulk rock REE pattern is typical for cumulate plutonic bodies (Montanini *et al.*, 2008) and similar to that of the metagabbro from Allalin (Fig. 6a, Mahlen *et al.*, 2005), although at lower REE concentrations. It is possible that the measured trace element composition of this sample is slightly biased towards plagioclase, which has low REE and positive Eu anomaly (e.g. Tribuzio *et al.*, 1996). The zircon age of 166.7 ± 2.8 Ma is therefore interpreted to date the intrusions of the protolith gabbro in the Middle Jurassic. Within the ZSZ ophiolites, metagabbros from Allalin and Mellichen, yield similar ages of 164.0 ± 2.7 Ma and 163.5 ± 1.8 Ma respectively (Rubatto *et al.*, 1998). Comparable ages were constrained for other metagabbros found in several ophiolitic tectonic units in the Western Alps (Monviso and Gets nappe), which ranges from 148 ± 2 Ma to 166 ± 2 Ma (Bill *et al.*, 1997; Costa and Caby, 2001; Rubatto and Hermann, 2003). These ages represents protolith magmatic ages related to the Piemonte-Ligurian oceanic crust formation. Since the contact between the metagabbro the TGU metasedimentary sequence is interpreted as a tectonic contact, the age similarity further suggest that the metagabbro underlying the TGU is part of the ZSZ (Fig. 1).

The association of mafic and felsic rocks is found both in the ZSZ and TGU, but major discrepancies exist in bulk rock geochemistry. The mafic $fels_{TGU1}$ from TGU were previously studied and compared to ZSZ eclogites by Weber and Bucher (2015). As opposed to TGU mafic $fels_{TGU1}$ that show OIB affinity, ZSZ eclogites from different localities, correspond to MORB composition, as already suggested in previous studies (Beccaluva *et al.*, 1984; Pfeifer *et al.*, 1989). The Chondrite normalized REE plot (Fig. 6a) and the Th/Yb–Nb/Yb binary plot (Fig. 8) confirms that the metamafic rocks in the TGU and ZSZ have different chemistry and thus different origin. Moreover, the Grt-schist and the Cld-schist metasediments show a slightly enriched REE trend compared to the GPI ZSZ metasediment from Mahlen *et al.* (2005), which suggests a different source of felsic sedimentation for the TGU. Even though the TGU and the ZSZ share a similar *P–T* path and peak metamorphic age (Chap. 2), the different nature of the lithologies composing each tectonic unit suggest that the TGU represent a new type of sedimentary cover associated to the Piemonte-Ligurian Ocean without equivalent within the Western Alps.

8. CONCLUSIONS

(1) The TGU is new type of allochthonous sedimentary cover of the Piemont-Ligurian oceanic crust in the Western Alps.

(2) The TGU is a meta-volcanoclastic sequence composed of mafic and felsic input that have significantly different bulk composition. Similar zircon population of Permian age found in every lithology suggests a short transport of the sedimentary component.

(3) The felsic material composing the TGU is interpreted as continental input represented by an important population of Permian zircon and detrital material, which chemistry has affinities with UCC. The continental basement that sourced the detrital material could either be a passive continental margin or a continental outlier.

(4) The mafic material has an OIB-like bulk rock composition and contains scarce Permian zircon grains that have a similar source to the felsic detrital material. The mafic component was either deposited in situ at the oceanic floor or remobilized from an adjacent source.

(5) The TGU overall structure shows a double recumbent antiform syncline closing southwards. The lithostratigraphic sequence is interpreted as a dominant basal layer composed of mafic schists topped by mafic fels. The basal tectonic contact of the TGU is marked by discordant foliation between the mafic schist and the ultramafic rocks from the ZSZ.

ACKNOWLEDGEMENTS

I am grateful to D. Rubatto for her help with the fieldwork, as well as the constructive discussion, and the thorough revision of the Chapter. I thank J. Hermann for his valued help on the field and the fruitful conversation. I thank P. Lanari for productive discussion. I thank D. Peters and T. Pettke for their help with the lab work. Further thanks go to D. Moynihan, T. G. Lee, E. Kempf and J. Reynes for their assistance during fieldwork.

BIBLIOGRAPHY

Ague, J. J. (2003). Fluid Flow in the Deep Crust. *Treatise on Geochemistry*, 195–228.

Amato, J. M., Johnson, C. M., Baumgartner, L. P. & Beard, B. L. (1999). Rapid exhumation of the Zermatt-Saas ophiolite deduced from. *Earth and Planetary Science Letters* **171**, 425–438.

Angiboust, S. & Agard, P. (2010). Initial water budget: The key to detaching large volumes of eclogitized oceanic crust along the subduction channel? *Lithos*. Elsevier B.V. **120**, 453–474.

Angiboust, S., Agard, P., Jolivet, L. & Beyssac, O. (2009). The Zermatt-Saas ophiolite: The largest (60-km wide) and deepest (c. 70-80km) continuous slice of oceanic lithosphere detached from a subduction zone? *Terra Nova*.

Angiboust, S., Yamato, P., Hertgen, S., Hyppolito, T., Bebout, G. E. & Morales, L. (2017). Fluid pathways and high-P metasomatism in a subducted continental slice (Mt. Emilius klippe, W. Alps). *Journal of Metamorphic Geology* **35**, 471–492.

Bach, W., Bernhard, P. E., Hart, S. R. & Blusztajn, J. S. (2003). Geochemistry of hydrothermally altered oceanic crust: DSDP/ODP Hole 504B-Implications for seawater-crust exchange budgets and Sr-and Pb-isotopic evolution of the mantle. *Geochemistry, Geophysics, Geosystems* **4**, 40–55.

Ballèvre, M., Kienast, J.-R. & Vuichard, J.-P. (1986). La “nappe de la Dent blanche” (Alpes occidentales) : deux unités austroalpines indépendantes. *Eclogae Geologicae Helvetiae* **79**, 57–74.

Bearth, P. (1952). Geologic und Petrographic des Monte Rosa. *Beiträge Geologische Karte Schweitz* **NF 96**, 94 pp.

Bearth, P. (1967). Die ophiolite der Zone von Zermatt-Saas Fee. *Beiträge Geologische Karte Schweitz* **132**, 1–130.

Beccaluva, L., Macciotta, G., Piccardo, G. B. & Zeda, O. (1984). Petrology of lherzolitic rocks from the Northern Apennine ophiolites. *Lithos* **17**, 299–316.

Beltrando, M., Manatschal, G., Mohn, G., Dal Piaz, G. V., Vitale Brovarone, A. & Masini, E. (2014). Recognizing remnants of magma-poor rifted margins in high-pressure orogenic belts: The Alpine case study. *Earth-Science Reviews*. Elsevier B.V. **131**, 88–115.

Beltrando, M., Rubatto, D. & Manatschal, G. (2010). From passive margins to orogens: The link between ocean-continent transition zones and (ultra)high-pressure metamorphism. *Geology* **38**, 559–562.

Bertrand, J. M., Paquette, J. L. & Guillot, F. (2005). Permia zircon U-Pb ages in the Gran Paradiso massif: Revisiting post-Variscan events in the Western Alps. *Schweizerische Mineralogische und Petrographische Mitteilungen* **85**, 15–29.

Bill, M., Bussy, F., Cosca, M., Masson, H. & Hunziker, J. C. (1997). High-precision U-Pb and 40Ar/ 39Ar dating of an Alpine ophiolite (Gets nappe, French Alps). *Eclogae Geologicae Helvetiae* **90**, 43–54.

Black, L. P., Kamo, S. L., Allen, C. M., Aleinikoff, J. N., Davis, D. W., Korsch, R. J. & Foudoulis, C. (2003). TEMORA 1: A new zircon standard for Phanerozoic U-Pb geochronology. *Chemical Geology* **200**, 155–170.

Brouwer, F. M., Burri, T., Engi, M. & Berger, A. (2005). Eclogite relics in the Central Alps: PT - evolution, Lu-Hf ages and implications for formation of tectonic mélange zones. *Schweizerische Mineralogische und Petrographische Mitteilungen* **85**, 147–174.

Bucher, K., Fazis, Y., de Capitani, C. & Grapes, R. (2005). Blueschists, eclogites, and decompression assemblages of the Zermatt-Saas ophiolite: High-pressure metamorphism of subducted Tethys lithosphere. *American Mineralogist* **90**, 821–835.

Bucher, K., Weisenberger, T. B., Klemm, O. & Weber, S. (2019). Decoding the complex internal chemical structure of garnet porphyroblasts from the Zermatt area, Western Alps. *Journal of Metamorphic Geology* **37**, 1151–1169.

Bucher, K., Weisenberger, T. B., Weber, S., Klemm, O. & Corfu, F. (2020). The Theodul Glacier Unit, a slab of pre-Alpine rocks in the Alpine meta-ophiolite of Zermatt-Saas, Western Alps. *Swiss Journal of Geosciences*. Springer International Publishing **113**, 1–22.

Bussy, F. & Cadoppi, P. (1996). U-Pb zircon dating of granitoids from the Dora-Maira massif (western Italian Alps).pdf. *Schweizerische Mineralogische und Petrographische Mitteilungen* **76**, 217–233.

Bussy, F., Venturini, G., Hunziker, J. & Martinotti, G. (1998). U-Pb ages of magmatic rocks of the western Austroalpine Dent-Blanche-Sesia Unit. *Schweizerische Mineralogische und Petrographische Mitteilungen* **78**, 163–168.

Cannat, M. *et al.* (1995). Thin crust, ultramafic exposures, and rugged faulting patterns at the Mid-Atlantic Ridge (22°-24°N). *Geology* **23**, 49–52.

Cartwright, I. & Barnicoat, A. C. (1999). Stable isotope geochemistry of Alpine ophiolites: A window to ocean-floor hydrothermal alteration and constraints on fluid-rock interaction during high-pressure metamorphism. *International Journal of Earth Sciences* **88**, 219–235.

Cenki-Tok, B. *et al.* (2011). Preservation of Permian allanite within an Alpine eclogite facies shear zone at Mt Mucrone, Italy: Mechanical and chemical behavior of allanite during mylonitization. *Lithos*. Elsevier B.V. **125**, 40–50.

Compagnoni, R. (1977). The Sesia-Lanzo Zone: high pressure-low temperature metamorphism in the Austroalpine continental margin. *Rendiconti della Società Italiana di Mineralogia e Petrologia* **33**, 335–374.

Compagnoni, R., Elter, G. & Lombardo, B. (1974). Eterogeneità stratigrafica del complesso degli "Gneiss minuti" nel Massiccio cristallino del Gran Paradiso. *Mem. Soc. Geol. It.* **13**, 227–239.

Costa, S. & Caby, R. (2001). Evolution of the Ligurian Tethys in the western Alps: Sm/Nd and U/Pb geochronology and rare-earth element geochemistry of the montgenèvre ophiolite (France). *Chemical Geology* **175**, 449–466.

Cotta, A. J. B., Enzweiler, J., Wilson, S. A., Pérez, C. A., Nardy, A. J. R. & Larizzatti, J. H. (2007). Homogeneity of the geochemical reference material BRP-1 (paranábasin basalt) and assessment of minimum mass. *Geostandards and Geoanalytical Research* **31**, 379–393.

Dal Piaz, G. V. (1964). II cristallino antico del versante meridionale del Monte Rosa: paraderivati a prevalente metamorphisme alpino. *Rendiconti della Società Italiana di Mineralogia e Petrologia* **20**, 101–135.

Dal Piaz, G. V. (1979). Manganiferous quartzitic schists of the piemonte ophiolite Nappe-in the Valsesia-valtournach arc, Italian Western Alps. *Mem. Sci. Geol. Gia Mom. degli Ist. Geol. Miner. dell Univ. di Padova* **24**.

Dal Piaz, G. V., Bistacchi, A. & Massironi, M. (2003). Geological outline of the Alps. *Episodes* **26**, 175–180.

Dal Piaz, G. V., Cortiana, G., Del Moro, A., Martin, S., Pennacchioni, G. & Tartarotti, P. (2001). Tertiary age and paleostructural inferences of the eclogitic imprint in the Austroalpine outliers and zermatt-saas ophiolite, Western Alps. *International Journal of Earth Sciences* **90**, 668–684.

Dal Piaz, G. V. & Ernst, W. G. (1978). Areal geology and petrology of eclogites and associated metabasites of the Piemonte ophiolite nappe, breuil-st. Jacques area, Italian Western Alps. *Tectonophysics* **51**, 99–126.

Dal Piaz, G. V. & Lombardo, B. (1986). Early Alpine eclogite metamorphism in the Penninic Monte Rosa-Gran Paradiso basement nappes of the northwestern Alps. *Memoir of the Geological Society of America* **164**, 249–265.

De Meyer, C. M. C., Baumgartner, L. P., Beard, B. L. & Johnson, C. M. (2014). Rb-Sr ages from phengite inclusions in garnets from high pressure rocks of the swiss western alps. *Earth and Planetary Science Letters*. Elsevier B.V. **395**, 205–216.

Dick, H. J. B., Natland, J. H. & Ildefonse, B. (2006). Past and future impact of deep drilling in the oceanic crust and mantle. *Oceanography* **19**, 72–80.

Dickin, A. P. & Jones, N. W. (1983). Relative elemental mobility during hydrothermal alteration of a basic sill, Isle of Skye, N.W. Scotland. *Contributions to Mineralogy and Petrology* **82**, 147–153.

Dilek, Y. & Furnes, H. (2011). Ophiolite genesis and global tectonics: Geochemical and tectonic fingerprinting of ancient oceanic lithosphere. *Bulletin of the Geological Society of America* **123**, 387–411.

Dilek, Y. & Furnes, H. (2014). Ophiolites and their origins. *Elements* **10**, 93–100.

Dinelli, E., Lucchini, F., Mordenti, A. & Paganelli, L. (1999). Geochemistry of Oligocene-Miocene sandstones of the northern Apennines (Italy) and evolution of chemical features in relation to provenance changes. *Sedimentary Geology* **127**, 193–207.

Duchêne, S., Blichert-Toft, J., Luais, B., Télouk, P., Lardeaux, J. M. & Albarède, F. (1997). The Lu-Hf dating of garnets and the ages of the Alpine high-pressure metamorphism. *Nature* **387**, 586–589.

Dungan, M. A., Vance, J. A. & Blanchard, D. P. (1983). Geochemistry of the Shuksan Greenschists and Blueschists, North Cascades, Washington: Variably Fractionated and Altered Metabasalts of Oceanic Affinity. *Contributions to Mineralogy and Petrology* **82**, 131–146.

Engi, M., Scherrer, N. C. & Burri, T. (2001). Metamorphic evolution of pelitic rocks of the Monte Rosa nappe: Constraints from petrology and single grain monazite age data. *Schweizerische Mineralogische und Petrographische Mitteilungen* **81**, 305–328.

Escher, A., Hunziker, J.-C., Marthaler, M., Masson, H., Sartori, M. & Steck, A. (1997). Geologic framework and structural evolution of the western Swiss-Italian Alps. .

Escher, A., Masson, H. & Steck, A. (1993). Nappe geometry in the Western Swiss Alps. *Journal of Structural Geology* **15**, 501–509.

Ewing, T. A., Hermann, J. & Rubatto, D. (2013). The robustness of the Zr-in-rutile and Ti-in-zircon thermometers during high-temperature metamorphism (Ivrea-Verbano Zone, northern Italy). *Contributions to Mineralogy and Petrology* **165**, 757–779.

Fassmer, K., Obermüller, G., Nagel, T. J., Kirst, F., Froitzheim, N., Sandmann, S., Miladinova, I., Fonseca, R. O. C.

& Münker, C. (2016). High-pressure metamorphic age and significance of eclogite-facies continental fragments associated with oceanic lithosphere in the Western Alps (Etirol-Levaz Slice, Valtournenche, Italy). *Lithos*.

Gale, A., Dalton, C. A., Langmuir, C. H., Su, Y. & Schilling, J. G. (2013). The mean composition of ocean ridge basalts. *Geochemistry, Geophysics, Geosystems* **14**, 489–518.

Green, T. H., Brunfelt, A. O. & Heier, K. S. (1969). Rare earth element distribution in anorthosites and associated high grade metamorphic rocks, Lofoten-Vesteraalen, Norway. *Earth and Planetary Science Letters* **7**, 93–98.

Groppo, C., Beltrando, M. & Compagnoni, R. (2009). The P-T path of the ultra-high pressure Lago Di Cignana and adjoining high-pressure meta-ophiolitic units: Insights into the evolution of the subducting Tethyan slab. *Journal of Metamorphic Geology* **27**, 207–231.

Guillong, M., Meier, D. L., Allan, M. M., Heinrich, C. A. & Yardley, B. W. D. (2008). SILLS: A Matlab-Based Program for the Reduction of Laser Ablation ICP–MS Data of Homogeneous Materials and Inclusions. *Mineralogical Association of Canada Short Course* **40**, 328–333.

Hellman, P. L., Smith, R. E. & Henderson, P. (1979). The mobility of the rare earth elements: Evidence and implications from selected terrains affected by burial metamorphism. *Contributions to Mineralogy and Petrology* **71**, 23–44.

Jochum, K. P. *et al.* (2011). Determination of reference values for NIST SRM 610-617 glasses following ISO guidelines. *Geostandards and Geoanalytical Research* **35**, 397–429.

Jochum, K. P., Willbold, M., Raczek, I., Stoll, B. & Herwig, K. (2005). Chemical Characterisation of the USGS Reference Glasses GSA-1G, GSC-1G, GSD-1G, GSE-1G, BCR-2G, BHVO-2G and BIR-1G Using EPMA, ID-TIMS, ID-ICP-MS and LA-ICP-MS. *Geostandards and Geoanalytical Research* **29**, 285–302.

Jöns, N., Bach, W. & Schroeder, T. (2009). Formation and alteration of plagiogranites in an ultramafic-hosted detachment fault at the Mid-Atlantic Ridge (ODP Leg 209). *Contributions to Mineralogy and Petrology* **157**, 625–639.

Kelley, K. A., Plank, T., Ludden, J. & Staudigel, H. (2003). Composition of altered oceanic crust at ODP Sites 801 and 1149. *Geochemistry, Geophysics, Geosystems* **4**.

Kirst, F. & Leiss, B. (2016). Kinematics of syn- and post-exhumational shear zones at Lago di Cignana (Western Alps, Italy): constraints on the exhumation of Zermatt–Saas (ultra)high‐pressure rocks and deformation along the Combin Fault and Dent Blanche Basal Thrust. *Int J Earth SciGeol Rundsch)*.

Kunz, B. E., Manzotti, P., von Niederhäusern, B., Engi, M., Darling, J. R., Giuntoli, F. & Lanari, P. (2018). Permian high-temperature metamorphism in the Western Alps (NW Italy). *International Journal of Earth Sciences*. Springer Berlin Heidelberg **107**, 203–229.

Lapen, T. J., Johnson, C. M., Baumgartner, L. P., Mahlen, N. J., Beard, B. L. & Amato, J. M. (2003). Burial rates during prograde metamorphism of an ultra-high-pressure terrane: An example from Lago di Cignana, western Alps, Italy. *Earth and Planetary Science Letters* **215**, 57–72.

Li, X. P., Rahn, M. & Bucher, K. (2004). Serpentinites of the Zermatt-Saas ophiolite complex and their texture evolution. *Journal of Metamorphic Geology* **22**, 159–177.

Liati, A., Gebauer, D. & Fanning, C. M. (2003). The youngest basic oceanic magmatism in the Alps (Late Cretaceous; Chiavenna unit, Central Alps): Geochronological constraints and geodynamic significance. *Contributions to Mineralogy and Petrology* **146**, 144–158.

Liati, A., Gebauer, D. & Fanning, M. (2000). U-Pb SHRIMP dating of zircon from the Novate granite (Bergeil, Central Alps): evidence for Oligocene-Miocene magmatism, Jurassic/Cretaceous continental rifting and opening of the Valais trough. *Schweizerische Mineralogische und Petrographische Mitteilungen* **80**, 305–316.

Ludwig, K. R. (2003). Isoplot/Ex version 3.0. A geochronological toolkit for Microsoft Excel. *Berkeley Geochronological Centre Spec. Pub.* **Berkeley**, p.70.

Ludwig, K. R. (2012). User's manual for Isoplot 3.75 a geochronological toolkit for microsoft excel. *Berkeley Geochronological Centre Spec. Pub.* **Special Pu**, 75 p.

Mahlen, N. J., Johnson, C. M., Baumgartner, L. P. & Beard, B. L. (2005). Provenance of Jurassic Tethyan sediments in the HP/UHP Zermatt-Saas ophiolite, western Alps. *Bulletin of the Geological Society of America* **117**, 530–544.

Manatschal, G., Marquer, D. & Früh-Green, G. L. (2000). Channelized fluid flow and mass transfer along a rift-related detachment fault (Eastern Alps, Southeast Switzerland). *Bulletin of the Geological Society of America* **112**, 21–33.

Manzotti, P. & Ballèvre, M. (2013). Multistage garnet in high-pressure metasediments: Alpine overgrowths on variscan detrital grains. *Geology* **41**, 1151–1154.

Manzotti, P., Ballèvre, M. & Dal Piaz, G. V. (2017). Continental gabbros in the dent blanche tectonic system (Western alps): From the pre-alpine crustal structure of the adriatic palaeomargin to the geometry of an alleged subduction interface. *Journal of the Geological Society* **174**, 541–556.

Manzotti, P., Poujol, M. & Ballèvre, M. (2015). Detrital zircon geochronology in blueschist-facies meta-conglomerates from the Western Alps: implications for the late Carboniferous to early Permian palaeogeography. *International Journal of Earth Sciences* **104**, 703–731.

Manzotti, P., Rubatto, D., Darling, J., Zucali, M., Cenki-Tok, B. & Engi, M. (2012). From Permo-Triassic lithospheric thinning to Jurassic rifting at the Adriatic margin: Petrological and geochronological record in Valtournenche (Western Italian Alps). *Lithos*. Elsevier B.V. **146–147**, 276–292.

Massonne, H. J. & Chopin, C. (1989). P-T history of the Gran Paradiso (western Alps) metagranites based on phengite geobarometry. *Evolution of metamorphic belts* 545–549.

McLennan, S. M. (1989). Rare earth elements in sedimentary rocks: influence of provenance and sedimentary processes. *Reviews in Mineralogy and Geochemistry* **21**, 169–200.

McLennan, S. M. (2001). Relationships between the trace element composition of sedimentary rocks and upper continental crust. *Geochemistry, Geophysics, Geosystems* **2**.

McLennan, S. M., Hemming, S., McDaniel, D. K. & Hanson, G. N. (1993). Geochemical approaches to sedimentation, provenance, and tectonics. *Special Paper of the Geological Society of America* **284**, 21–40.

Monjoie, P., Bussy, F., Schaltegger, U., Mulch, A., Lapierre, H. & Pfeifer, H. R. (2007). Contrasting magma types

and timing of intrusion in the Permian layered mafic complex of Mont Collon (Western Alps, Valais, Switzerland): Evidence from U/Pb zircon and 40Ar/39Ar amphibole dating. *Swiss Journal of Geosciences* **100**, 125–135.

Montanini, A., Tribuzio, R. & Vernia, L. (2008). Petrogenesis of basalts and gabbros from an ancient continent-ocean transition (External Liguride ophiolites, Northern Italy). *Lithos* **101**, 453–479.

Palme, H., Lodders, K. & Jones, A. (2010). Solar system abundances of the elements. *Astrophysics and Space Science Proceedings* 379–417.

Paquette, J. L., Chopin, C. & Peucat, J. J. (1989). U-Pb zircon, Rb-Sr and Sm-Nd geochronology of high- to very-high-pressure meta-acidic rocks from the western Alps. *Contributions to Mineralogy and Petrology* **101**, 280–289.

Paton, C., Hellstrom, J., Paul, B., Woodhead, J. & Hergt, J. (2011). Iolite: Freeware for the visualisation and processing of mass spectrometric data. *Journal of Analytical Atomic Spectrometry* **26**, 2508–2518.

Paulick, H., Bach, W., Godard, M., De Hoog, J. C. M., Suhr, G. & Harvey, J. (2006). Geochemistry of abyssal peridotites (Mid-Atlantic Ridge, 15°20′N, ODP Leg 209): Implications for fluid/rock interaction in slow spreading environments. *Chemical Geology* **234**, 179–210.

Pearce, J. A. (2008). Geochemical fingerprinting of oceanic basalts with applications to ophiolite classification and the search for Archean oceanic crust. *Lithos* **100**, 14–48.

Pearce, J. A. (2014). Immobile element fingerprinting of ophiolites. *Elements* **10**, 101–108.

Pennacchioni, G. (1996). Progressive eclogitization under fluid-present conditions of pre-Alpine mafic granulites in the Austroalpine Mt Emilius Klippe (Italian Western Alps). *Journal of Structural Geology* **18**, 549–561.

Péron-Pinvidic, G. & Manatschal, G. (2009). The final rifting evolution at deep magma-poor passive margins from Iberia-Newfoundland: A new point of view. *International Journal of Earth Sciences* **98**, 1581–1597.

Pesenti, C., Zucali, M., Manzotti, P., Diella, V. & Risplendente, A. (2012). Linking U-Th-Pb monazite dating to partial melting microstructures: Application to the Valpelline series (Austroalpine domain, Western Alps). *Rendiconti Online Societa Geologica Italiana* **22**, 183–185.

Peters, D. & Pettke, T. (2017). Evaluation of Major to Ultra Trace Element Bulk Rock Chemical Analysis of Nanoparticulate Pressed Powder Pellets by LA-ICP-MS. *Geostandards and Geoanalytical Research* **41**, 5–28.

Pettke, T., Oberli, F., Audétat, A., Guillong, M., Simon, A. C., Hanley, J. J. & Klemm, L. M. (2012). Recent developments in element concentration and isotope ratio analysis of individual fluid inclusions by laser ablation single and multiple collector ICP-MS. *Ore Geology Reviews*. Elsevier B.V. **44**, 10–38.

Pfeifer, H., Colombi, A. & Ganguin, J. (1989). Zermatt-Saas and Antrona Zone: a petrographic and geochemical comparison of polyphase metamorphic ophiolites of the West-Central Alps. *Schweizerische Mineralogische und Petrographische Mitteilungen* **69**, 217–236.

Plank, T. (2014). The Chemical Composition of Subducting Sediments. *Treatise on Geochemistry: Second Edition*. Elsevier Ltd., 607–629.

Plank, T. & Langmuir, C. H. (1998). The chemical composition of subducting sediment and its consequences for

the crust and mantle. *Chemical Geology* **145**, 325–394.

Pleuger, J., Froitzheim, N. & Jansen, E. (2005). Folded continental and oceanic nappes on the southern side of Monte Rosa (western Alps, Italy): Anatomy of a double collision suture. *Tectonics* **24**, 1–22.

Pleuger, J., Roller, S., Walter, J. M., Jansen, E. & Froitzheim, N. (2007). Structural evolution of the contact between two Penninic nappes (Zermatt-Saas zone and Combin zone, Western Alps) and implications for the exhumation mechanism and palaeogeography. *International Journal of Earth Sciences* **96**, 229–252.

Reinecke, T. (1998). Prograde high- to ultrahigh-pressure metamorphism and exhumation of oceanic sediments at Lago di Cignana, Zermatt-Saas Zone, western Alps. *Lithos* **42**, 147–189.

Rubatto, D. (2002). Zircon trace element geochemistry: Partitioning with garnet and the link between U-Pb ages and metamorphism. *Chemical Geology* **184**, 123–138.

Rubatto, D. (2017). *Zircon: The Metamorphic Mineral*. *Reviews in Mineralogy and Geochemistry*.

Rubatto, D., Gebauer, D. & Compagnoni, R. (1999). Dating of eclogite-facies zircons: The age of Alpine metamorphism in the Sesia-Lanzo Zone (Western Alps). *Earth and Planetary Science Letters* **167**, 141–158.

Rubatto, D., Gebauer, D. & Fanning, M. (1998). Jurassic formation and Eocene subduction of the Zermatt-Saas-Fee ophiolites: Implications for the geodynamic evolution of the Central and Western Alps. *Contributions to Mineralogy and Petrology* **132**, 269–287.

Rubatto, D. & Hermann, J. (2003). Zircon formation during fluid circulation in eclogites (Monviso, Western Alps): Implications for Zr and Hf budget in subduction zones. *Geochimica et Cosmochimica Acta* **67**, 2173–2187.

Rubatto, D., Regis, D., Hermann, J., Boston, K., Engi, M., Beltrando, M. & McAlpine, S. R. B. (2011). Yo-yo subduction recorded by accessory minerals in the Italian Western Alps. *Nature Geoscience*. Nature Publishing Group **4**, 338–342.

Rudnick, R. L. & Gao, S. (2003). Composition of the continental crust. *Treatise on Geochemistry* **3**, 1–64.

Sandmann, S., Nagel, T. J., Herwartz, D., Fonseca, R. O. C., Kurzawski, R. M., Münker, C. & Froitzheim, N. (2014). Lu–Hf garnet systematics of a polymetamorphic basement unit: new evidence for coherent exhumation of the Adula Nappe (Central Alps) from eclogite-facies conditions. *Contributions to Mineralogy and Petrology* **168**, 1–21.

Sartori, M. (1987). Structure de la zone du Combin entre les Diablons et Zermatt (Valais). *Eclogae Geologicae Helvetiae* **80**, 789–814.

Schmid, S. M., Fügenschuh, B., Kissling, E. & Schuster, R. (2004). Tectonic map and overall architecture of the Alpine orogen. *Eclogae Geologicae Helvetiae* **97**, 93–117.

Seitz, S., Putlitz, B., Baumgartner, L. P. & Bouvier, A. S. (2018). The role of crustal melting in the formation of rhyolites: Constraints from SIMS oxygen isotope data (Chon Aike Province, Patagonia, Argentina). *American Mineralogist* **103**, 2011–2027.

Sláma, J. *et al.* (2008). Plešovice zircon - A new natural reference material for U-Pb and Hf isotopic microanalysis. *Chemical Geology* **249**, 1–35.

Spalla, M. I., Lardeaux, J. M., Dal Piaz, G. V., Gosso, G. & Messiga, B. (1996). Tectonic significance of Alpine

eclogites. *Journal of Geodynamics* **21**, 257–285.

Spandler, C., Hermann, J., Arculus, R. & Mavrogenes, J. (2004). Geochemical heterogeneity and element mobility in deeply subducted oceanic crust; insights from high-pressure mafic rocks from New Caledonia. *Chemical Geology* **206**, 21–42.

Stacey, J. S. & Kramers, J. D. (1975). Approximation of terrestrial lead isotope evolution by a two-stage model. *Earth and Planetary Science Letters* **26**, 207–221.

Stampfli, G. M., Borel, G. D., Marchant, R. & Mosar, J. (2002). Western Alps geological constraints on western Tethyan reconstructions. *Journal of the Virtual Explorer* **8**, 75–104.

Staudigel, H., Davies, G. R., Hart, S. R., Marchant, K. M. & Smith, B. M. (1995). Large scale isotopic Sr, Nd and O isotopic anatomy of altered oceanic crust: DSDP/ODP sites417/418. *Earth and Planetary Science Letters* **130**, 169–185.

Staudigel, H. & Hart, S. R. (1983). Alteration of basaltic glass: Mechanisms and significance for the oceanic crust-seawater budget. *Geochimica et Cosmochimica Acta* **47**, 337–350.

Staudigel, H., Plank, T., White, B. & Schmincke, U. (1996). Fluxes During Seafloor Alteration of the Basaltic Crust ' DSDP Sites have pointed to the AND. *Geophysical Monograph* **96**, 19–37.

Steck, A. (1990). une carte des zones de cisaillement ductile des Alpes Centrales. *Eclogae geol. Helv.* **83/3**, 603–627.

Steiger, R. H. & Jäger, E. (1977). Subcommission on geochronology: Convention on the use of decay constants in geo- and cosmochronology. *Earth and Planetary Science Letters* **36**, 359–362.

Sun, S. S. & McDonough, W. F. (1989). Chemical and isotopic systematics of oceanic basalts: Implications for mantle composition and processes. *Geological Society Special Publication* **42**, 313–345.

Taylor, S. R. & Mclennan, S. M. (1995). The geochemical the continental evolution crust. *Reviews in Mineralogy and Geochemistry* **33**, 241–265.

Taylor, S. R. & McLennan, S. M. (1985). *The continental crust: Its composition and evolution*. .

Tribuzio, R., Messiga, B., Vannucci, R. & Bottazzi, P. (1996). Rare earth element redistribution during high-pressure - Low-temperature metamorphism in ophiolitic Fe-gabbros (Liguria, northwestern Italy): Implications for light REE mobility in subduction zones. *Geology* **24**, 711–714.

Trümpy, R. (1975). Penninic-Austroalpine boundary in the Swiss Alps: a presumed former continental margin and its problems. *American Journal of Science* **275**-**A**, 209–238.

Valley, J. W. (2003). Oxygen isotopes in zircon. *Reviews in Mineralogy and Geochemistry* **53**, 343–385.

Vannay, J.-C. & Allemann, R. (1990). La zone piémontaise dans le Haut- Valtournanche (Val d ' Aoste , Italie). *Eclogae Geologicae Helvetiae* **83**, 21–39.

Watt, G. R., Griffin, B. J. & Kinny, P. D. (2000). Charge contrast imaging of geological materials in the environmental scanning electron microscope. *American Mineralogist* **85**, 1784–1794.

Weber, S. & Bucher, K. (2015). An eclogite-bearing continental tectonic slice in the Zermatt-Saas high-pressure ophiolites at Trockener Steg (Zermatt, Swiss Western Alps). *Lithos*. Elsevier B.V. **232**, 336–359.

Weber, S., Sandmann, S., Miladinova, I., Fonseca, R. O. C., Froitzheim, N., Münker, C. & Bucher, K. (2015). Dating the initiation of Piemonte-Liguria Ocean subduction: Lu–Hf garnet chronometry of eclogites from

the Theodul Glacier Unit (Zermatt-Saas zone, Switzerland). *Swiss Journal of Geosciences* **108**, 183–199.

Whitehouse, M. J. & Kamber, B. S. (2005). Assigning dates to thin gneissic veins in high-grade metamorphic terranes: A cautionary tale from Akilia, southwest Greenland. *Journal of Petrology* **46**, 291–318.

Whitney, D. L. & Evans, B. W. (2010). Abbreviations for names of rock-forming minerals. *American Mineralogist* **95**, 185–187.

Widmer, T., Ganguin, J. & Thompson, A. B. (2000). Ocean floor hydrothermal veins in eclogite facies rocks of the Zermatt-Saas Zone, Switzerland. *Schweizerische Mineralogische und Petrographische Mitteilungen* **80**, 63–73.

Wiedenbeck, M. *et al.* (2004). Further characterisation of the 91500 zircon crystal. *Geostandards and Geoanalytical Research* **28**, 9–39.

Wiedenbeck, M., Allé, P., Corfu, F., Griffin, W. L., Meier, M., Oberli, F., Quadt, A. VON, Roddick, J. C. & Spiegel, W. (1995). Three Natural Zircon Standards for U-Th-Pb, Lu-Hf, Trace Element and Ree Analyses. *Geostandards Newsletter* **19**, 1–23.

Zheng, Y.-F. (1993). Calculation of oxygen isotope fractionation in anhydrous silicate minerals. *Geochimica et Cosmochimica Acta* **57**, 1079–1091.

Zucali, M., Manzotti, P., Diella, V., Pesenti, C., Rispendente, A., Darling, J. & Engi, M. (2011). Permian tectonometamorphic evolution of the Dent-Blanche Unit (Austroalpine domain, Western Italian Alps). *Rendiconti Online Societa Geologica Italiana* **15**, 139–142.

SUPPLEMENTARY MATERIAL

Supplementary Figures:

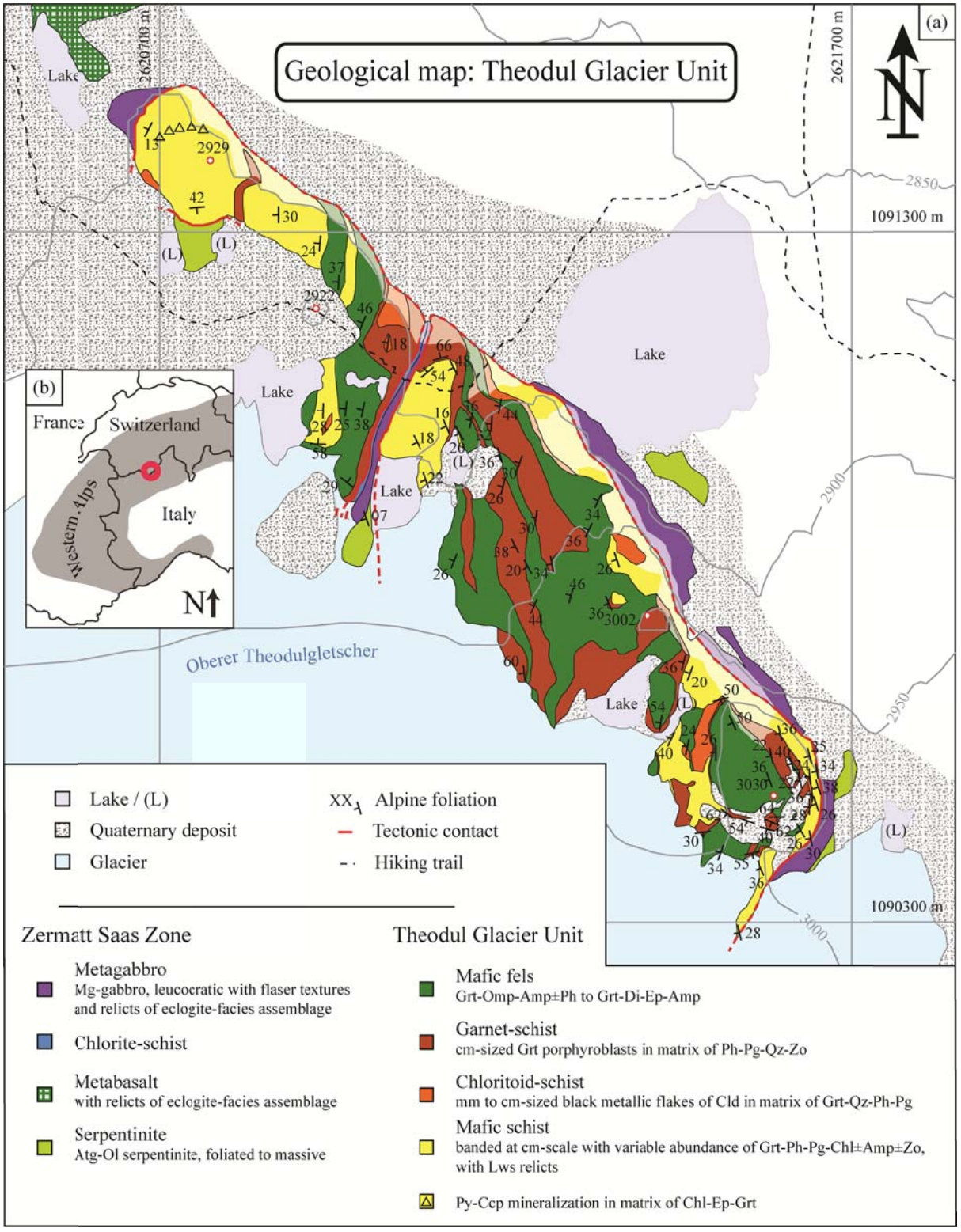

Figure S1: (a) Geological map of the Theodul Glacier Unit with location of foliation measurements. (b) Inset showing the position of TGU within the Western Alps.

Supplementary Tables:

All supplementary tables are stored on a CD in a folder labelled “SupplementaryTablesChapter1”.

Table S1: List of samples, localisation, mineral assemblage and description.

Table S2: SIMS oxygen isotope analyses of zircons.

Table S3: LA-ICP-MS bulk rock analyses.

Table S4: U, Th, Pb SIMS zircon data.

Table S5: LA-ICP-MS zircon trace element analyses.

CHAPTER 2

Pressure–temperature–time evolution of subducted crust revealed by complex garnet zoning (Theodul Glacier Unit, Switzerland)

Thomas Bovay[1], Pierre Lanari[1], Daniela Rubatto[1,2], Matthijs Smit[3], Francesca Piccoli[1]

[1]Institute of Geological Sciences, University of Bern, 3012 Bern, Switzerland

[2]Institut des Sciences de la Terre, University of Lausanne, 1015 Lausanne, Switzerland

[3]Departement of Earth, Ocean and Atmospheric Sciences, University of British Colombia, Canada

Short title: Garnet petrochronology of subducted crust

KEYWORDS

Phase equilibria; Quantitative compositional mapping; Lu-Hf garnet-whole rock geochronology; Zr-in-rutile thermometry; Zermatt-Saas Unit

In revision for *Journal of Metamorphic Geology*

ABSTRACT

Collisional orogens commonly include mono-metamorphic and poly-metamorphic units, and their different evolution can be difficult to recognise and reconcile. The Theodul Glacier Unit (TGU) in the Western Alps consists of an association of metasedimentary and metamafic rocks embedded within the Zermatt-Saas tectonic unit. In spite of recent petrological studies, it is yet unclear whether these rocks underwent one or multiple metamorphic cycles. In this study, different lithologies from the TGU unit (mafic schist, mafic fels and chloritoid-schist) were investigated for petrography, quantitative compositional mapping of garnet, thermodynamic modelling and Lu-Hf garnet dating. The data reveal a coherent mono-metamorphic history with a β-shape Pressure-Temperature (*P–T)* path characteristic of oceanic subduction. Garnet Lu-Hf ages yield a restricted garnet crystallization time window between 50.3 and 48.8 Ma (± 0.5%, 2SD). A prograde metamorphic stage recorded in garnet cores yields conditions of 490 ± 15 °C and 1.75 ± 0.05 GPa. Maximum pressure conditions of 2.65 ± 0.10 GPa and 580 ± 15 °C were reached at 50.3 ± 0.3 Ma. Initial exhumation was rapid and led to isothermal decompression to 1.50 ± 0.10 GPa within 1 Myr. This decompression was associated with lawsonite breakdown in mafic schist and in mafic fels, causing intense fluid-rock interaction within and between different lithotypes. This process is recorded in garnet textures and trace element patterns, and in the major element composition of K-white mica. Initial exhumation was followed by re-heating of ~30°C at a pressure of 1.50 ± 0.10 GPa. Perturbation of the subduction-zone thermal structure may be related to upwelling of hot asthenospheric mantle material and transient storage of the unit at the crust–mantle boundary.

1. INTRODUCTION

A metamorphic cycle involves a sequence of prograde and retrograde transformations affecting the rock texture and mineral compositions. However, the transformation is rarely complete and mineral relics are key to decipher pressure and temperature (*P*–*T*) evolution. In the case of poly-metamorphism, several metamorphic cycles are experienced by a rock and can lead to the preservation of multi-stage relicts (e.g. Rubatto et al. 1999; Herwartz et al. 2011). Garnet is a common rock-forming mineral known to be resilient to re-equilibration (Baxter et al. 2013) and therefore is a good recorder of poly-metamorphism (Feenstra et al. 2007; Putnis 2009; Angiboust et al. 2017; Lanari et al. 2017; Giuntoli et al. 2018a; Thiessen et al. 2019). The study of garnet texture and chemical composition give insights into its growth history. When temperatures are low enough to prevent intracrystalline diffusion, continuous garnet growth over a *P*–*T* segment produces a typical chemical zoning witnessing local equilibrium between the garnet crystal and the matrix of the rock at the time of garnet growth (Spear 1988). For example, Mn strongly partitions into garnet and spessartine is consequently enriched in the core relative to the rim composition and exhibits a bell-shape zoning pattern (Hollister 1966). On the other hand, a sharp compositional contact between distinct garnet zones within a single crystal is commonly interpreted as reflecting two distinct metamorphic stages or metamorphic cycles (Compagnoni 1977; Le Bayon and Ballèvre 2004; Manzotti and Ballèvre 2013; Giuntoli et al. 2018a). In addition to distinct metamorphic stages and/or cycles, sharp compositional zoning can be attributed to infiltration of components via externally-derived fluids (e.g. Jamtveit and Hervig 1994; Angiboust et al. 2014). Garnet major element composition is additionally influenced by the reactive bulk composition, which is the bulk composition of the reactive volume (e.g. Lanari and Engi 2017). The reactive bulk composition changes during garnet growth by fractionation (Evans 2004; Konrad-Schmolke et al. 2011) affecting the isopleth positions in equilibrium phase diagrams (Spear 1988; Lanari and Engi 2017). In addition, the same garnet composition can be predicted to be stable under different geotherms (e.g. at *HT-LP* and *LT-HP*) for a given bulk composition (see Fig. 8 in Lanari & Engi, 2017). This will inevitably complicate the interpretation of garnet zoning and the distinction between mono- and poly-metamorphic growth.

Besides its chemistry, garnet geochronology enables time constraints, providing a further key tool to distinguish between mono- and poly-metamorphic growth. Both Lu-Hf and Sm-Nd systematics can be employed as chronometers in garnet, because for both systems garnet solely fractionates parent over daughter forming an unusually high parent/daughter isotope ratio (Baxter et al. 2017). The main advantage of Lu-Hf geochronology is that the diffusivity of Hf is low with respect to Nd, making Lu-Hf systematics less susceptible to be affected by diffusive isotope re-

equilibration (Scherer et al. 2000; Kohn 2009; Smit et al. 2013; Bloch et al. 2015). During garnet growth, Lu is generally enriched in the garnet core due to the high compatibility of Lu in garnet (e.g. Konrad-Schmolke et al. 2008a). As a consequence, Lu-Hf ages of bulk garnet crystals are typically biased toward the initial stage of garnet growth (Otamendi et al. 2002; Lapen et al. 2003; Skora et al. 2006; Konrad-Schmolke et al. 2008a). However, complex Lu zoning in garnet are sometimes observed, where distinct garnet zones are enriched in Lu. Such element distribution might increase the complexity of age interpretation, especially if garnet growth duration between Lu maxima exceeds analytical precision (Lapen et al. 2003; Skora et al. 2006; Smit et al. 2010).

In the Western Alps, the recognition of, and distinction between, mono- and polycyclic metamorphic terranes has become of crucial importance in tectonic and paleogeographic reconstructions. Mono-metamorphic units are clearly present in the form of terranes comprising Mesozoic sediments and Jurassic-Cretaceous oceanic crust metamorphosed during the Alpine orogeny (e.g. Zermatt-Saas Zone, ZSZ). Poly-metamorphic units are found or suspected in various locations. These are interpreted as portion of continental basements, which in addition to their Alpine overprint, record Permian and/or older metamorphism (e.g. the Sesia Zone and Dent Blanche) (Manzotti et al. 2014). An example of a unit that is potentially poly-metamorphic, yet not fully identified as such, is the Theodul Glacier Unit (TGU)—a metasedimentary sliver embedded within the ZSZ (Figure 1) that has been described as a coherent unit (Weber & Bucher, 2015). This unit largely preserves an Alpine, high-pressure assemblage, but was recently interpreted as poly-metamorphic, based on the investigation of garnet textures and thermodynamic modelling (Bucher et al. 2019, 2020). The TGU has been therefore interpreted as a small continental outlier embedded in the oceanic units of the ZSZ. Alternatively, the unit could be mono-metamorphic, representing a sedimentary sequence deposited on the oceanic crust of the ZSZ ophiolite, much alike the metasediments of the Lago di Cignana locality (Reinecke 1998).

To better establish the metamorphic history and tectonic significance of the TGU, various rocks from this unit were subjected to a multi-method analysis. Two potentially poly-metamorphic metasedimentary lithologies were studied and their results compared with those from metamafic rocks, with the latter being used as benchmark to characterize the mono-metamorphic character of the *P–T* path of this unit. The mono- versus poly-metamorphic character of garnet in the metasedimentary rocks was assessed based on petrological observations, quantitative compositional mapping, thermodynamic modelling, and Lu-Hf chronology. Additional compositional mapping and thermodynamic modelling was performed on phengite, and rutile Zr content and chloritoid stability were used to constrain temperature conditions at specific metamorphic stage. Our results show that

the TGU is a mono-metamorphic unit that followed a β-shape *P*–*T* path during the Eocene Alpine metamorphic cycle.

2. GEOLOGICAL AND TECTONIC SETTINGS

The Penninic domain in the Western Alps is a complexly folded nappe stack of rocks with continental and oceanic origin that have different metamorphic histories and were assembled during the Alpine orogeny. The ZSZ is a south Penninic tectonic unit made of Mesozoic ophiolites that underwent UHP and eclogitic HP metamorphism (Bearth 1967; Dal Piaz and Ernst 1978; Reinecke 1991) during Eocene (Duchêne et al. 1997; Rubatto et al. 1998; Amato et al. 1999; Lapen et al. 2003; De Meyer et al. 2014). It has been interpreted as being an exhumed relict of the Piemont Ligurian oceanic lithosphere with mid-ocean ridge affinity (Bearth 1967), which is now sandwiched between the underlying Briançonnais basement (e.g. the Monte Rosa and the Gran Paradiso massifs) and the overlying Austroalpine units (e.g. the Sesia-Dent Blanche nappe system) (Escher et al. 1997). The ZSZ is made of an association of ultramafic rocks, mafic rocks and metasediments, representing a dismembered ophiolitic sequence (Bearth 1967). Whether the ZSZ is a coherent piece of oceanic lithosphere, which was then only partially disrupted during exhumation (Angiboust et al. 2009), or whether it is a tectonic mélange of different tectonic slices (Bousquet et al. 2008; Groppo et al. 2009; Negro et al. 2013) is still unclear.

The ophiolites of the ZSZ consist of metamorphosed metabasalts, metagabbros of Jurassic protolith age (Rubatto et al. 1998; Rubatto and Hermann 2003; Pleuger et al. 2007; Beltrando et al. 2010) situated on top of a thick section of serpentinite (Pleuger et al. 2007; Fassmer et al. 2016; Kirst and Leiss 2016). The oceanic sedimentary cover—also referred to as Schist Lustrés or Bündnerschiefer—is mainly composed of marbles, schists, calcareous schists, meta-radiolarites and Mn-bearing meta-cherts with a Jurassic to Cretaceous protolith (Bearth 1967). The sediments that overlie the meta-basalts and gabbros form a thin continuous cover of the oceanic crust (Dal Piaz 1979). The overall stratigraphy shows slow spreading ridge affinity (Dilek and Furnes 2014).

Three kilometer-thick slices of the continental crust that was reworked at high pressure conditions occur discontinuously throughout the ZSZ section, especially in its uppermost part: Etirol-Levaz, Glacier Rafray and Monte Emilius. They are either localized within the ophiolitic nappe of the ZSZ (Ballèvre et al. 1986; Dal Piaz 2001; Beltrando et al. 2010; Fassmer et al. 2016; Kirst and Leiss 2016; Angiboust et al. 2017) or along the tectonic contact between the Combin zone and ZSZ (Dal Piaz et al. 2001). Two different origins have been proposed for these continental slices: (1) They are slivers of one of the adjacent continental units, which were incorporated into the ZSZ during the Alpine orogeny (Pleuger et al. 2007; Kirst and Leiss 2016). This interpretation explains the similarities

with the typical characteristics of the Sesia-Zone and the Dent Blanche nappe (Pleuger et al. 2007). (2) They are fragments of continental crust that were dismembered during Permian to Jurassic extension to form extensional allochtons over the Mesozoic oceanic crust (Beltrando et al., 2010; Dal Piaz, 2001). In the latter case they would form a paleogeographic entity with the ZSZ zone (Fassmer et al. 2016). A similar close relationship between continental basement slices and serpentinites is commonly found along ocean-continent transition zones (OCT), where movements along detachment faults dipping underneath the thinned continental margin results in the tectonic erosion of small pieces of the margin (Péron-Pinvidic and Manatschal 2009; Beltrando et al. 2010, 2014; Vitale Brovarone et al. 2011).

The TGU is located SW of the village of Zermatt in Switzerland, close to the Trockener Steg cable car station. The outcropping rocks show little weathering as the retreat of the "Oberer Theodulgletscher" occurred only during the last three decades. The TGU is an association of metasedimentary and metamafic rocks embedded within the ZSZ unit (Figure 1), which has been mapped as a coherent unit (Weber & Bucher 2015; Chapter 1). The mafic rocks from TGU show Within Plate Basalt chemistry (Weber and Bucher 2015). Thermodynamic models of the eclogitic rocks based on garnet chemistry suggests a mono-metamorphic history with a peak metamorphism at 2.20 ± 0.10 GPa and 580 ± 50 °C, slightly lower than those of the ZSZ eclogites (Weber and Bucher 2015). Garnet Lu-Hf dating of mafic rocks record prograde metamorphic mineral growth and yield an Alpine age at 58-56 Ma (Weber et al. 2015), which is slightly older than the peak metamorphism of ZSZ dated between 50 and 40 Ma (Duchêne et al. 1997; Rubatto et al. 1998; Lapen et al. 2003; De Meyer et al. 2014; Dragovic et al. 2020). On the other hand, zircon U-Pb dating yield an age of 295 ± 16 Ma, which were interpreted to date pre-Alpine granulite-facies metamorphism (Bucher et al. 2020). The metasedimentary rocks have been described as an association of garnet-phengite schists and garnet-biotite schists (Weber and Bucher 2015). Detailed field investigation (Figure 1) resulted in the subdivision of the garnet-phengite schist lithology into two lithological units: garnet schist and mafic schist. In addition, the garnet-biotite schists are re-named as chloritoid-schist (Cld-schist), consistent with the observed mineral assemblage (see below). In summary, the highly foliated metasedimentary rocks consist of an intricate imbrication of mafic schist, garnet schist and Cld-schist that constitute a coherent unit. Large garnet porphyroblasts in the garnet schist recorded two metamorphic stages: a pre-Alpine granulitic core stable at ~0.7 GPa and ~780 °C is overgrown by an Alpine rim generation formed at ~1.7 GPa and ~530 °C (Bucher et al. 2019). Cation diffusion across the contact between the two garnet generations occurred at 530–580 °C and relaxed zoning for c. 10 Ma (Bucher et al. 2019).

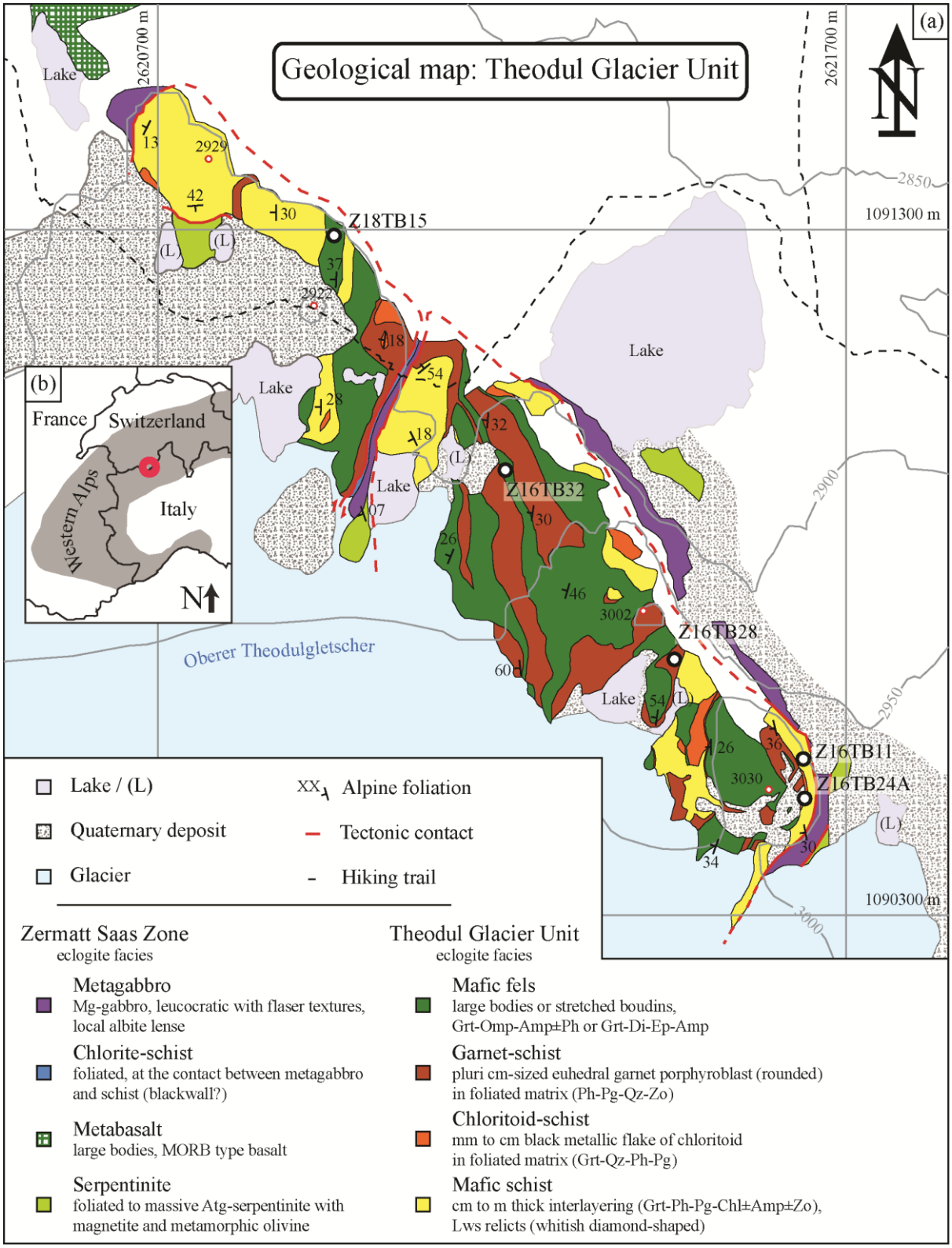

***Figure 1:** (a) Geological map of the Theodul Glacier Unit (TGU). Black and white spots show sample location. (b) Geolocalisation of the TGU in the Western Alps in Switzerland.*

3. PETROLOGICAL DESCRIPTION

To better constrain the *P–T* conditions experienced by the TGU, we performed a petrological study focusing on mafic fels and metasedimentary schists. In this study, three types of lithologies are investigated: the mafic fels, the mafic schist and the Cld-schist.

3.1. Mafic fels

Mafic fels rocks occur either as large bodies of 10 m wide and 10-100 m long, or as smaller, stretched boudins of various sizes (cm to m) embedded within the surrounding schists (Figure 2a). This variable lithology can be described by two characteristic types of mineral assemblage (Table 1) (Figure 2b,c). The first type of TGU mafic fels (represented by sample Z18TB15) has an assemblage of garnet-omphacite-amphibole±phengite (Figure 2b,d,e), similar to that described by Weber and Bucher (2015). The second rock type (sample Z16TB32) shows an assemblage of garnet, diopside, zoisite and/or zoisite-epidote solid solution, and amphibole (Figure 2c). Due to the highly variable mineral modal composition of the mafic rocks, in the field they range in colour from milky to dark green (Figure 2a,b,c,d). Garnet grains are mostly euhedral with diameters between 1 and 5 mm. Mafic boudins exhibit undeformed cross-cutting veinlets of garnet-diopside-amphibole-quartz-calcite and show a continuous layer of euhedral garnet at the contact with the host rock on both vein side. Retrogression locally replaced the main HP mineral assemblage with chlorite, amphibole, epidote, paragonite, albite and titanite. Retrogressed domains in mafic fels show abundant albite-epidote veins.

Sample	Latitude	Longitude	Major phases	Minor phases
Mafic fels				
Z16TB32	45°58'9.66"N	7°42'42.84"E	Grt + Ep + Di + Amp	Qz + Ttn + Ap
Z18TB15	45°58'20.9''N	7°42'34.8''E	Omp + Grt + Amp	Ep + Qz + Ph + Pg + Chl + Ap + Rt + Ttn
Mafic schist				
Z16TB11	45°58'1.04"N	7°43'0.53"E	Grt + Qz + Ph + Pg + Amp + Ep	Chl + Ab + Rt + Ttn + Ap
Z16TB28	45°58'1.26"N	7°42'56.64"E	Grt + Ep + Chl + Qz + Ph	Ttn + Rt + Ab + Ap
Cld-schist				
Z16TB24A	45°57'54.72"N	7°43'4.62"E	Grt + Qz + Ph + Pg + Cld + Amp	Chl + Rt + Ttn

***Table 1*: Sample list including geolocalisation and mineral assemblages.**

3.2. Mafic schist

A variety of mafic schists are found interlayered at the centimetre to metre scale. The layers are oriented parallel to the main foliation and the transition from one type to another can be either gradual (mm to cm) or sharp (Figure 2f). The mineral assemblage common to every type of mafic schist is garnet-phengite-paragonite-quartz-chlorite (Figure 2g), with additional zoisite and amphibole (Table 1). Mineral abundance can vary considerably; for example, sample Z16TB11 comprises <1 vol% of zoisite and 15% amphibole, whereas sample Z16TB28 contains 10 to 35%

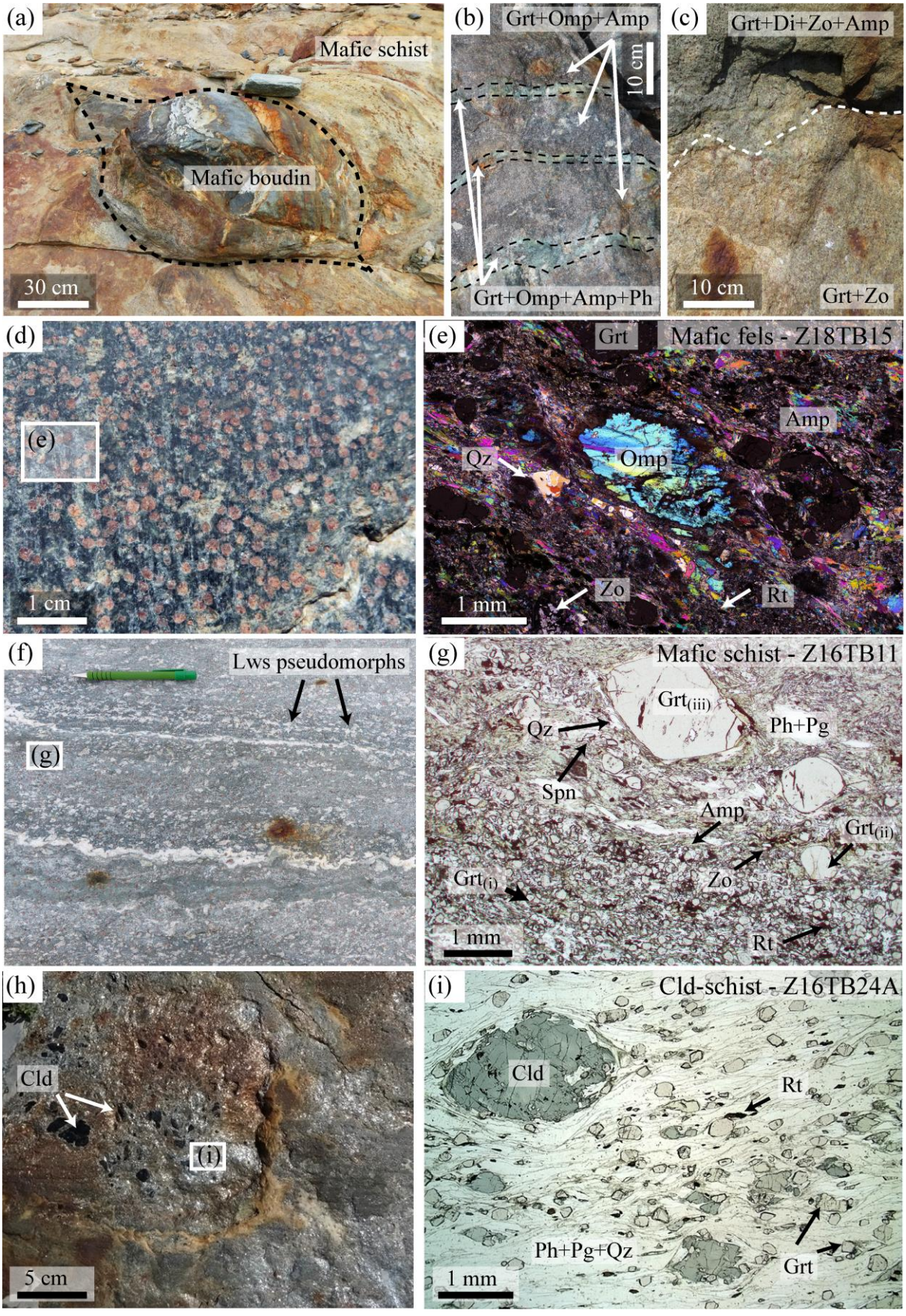
(a)
Mafic schist
Mafic boudin
30 cm
(b)
Grt+Omp+Amp
10 cm
Grt+Omp+Amp+Ph
(c)
Grt+Di+Zo+Amp
10 cm
Grt+Zo
(d)
(e)
1 cm
(e)
Grt
Mafic fels - Z18TB15
Amp
Qz
Omp
Zo
Rt
1 mm
(f)
Lws pseudomorphs
(g)
(g)
Mafic schist - Z16TB11
Grt(iii)
Qz
Ph+Pg
Spn
Amp
Grt(ii)
Grt(i)
Zo
1 mm
Rt
(h)
Cld
(i)
5 cm
(i)
Cld-schist - Z16TB24A
Cld
Rt
Ph+Pg+Qz
Grt
1 mm

Figure 2: Outcrop photographs and sample microphotographs from the representative lithologies of the TGU. Mineral abbreviations follow Whitney and Evans (2010). White squares in (d), (f) and (h) are representative location of indicated microphotograph. (a) Mafic boudin stretched within the schists. (b) Outcrop view of banded mafic fels. (c) Outcrop view of mafic fels with smooth transition between Di-rich to Zo-rich domain. (d) Outcrop view of mafic fels: lighter areas are predominantly Omp-rich, whereas darker areas are Amp-rich. (e) Microphotograph of mafic fels Z18TB15 showing textural equilibrium between Omp and Grt, both surrounded by Amp. (f) Outcrop view of mafic schist. Layering is parallel with the well-developed foliation. White diamonds-shaped domains are interpreted as pseudomorphs after lawsonite. (g) Scanned thin section of mafic schist Z16TB11 showing transition from a zone rich in small garnet (<200 µm, bottom of image) to a zone richer in garnet porphyroblasts. (h) Outcrop view of a Cld-schist, with dark flaky chloritoid. (i) Scanned thin section image of Cld-schist Z16TB24A: the foliation is marked by Ph+Pg+Qz.

zoisite and up to 5% amphibole. Pseudomorphs after lawsonite were observed in every type of mafic schist (Figure 2f). These occur as whitish diamond-shaped mineral aggregates of up to 1 cm and are composed of zoisite-quartz-paragonite, sometimes with small euhedral garnet. Three main garnet populations are observed in the mafic schists (Figure 2g). (i) Sub-euhedral grains in the mineral matrix, which are up to 200 µm in diameter and are mostly inclusion free. These occur either as banding of mm to cm scale in which each grain is stretched along the main foliation, or as clusters. This garnet type preserves complex zoning with relict cores and a distinct chemical composition from the other garnet types (see below). (ii) Euhedral grains of 0.2-0.7 mm in diameter; these matrix garnet dos not contain relict cores. (iii) Euhedral garnet of 1-7 mm in diameter, which are rich in inclusion of various minerals (zoisite, rutile, titanite, apatite, pyrite, amphibole, quartz, zircon and white mica). Inclusion textures in garnet vary from sample to sample and indicate syn to post kinematic entrapment. Greenschist-facies retrogression caused local growth of chlorite and amphibole rims around garnet, titanite rims around rutile, and production of minor poikilitic albite.

3.3. Chloritoid schist

This lithology was previously mapped by Weber & Bucher (2015) as garnet-biotite schists. In the investigated samples biotite was not identified. Instead, abundant chloritoid flakes were observed along the Alpine foliation, hence here the term Cld-schist is preferred. This lithology (sample Z16TB24A) is typified by black metallic flakes of chloritoid in a foliated matrix of garnet, quartz, phengite and paragonite (Figure 2h,i, Table 1). Rare altered amphibole porphyroblasts and elongated rutile are also present. Garnet grains are euhedral with a diameter of 0.2–0.4 mm and occasionally show an atoll-shaped texture. The lithology contains garnet-chloritoid-quartz veins.

4. ANALYTICAL METHODS

4.1. Scanning electron microscope and electron micro probe

Sample imaging (back-scattered electron mode) was performed using a scanning electron microscope (SEM) ZEISS EVO50 at the Institute of Geological Sciences (University of Bern) with 20 keV acceleration voltage and 1 nA beam current.

Quantitative analyses of garnet, white mica and chloritoid were performed with the electron probe micro analyser (EPMA) JEOL JXA-8200 superprobe at the Institute of Geological Science (University of Bern). Spot analyses were performed using 15 keV accelerating voltage, 20 nA specimen current, and 40 s dwell time (10 s for each background after 20s on peak). Nine oxide components were obtained using synthetic and natural standards: almandine (SiO_2,Al_2O_3,FeO), albite (Na_2O), anorthite (CaO), orthoclase (K_2O), forsterite (MgO), ilmenite (TiO_2), tephroite (MnO).

Quantitative compositional maps were generated from X-ray intensity maps using spot analyses acquired in the same area as internal standards. The X-ray maps were measured by WDS with 15 keV accelerating voltage and 100 nA specimen current, with various dwell time and resolutions. Nine elements (Si, Ti, Al, Fe, Mn, Mg, Na, Ca, K) were measured at the specific wavelength in two successive passes (with Na, Ca and K analysed on the first scan). Compositional maps were processed using XMapTools 3.2.1 (Lanari et al. 2014, 2019). Garnet and phengite structural formula were calculated for each X-Ray intensity maps using the external functions available in XMapTools and considering a minimum of 17 internal standards. Representative compositions of each garnet and phengite growth zone were obtained by averaging pixels from manually selected areas. The domains were chosen in a way to avoid any mixing between garnet and phengite generations, and excluding mineral inclusions.

4.2. Bulk rock chemistry

Bulk rock chemical analyses were conducted at the Institute of Geological Sciences, University of Bern (Switzerland). Rock samples were crushed by using a stainless steel mortar and pestle. They were then dry milled in an agate ring mill for 30 min. Each run of sample was bracketed by sand quartz milling for 15min in order to clean the receptacle. Nanoparticulate pressed powder pellets (PPP) were created following the procedure described in Peters and Pettke (2017) by using microcrystalline cellulose as a binder. The PPP were analysed using a laser ablation inductively coupled plasma mass spectrometer (LA-ICP-MS) consisting of a GeoLas-Pro 193 nm ArF Excimer laser system (Lambda Physik, Göttingen, Germany) in combination with an ELAN DRC-e quadrupole mass spectrometer (Perkin Elmer, Waltham, MA, USA). Calibration was based on GSD-1G (Jochum et al. 2011) reference material. BRP-1 (Cotta et al. 2007) was used as a secondary standard (Peters and

Pettke 2017) and accuracy was always better than 10%. Pressed powder pellets were measured in single spot mode with and energy density of 6 Jcm^{-2} at a repetition rate of 10 Hz and a beam size of 90 µm. Six analyses were measured for each PPP. The surface area was cleaned by pre-ablation using a larger spot size and for each analysis the signal was integrated over a 50-60 s. Data reduction was performed offline by using the software SILLS (Guillong et al. 2008) and limits of detection were calculated after Pettke *et al.* (2012). Internal standardization was done by assuming (i) a fixed total of 100 wt% for major and trace elements, minus volatiles determined by loss on ignition; (ii) all Fe is present as Fe_2O_3.

4.3. Trace element analysis

LA-ICP-MS mineral analyses were conducted using two different instruments at the Institute of Geological Sciences, University of Bern (Switzerland). Part of the punctual analyses were achieved with a GeoLas-Pro 193 nm ArF Excimer laser system (Lambda Physik, Göttingen, Germany) in combination with an ELAN DRC-e quadrupole mass spectrometer (Perkin Elmer, Waltham, MA,USA). Mapping and the second part of mineral punctual analyses were conducted using a Resonetics RESOlutionSE 193nm excimer laser system equipped with a S-155 large volume constant geometry chamber (Laurin Technic, Australia). The laser system was coupled to an Agilent 7900 quadrupole ICP-MS instrument. Calibration was performed using reference material GSD-1G (Jochum et al. 2005), whereas NIST 612 (Jochum et al. 2011) was used as secondary standard with three ablation spots each. Data were reduced offline employing SILLS (Guillong et al. 2008) and Iolite v7.08 (Paton et al. 2011). Drift was linearly corrected by bracketing the unknowns with the calibration material and LODs were calculated according to Pettke *et al.* (2012). Beam diameter was adapted according to grain size.

On the Resonetics RESOlutionSE 193nm excimer laser system garnet was ablated at 5 Hz and a fluence of 4 $J{\cdot}cm^{-2}$, during post acquisition quantification processing ^{27}Al was used as internal standard (11 wt%). On the GeoLas-Pro 193 nm ArF Excimer laser system garnet was ablated at 10 Hz and 9 $J{\cdot}cm^{-2}$, during post acquisition quantification processing internal standardization was done by summing the measured mass fraction of element oxides to 100 wt% assuming garnet as anhydrous phase. Accuracy on secondary standard was better than 10% for all elements.

Rutile was ablated on the GeoLas-Pro 193 nm ArF Excimer laser system at 8 Hz and a fluence of 6 $J{\cdot}cm^{-2}$. During post acquisition quantification processing ^{49}Ti was used as internal standard (59.94 wt%). Accuracy on secondary standard NIST 612 was within 10% for all elements and 20% for Zr.

Garnet trace element maps were acquired on standard 30 µm thick polished thin sections using a comparable protocol to that described in Raimondo *et al.* (2017) and George *et al.* (2018). The laser was operated at a repetition rate of 10 Hz, a fluence of 7 $J \cdot cm^{-2}$ and a continuous scan speed of 10 µm/s, using a beam diameter of 12 or 16 µm. Line spacing was adapted accordingly to the beam diameter. A total of 31 elements were measured for a total sweep time of 0.46 s, where dwell times were 0.01 s for most masses with the exception of LREE (from La to Gd = 0.02 s), and Hf (0.03 s). During post acquisition quantification processing ^{27}Al was used as internal standard (11 wt%). Image processing was performed using XMapTools 3.2.1.

4.4. Lu-Hf geochronology

For Lu-Hf garnet geochronology, bulk rock powders and mineral separates were prepared at the Institute of Geological Sciences, University of Bern (Switzerland). High quality mineral separates were obtained by applying high voltage discharge on rock samples using SelFrag Lab system. Mesh size allowing specific mineral fraction separation was adapted for each sample. The fragmented material was then dried in an oven at 60 °C. Multi-grain garnet separates were carefully prepared under a binocular microscope. Whole-rock powders were made by crushing rock samples in a stainless steel mortar and pestle. Samples were then dry milled in an agate ring mill for 30 min. Each sample run was bracketed by sandquartz milling for 15min in order to clean the receptacle. Chemical digestion and isotopic analyses were conducted at the Pacific Center for Isotope and Geochemical Research, University of British Columbia. Garnet separates and whole-rock powders were weighed in screw-top PFA beakers following admixing of a ^{176}Lu-^{180}Hf isotope tracer. Garnet dissolution was done by cycling HF-HNO_3-$HClO_4$ and HCl with intermittent solution dry-down. This method dissolves garnet without co-dissolving zircon (Scherer et al. 2000; Lagos et al. 2007). Whole-rock powders were dissolved in HF-HNO_3 kept at 180 °C for 5 days in Parr® high-pressure digestion vessels. Solutions containing dissolved mineral and whole-rock chemical matrices were loaded onto pre-conditioned 12 mL Teflon® columns containing Eichrom® Ln-spec resin and Lu and Hf were isolated and purified using the methods of Münker, Weyer, Scherer & Mezger (2001). The Lu and Hf isotope measurements were carried out using a Nu Instruments Plasma I multi-collector ICPMS (MC-ICPMS) instrument. The $^{176}Lu/^{175}Lu$ of unknowns was determined using ^{176}Yb interference corrections on the basis of a linear correlation between $\ln(^{176}Yb/^{171}Yb)$-$\ln(^{174}Yb/^{171}Yb)$, which was determined by replicate Yb standard measurements (Blichert-Toft et al. 2002). Hafnium mass bias was corrected assuming the exponential law and applying $^{179}Hf/^{177}Hf = 0.7325$. All Hf isotope ratios are reported relative to JMC-475 ($^{176}Hf/^{177}Hf = 0.282163$; Blichert-Toft, Chauvel, & Albarède (1997)), for which long-term external reproducibility is 0.3 εHf at the concentration typical of garnet samples. The

external reproducibility (2 SD) of unknowns was estimated on the basis of the external reproducibility for JMC-475, which was measured at concentrations that bracketed those of the unknowns (Bizzarro et al. 2003). Total procedural Hf blanks during the course of the analytical session were 12 pg or lower. Isochron regressions and age calculations were done using Isoplot version 3.27 (Ludwig 2003), applying 1.867×10^{-11} yr^{-1} for $\lambda^{176}Lu$ (Scherer et al. 2001; Söderlund et al. 2004). All uncertainties are reported at the 2 SD level.

4.5. Phase equilibrium modelling

The *P–T* conditions for garnet formation were determined using the program GrtMod 1.6.2 (Lanari et al. 2017). The software is based on an iterative garnet fractionation process from known initial bulk rock composition. Each successive numerical simulation of garnet growth aims to match the observed quantitative chemical composition of specific garnet growth zone, with the following input parameters: (1) the bulk rock composition, (2) the water available in the system, (3) the oxidation state of the system, and (4) the garnet composition of each zone considered. The optimization routine produces for each growth stage "optimal" *P–T* conditions and an uncertainty envelope by minimizing the differences between the measured and the modelled garnet compositions while optimizing the reactive bulk composition. Garnet fractionation and/or resorption was simulated successively for every growth stage, where garnet resorption of previous garnet growth stage(s) will affect and reduce their fractionated volume. A software option can prevent resorption in case of isolated growth zone or clear absence resorption textures; if not mentioned otherwise, the amount of resorption was systematically part of the optimization. Gibbs energy minimizations were performed using Theriak-Domino (De Capitani and Brown 1987; De Capitani and Petrakakis 2010) and the internally-consistent thermodynamic dataset of Holland and Powell (1998) and subsequent updates gathered in tc55 (see below). The chemical system was restricted to SiO_2-TiO_2-Al_2O_3-FeO-MnO-MgO-CaO-Na_2O-K_2O-H_2O-O_2. The following solid solution models were used: feldspar (Holland and Powell 2003; Baldwin et al. 2005); spinel, biotite (White et al. 2007); epidote, cordierite, talc, staurolite, chlorite, carpholite and garnet (Holland & Powell, 1998); clinopyroxene (Green et al. 2007); chloritoid (White et al. 2000); white mica (Coggon and Holland 2002); amphibole (Diener et al. 2007). Water saturation was applied to all models and excess oxygen of 0.005 mol was used for sample Z16TB32. These values were adjusted with *T–X* diagram, notably the excess oxygen in Z16TB32 was adapted to reproduce the observed mode of epidote. For each simulation, the output parameters are: (1) the composition of the reactive bulk, (2) the garnet pressure and temperature equilibrium condition, (3) the garnet composition, (4) the volume of garnet fractionated and/or resorbed for the actual and each of the previous garnet growth simulations. The

robustness of the results produced by GrtMod was systematically evaluated. (1) The volume of previous garnet fractionated was compared to observations on each sample. (2) The quality of the solution (i.e., the difference between observed and modelled garnet composition) was monitored using tolerance factor C_0 with a maximal threshold of 0.05. (3) The coexisting phases predicted to be stable for the same reactive bulk composition were simulated using Theriak-Domino at pressure and temperature condition of garnet equilibrium. The simulated assemblage was compared with mineral inclusions observed in garnet.

Two independent methods were applied for white mica thermobarometry. (1) By intersection of two independent isopleths, Si in atoms per formula unit (apfu) and X_{Mg} (X_{Mg} =Mg/(Mg+Fe)), obtained by forward modelling with the software Theriak-Domino. White mica fractionation was not considered as it has no major effect on modelled compositions (Airaghi et al. 2017). For each compositional group of average X_{Mg} and Si(apfu) values, *P–T* estimates are presented as an "optimal" solution together with an uncertainty envelope obtained using the GrtMod method adapted here for K-white mica. (2) Inverse modeling using the method and solid-solution model of Dubacq *et al.* (2010) were calculated with the program ChlMicaEqui (Lanari 2012). For a given potassic white mica composition in equilibrium with quartz and water, the equilibrium conditions are represented by a line in *P–T* space along which the interlayer water content varies (Dubacq et al. 2010).

The *P–T* conditions of chloritoid were determined using X_{Mg} (X_{Mg} =Mg/(Mg+Fe) isopleths modeled with Theriak-Domino.

4.6. Zr-in-rutile thermometry

Calculation were performed using the "combined model" of Kohn (2020) assuming growth at the maximum pressure determined for our samples (2.65 GPa; see below), thus providing maximum *T* estimates. The sources of uncertainty to be propagated onto Zr-in-rutile temperature estimates are the effect of analytical uncertainty of Zr measurement and uncertainty inherent in the calibration (~2 % for 500–650 °C, Kohn (2020)). The Zr analytical error was estimated to be ± 20 %, which corresponds to an uncertainty of ± 15–20 °C for the 500–650 °C temperature range. Combined with the internal error of the calibration of Kohn (2020), total uncertainty of ± 35 °C is estimated for the same temperature range. The presence of quartz and zircon in the schists ensures an activity of SiO_2 and ZrO_2 for application of the thermometry.

5. RESULTS

5.1. Mineral texture and chemistry

5.1.1. Garnet chemistry

Major and trace element compositional maps of garnet from the mafic fels, mafic schist and Cld-schist are shown in Figure 3, 4, 5, 6 and in the Figure S1, S2, S3, S4. Pixels selected in specified regions-of-interest to reflect the main chemical zoning observed in garnet chemical maps allow for a discrimination of several populations of garnet in each sample (Figure 3d, 3h, 4c, 4g, 5c). The average composition of each growth zone is reported in Table S1 and Table S2.

Mafic fels samples Z16TB32 and Z18TB15. Garnet composition ranges between Grs_{30} and Grs_{50} with pyrope content below Prp_{20}. Garnet cores are systematically enriched in Mn up to Sps_{20} in sample Z18TB15 and Sps_{15} in Z16TB32. In sample Z16TB32, Ca and Mn decrease from core ($Grt_{MF,1a}$) to rim ($Grt_{MF,2a}$) following a bell-shaped profile that is mirrored by Fe and Mg (Figure 3a-d). Irregular Ca enrichment is observed along rims (Figure 3a). In sample Z18TB15, Mn decreases from core ($Grt_{MF,1b}$) to rim ($Grt_{MF,2b}$) following a bell-shaped profile associated with Fe increase (Figure 3b,h). The distribution of Ca is more complex, with a Ca-poor core, a Ca-rich mantle and a Ca-poor rim (Figure 3e). The numerous garnet grains investigated locally show a discontinuous 0.2–0.3 mm rim that is enriched in Mg and depleted in Mn, Fe and Ca (Figure 3e-h). In sample Z18TB15, garnet shows strong concentric trace element zoning, with maximum heavy-REE (HREE) concentrations in cores decreasing towards the rim and local patchy Y+HREE enrichment in mantle (Figure 6a, Figure S1). The discontinuous rim defined by major elements (Figure 3e-h) is enriched in Co, Zn, Y, Eu, MREE, and depleted in Ti, V, Cr, and HREE.

Mafic schist samples Z16TB11 and Z16TB28. The small garnet grains in the matrix exhibit two chemically distinct zones with a sharp and irregular boundary that is less than 1 µm thick (Figure 4a-

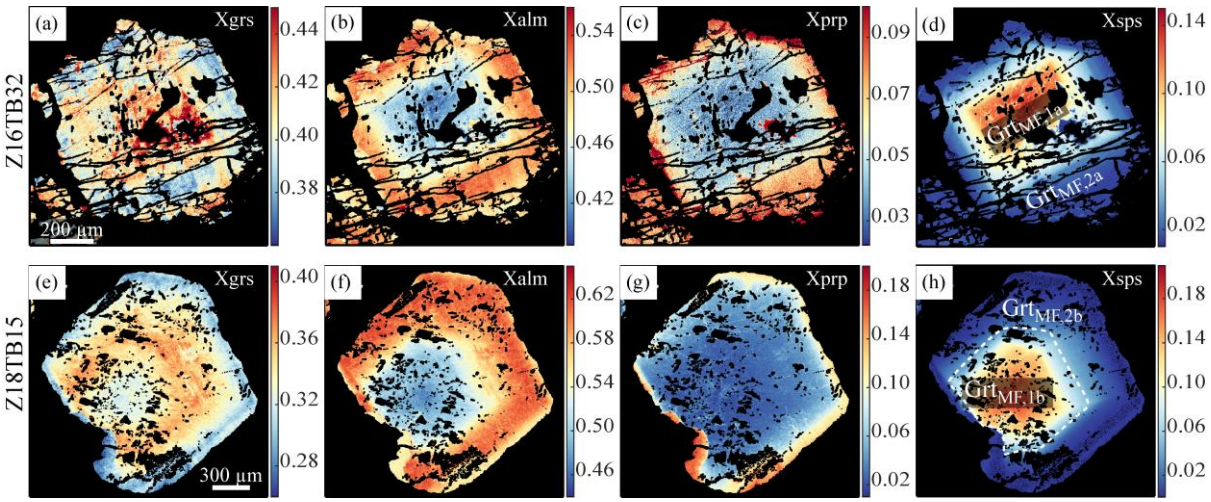

Figure 3: : End-member compositional maps of garnet generated using XMapTools (Lanari et al. 2014, 2019) from the mafic fels sample Z16TB32 (a-d) and sample Z18TB15 (e-f).

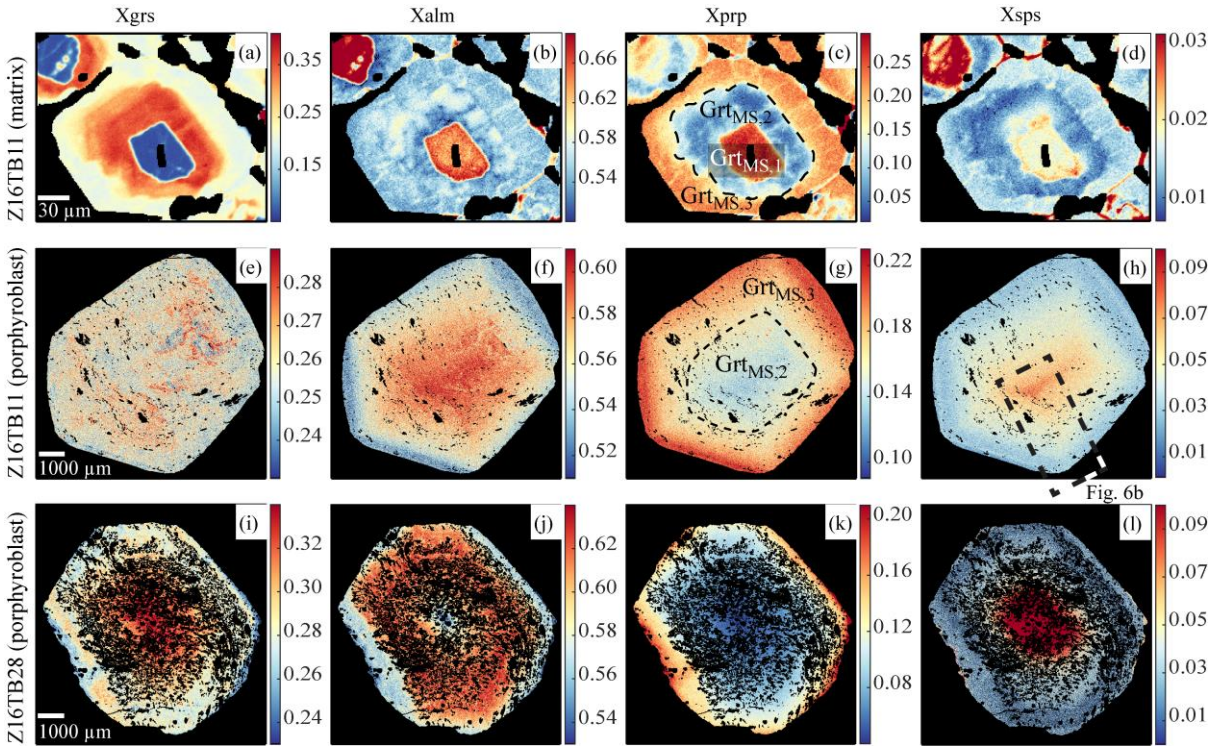

Figure 4: End-member compositional maps of small garnet crystals from the mafic schist sample Z16TB11(a-d), and garnet porphyroblasts from sample Z16B11(e-h) and sample Z16TB28(i-l).

d, 7a). The cores ($Grt_{MS,1}$) are enriched in Fe, Mg and Mn, and depleted in Ca ($Alm_{64-68}Prp_{23-27}Grs_{13-15}Sps_{1-3}$) compared to the rims. Mn enrichment domains are observed along the core-rim boundary (Figure 4d). The euhedral rims are zoned, with an inner part ($Grt_{MS,2}$) that is distinctly richer in Ca and poorer in Mg ($Alm_{54-59}Prp_{5-8}Grs_{32-36}Sps_{1-2}$) than the outer part ($Grt_{MS,3}$, $Alm_{54-59}Prp_{19-22}Grs_{21-25}Sps_{1-2}$). Larger garnet porphyroblasts (Figure 4e-l, 7b) are characterized by smooth concentric zoning, with Mg concentrations increasing towards the rim, and decreasing Fe and Mn. Ca zoning is locally more patchy and inhomogeneous in sample Z16TB11. The chemical composition of these porphyroblasts ($Alm_{54-62}Prp_{8-22}Grs_{24-32}Sps_{1-9}$) is similar to that of the rim of matrix garnet, except that Mn core concentrations are slightly higher. In sample Z16TB11, garnet porphyroblasts display only minor trace-element zoning (Figure 6b, Figure S2). Euhedral oscillatory zoning at the 50 µm scale is visible in Cr, Y and HREE, and sector zoning is observed for Y and REE within garnet mantle and rim. REE patterns (Figure 8a) show a homogeneous increase for LREE and MREE, and flat HREE pattern starting from Ho. The latter decrease only slightly from core to rim. Garnet porphyroblasts from

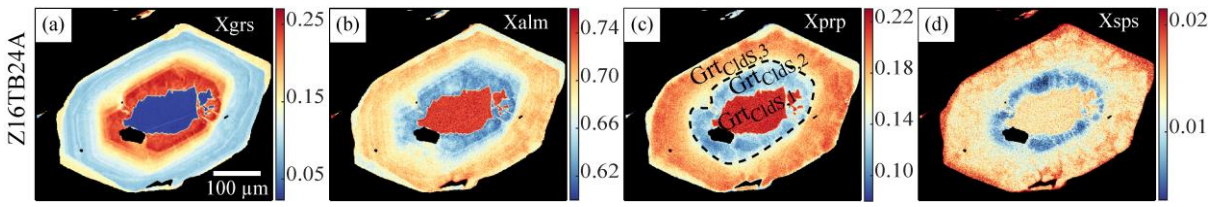

Figure 5: ***End-member compositional maps of garnets from the Cld-schist sample Z16TB24A.***

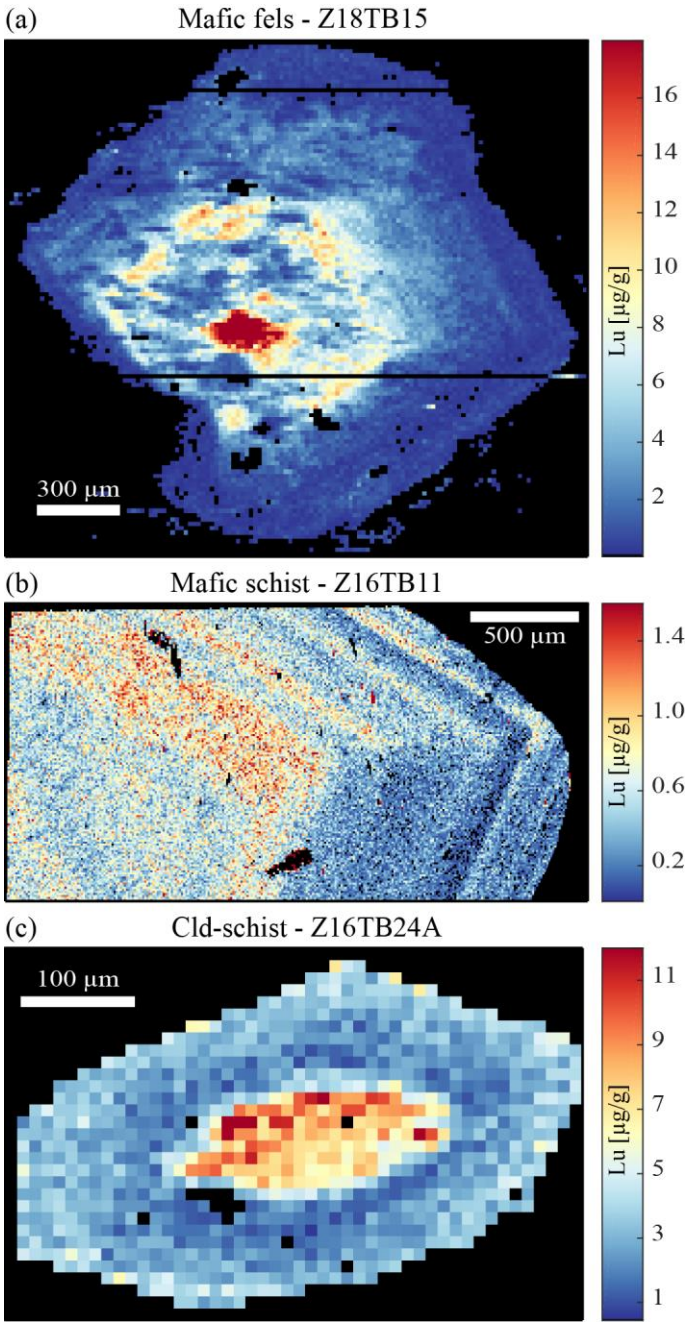

Figure 6: Trace element LA-ICP-MS compositional maps of Lu in garnet for the three rock types dated by Lu-Hf.

sample Z16TB28 (Figure 8c) show homogeneous increase from MREE towards HREE. There is a marked decrease in Gd_N/Yb_N (N= Chondrite normalized) from core to rim. For the small garnet grains that display sharp chemical zoning the spatial resolution of the ablation spot is insufficient to resolve all the domains described by EPMA measurement, particularly for the rim. REE normalized patterns (Figure 8b) show comparable HREE composition between core and rim, with a Gd_N/Yb_N relatively close to unity. The cores are generally richer in MREE and have a marked negative Eu anomaly, which is not observed for the rims.

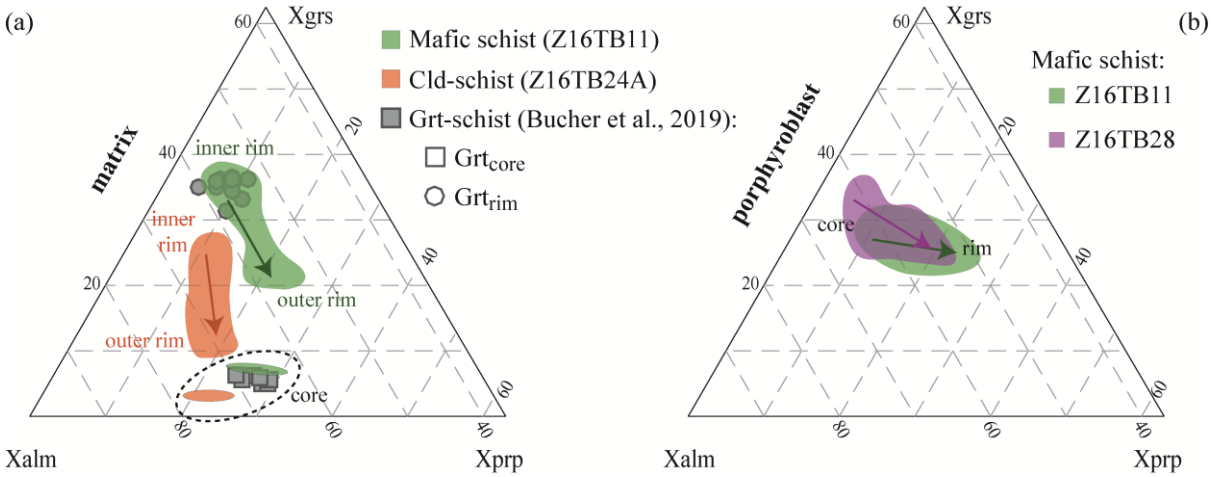

Figure 7: Ternary chemical diagram showing the range of garnet composition in X_{grs}-X_{alm}-X_{prp}. Range of compositional data were exported from compositional maps (Figure S6). (a) Small garnet grains from the mafic schist (Z16TB11, area drawn on the basis of 30.137 pixels) and Cld-schist (Z16TB24A, area drawn on the basis of 111.072 pixels), compared with garnet compositions from Bucher et al. (2019). (b) Garnet porphyroblasts from the mafic schist samples Z16TB11 (area drawn on the basis of 516.869 pixels) and Z16TB28 (area drawn on the basis of 209.512 pixels).

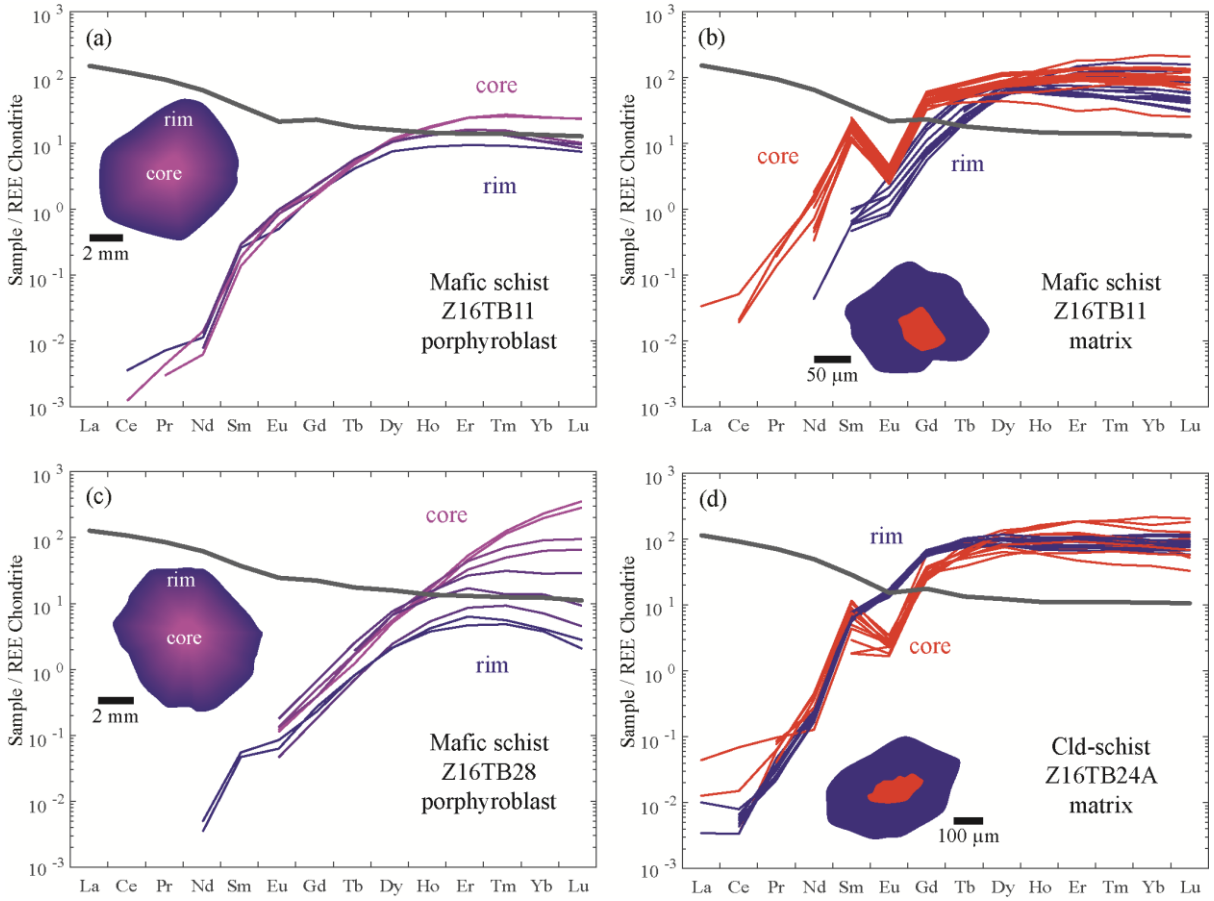

Figure 8: REE chondrite-normalized concentrations of bulk rock (black) and garnet (red, violet and blue) from different samples. Normalization data: Taylor & McLennan (1985).

Chloritoid-schist sample Z16TB24A. Garnet has two distinct chemical zones (Figure 5, 7a) separated by a sharp 1-µm contact. The xenomorphic core ($Grt_{CldS,1}$) is depleted in Ca and enriched in Fe and Mg ($Alm_{72-76}Prp_{20-24}Grs_{3-6}Sps_{1}$) compared to the rims. The euhedral rims are zoned with decreasing Ca and increasing Mg, Fe and Mn from the inner ($Grt_{CldS,2}$) to the outer part ($Grt_{CldS,3}$, $Alm_{54-58}Prp_{15-17}Grs_{26-30}Sps_{0.1-0.2}$ to $Alm_{60-68}Prp_{8-12}Grs_{23-27}Sps_{<1}$, respectively). A Ca- and Mn-rich discontinuous domain of up to 15 µm width is observed along the external rim. Thin radial channels with similar chemical composition as the external rim run towards the mineral core (Figure 5d). Trace element mapping (Figure 6c, Figure S3) highlights the strong chemical difference between core and rim, as described for major elements. The core is enriched in V, Cr, Li, Co, Y and HREE compared to the inner rim. The external rim is depleted in V and Ti, and enriched in Cr, Co and MREE, compared to the inner rim. On a logarithmic scale, the REE pattern of garnet core and rim largely overlap (Figure 8d) but the core is characterised by lower Gd and a marked Eu negative anomaly, which is not present in the rim.

5.1.2. K-white mica and chloritoid major element chemistry

The compositional variability of potassic white mica from mafic schists (Z16TB11 and Z16TB28), and the chloritoid-schist (Z16TB24A) was investigated. In every sample, mica flakes are preferentially oriented along the main foliation and microstructural criteria are not sufficient to discriminate different populations. However, the compositional maps highlighted in Figure 9 reveal variations in the Si a.p.f.u. and X_{Mg}. Pixels selected in specified regions-of-interest on the Si(apfu) and X_{Mg} binary plots were adjusted to reflect the main textural domains and allow for a discrimination of several populations of K-white mica in each sample (Figure 9). Representative average phengite compositions were extracted from the elemental maps and are reported in Table S3.

Mafic schist samples Z16TB11 and Z16TB28. Three K-white mica populations were identified in sample Z16TB11 (Figure 9a,c) and five in Z16TB28 (Figure 9d,f). The three mica populations of Z16TB11 ($Ph_{MS,1a}$, $Ph_{MS,2a}$ and $Ph_{MS,3a}$) have comparable microtextural location and spatial distribution than the three first population of Z16TB28 ($Ph_{MS,1b}$, $Ph_{MS,2b}$ and $Ph_{MS,3b}$). The first mica population ($Ph_{MS,1a}$ and $Ph_{MS,1b}$) is located in the central zone of elongated mica flakes stretched along the main foliation. It has on average 3.33 ± 0.02 Si(apfu) and 0.76 ± 0.02 X_{Mg} in sample Z16TB11 and 3.40 ± 0.02 Si(apfu) and 0.79 ± 0.02 X_{Mg} in sample Z16TB28. The second population of mica ($Ph_{MS,2a}$ and $Ph_{MS,2b}$) occurs either on the edge of the first population clusters or as single grains in the foliation. It has on average Si(apfu) of 3.29 ± 0.02 and X_{Mg} of 0.71 ± 0.02 in sample Z16TB11 and Si(apfu) of 3.34 ± 0.02 and X_{Mg} of 0.72 ± 0.02 in sample Z16TB28. The third mica group ($Ph_{MS,3a}$ and $Ph_{MS,3b}$) is found on the edge the second population clusters or as isolated grains. The Si(apfu) content is 3.22 ± 0.02

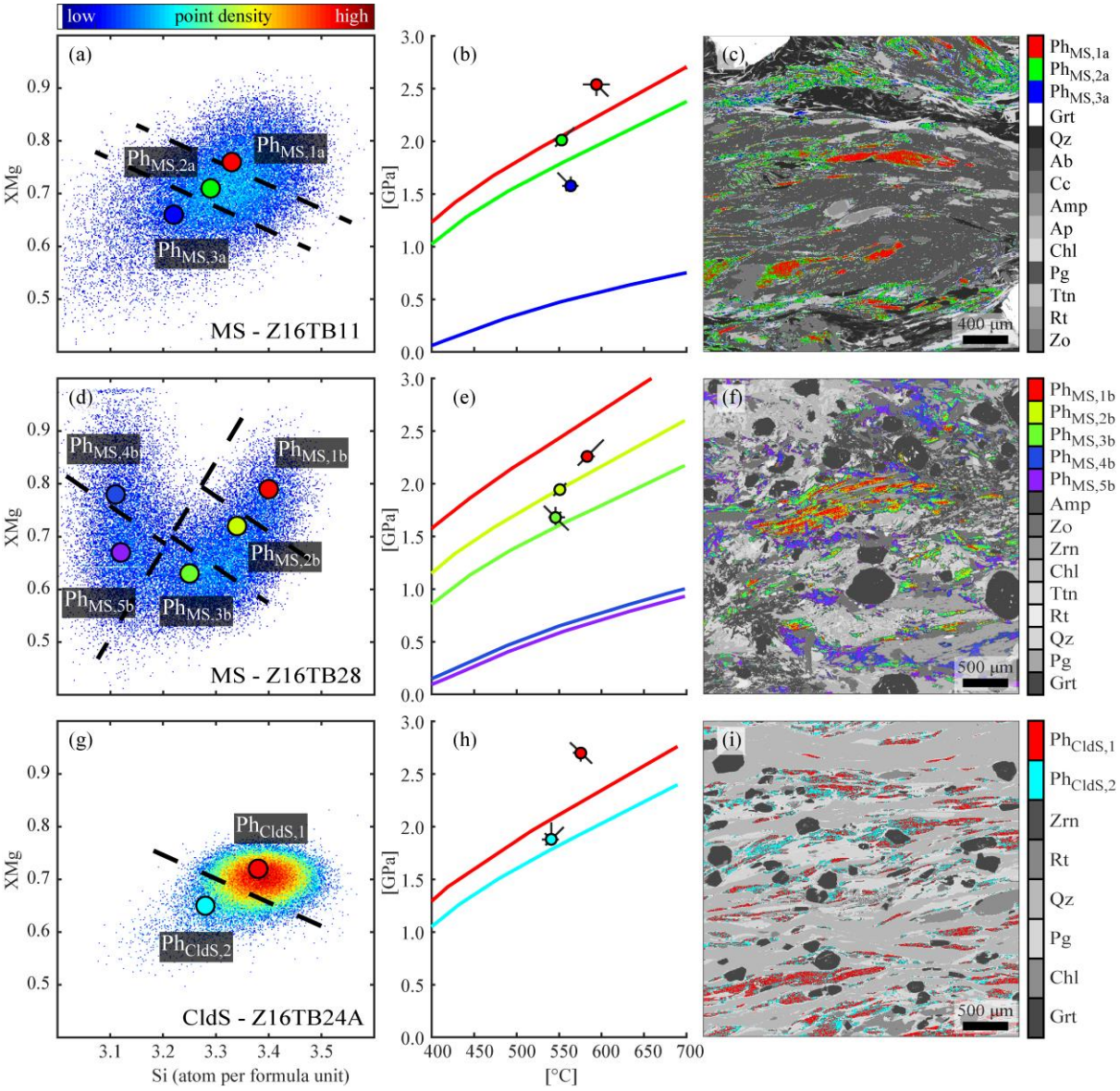

Figure 9: Phengite population discrimination plots. Each row corresponds to a sample: mafic schist Z16TB11(a-c), mafic schist Z16TB28(d-f), Cld-schist Z16TB24A(g-i). First column: Si(atom per formula unit)-XMg binary diagram with color scale corresponding to point density (log-scale). Spots show the average composition of each phengite group used for modelling. Dashed-lines represent the boundary between the different compositional groups. Second column: P–T estimates based on mica compositions. The spots represent the intersection between X_{Mg} and Si(apfu) isopleths, whereas line correspond to phengite-quartz-water equilibria (see text). Third column: spatial relation among phengite groups and other phases (in gray).

and X_{Mg} is 0.66 ± 0.02 in sample Z16TB11 and Si(apfu) of 3.24 ± 0.02 and X_{Mg} of 0.64 ± 0.02 in sample Z16TB28. The last two populations ($Ph_{MS,4b}$ and $Ph_{MS,5b}$) are only observed in Z16TB28 and are characterized by a lower Si(apfu) than the three previous generations (Figure 9d). They are texturally associated to zoisite and paragonite, and form patchy aggregates, which sometimes rim the previously described mica population (Figure 9f). On average, $Ph_{MS,4b}$ Si(apfu) content is 3.11 ± 0.02 and X_{Mg} is 0.78 ± 0.02, whereas $Ph_{MS,5b}$ Si(apfu) content is 3.12 ± 0.02 and X_{Mg} is 0.67 ± 0.02.

Chloritoid-schist sample Z16TB24A. Two populations of K-white mica were identified (Figure 9g). The first population ($Ph_{CldS,1}$) is located in the central zone of elongated mica aggregates

stretched along the main foliation (Figure 9i). It has on average 3.38 ± 0.02 Si(apfu) and 0.72 ± 0.02 X_{Mg}. The second population of mica ($Ph_{CldS,2}$) occur either on the edge of the first population clusters or as single grains in the foliation. It has on average Si(apfu) of 3.28 ± 0.02 and X_{Mg} of 0.65 ± 0.02. Chloritoid from the Cld-schist (Table S4) varies in X_{Mg} from 0.25 to 0.38, where higher values are representative of the core and decrease towards the external part of the rim (Figure S5).

5.1.3. Rutile

Among the studied samples, rutile was found in mafic and Cld-schist with a range in grain size varying from few to 100 µm. All rutile analysed were located in the matrix except two grains found as inclusion in garnet (mafic schist Z16TB11 and Z16TB28). Grains for analyses were carefully selected to avoid possible contamination by inclusions and fractures. Analyses (Table S5) were screened for contamination from inclusions based on high Si, Na, Al, Mn, Fe, Y, Sn, Hf and Zr contents. The average concentration of Zr in rutile (Table 2) within the mafic schist is 36 ± 3 µg/g in sample Z16TB11 and 40 ± 4 µg/g in sample Z16TB28. Rutile inclusions in garnet contain 36 µg/g (sample Z16TB11) and 27 µg/g (sample Z16TB28) Zr. The average Zr concentration in the rutile from Cld-schist (sample Z16TB24A) is 40 ± 5 µg/g. The Zr concentration in rutile is similar within uncertainty among the different lithologies.

Lithology	Sample	N	Zr-Rutile [µg/g]				Pressure [GPa]	Zr-in-Rutile T [°C]			
			Min	Max	Average	SD		Min	Max	Average	Error
Matrix											
Mafic schist	Z16TB11	16	31	40	36	3	2.65	524	540	534	35
Mafic schist	Z16TB28	25	33	49	40	4	2.65	528	555	541	35
Cld-schist	Z16TB24A	24	31	49	40	5	2.65	524	555	541	35
Inclusion in garnet											
Mafic schist	Z16TB11	1	-	-	36	-	2.65	-	-	534	35
Mafic schist	Z16TB28	1	-	-	27	-	2.65	-	-	515	35

Number of grain analyzed (N), Minimum (Min), Maximum (Max), Standard Deviation (SD)

Table 2: Thermometric estimates determined by Zr-in-rutile thermometry (Kohn 2020).

5.2. Thermobarometry

5.2.1. Thermodynamic modelling

The *P*–*T* stability conditions of garnet, phengite and chloritoid were determined for the investigated samples using the strategy outlined above; results are shown in Figure 9, 10, 11. The reactive bulk compositions used are reported in Table S6. After careful identification of representative chemical garnet zones in each sample, average garnet chemical compositions were extracted from the elemental maps (Table S1) from the domains shown in Figure 3d, 3h, 4c, 4g and 5c. Minor chemical variations within the domains for sample Z18TB15, Z16TB24A and Z16TB11 were probably controlled by kinetics rather than chemical equilibrium and were not considered.

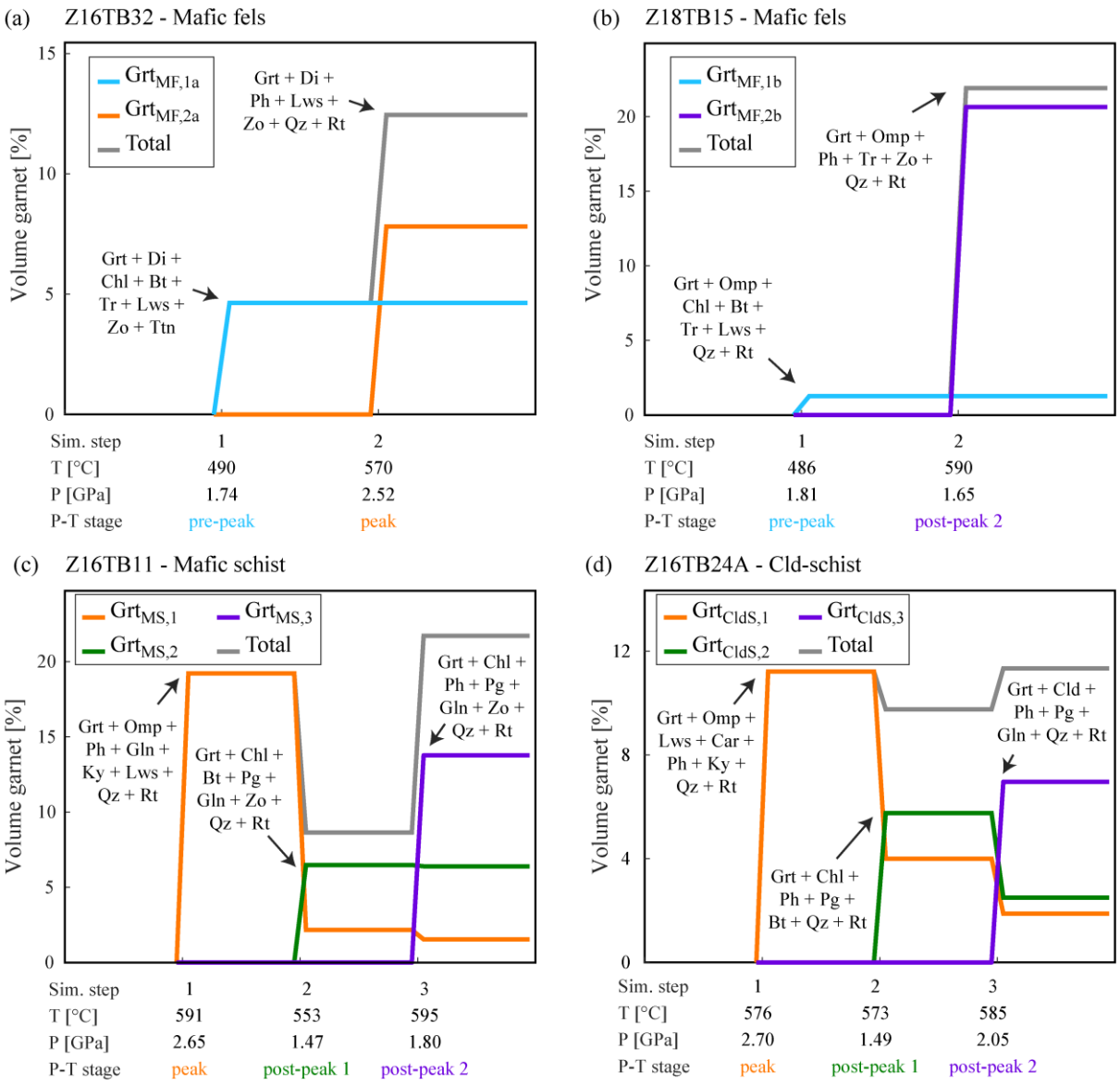

Figure 10: Garnet growth/resorption history for different samples obtained using GrtMod. The evolution of volume fraction (in vol%) of each growth zone are plotted for each step. The curve labelled "Total" shows the evolution of the total amount of garnet in the system. The P–T conditions of each steps are the optimal conditions determined by the model. The modelled mineral assemblages is indicated for each garnet growth step.

Mafic fels sample (Z16TB32). The garnet core $Grt_{MF,1a}$ (Figure 3d) is predicted to be stable at 490 ± 10 °C and 1.74 ± 0.05 GPa (TF: 0.011) with 5 vol% of garnet (Figure 10a). The modelled phase assemblage is Grt+Omp+Chl+Bt+Tr+Lws+Ttn+Qz. The rim stage $Grt_{MF,2a}$ (Figure 3d) is modelled at 570 ± 10 °C and 2.52 ± 0.10 GPa (TF: 0.023; 8 vol% garnet) without permitting resorption of $Grt_{MF,1a}$ (Figure 10a). The modelled phase assemblage at these conditions is Grt+Omp+Ph+Lws+Qz+Rt.

Mafic fels sample (Z18TB15). The garnet core $Grt_{MF,1b}$ (Figure 3h) is predicted to be stable at 486 ± 15 °C and 1.81 ± 0.05 GPa (TF: 0.046) with 2 vol% of garnet (Figure 10b). The modelled phase assemblage is Grt+Omp+Chl+Bt+Tr+Lws+Qz+Rt. The rim stage $Grt_{MF,2b}$ (Figure 3h) is modelled at 590 ± 15 °C and 1.65 ± 0.15 GPa (TF: 0.003) with the formation of 21 vol% of garnet without requiring

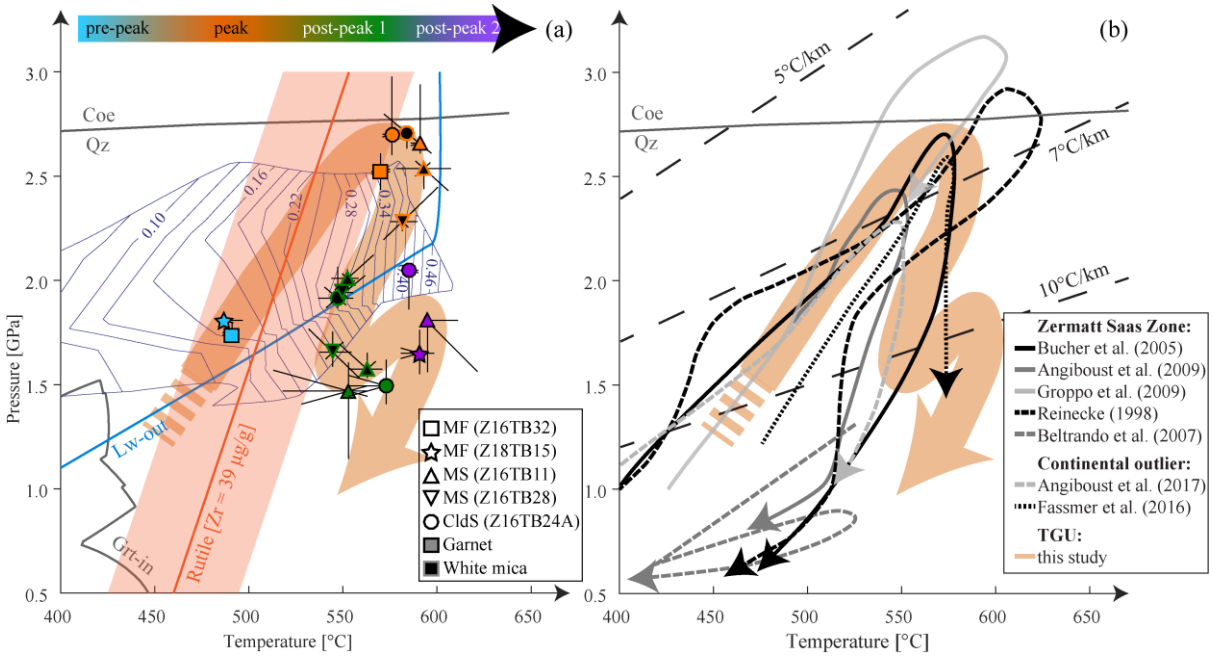

Figure 11: Pressure-Temperature path of the TGU and the ZSZ tectonic unit. (a) Synthetic P–T diagram compiling the thermobarometric results from the four investigated samples. Abbreviation for the lithologies are: MF – mafic fels, MS – Mafic schist, CldS – Cld-schist. Theriak-Domino results: i) isopleths shown in blue are XMg in chloritoid (Cld-schist, Z16TB24A); ii) The Grt-in curve (mafic fels, Z18TB15) is shown in gray. (b) P–T diagram showing a compilation of published P–T paths from other localities in the ZSZ tectonic unit and published P–T path from continental outlier in the vicinity of the TGU.

resorption of $Grt_{MF,1b}$ (Figure 10b). The modelled phase assemblage at these conditions is Grt+Omp+Ms+Tr+Zo+Qz+Rt.

Mafic schists (sample Z16TB11). The garnet core composition $Grt_{MS,1}$ (Figure 5c) is modelled at temperature of 591 ± 10 °C and pressure ranging between 2.65 to 2.85 GPa with optimal solution at 2.65 GPa (TF: 0.039). The modelled phase assemblage is Grt+Omp+Ph+Gln+Ky+Lws+Qz+Rt (Figure S7) and contains 19 vol% of garnet (Figure 10c). Simulation for the inner rim stage $Grt_{MS,2}$ (Figure 5c) predicts strong resorption of $Grt_{MS,1}$ (17 vol%) and lead to the formation of 6 vol% of garnet $Grt_{MS,2}$ (Figure 10c) at 553 +10/-50 °C and 1.47 +0.15/-0.35 GPa (TF: 0.059). The modelled phase assemblage for $Grt_{MS,2}$ is Grt+Chl+Pg+Bt+Gln+Zo+Qz+Rt (Figure S8). The simulation for the external rim $Grt_{MS,3}$ (Figure 5c) predicts the observed garnet composition at 595 +25/-10 °C and 1.80 +0.05/-0.30 GPa (TF: 0.034). Previously fractionated garnet stages are only slightly affected with 1 vol% resorption of $Grt_{MS,1}$, with up to 14 vol% garnet fractionation of $Grt_{MS,3}$ (Figure 10c). The modelled phase assemblage is Grt+Chl+Ph+Pg+Gln+Zo+Qz+Rt (Figure S9). Intersection of Si(apfu) and X_{Mg} isopleth in phengite (Figure 9b) is observed at 590 ± 15 °C and 2.5 ± 0.1 GPa for $Ph_{MS,1a}$. The second population $Ph_{MS,2a}$ is modelled at lower pressure and slightly lower temperature of 550 ± 10 °C and 2.0 ± 0.1 GPa. The last group $Ph_{MS,3a}$ shows lower pressure conditions and similar temperature compared to $Ph_{MS,2a}$ at 560 ± 10 °C and 1.6 ± 0.1 GPa. Assuming similar temperature for each population phengite-

quartz-water inverse method provides pressure estimates of 2.2 ± 0.1 GPa ($Ph_{MS,1a}$), 1.8 ± 0.1 GPa ($Ph_{MS,2a}$) and 0.5 ± 0.1 GPa ($Ph_{MS,3a}$).

Mafic schist sample Z16TB28. Si(apfu) and X_{Mg} isopleths of phengite (Figure 9e) intersect at 580 +20/-15 °C and 2.3 +0.3/-0.1 GPa for the first group $Ph_{MS,1b}$, and 550 ± 10 °C and 2.0 ± 0.1 GPa for the second group $Ph_{MS,2b}$. The third population $Ph_{MS,3b}$ is modelled at 550 ± 10 °C and 1.7 ± 0.1 GPa, thus at lower pressure conditions compared to $Ph_{MS,2b}$. Assuming similar temperature for each population, the phengite-quartz-water method retrieved pressures of 2.6 ± 0.1 GPa ($Ph_{MS,1b}$), 2.0 ± 0.1 GPa ($Ph_{MS,2b}$) and 1.6 ± 0.1 GPa ($Ph_{MS,3b}$). Populations $Ph_{MS,4b}$ and $Ph_{MS,4b}$ can only be modelled using the method of Dubacq *et al.* (2010)—there are no intersection of the isopleths in the *P–T* space—and both indicate much lower pressure conditions below 1 GPa (Figure 9e).

Chloritoid-schist sample Z16TB24A. The garnet core composition $Grt_{CldS,1}$ (Figure 4c) is predicted to be stable at 576 ± 10 °C and 2.70 +0.30/-0.10 GPa (TF: 0.046). The modelled phase assemblage is Grt+Omp+Car+Ph+Ky+Lws+Qz+Rt, and contain 11 vol% of garnet (Figure 10d). Simulation for the inner rim stage $Grt_{CldS,2}$ (Figure 4c) indicates resorption of previous stage $Grt_{CldS,1}$ (7 vol%) and the formation of 6 vol% of garnet $Grt_{CldS,2}$ (Figure 10d) at 573 °C +10/-30 °C and 1.49 ± 0.10 GPa (TF: 0.048). The modelled phase assemblage is Grt+Chl+Ph+Pg+Bt+Qz+Rt. The simulation for the external rim $Grt_{CldS,3}$ (Figure 4c) is modelled at 585 ± 10 °C and 2.05 +0.05/-0.40 GPa (TF: 0.049). Previously formed garnet growth zones are slightly affected with 2 vol% resorption of $Grt_{CldS,1}$ and 3 vol% of $Grt_{CldS,2}$ respectively (Figure 10d). The associated paragenesis is Grt+Ctd+Ph+Pg+Gln+Qz+Rt. The intersection of Si(apfu) and X_{Mg} phengite isopleths (Figure 9h) provides conditions of 570 ± 10 °C and 2.7 ± 0.1 GPa for $Ph_{CldS,1}$ and 540 ± 10 °C and 1.9 ± 0.1 GPa for $Ph_{CldS,2}$. Assuming a similar temperature for each population the phengite-quartz-water method indicates pressure of 2.3 ± 0.1 GPa ($Ph_{CldS,1}$) and 1.9 ± 0.1 GPa ($Ph_{CldS,2}$). The X_{Mg} isopleth of chloritoid (Figure 11a) are compatible with chloritoid core formation at 580 ± 10 °C between 18 and 2.5 ± 0.1 GPa. The external rim is modelled between 1.5 and 2.5 ± 0.1 GPa for a temperature of 550 ± 10 °C.

5.3. Zr-in-rutile thermometry

Zr-in-rutile temperatures were calculated assuming a pressure of 2.65 GPa to provide an independent constraint on the temperature (Table 2). Averaged temperature for rutile found in the mafic schist retrieved 534 ± 35 °C for sample Z16TB11 and 541 ± 35 °C for sample Z16TB28. The two rutile grains found as inclusion in garnet gave 534 ± 35 °C (sample Z16TB11) and 515 ± 35 °C (sample Z16TB28) respectively. In the Cld-schist (sample Z16TB24A) the average temperature is 541 ± 35 °C. These results witness homogeneous temperature of crystallization among the lithologies of TGU, at the only exception of the rutile inclusion showing slightly lower temperature in sample Z16TB28.

5.4. Garnet Lu-Hf chronology

The garnet crystals observed in the different lithologies of the TGU present high variability in size, composition and texture. Key samples were selected (Figure S10) to correlate the garnet size fraction with garnet compositional zoning. In the mafic fels sample Z18TB15, the compositional zoning in garnet is comparable among all the grains at a sample scale and two garnet fractions were selected, the first one having a diameter between 0.25–0.50 mm and the second comprising larger grains. Four garnet fractions, comprising two from either size fraction, yielded a Lu-Hf age of 50.3 ± 0.3 Ma (mean square weighted deviation (MSWD) = 1.5; Figure 12a).

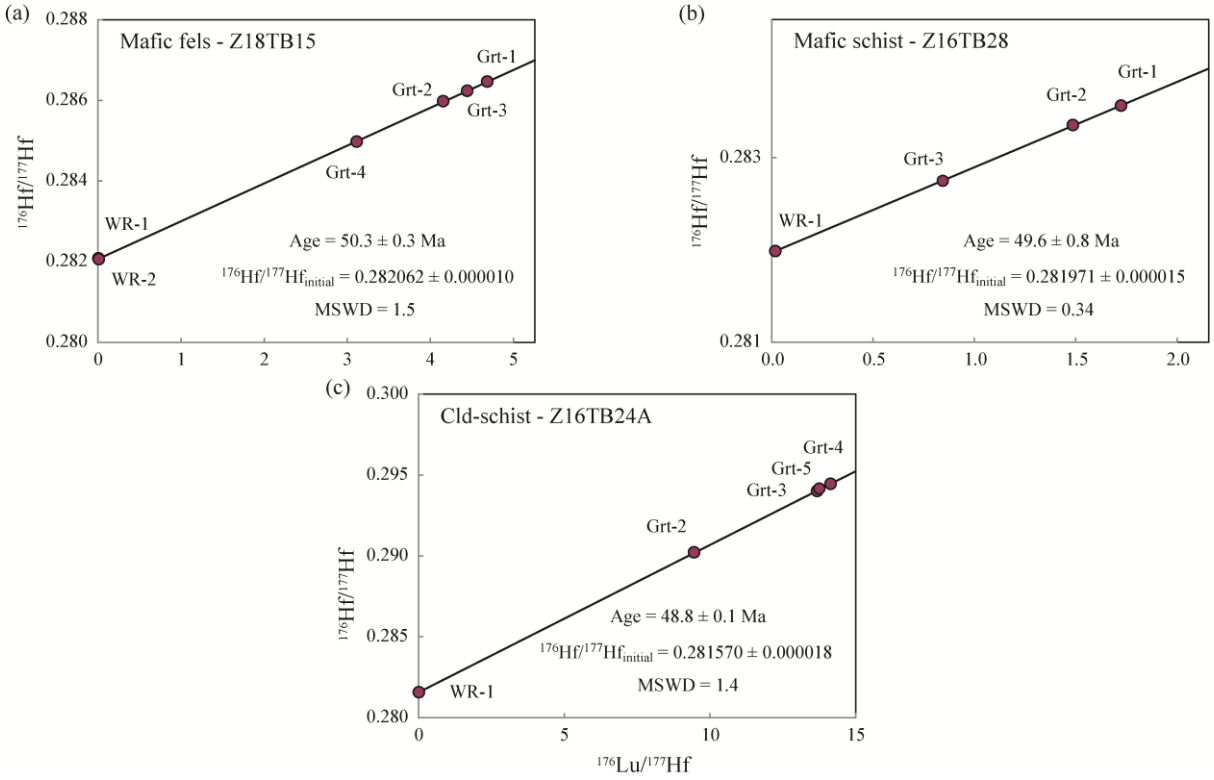

Figure 12: Lu-Hf isochrones for the studied samples. (a) mafic fels Z18TB15. (b) mafic schist Z16TB28. (d) Cld-schist Z16TB24A.

Two garnet types were targeted for the schists (Z16TB28 and Z16TB24A). In the mafic schist Z16TB28, garnet porphyroblasts do not show complex textures and have a restricted compositional range. In sample Z16TB28, garnet grains with diameter over 2 mm were picked. The material yielded a Lu-Hf age of 49.6 ± 0.8 Ma (MSWD = 0.34; n = 3; Figure12b). Small garnets with complex and sharp chemical zoning are present in the Cld-schist Z16TB24A and in mafic schist. This garnet type was picked in the Cld-schist because this is the only garnet type observed in this lithology. Two garnet fractions were differentiated in sample Z16TB24A: the first fraction contains garnet grains with diameter between 250 and 500 µm and the second garnet grains with diameter >500 µm. The sample yielded a Lu-Hf age of 48.8 ± 0.1 Ma (MSWD = 1.4; n = 4 ; Figure 12c). All samples yielded Lu-Hf dates with uncertainties of 1 %RSD or better (Table 3). The relatively high $^{176}Lu/^{177}Hf$ for Z18TB15

Sample fraction	Concentration		Isotope ratios				Final data			
	Lu [ppm]	Hf [ppm]	$^{176}Lu/^{177}Hf$	2SD	$^{176}Hf/^{177}Hf$	2SD	Lu-Hf age (Ma)	MSWD	$^{176}Hf/^{177}Hf_{initial}$	2SD
Mafic fels - Z18TB15										
Grt-1	2.26	0.068	4.68700	0.0120	0.286466	0.000047				
Grt-2	1.82	0.062	4.15700	0.0100	0.285977	0.000041				
Grt-3	2.31	0.074	4.44600	0.0110	0.286234	0.000031				
Grt-4	1.83	0.083	3.11500	0.0080	0.284978	0.000037				
WR-1	0.336	7.26	0.006555	0.000016	0.282081	0.000015				
WR-2	0.508	6.58	0.010954	0.000027	0.282061	0.000014				
					All analyses included:		50.3 ± 0.3	1.5	0.282062	0.000010
Mafic schist - Z16TB28										
Grt-1	1.49	0.123	1.72300	0.0040	0.283566	0.000026				
Grt-2	1.37	0.131	1.48600	0.0040	0.283354	0.000024				
Grt-3	1.38	0.231	0.845800	0.0021	0.282745	0.000031				
WR-1	0.936	7.79	0.017020	0.000040	0.281988	0.000016				
					All analyses included:		49.6 ± 0.8	0.34	0.281971	0.000015
Cld-schist - Z16TB24A										
Grt-2	2.52	0.038	9.45700	0.0240	0.290219	0.000040				
Grt-3	3.74	0.038	14.1400	0.0400	0.294459	0.000043				
Grt-4	3.63	0.038	13.6800	0.0300	0.294014	0.000044				
Grt-5	3.62	0.034	13.7400	0.0340	0.294139	0.000050				
WR-1	0.444	7.96	0.007897	0.000020	0.281576	0.000018				
					All analyses included:		48.8 ± 0.1	1.4	0.281570	0.000018

Standard deviation (SD)

Table 3: Lu-Hf isotope data and apparent ages.

(>4) and Z16TB24A (>13) returned extremely good precision of ±0.3 %RSD and ±0.2 %RSD, respectively.

6. DISCUSSION

6.1. Mineral sequence and *P–T* path of the TGU

The multiple, independent *P–T* constraints obtained from the TGU samples can be divided into peak-*P* metamorphic conditions and conditions that represent earlier (pre-peak) and later (post-peak) metamorphism (Figure 10, 11a). These distinct metamorphic stages were determined according to similar *P–T* estimates simulated in different mineral growth zones described previously.

Pre-peak metamorphic conditions are inferred from the numerical simulation of garnet for the mafic fels samples Z16TB32 and Z18TB15. Garnet cores $Grt_{MM,1a}$ and $Grt_{MM,1b}$ record the earliest growth of garnet at *P–T* conditions of 490 ± 15 °C and 1.75 ± 0.05 GPa (Figure 11a). Equilibrium phase diagram calculations using pristine bulk rock compositions show that the garnet-in curve is at a temperature, which is about 50 °C lower than these values (Figure 11a). This discrepancy could be explained either by overstepping to provide the driving force necessary for porphyroblast nucleation and growth (Spear 2017; Spear and Pattison 2017; Wolfe and Spear 2018; Spear and Wolfe 2019) or off-center sectioning of garnet. This would have particular impact on the apparent Mn concentration of the garnet nucleus, which is essential to constrain the initiation of the metamorphic growth based on equilibrium thermodynamic modelling (Lanari et al. 2017).

At the mineral scale, fluid rock interaction commonly leads to fracturing (Angiboust et al. 2011; Giuntoli et al. 2018b, a) and pseudomorphic (and often non-isochemical) replacement via interface-coupled dissolution and re-precipitation (Putnis 2002; Konrad-Schmolke et al. 2018), which may overprint previous chemical information. At the sample scale such fluid-rock interactions can significantly modify the bulk rock composition. It is thus possible that, of the two garnet generations, only the latest stage ($Grt_{MS,2}$, $Grt_{MS,3}$, $Grt_{CldS,2}$, $Grt_{CldS,3}$) represents an equilibrium with the bulk rock as measured. These issues are the prime reason why metasomatism can compromise the reliability of thermodynamic models based on the bulk rock composition (Evans 2004). In our samples, post-peak metamorphism garnet textures in mafic schists (Figure 4a-d) and Cld-schist (Figure 5) suggest strong fluid-rock interaction. Nevertheless, the *P–T* conditions estimated for peak-*P* metamorphism are in remarkable agreement. High-pressure *P–T* conditions of 580 ± 15 °C and 2.65 ± 0.10 GPa are consistently recorded by garnet in each lithology. These results are consistent with maximum Zr-in-rutile temperature estimates retrieved from homogeneous rutile populations present in different schist samples (Figure 11a). Moreover, K-white mica found in the mafic schist and in the Cld-schist also record similar peak metamorphism conditions (Figure 11a), as determined on the basis of two independent methods: (1) the pressure dependency of Si(apfu) content and the temperature dependency of X_{Mg} in phengite (Massonne and Schreyer 1987), and (2) the quartz-water-phengite barometer of Dubacq *et al.* (2010). Potassic white mica *P–T* conditions obtained by multi-equilibrium show similar results to the phase diagrams, although at slightly lower pressure conditions for sample Z16TB11 (mafic schist) and sample Z16TB24A (Cld-schist) and higher pressure condition for sample Z16TB28 (mafic schist) (Figure 9b,e,h), but within the absolute uncertainty of the method (± 0.25 GPa; Lanari and Duesterhoeft, 2019). The good agreement between *P–T* estimates from different samples and using different thermobarometric methods—some of them not relying on the reactive bulk composition—indicates minor or insignificant chemical change for major and minor elements by metasomatism and validate the use of bulk rock chemistry for phase equilibrium modelling in the case of pre-peak and peak-*P* conditions.

The cores of garnet in Cld-schist Z16TB24A and mafic schist Z16TB11 are attributed to the peak-*P* stage, and they show similar REE trends (Figures 8b,d) with minor negative Eu anomalies. The presence of a Eu anomaly in garnet is commonly associated to growth in equilibrium with plagioclase in amphibolite- to granulite-facies rocks (e.g. Hermann and Rubatto 2003; Martin et al. 2011; Rubatto et al. 2011; Manzotti et al. 2012; Gauthiez-Putallaz et al. 2016). The presence of plagioclase during garnet growth is however excluded in these samples based on the thermodynamic models. It is possible that the Eu anomaly in peak-*P* garnet is inherited from the bulk rock (Grevel et al. 2010; Gauthiez-Putallaz et al. 2016), which likewise show a small negative Eu anomaly (Figure 8, Table S7).

Alternatively, the Eu anomaly in the garnet core may reflect the presence of lawsonite in every sample during prograde metamorphism (Figure 10), as confirmed by modelling and field evidence (Figure 2c). This mineral can have a significant positive Eu-anomaly and thus has the capacity to influence Eu budget in coexisting garnet (Spandler et al. 2003; Usui et al. 2007; Vitale Brovarone et al. 2014; Hara et al. 2018).

Post-peak metamorphic conditions are recorded in every lithology investigated here (Figure 11a). These can be sub-divided further into 1) conditions at medium pressure and temperatures slightly lower to those occurring during peak-*P* metamorphism (post-peak 1), and 2) conditions at similar pressure but higher temperatures than post-peak 1 (post-peak 2) (Figure 10, 11a). Post-peak 1 is recorded by mica populations $Ph_{MS,2a}$ and $Ph_{MS,2b}$ in the mafic schists (Z16TB11, Z16TB28), and $Ph_{CldS,2}$ in the Cld-schist (Z16TB24A). The composition of these mica population all plot in a restricted *P*–*T* region located just below the lawsonite-out curve (Figure 11a) at 550 ± 15 °C and 2.00 ± 0.10 GPa with a good correspondence among phase diagram and multi-equilibrium methods (Figure 9b,e,h). Fluids are known to promote K-white mica re-equilibration (Konrad-Schmolke et al. 2011; Airaghi et al. 2017). It is therefore possible that fluid released by lawsonite breakdown allowed partial K-white mica re-equilibration by replacement reactions. The lower limit of post-peak 1 conditions is constrained at 555 ± 15 °C and 1.55 ± 0.10 GPa, as indicated by garnet from the Cld-schist ($Grt_{CldS,2}$; Z16TB24A) and the mafic schist ($Grt_{MS,2}$; Z16TB11), as well as by K-white mica from the mafic schists ($Ph_{MS,3a}$ in Z16TB11; $Ph_{MS,3b}$ in Z16TB28). Thermodynamic results for phengite for this stage coincide when comparing phase diagram and multi-equilibrium results (Figure 9e,h), except for sample Z16TB11 for which a 1 GPa discrepancy is found (Figure 9b). Post-peak 2 conditions (Figure 11a) are constrained by garnet from Cld-schist ($Grt_{CldS,3}$ in Z16TB24A), mafic schist ($Grt_{MS,3}$ in Z16TB11) and mafic fels ($Grt_{MM,2b}$; Z18TB15). The *P*–*T* conditions are similar for $Grt_{MS,3}$ and $Grt_{MM,2b}$ at 590 ± 15 °C and 1.70 ± 0.10 GPa, which can indicate heating from post-peak 1 if both represent a single *P*–*T* cycle. The pressure stability condition of $Grt_{CldS,3}$ is 2.05 +0.05/-0.40 GPa (Figure 10a,b,d), such pressure uncertainty is caused by a strong pressure dependency on minor garnet chemical variations in the model. A minimum pressure of ~1.9 GPa is constrained by the chloritoid-in curve with X_{Mg} at 0.38 (Figure 11a). The late phengite generation in the mafic schist (sample Z16TB28: $Ph_{MS,4a}$, $Ph_{MS,5a}$) cannot be modelled in the phase diagram (Figure 9e) but indicates lower pressure conditions via multi-equilibrium ($P < 0.6$ GPa for $T < 600$ °C).

In the mafic schist Z16TB11, garnet porphyroblasts have comparable compositional variations in major elements than the rim of small garnet grains with sharp zoning (Figure 7a,b) demonstrating that large scale equilibrium was achieved (Lanari and Engi 2017). This implies that the garnet porphyroblasts have equivalent *P*–*T* conditions than the small garnet rims and consequently

grew during subsequent heating. This is supported by the thermodynamic modelling of garnet modes and compositions, which predicts significant new garnet growth at stage $Grt_{MS,2}$ and $Grt_{MS,3}$ (6 vol% and 13 vol%, respectively, Figure 10b). Additionally, the REE patterns of garnet porphyroblasts and rims of small grains have a comparable trend, without negative Eu anomalies (Figure 8a,b,c). This is probably due to lawsonite breakdown releasing Eu (Figure 10) and Eu-uptake into the growing garnet. There is a notable difference in HREE mass fraction, with small garnet rims being more HREE-enriched than the porphyroblasts. This difference may reflect microscopic chemical contrasts in the bulk rock chemistry. The fine interlayering of chemical domains in the mafic schist (Figure 2c) could be the origin of the variation in REE content between garnet types, which could have grown from different local bulk compositions. The rim of garnet from Cld-schist Z16TB24A is richer in MREE than the rim of small garnet in mafic schist Z16TB11 (Figure 8b,d). This difference could reflect the presence of zoisite sequestering the MREE in the schist (Spandler et al. 2003; Konrad-Schmolke et al. 2008b).

6.2. Resorption and re-equilibration of garnet

Sharp chemical zoning is observed in the small garnets from the mafic schist (Figure 4a-d) and the Cld-schist (Figure 5) and significant variations in major element chemistry are observed between garnet core and rim, where each of these garnet zones clusters in distinct areas (Figure 7a). Moreover, Mn is highly compatible in garnet (Hollister 1966) and shows irregular enrichment in the garnet rim (Figure 4d,5d). Garnet crystals with discontinuous chemical zoning comparable to those found in the TGU rocks have been interpreted as having recorded either a mono- or a poly-metamorphic history (Vance and O'nions 1990; Gaidies et al. 2006; Konrad-Schmolke et al. 2008a). In the Alps, most cases of poly-metamorphic garnet are reported from felsic metamorphic rocks, where Permian amphibolite to granulite-facies garnet was partially overprinted by eclogite-facies assemblages during Alpine subduction. Examples of similar garnet have been described in several localities including the Sesia Zone (Lanari et al. 2017; Giuntoli et al. 2018b, a), the Dent Blanche tectonic system (Manzotti et al. 2012), the Money unit in the Gran Paradiso Massif (Manzotti and Ballèvre 2013), the Mt. Emilius klippe (Angiboust et al. 2017; Hertgen et al. 2017) and in Corsica (Martin et al. 2011). A similar interpretation was given for poly-metamorphic garnet in mafic rocks in the Adula nappe, Central Alps (Herwartz et al. 2011; Sandmann et al. 2014). On the other hand, mono-metamorphic garnet presenting complex internal textures was described in both mafic rocks in the Monviso unit (Angiboust et al. 2011, 2012a, 2014; Rubatto and Angiboust 2015; Locatelli et al. 2018), in the Tauern window, Eastern Alps (Kurz et al. 1998) and also postulated for felsic rocks in the Sesia Zone (Konrad-Schmolke et al. 2006). In the mono-metamorphic scenario, mechanisms

invoked to explain the garnet textures were: (1) garnet fractional crystallisation, (2) free fluid fractionation, (3) availability of water in the system (4) kinetics related to element supply required for garnet growth.

In the TGU, different stages of garnet growth were constrained by the number of chemical zones determined in the garnet compositional maps. For each simulation equilibrium was assumed and pre-existing garnet was allowed to be preserved (fractionated) and/or resorbed. The water content required in the simulation to match the observed paragenesis was investigated prior to each modelling step, where equilibrium phase diagrams were calculated with pristine or fractionated bulk rock chemistry (Figure S7, S8, S9). In every case, the best result was achieved with water saturation and was implemented as an input parameter in the simulation, which did not prevent development of successive garnet resorption and overgrowth steps matching the observations (Figure 10). Moreover, intracrystalline diffusion in garnet is sluggish below 600 °C (Caddick et al. 2010) and garnet interiors are isolated from chemical equilibrium with the matrix, preventing re-equilibration (Hollister, 1966; Kohn, 2003; Spear, 1988). Consequently, interaction with a free fluid phase, which is out of equilibrium with pre-existing garnet in a water-saturated system is the best candidate to trigger mineral reactions and mineral re-equilibration (Ferry 1983; Putnis 2009). The origin of such fluid is commonly associated to mineral dehydration reactions (Schmidt and Poli 1998), and could be internally or externally derived. The *P–T* conditions of K-white mica re-equilibration by dissolution-precipitation together with the results of thermodynamic modelling on garnet constrained fluid-rock interaction to happen during the first stage of decompression at around 560 ± 10 °C and 1.9 ± 0.1 GPa (Figure 11a).

One possibility for the release of fluids and consequent fluid-rock interaction is lawsonite dehydration, as the lawsonite out curve is crossed during the exhumation path (Figure 11a). Because lawsonite contains 11-12 wt% H_2O (Okamoto and Maruyama 1999; Poli and Schmidt 2002), this dehydration reaction can lead to significant water release during retrogression, as described for other metaophiolites of the western Alps (Reinecke 1998; Groppo et al. 2009; Angiboust and Agard 2010; Angiboust et al. 2012b; Vitale Brovarone and Beyssac 2014). In the investigated rock types, lawsonite is predicted to be stable at pressure peak conditions (Figure 10a,b,c) with varying modal abundance: 26 vol% in mafic fels (Z16TB32), 22% in mafic schist (Z16TB11) and 1% in Cld-schist (Z16TB24A). Forward modelling using Theriak Domino simulating an isothermal decompression from pressure peak (580 °C, 2.65 GPa) to stage 2 of decompression (555 °C, 1.55 GPa), shows variable amount of water release associated to hydrous mineral phases breakdown: ~0.5 wt% water release in the Cld-schist due to successive carpholite and lawsonite

breakdown; ~1.5 wt% water release in the mafic schist, where Lws-out reaction produces zoisite; ~2.5 wt% water release in the mafic fels, where lawsonite is replaced by zoisite and quartz (Figure S11). These values are above the threshold for pore connectivity (2 vol%) that allows water migration in eclogite (Mibe et al. 2003). Moreover, lawsonite breakdown results in trace element release that could explain the decrease in negative Eu anomaly in the garnet of the micaschist and Cld-schists between the core and the rim (Figure 8b,d). These fluids may have circulated along preferential pathways within and across samples, such as in the garnet-rich zone in the mafic schist, where most grains have complex replacement textures.

Based on field observations and a detailed petrological study, we identified structures indicating intense deformation, such as mafic boudin stretched within the schists and veinlets with high-pressure assemblage (garnet-diopside) cross cutting the mafic fels (Figure 2a, Figure S12a). Additionally, some schist layers contain abundant deformed clusters of garnet grains that show replacement textures, and which could be interpreted as brittle shear zones (Figure S12b). These features are comparable to what was described in the high pressure shear zones within the Monviso eclogites, and that have been linked to ductile shearing, brittle failure and fluid-rock interaction (Angiboust et al. 2012a; Locatelli et al. 2018, 2019). In this case, it is also possible that the garnet textures observed at the microscale indicate fluid pulses and are linked to seismic brecciation and intermediate-depth earthquakes observed in active subduction zones.

6.3. Garnet and the mono-metamorphic nature of the TGU

All *P*–*T* conditions and domains discussed so far could represent a single cycle of burial and exhumation for the TGU. Determining this issue with certainty—and interpreting the *P*–*T* data in terms of tectonic and geodynamic processes—may prove to be difficult on the basis of *P*–*T* data alone. Garnet geochronology provides absolute age constraints needed to solve the mono- versus poly-metamorphic character of the TGU, as it has been shown in other studies in the Alps with similar complex garnet chemical zoning (Herwartz et al. 2011; Sandmann et al. 2014). In this study, the three dated samples yield similar Lu-Hf age between 50.3 ± 0.3 and 48.8 ± 0.1 Ma. In each sample the initial $^{176}Hf/^{177}Hf$ is lower than the CHUR value as expected for crustal samples. Notably, there is no resolvable age difference between sample Z16TB24A, which shows complex textures with sharp chemical transition between core and rim, and samples where garnet shows continuous single-stage growth zoning (Z16TB28, Z18TB15). It is doubtful that these ages are significantly influenced by diffusional re-equilibration of either Lu or Hf. Lutetium distributions show sharp and euhedral zoning and even fine oscillations, indicating primary HREE growth zoning is preserved and diffusional re-equilibration did not occur on scales larger than microns. Given that diffusivity of Hf^{4+}

in garnet is even slower than that of Lu^{3+} (Ganguly and Tirone 1999; Bloch et al. 2015), we interpret the Lu-Hf ages as each reflecting garnet growth during the Alpine metamorphic history of the tectonic unit. These results confirm that the lithologies of the TGU underwent a single Alpine metamorphic cycle with early garnet growth between 50-49 Ma.

Garnet porphyroblasts from the mafic schist (Z16TB11), used for GrtMod thermodynamic models, has the highest Lu concentration in the garnet core, whereas the rim is characterized by oscillatory and sector zoning (Figure 6b); the dated garnet porphyroblasts in the mafic schist (Z16TB28) present similar major element compositions (Figure 7b) and similar REE core to rim patterns (Figure 8a,c). In both mafic schist samples (Z16TB11 and Z16TB28) garnet porphyroblasts show HREE-depleted rims compared to their core (Figure 8a,b), possibly reflecting Rayleigh fractionation of elements that are compatible in garnet (Otamendi et al. 2002; Moore et al. 2013), even though core to rim HREE depletion is more marked in Z16TB28. This latter discrepancy is probably due either to local trace element bulk composition effects or to off-center sectioning of the mineral in garnet from Z16TB11. We interpret the Lu distribution in Z16TB11 as representative for the dated sample Z16TB28.

As discussed above, garnet in these samples records complex zoning that represents a substantial range in *P–T* conditions and thus a time span. In a bulk-grain garnet analysis, and in the absence of diffusional re-equilibration of Lu and Hf, the Lu-Hf age may be biased towards zones that contribute most to the bulk-grain Lu budget (e.g. Lapen et al., 2003; Smit et al., 2010). Garnet in all samples investigated shows Lu-enriched cores and thus the Lu-Hf ages in these samples can be generally taken to represent the early stage of garnet growth, as is common in eclogite-facies garnet (Lapen et al. 2003; Skora et al. 2006; Smit et al. 2010). Therefore, the Lu zoning in each garnet type (Figure 6) can further assist in assigning the age to a particular *P–T* stage.

The three Lu-Hf ages are different outside analytical uncertainty. GrtMod thermodynamic models predict that garnet from the mafic fels is the only one to record early stage of TGU metamorphism. This garnet type yields the oldest age (50.3 ± 0.3 Ma), probably representing the initiation of TGU prograde metamorphism. The Lu-rich core of garnet with sharp chemical zoning from the Cld-schists is predicted stable at maximum metamorphic pressure, which consequently occurred ~1.5 Ma later at 48.8 ± 0.1 Ma. Finally, major element composition and REE normalized pattern in garnet porphyroblasts from the mafic schist indicate growth during the re-heating stage. The garnet porphyroblasts yielded 49.6 ± 0.8 Ma, which is within uncertainty of the age of the small garnet. The data argue for rapid first decompression and exhumation, within 1 Ma.

The ages obtained for Alpine metamorphism in this study are consistent with what was determined with various dating methods for Alpine metamorphism in the surrounding

metaophiolites from the Western Alps: 52-40 Ma for eclogites from ZSZ on the basis of zircon and garnet dating (Rubatto *et al.*, 1998; Amato *et al.*, 1999; Lapen *et al.*, 2003; Meyer et al., 2014; Skora *et al.*, 2015; Dragovic *et al.*, 2020), as well as Rb-Sr geochronology of mica inclusions in garnet (De Meyer et al. 2014). Comparable ages are recorded in the Monviso metaophiolite, which underwent a similar *P*–*T* evolution during Alpine subduction: 49.2 ± 1.2 Ma for garnet (Duchêne et al. 1997), and 46-45 Ma for high pressure zircon rims in eclogites (Rubatto and Hermann 2003; Rubatto and Angiboust 2015). Garnet from eclogites from the continental slice of Etirol-Levaz yielded older ages of 61.8 ± 1.8 Ma and 52.4 ± 2.1 Ma, which could indicate a different timing of subduction-related metamorphism in several sub-units (Fassmer et al. 2016). High pressure zircon in an eclogite from the Etirol-Levaz unit was dated at 47.5 ± 1.0 Ma, in agreement with other metaophiolite slices (Beltrando et al. 2010).

6.4. Geothermal gradient and comparison with surrounding tectonic units

The recognition of the *P*–*T*–time data as representing a single metamorphic cycle enables interpretation of these data in terms of tectonic and geodynamic processes. The *P*–*T*–time path of the TGU is characterized by two metamorphic maxima occurring at approximately the same temperature but significantly different pressures (Figure 11a). Thermal structure fluctuations in subduction zones could either be linked to the thermal structure of the lithosphere itself (Peacock and Wang 1999), to variation in the rate of subduction (Peacock and Wang 1999), or to endothermic reactions in the subducting lithologies (Reinecke 1998). The prograde *P*–*T* path is characterized by a steep increase in pressure of ~1 GPa over ~90 °C (Figure 11b), indicating rapid burial with only minor thermal re-equilibration. The maximum *P*–*T* conditions lie on a cold geotherm of ~6 °C/km expected for rapid burial of cold surface sediment (Philpotts and Ague 2009). This prograde-to-peak evolution is comparable to what was previously reported for tectonic units in the same region in the Western Alps (Figure 11b), e.g. ZSZ (Reinecke 1998; Bucher et al. 2005; Angiboust et al. 2009; Groppo et al. 2009), Etirol-Levaz Unit (Fassmer et al. 2016), and Monviso (Angiboust et al. 2012b). In these units, peak metamorphism is followed by isothermal decompression, e.g. ZSZ in Pfulwe (Bucher et al. 2005), Lago di Cignana (Reinecke 1998) and Täschalp (Barnicoat and Fry 1986) and for some Alpine continental outliers (Fassmer et al. 2016; Angiboust et al. 2017). Such *P*–*T* trajectory is possible if the tectonic units follow a rapid exhumation after decoupling from the descending slab (Rubatto and Hermann 2001; Philpotts and Ague 2009). Numerical simulations that report pressure and temperature pathways of rocks during collision and subsequent exhumation correlate an isothermal pressure drop with the onset of slab break off (Vogt and Gerya 2014), which may be the geodynamic process governing initial exhumation of the TGU as well.

After a first stage of near isothermal decompression, the exhumation path of the TGU reflects a minor almost isobaric heating episode lying on a slightly hotter geotherm of ~10 °C/km. The pressure increase is not significant, since it is only constrained by the chloritoid isopleth, which could also reflect minor inconsistencies in themodynamic data. Similar β-shape *P*–*T* paths have been reported for many orogens indicating that thermal pulses during retrogression are potentially a common feature during orogeny. Examples of β-shaped *P*–*T* paths are reported for many HP terranes worldwide (O'Brien 2000; Wilke et al. 2010; Gao et al. 2011; Whitney et al. 2011; Faryad et al. 2019), including the Tauern window in the Eastern Alps (e.g. Ratschbacher et al. 2004; Kurz et al. 2008), the Lepontine Dome in the Central Alps (Wiederkehr et al. 2008), the Internal Penninic Nappes in the Western Alps (e.g. Borghi et al. 1996; Rubatto and Hermann 2001; Brouwer et al. 2002) and the Upper Penninic Nappes in the Western Alps (Messiga and Scambelluri 1991; Beltrando et al. 2007). Various mechanisms have been invoked to affect geothermal gradient and explain the subsequent re-heating step, such as radiogenic heat production of additionally accreted continental blocks (Wiederkehr *et al.*, 2008), slab breakoff (Kurz et al. 1998; Brouwer et al. 2002), continental collision after the end of oceanic lithosphere subduction (Borghi *et al.*, 1996), mantle delamination (Henk *et al.,* 2000), slowing exhumation rate (e.g. Wilke et al., 2010), asthenospheric inflow ahead of the spreading ridge (Abers *et al.,* 2016), transient storage at MOHO depth during exhumation (Walsh and Hacker 2004) and multiple short-lived burial-exhumation cycles associated to orogen-scale alternating between shortening and extensional deformation (Beltrando *et al.* 2007). Recent study focusing on exhumation mechanisms of metamorphic rocks by numerical modelling stressed the importance of advective and conductive heating from the mantle, rather than radiogenic or shear heating, as best candidates to explain rapid (short-lived) heating of rocks during exhumation (Sizova et al. 2019). The numerical results show β-shaped *P*–*T*–time path with re-heating up to 200 °C at various pressure (0.5 to 1.5 GPa) and involve asthenospheric upwelling associated to slab rollback, or slab bending, or crustal exhumation paired with slab breakoff, as prime driver for late orogenic heating during exhumation (Sizova et al. 2019). In case of the TGU, the imprint of such processes would be relatively strong, as this unit is structurally located on top of the subducted oceanic crust and is therefore located closest to the slab-mantle interface where thermal anomalies would be most intense. Moreover, a β-shape *P*–*T* path for TGU is coherent with the exhumation paths proposed for the ZSZ (Figure 11b; e.g. Bucher *et al.*, 2005; Angiboust *et al.,* 2009).

6.5. Comparison with previous findings

Complex garnet textures with sharp chemical zoning in the TGU were previously interpreted as the result of polycyclic record (Bucher et al. 2019). The garnet zoning patterns of the schist

samples investigated in this study (Z16TB11, Z16TB24A) show good correspondence with those observed by Bucher *et al.* (2019). In both cases, a marked compositional difference is present between garnet core and rim (Figure 7a). However, in this study Lu-Hf geochronological data obtained for garnet from different lithologies returned coherent Alpine ages in every sample. Particularly, the Alpine age in Cld-schist (Z16TB24A) where garnet has a discontinuous core-rim zoning, does not show any evidence of a pre-Alpine (Permian) metamorphic stage as suggested by Bucher *et al.* (2019). This study demonstrates that such textural record is compatible with a mono-metamorphic evolution of the TGU. As a main consequence, there is no longer discrepancy for the TGU Alpine peak *P–T* conditions between the mafic fels at 2.2 ± 0.10 GPa and 580 ± 50 °C (Weber and Bucher 2015), and the schist at ~1.7 GPa and ~530 °C (Bucher et al. 2019). The garnet core in the schists (granulitic according to Bucher *et al.*, 2019) is re-interpreted as representing Alpine peak-*P* conditions, corresponding to the maximum *P–T* conditions inferred in the TGU mafic fels at 2.65 ± 0.10 GPa and 580 ± 15 °C (this study; Weber and Bucher, 2015). Likewise, the maximum *P–T* conditions for the metapelites in Bucher *et al.* (2019) corresponds to the initiation of the re-heating stage after the first step of exhumation, rather than the Alpine peak-*P* for these rocks.

The 50-49 Ma Lu-Hf garnet ages obtained for all lithologies are slightly younger than the Lu-Hf garnet ages described by Weber *et al.* (2015) from garnet in mafic fels (56.5 ± 2.7 Ma and 58.2 ± 1.4 Ma). This study favours a synchronous *P–T* path between TGU and ZSZ unit during Eocene, rather than supporting a continuous subduction during the Paleocene restoration phase (Weber et al. 2015).

Compositional maps of the garnet in the Cld-schist (Z16TB24A) (Figure 4a-d) and the matrix garnet of the mafic schist (Z16TB11) (Figure 5) both present a sharp chemical boundary between core and rim observed in each major element at the lateral high resolution of the EMPA map (~1 µm in garnet, see Lanari and Piccoli, 2020). Pristine chemical zoning could be modified by diffusional relaxation, which is dependent on cooling rate and grain size (Dodson 1973), because there is a strong dependence between cation diffusivity and temperature in minerals (Caddick et al. 2010). The sharp zoning shows no evidence of diffusional re-equilibration of relatively fast diffusing divalent cations at sharp chemical interfaces in garnet, such as Fe, Mg and Mn (Carlson 2006; Perchuk et al. 2009; Li et al. 2018). This result is inconsistent with the interpretation that the TGU resided at 530 – 580 °C for c. 10 Ma (Bucher et al. 2019), but rather argue for a fast *P–T* cycle as suggested by our Lu-Hf data.

7. CONCLUSIONS

The *P–T* path reconstructed for the TGU unit combined with Lu-Hf dating of garnet reveals a coherent mono-metamorphic history during Eocene, which is in agreement with the surrounding ZSZ metaophiolites. After a first stage of decompression and slight cooling, the exhumation path of the TGU is affected by reheating event. Complex garnet textures are thus explained and reconciled with a mono-metamorphic evolution and a β-shape *P–T* path. The thermal pulse is best explained by hot asthenospheric mantle upwelling, favoured by TGU structural position located atop of the subducted oceanic crust and therefore closer to the slab-mantle interface. During TGU exhumation path, lawsonite dehydration reaction occurring in both the mafic schist and the mafic fels is seen as main fluid source for fluid-rock interaction. The presence of significant amounts of fluids leads to complex texture development in garnet from the schist, REE pattern discrepancies between garnet core and rim in the schists, K-white mica re-equilibration in the schists and vein formation in the mafic fels.

ACKNOWLEDGEMENTS

We are grateful to J. Hermann and T. Ewing for constructive discussion. We thank D. Peters and J. Cutts for their help with the lab work. Further thanks go to D. Moynihan, T. G. Lee, J. Reynes and E. Kempf for their assistance during fieldwork. This work was supported by the Swiss National Science Foundation [Project N. 200021_166280 and 206021_170722 to D. Rubatto].

BIBLIOGRAPHY

Abers GA, Eilon Z, Gaherty JB, et al (2016) Southeast Papuan crustal tectonics: Imaging extension and buoyancy of an active rift. J Geophys Res Solid Earth 951–971. https://doi.org/10.1002/2015JB012621

Airaghi L, Lanari P, de Sigoyer J, Guillot S (2017) Microstructural vs compositional preservation and pseudomorphic replacement of muscovite in deformed metapelites from the Longmen Shan (Sichuan, China). Lithos 282–283:262–280. https://doi.org/10.1016/j.lithos.2017.03.013

Amato JM, Johnson CM, Baumgartner LP, Beard BL (1999) Rapid exhumation of the Zermatt-Saas ophiolite deduced from. Earth Planet Sci Lett 171:425–438

Angiboust S, Agard P (2010) Lithos Initial water budget : The key to detaching large volumes of eclogitized oceanic crust along the subduction channel ? LITHOS 120:453–474. https://doi.org/10.1016/j.lithos.2010.09.007

Angiboust S, Agard P, Jolivet L, Beyssac O (2009) The Zermatt-Saas ophiolite: The largest (60-km wide) and deepest (c. 70-80km) continuous slice of oceanic lithosphere detached from a subduction zone? Terra Nov. https://doi.org/10.1111/j.1365-3121.2009.00870.x

Angiboust S, Agard P, Raimbourg H, et al (2011) Subduction interface processes recorded by eclogite-facies shear zones (Monviso, W. Alps). Lithos 127:222–238. https://doi.org/10.1016/j.lithos.2011.09.004

Angiboust S, Agard P, Yamato P, Raimbourg H (2012a) Eclogite breccias in a subducted ophiolite: A record of intermediatedepth earthquakes? Geology 40:707–710. https://doi.org/10.1130/G32925.1

Angiboust S, Langdon R, Agard P, et al (2012b) Eclogitization of the Monviso ophiolite (W. Alps) and implications on subduction dynamics. J Metamorph Geol 30:37–61. https://doi.org/10.1111/j.1525-1314.2011.00951.x

Angiboust S, Pettke T, De Hoog JCM, et al (2014) Channelized fluid flow and eclogite-facies metasomatism along the subduction shear zone. J Petrol 55:883–916. https://doi.org/10.1093/petrology/egu010

Angiboust S, Yamato P, Hertgen S, et al (2017) Fluid pathways and high-P metasomatism in a subducted continental slice (Mt. Emilius klippe, W. Alps). J Metamorph Geol 35:471–492. https://doi.org/10.1111/jmg.12241

Baldwin JA, Powell R, Brown M, et al (2005) Modelling of mineral equilibria in ultrahigh-temperature metamorphic rocks from the Anápolis-Itauçu Complex, central Brazil. J Metamorph Geol 23:511–531. https://doi.org/10.1111/j.1525-1314.2005.00591.x

Ballèvre M, Kienast J-R, Vuichard J-P (1986) La “nappe de la Dent blanche” (Alpes occidentales) : deux unités austroalpines indépendantes. Eclogae Geol Helv 79:57–74

Barnicoat AC, Fry N (1986) High-pressure metamorphism of the Zermatt-Saas ophiolite zone, Switzerland. J Geol Soc London 143:607–618. https://doi.org/10.1144/gsjgs.143.4.0607

Baxter EF, Caddick MJ, Ague JJ (2013) Garnet: Common mineral, uncommonly useful. Elements 9:415–419. https://doi.org/10.2113/gselements.9.6.415

Baxter EF, Caddick MJ, Dragovic B (2017) Garnet: A Rock-Forming Mineral Petrochronometer. Rev Mineral Geochemistry 83:469–533. https://doi.org/10.2138/rmg.2017.83.15

Bearth P (1967) Die ophiolite der Zone von Zermatt-Saas Fee. Beiträge Geol Karte Schweitz 132:1–130

Beltrando M, Hermann J, Lister G, Compagnoni R (2007) On the evolution of orogens: Pressure cycles and deformation mode switches. Earth Planet Sci Lett 256:372–388. https://doi.org/10.1016/j.epsl.2007.01.022

Beltrando M, Manatschal G, Mohn G, et al (2014) Recognizing remnants of magma-poor rifted margins in high-pressure orogenic belts: The Alpine case study. Earth-Science Rev 131:88–115. https://doi.org/10.1016/j.earscirev.2014.01.001

Beltrando M, Rubatto D, Manatschal G (2010) From passive margins to orogens: The link between ocean-continent transition zones and (ultra)high-pressure metamorphism. Geology 38:559–562. https://doi.org/10.1130/G30768.1

Bizzarro M, Baker JA, Ulfbeck D (2003) A new digestion and chemical separation technique for rapid and highly reproducible determination of Lu/Hf and Hf isotope ratios in geological materials by mc-ICP-MS. Geostand Newsl 27:133–145. https://doi.org/10.1111/j.1751-908X.2003.tb00641.x

Blichert-Toft J, Boyet M, Télouk P, Albarède F (2002) 147Sm-143Nd and 176Lu-176Hf in eucrites and the differentiation of the HED parent body. Earth Planet Sci Lett 204:167–181. https://doi.org/10.1016/S0012-821X(02)00976-7

Blichert-Toft J, Chauvel C, Albarède F (1997) Separation of Hf and Lu for high-precision isotope analysis of rock samples by magnetic sector-multiple collector ICP-MS. Contrib to Mineral Petrol 127:248–260

Bloch E, Ganguly J, Hervig R, Cheng W (2015) 176Lu–176Hf geochronology of garnet I: experimental determination of the diffusion kinetics of Lu3+ and Hf4+ in garnet, closure temperatures and geochronological implications. Contrib to Mineral Petrol 169:. https://doi.org/10.1007/s00410-015-1109-8

Borghi A, Compagnoni R, Sandrone R (1996) Composite P-T paths in the Internal Penninic Massifs of the Western Alps: Petrological constraints to their thermo-mechanical evolution. Eclogae Geol Helv 89:345–367

Bousquet R, Oberhansli R, Goffe B, et al (2008) Metamorphism of metasediments at the scale of an orogen: a key to the Tertiary geodynamic evolution of the Alps. Geol Soc London, Spec Publ 298:393–411. https://doi.org/10.1144/SP298.18

Brouwer FM, Vissers RLM, Lamb WM (2002) Structure and metamorphism of the Gran Paradiso massif, western Alps, Italy. Contrib to Mineral Petrol 143:450–470. https://doi.org/10.1007/s00410-002-0357-6

Bucher K, Fazis Y, de Capitani C, Grapes R (2005) Blueschists, eclogites, and decompression assemblages of the Zermatt-Saas ophiolite: High-pressure metamorphism of subducted Tethys lithosphere. Am Mineral 90:821–835. https://doi.org/10.2138/am.2005.1718

Bucher K, Weisenberger TB, Klemm O, Weber S (2019) Decoding the complex internal chemical structure of garnet porphyroblasts from the Zermatt area, Western Alps. J Metamorph Geol 37:1151–1169. https://doi.org/10.1111/jmg.12506

Bucher K, Weisenberger TB, Weber S, et al (2020) The Theodul Glacier Unit, a slab of pre-Alpine rocks in the Alpine meta-ophiolite of Zermatt-Saas, Western Alps. Swiss J Geosci 113:1–22. https://doi.org/10.1186/s00015-020-00354-6

Caddick MJ, Konopásek J, Thompson AB (2010) Preservation of garnet growth zoning and the duration of prograde metamorphism. J Petrol 51:2327–2347. https://doi.org/10.1093/petrology/egq059

Carlson WD (2006) Rates of Fe, Mg, Mn, and Ca diffusion in garnet. Am Mineral 91:1–11. https://doi.org/10.2138/am.2006.2043

Coggon R, Holland TJB (2002) Mixing properties of phengitic micas and revised garnet-phengite thermobarometers. J Metamorph Geol 20:683–696. https://doi.org/10.1046/j.1525-1314.2002.00395.x

Compagnoni R (1977) The Sesia-Lanzo Zone: high pressure-low temperature metamorphism in the Austroalpine continental margin. Rend della Soc Ital di Mineral e Petrol 33:335–374

Cotta AJB, Enzweiler J, Wilson SA, et al (2007) Homogeneity of the geochemical reference material BRP-1 (paranábasin basalt) and assessment of minimum mass. Geostand Geoanalytical Res 31:379–393. https://doi.org/10.1111/j.1751-908X.2007.00111.x

Dal Piaz GV (1979) Manganiferous quartzitic schists of the piemonte ophiolite Nappe-in the Valsesia-valtournach arc, Italian Western Alps. Mem Sci Geol Gia Mom degli Ist Geol Miner dell Univ di Padova 24:

Dal Piaz GV (2001) History of tectonic interpretations of the Alps. J Geodyn 32:99–114. https://doi.org/10.1016/S0264-3707(01)00019-9

Dal Piaz GV, Cortiana G, Del Moro A, et al (2001) Tertiary age and paleostructural inferences of the eclogitic imprint in the Austroalpine outliers and zermatt-saas ophiolite, Western Alps. Int J Earth Sci 90:668–684. https://doi.org/10.1007/s005310000177

Dal Piaz GV, Ernst WG (1978) Areal geology and petrology of eclogites and associated metabasites of the Piemonte ophiolite nappe, breuil-st. Jacques area, Italian Western Alps. Tectonophysics 51:99–126. https://doi.org/10.1016/0040-1951(78)90053-7

De Capitani C, Brown TH (1987) The computation of chemical equilibrium in complex systems containing non-ideal solutions. Geochim Cosmochim Acta 51:2639–2652

De Capitani C, Petrakakis K (2010) The computation of equilibrium assemblage diagrams with Theriak/Domino software. Am Mineral 95:1006–1016. https://doi.org/10.2138/am.2010.3354

De Meyer CMC, Baumgartner LP, Beard BL, Johnson CM (2014) Rb-Sr ages from phengite inclusions in garnets from high pressure rocks of the swiss western alps. Earth Planet Sci Lett 395:205–216. https://doi.org/10.1016/j.epsl.2014.03.050

Diener JFA, Powell R, White RW, Holland TJB (2007) A new thermodynamic model for clino- and orthoamphiboles in the system Na2O-CaO-FeO-MgO-Al2O3-SiO2 -H2O-O. J Metamorph Geol 25:631–656. https://doi.org/10.1111/j.1525-1314.2007.00720.x

Dilek Y, Furnes H (2014) Ophiolites and their origins. Elements 10:93–100. https://doi.org/10.2113/gselements.10.2.93

Dodson MH (1973) Closure temperature in cooling geochronological and petrological systems. Contrib to Mineral Petrol 40:259–274. https://doi.org/10.1007/BF00373790

Dragovic B, Angiboust S, Tappa MJ (2020) Petrochronological close-up on the thermal structure of a paleo-subduction zone (W. Alps). Earth Planet Sci Lett 547:116446. https://doi.org/10.1016/j.epsl.2020.116446

Dubacq B, Vidal O, de Andrade V (2010) Dehydration of dioctahedral aluminous phyllosilicates:

Thermodynamic modelling and implications for thermobarometric estimates. Contrib to Mineral Petrol 159:159–174. https://doi.org/10.1007/s00410-009-0421-6

Duchêne S, Blichert-Toft J, Luais B, et al (1997) The Lu-Hf dating of garnets and the ages of the Alpine high-pressure metamorphism. Nature 387:586–589. https://doi.org/10.1038/42446

Escher A, Hunziker J-C, Marthaler M, et al (1997) Geologic framework and structural evolution of the western Swiss-Italian Alps

Evans TP (2004) A method for calculating effective bulk composition modification due to crystal fractionation in garnet-bearing schist: Implications for isopleth thermobarometry. J Metamorph Geol 22:547–557. https://doi.org/10.1111/j.1525-1314.2004.00532.x

Faryad SW, Baldwin SL, Jedlicka R, Ježek J (2019) Two-stage garnet growth in coesite eclogite from the southeastern Papua New Guinea (U)HP terrane and its geodynamic significance. Contrib to Mineral Petrol 174:1–16. https://doi.org/10.1007/s00410-019-1612-4

Fassmer K, Obermüller G, Nagel TJ, et al (2016) High-pressure metamorphic age and significance of eclogite-facies continental fragments associated with oceanic lithosphere in the Western Alps (Etirol-Levaz Slice, Valtournenche, Italy). Lithos. https://doi.org/10.1016/j.lithos.2016.02.019

Feenstra A, Petrakakis K, Rhede D (2007) Variscan relicts in Alpine high- P pelitic rocks from Samos (Greece): Evidence from multi-stage garnet and its included minerals. J Metamorph Geol 25:1011–1033. https://doi.org/10.1111/j.1525-1314.2007.00741.x

Ferry JM (1983) On the control of temperature, fluid composition, and reaction progress during metamorphism. Am J Sci 283-A:201–232

Gaidies F, Abart R, De Capitani C, et al (2006) Characterization of polymetamorphism in the Austroalpine basement east of the Tauern Window using garnet isopleth thermobarometry. J Metamorph Geol 24:451–475. https://doi.org/10.1111/j.1525-1314.2006.00648.x

Ganguly J, Tirone M (1999) Diffusion closure temperature and age of a mineral with arbitrary extent of diffusion: Theoretical formulation and applications. Earth Planet Sci Lett 170:131–140. https://doi.org/10.1016/S0012-821X(99)00089-8

Gao XY, Zheng YF, Chen YX (2011) U-Pb ages and trace elements in metamorphic zircon and titanite from UHP eclogite in the Dabie orogen: Constraints on P-T-t path. J Metamorph Geol 29:721–740. https://doi.org/10.1111/j.1525-1314.2011.00938.x

Gauthiez-Putallaz L, Rubatto D, Hermann J (2016) Dating prograde fluid pulses during subduction by in situ U–Pb and oxygen isotope analysis. Contrib to Mineral Petrol 171:1–20. https://doi.org/10.1007/s00410-015-1226-4

George FR, Gaidies F, Boucher B (2018) Population-wide garnet growth zoning revealed by LA-ICP-MS mapping: implications for trace element equilibration and syn-kinematic deformation during crystallisation. Contrib to Mineral Petrol 173:1–22. https://doi.org/10.1007/s00410-018-1503-0

Giuntoli F, Lanari P, Burn M, et al (2018a) Deeply subducted continental fragments - Part 2: Insight from petrochronology in the central Sesia Zone (western Italian Alps). Solid Earth 9:191–222. https://doi.org/10.5194/se-9-191-2018

Giuntoli F, Lanari P, Engi M (2018b) Deeply subducted continental fragments - Part 1: Fracturing, dissolution-precipitation, and diffusion processes recorded by garnet textures of the central Sesia Zone (western Italian Alps). Solid Earth 9:167–189. https://doi.org/10.5194/se-9-167-2018

Green E, Holland T, Powell R (2007) An order-disorder model for omphacitic pyroxenes in the system jadeite-diopside-hedenbergite-acmite, with applications to eclogitic rocks. Am Mineral 92:1181–1189. https://doi.org/10.2138/am.2007.2401

Grevel C, Schreyer W, Grevel K-DS (2010) REE distribution, mobilization and fractionation in the coesite-bearing “pyrope quartzite” and related rocks of the Dora-Maira Massif, Western Alps. Eur J Mineral 21:1213–1224. https://doi.org/10.1127/0935-1221/2009/0021-1967

Groppo C, Beltrando M, Compagnoni R (2009) The P-T path of the ultra-high pressure Lago Di Cignana and adjoining high-pressure meta-ophiolitic units: Insights into the evolution of the subducting Tethyan slab. J Metamorph Geol 27:207–231. https://doi.org/10.1111/j.1525-1314.2009.00814.x

Guillong M, Meier DL, Allan MM, et al (2008) SILLS: A Matlab-Based Program for the Reduction of Laser Ablation ICP–MS Data of Homogeneous Materials and Inclusions. Mineral Assoc Canada Short Course 40:328–333

Hara T, Tsujimori T, Chang Q, Kimura JI (2018) In-situ Sr-Pb isotope geochemistry of lawsonite: A new method to investigate slab-fluids. Lithos 320–321:93–104. https://doi.org/10.1016/j.lithos.2018.09.001

Henk A, von Blanckenburg F, Finger F, et al (2000) Syn-convergent high-temperature metamorphism and magmatism in the Variscides: A discussion of potential heat sources. Geol Soc Spec Publ 179:387–399. https://doi.org/10.1144/GSL.SP.2000.179.01.23

Hermann J, Rubatto D (2003) Relating zircon and monazite domains to garnet growth zones: Age and duration of granulite facies metamorphism in the Val Malenco lower crust. J Metamorph Geol 21:833–852. https://doi.org/10.1046/j.1525-1314.2003.00484.x

Hertgen S, Yamato P, Morales LFG, Angiboust S (2017) Evidence for brittle deformation events at eclogite-facies P-T conditions (example of the Mt. Emilius klippe, Western Alps). Tectonophysics 706–707:1–13. https://doi.org/10.1016/j.tecto.2017.03.028

Herwartz D, Nagel TJ, Münker C, et al (2011) Tracing two orogenic cycles in one eclogite sample by Lu-Hf garnet chronometry. Nat Geosci 4:178–183. https://doi.org/10.1038/ngeo1060

Holland T, Powell R (2003) Activity-compositions relations for phases in petrological calculations: An asymetric multicomponent formulation. Contrib to Mineral Petrol 145:492–501. https://doi.org/10.1007/s00410-003-0464-z

Holland TJB, Powell R (1998) An internally consistent thermodynamic data set for phases of petrological interest. J Metamorph Geol 16:309–343. https://doi.org/10.1111/j.1525-1314.1998.00140.x

Hollister LS (1966) Garnet Zoning : An Interpretation Based on the Rayleigh Fractionation Model. 154:1647–1651

Jamtveit B, Hervig RL (1994) Constraints on transport and kinetics in constraints on transport hydrothermal systems from zoned garnet crystals. Science (80-) 263:505–508

Jochum KP, Weis U, Stoll B, et al (2011) Determination of reference values for NIST SRM 610-617 glasses

following ISO guidelines. Geostand Geoanalytical Res 35:397–429. https://doi.org/10.1111/j.1751-908X.2011.00120.x

Jochum KP, Willbold M, Raczek I, et al (2005) Chemical Characterisation of the USGS Reference Glasses GSA-1G, GSC-1G, GSD-1G, GSE-1G, BCR-2G, BHVO-2G and BIR-1G Using EPMA, ID-TIMS, ID-ICP-MS and LA-ICP-MS. Geostand Geoanalytical Res 29:285–302. https://doi.org/10.1111/j.1751-908x.2005.tb00901.x

Kirst F, Leiss B (2016) Kinematics of syn- and post-exhumational shear zones at Lago di Cignana (Western Alps, Italy): constraints on the exhumation of Zermatt–Saas (ultra)high‐pressure rocks and deformation along the Combin Fault and Dent Blanche Basal Thrust. Int J Earth SciGeol Rundsch). https://doi.org/10.1007/s00531-016-1316-1

Kohn MJ (2009) Models of garnet differential geochronology. Geochim Cosmochim Acta 73:170–182. https://doi.org/10.1016/j.gca.2008.10.004

Kohn MJ (2003) Geochemical Zoning in Metamorphic mineral. Treatise on Geochemistry 3:229–261

Kohn MJ (2020) A refined zirconium-in-rutile thermometer. Am Mineral 105:963–971

Konrad-Schmolke M, Babist J, Handy MR, O'Brien PJ (2006) The physico-chemical properties of a subducted slab from garnet zonation patterns (Sesia Zone, Western Alps). J Petrol 47:2123–2148. https://doi.org/10.1093/petrology/egl039

Konrad-Schmolke M, Halama R, Wirth R, et al (2018) Mineral dissolution and reprecipitation mediated by an amorphous phase. Nat Commun 9:1–9. https://doi.org/10.1038/s41467-018-03944-z

Konrad-Schmolke M, O'Brien PJ, de Capitani C, Carswell DA (2008a) Garnet growth at high- and ultra-high pressure conditions and the effect of element fractionation on mineral modes and composition. Lithos 103:309–332. https://doi.org/10.1016/j.lithos.2007.10.007

Konrad-Schmolke M, Zack T, O'Brien PJ, Barth M (2011) Fluid migration above a subducted slab - Thermodynamic and trace element modelling of fluid-rock interaction in partially overprinted eclogite-facies rocks (Sesia Zone, Western Alps). Earth Planet Sci Lett 311:287–298. https://doi.org/10.1016/j.epsl.2011.09.025

Konrad-Schmolke M, Zack T, O'Brien PJ, Jacob DE (2008b) Combined thermodynamic and rare earth element modelling of garnet growth during subduction: Examples from ultrahigh-pressure eclogite of the Western Gneiss Region, Norway. Earth Planet Sci Lett 272:488–498. https://doi.org/10.1016/j.epsl.2008.05.018

Kurz W, Handler R, Bertoldi C (2008) Tracing the exhumation of the eclogite zone (Tauern window, Eastern Alps) by 40Ar/39Ar dating of white mica in eclogites. Swiss J Geosci 101:191–206. https://doi.org/10.1007/s00015-008-1281-1

Kurz W, Neubauer F, Dachs E (1998) Eclogite meso- and microfabrics: implications for the burial and exhumation history of eclogites in the Tauern Window (Eastern Alps) from P - T - d paths. Tectonophysics 285:183–209

Lagos M, Scherer EE, Tomaschek F, et al (2007) High precision Lu-Hf geochronology of Eocene eclogite-facies rocks from Syros, Cyclades, Greece. Chem Geol 243:16–35. https://doi.org/10.1016/j.chemgeo.2007.04.008

Lanari P (2012) Micro-cartographie P-T-e dans les roches métamorphiques. Applications aux Alpes et à l'Himalaya. Grenoble University

Lanari P, Duesterhoeft E (2019) Modeling Metamorphic Rocks Using Equilibrium Thermodynamics and Internally Consistent Databases: Past Achievements, Problems and Perspectives. J Petrol 60:19–56. https://doi.org/10.1093/petrology/egy105

Lanari P, Engi M (2017) Local Bulk Composition Effects on Metamorphic Mineral Assemblages. Rev Mineral Geochemistry 83:55–102. https://doi.org/10.2138/rmg.2017.83.3

Lanari P, Giuntoli F, Loury C, et al (2017) An inverse modeling approach to obtain P–T conditions of metamorphic stages involving garnet growth and resorption. Eur J Mineral 29:181–199. https://doi.org/10.1127/ejm/2017/0029-2597

Lanari P, Piccoli F (2020) New horizons in quantitative compositional mapping – Analytical conditions and data reduction using XMapTools. IOP Conf Ser Mater Sci Eng 891:012016. https://doi.org/10.1088/1757-899x/891/1/012016

Lanari P, Vho A, Bovay T, et al (2019) Quantitative compositional mapping of mineral phases by electron probe micro-analyser. Geol Soc Spec Publ 478:39–63. https://doi.org/10.1144/SP478.4

Lanari P, Vidal O, De Andrade V, et al (2014) XMapTools: A MATLAB©-based program for electron microprobe X-ray image processing and geothermobarometry. Comput Geosci 62:227–240. https://doi.org/10.1016/j.cageo.2013.08.010

Lapen TJ, Johnson CM, Baumgartner LP, et al (2003) Burial rates during prograde metamorphism of an ultra-high-pressure terrane: An example from Lago di Cignana, western Alps, Italy. Earth Planet Sci Lett 215:57–72. https://doi.org/10.1016/S0012-821X(03)00455-2

Le Bayon B, Ballèvre M (2004) Field and petrological evidence for a Late Palaeozoic (Upper Carboniferous-Permian) age of the Erfaulet orthogneiss (Gran Paradiso, western Alps). Comptes Rendus - Geosci 336:1079–1089. https://doi.org/10.1016/j.crte.2004.04.004

Li B, Ge J, Zhang B (2018) Diffusion in garnet: a review. Acta Geochim 37:19–31. https://doi.org/10.1007/s11631-017-0187-x

Locatelli M, Verlaguet A, Agard P, et al (2019) Fluid Pulses During Stepwise Brecciation at Intermediate Subduction Depths (Monviso Eclogites, W. Alps): First Internally Then Externally Sourced. Geochemistry, Geophys Geosystems 20:5285–5318. https://doi.org/10.1029/2019GC008549

Locatelli M, Verlaguet A, Agard P, et al (2018) Intermediate-depth brecciation along the subduction plate interface (Monviso eclogite, W. Alps). Lithos 320–321:378–402. https://doi.org/10.1016/j.lithos.2018.09.028

Ludwig KR (2003) Isoplot/Ex version 3.0. A geochronological toolkit for Microsoft Excel. Berkeley Geochronological Cent Spec Pub Berkeley:p.70

Manzotti P, Ballèvre M (2013) Multistage garnet in high-pressure metasediments: Alpine overgrowths on variscan detrital grains. Geology 41:1151–1154. https://doi.org/10.1130/G34741.1

Manzotti P, Ballèvre M, Zucali M, et al (2014) The tectonometamorphic evolution of the Sesia–Dent Blanche nappes (internal Western Alps): review and synthesis. Swiss J Geosci 107:309–336.

https://doi.org/10.1007/s00015-014-0172-x

Manzotti P, Rubatto D, Darling J, et al (2012) From Permo-Triassic lithospheric thinning to Jurassic rifting at the Adriatic margin: Petrological and geochronological record in Valtournenche (Western Italian Alps). Lithos 146–147:276–292. https://doi.org/10.1016/j.lithos.2012.05.007

Martin LAJ, Rubatto D, Vitale Brovarone A, Hermann J (2011) Late Eocene lawsonite-eclogite facies metasomatism of a granulite sliver associated to ophiolites in Alpine Corsica. Lithos 125:620–640. https://doi.org/10.1016/j.lithos.2011.03.015

Massonne HJ, Schreyer W (1987) Phengite geobarometry based on the limiting assemblage with K-feldspar, phlogopite, and quartz. Contrib to Mineral Petrol 96:212–224. https://doi.org/10.1007/BF00375235

Messiga B, Scambelluri M (1991) Retrograde P-T-t path for the Voltri Massif eclogites (Ligurian Alps, Italy): some tectonic implications. J Metamorph Geol 9:93–109

Mibe K, Yoshino T, Ono S, et al (2003) Connectivity of aqueous fluid in eclogite and its implications for fluid migration in the Earth's interior. J Geophys Res Solid Earth 108:1–10. https://doi.org/10.1029/2002jb001960

Moore SJ, Carlson WD, Hesse M. . (2013) Origins of yttrium and rare earth element distributions in metamorphic garnet. J Metamorph Geol 31:663–689. https://doi.org/10.1111/jmg.12039

Münker C, Weyer S, Scherer EE, Mezger K (2001) Separation of high field strength elements (Nb, Ta, Zr, Hf) and Lu from rock samples for MC-ICPMS measurements. Geochemistry, Geophys Geosystems 2:. https://doi.org/10.1029/2001GC000183

Negro F, Bousquet R, Vils F, et al (2013) Thermal structure and metamorphic evolution of the Piemont-Ligurian metasediments in the northern Western Alps. Swiss J Geosci 106:63–78. https://doi.org/10.1007/s00015-013-0119-7

O'Brien PJ (2000) The fundamental Variscan problem: high-temperature metamorphism at different depths and high-pressure metamorphism at different temperatures. Orog Process Quantif Model Variscan Belt 179:369–386

Okamoto K, Maruyama S (1999) The high-pressure synthesis of lawsonite in the MORB+H2O system. Am Mineral 84:362–373. https://doi.org/10.2138/am-1999-0320

Otamendi JE, de la Rosa JD, Patino Douce AE, Castro A (2002) Rayleigh fractionation of heavy rare earths and yttrium during metamorphic garnet growth. Geology 30:159–162. https://doi.org/10.1130/0091-7613(2002)030<0159:RFOHRE>2.0.CO;2

Paton C, Hellstrom J, Paul B, et al (2011) Iolite: Freeware for the visualisation and processing of mass spectrometric data. J Anal At Spectrom 26:2508–2518. https://doi.org/10.1039/c1ja10172b

Peacock SM, Wang K (1999) Seismic consequences of warm versus cool subduction metamorphism: Examples from southwest and northeast Japan. Science (80-) 286:937–939. https://doi.org/10.1126/science.286.5441.937

Perchuk AL, Burchard M, Schertl HP, et al (2009) Diffusion of divalent cations in garnet: Multi-couple experiments. Contrib to Mineral Petrol 157:573–592. https://doi.org/10.1007/s00410-008-0353-6

Péron-Pinvidic G, Manatschal G (2009) The final rifting evolution at deep magma-poor passive margins from

Iberia-Newfoundland: A new point of view. Int J Earth Sci 98:1581–1597. https://doi.org/10.1007/s00531-008-0337-9

Peters D, Pettke T (2017) Evaluation of Major to Ultra Trace Element Bulk Rock Chemical Analysis of Nanoparticulate Pressed Powder Pellets by LA-ICP-MS. Geostand Geoanalytical Res 41:5–28. https://doi.org/10.1111/ggr.12125

Pettke T, Oberli F, Audétat A, et al (2012) Recent developments in element concentration and isotope ratio analysis of individual fluid inclusions by laser ablation single and multiple collector ICP-MS. Ore Geol Rev 44:10–38. https://doi.org/10.1016/j.oregeorev.2011.11.001

Philpotts A, Ague JJ (2009) Principles of igneous and metamorphic petrology, 2nd edn. Cambridge University Press

Pleuger J, Roller S, Walter JM, et al (2007) Structural evolution of the contact between two Penninic nappes (Zermatt-Saas zone and Combin zone, Western Alps) and implications for the exhumation mechanism and palaeogeography. Int J Earth Sci 96:229–252. https://doi.org/10.1007/s00531-006-0106-6

Poli S, Schmidt MW (2002) Petrology of Subducted Slabs. Annu Rev Earth Planet Sci 30:207–235. https://doi.org/10.1146/annurev.earth.30.091201.140550

Putnis A (2009) Mineral replacement reactions. Rev Mineral Geochemistry 70:87–124. https://doi.org/10.2138/rmg.2009.70.3

Putnis A (2002) Mineral replacement reactions: from macroscopic observations to microscopic mechanisms. Mineral Mag 66:689–708. https://doi.org/10.1180/0026461026650056

Raimondo T, Payne J, Wade B, et al (2017) Trace element mapping by LA-ICP-MS: assessing geochemical mobility in garnet. Contrib to Mineral Petrol 172:1–22. https://doi.org/10.1007/s00410-017-1339-z

Ratschbacher L, Dingeldey C, Miller C, et al (2004) Formation, subduction, and exhumation of Penninic oceanic crust in the Eastern Alps: Time constraints from 40Ar/39Ar geochronology. Tectonophysics 394:155–170. https://doi.org/10.1016/j.tecto.2004.08.003

Reinecke T (1998) Prograde high- to ultrahigh-pressure metamorphism and exhumation of oceanic sediments at Lago di Cignana, Zermatt-Saas Zone, western Alps. Lithos 42:147–189. https://doi.org/10.1016/s0024-4937(97)00041-8

Reinecke T (1991) Very high-pressure metamorphism and uplift of coesit-bearing metasediments from the Zermatt-Saas zone, Western Alps. Eur J Mineral 3:7–17

Rubatto D, Angiboust S (2015) Oxygen isotope record of oceanic and high-pressure metasomatism: a P-T-time-fluid path for the Monviso eclogites (Italy). Contrib to Mineral Petrol. https://doi.org/10.1007/s00410-015-1198-4

Rubatto D, Gebauer D, Compagnoni R (1999) Dating of eclogite-facies zircons: The age of Alpine metamorphism in the Sesia-Lanzo Zone (Western Alps). Earth Planet Sci Lett 167:141–158. https://doi.org/10.1016/S0012-821X(99)00031-X

Rubatto D, Gebauer D, Fanning M (1998) Jurassic formation and Eocene subduction of the Zermatt-Saas-Fee ophiolites: Implications for the geodynamic evolution of the Central and Western Alps. Contrib to Mineral Petrol 132:269–287. https://doi.org/10.1007/s004100050421

Rubatto D, Hermann J (2003) Zircon formation during fluid circulation in eclogites (Monviso, Western Alps): Implications for Zr and Hf budget in subduction zones. Geochim Cosmochim Acta 67:2173–2187. https://doi.org/10.1016/S0016-7037(02)01321-2

Rubatto D, Hermann J (2001) Exhumation as fast as subduction? Geology 29:3–6. https://doi.org/10.1130/0091-7613(2001)029<0003:EAFAS>2.0.CO;2

Rubatto D, Regis D, Hermann J, et al (2011) Yo-yo subduction recorded by accessory minerals in the Italian Western Alps. Nat Geosci 4:338–342. https://doi.org/10.1038/ngeo1124

Sandmann S, Nagel TJ, Herwartz D, et al (2014) Lu–Hf garnet systematics of a polymetamorphic basement unit: new evidence for coherent exhumation of the Adula Nappe (Central Alps) from eclogite-facies conditions. Contrib to Mineral Petrol 168:1–21. https://doi.org/10.1007/s00410-014-1075-6

Scherer EE, Cameron KL, Blichert-Toft J (2000) Lu-Hf garnet geochronology: Closure temperature relative to the Sm-Nd system and the effects of trace mineral inclusions. Geochim Cosmochim Acta 64:3413–3432. https://doi.org/10.1016/S0016-7037(00)00440-3

Scherer EE, Münker C, Mezger K (2001) Calibration of the Lutetium-Hafnium Clock. Science (80-) 293:683–688

Schmidt MW, Poli S (1998) Experimentally based water budgets for dehydrating slabs and consequences for arc magma generation. Earth Planet Sci Lett 163:361–379. https://doi.org/10.1016/S0012-821X(98)00142-3

Sizova E, Hauzenberger C, Fritz H, et al (2019) Late orogenic heating of (Ultra)high pressure rocks: Slab Rollback vs. Slab breakoff. Geosci 9:1–28. https://doi.org/10.3390/geosciences9120499

Skora S, Baumgartner LP, Mahlen NJ, et al (2006) Diffusion-limited REE uptake by eclogite garnets and its consequences for Lu-Hf and Sm-Nd geochronology. Contrib to Mineral Petrol 152:703–720. https://doi.org/10.1007/s00410-006-0128-x

Skora S, Mahlen NJ, Johnson CM, et al (2015) Evidence for protracted prograde metamorphism followed by rapid exhumation of the Zermatt-Saas Fee ophiolite. J Metamorph Geol 33:711–734. https://doi.org/10.1111/jmg.12148

Smit MA, Scherer EE, Bröcker M, Van Roermund HLM (2010) Timing of eclogite facies metamorphism in the southernmost Scandinavian Caledonides by Lu-Hf and Sm-Nd geochronology. Contrib to Mineral Petrol 159:521–539. https://doi.org/10.1007/s00410-009-0440-3

Smit MA, Scherer EE, Mezger K (2013) Lu-Hf and Sm-Nd garnet geochronology: Chronometric closure and implications for dating petrological processes. Earth Planet Sci Lett 381:222–233. https://doi.org/10.1016/j.epsl.2013.08.046

Söderlund U, Patchett PJ, Vervoort JD, Isachsen CE (2004) The 176Lu decay constant determined by Lu-Hf and U-Pb isotope systematics of Precambrian mafic intrusions. Earth Planet Sci Lett 219:311–324. https://doi.org/10.1016/S0012-821X(04)00012-3

Spandler C, Hermann J, Arculus RJ, Mavrogenes J (2003) Redistribution of trace elements during prograde metamorphism from lawsonite blueschist to eclogite facies; implications for deep subduction-zone processes. Contrib to Mineral Petrol 146:205–222. https://doi.org/10.1007/s00410-003-0495-5

Spear FS (1988) Metamorphic fractional crystallization and internal metasomatism by diffusional

homogenization of zoned garnets. Contrib to Mineral Petrol 99:507–517. https://doi.org/10.1007/BF00371941

Spear FS (2017) Garnet growth after overstepping. Chem Geol 466:491–499. https://doi.org/10.1016/j.chemgeo.2017.06.038

Spear FS, Pattison DRM (2017) The implications of overstepping for metamorphic assemblage diagrams (MADs). Chem Geol 457:38–46. https://doi.org/10.1016/j.chemgeo.2017.03.011

Spear FS, Wolfe OM (2019) Implications of overstepping of garnet nucleation for geothermometry, geobarometry and P–T path calculations. Chem Geol 530:. https://doi.org/10.1016/j.chemgeo.2019.119323

Taylor SR, McLennan SM (1985) The continental crust: Its composition and evolution

Thiessen EJ, Gibson HD, Regis D, et al (2019) High-grade metamorphism flying under the radar of accessory minerals. Geology 47:568–572. https://doi.org/10.1130/G45979.1

Usui T, Kobayashi K, Nakamura E, Helmstaedt H (2007) Trace element fractionation in deep subduction zones inferred from a lawsonite-eclogite xenolith from the Colorado Plateau. Chem Geol 239:336–351. https://doi.org/10.1016/j.chemgeo.2006.08.009

Vance D, O'nions RK (1990) Isotopic chronometry of zoned garnets: growth kinetics and metamorphic histories. Earth Planet Sci Lett 97:227–240

Vitale Brovarone A, Alard O, Beyssac O, et al (2014) Lawsonite metasomatism and trace element recycling in subduction zones. J Metamorph Geol 32:489–514. https://doi.org/10.1111/jmg.12074

Vitale Brovarone A, Beltrando M, Malavieille J, et al (2011) Inherited Ocean-Continent Transition zones in deeply subducted terranes: Insights from Alpine Corsica. Lithos 124:273–290. https://doi.org/10.1016/j.lithos.2011.02.013

Vitale Brovarone A, Beyssac O (2014) Lawsonite metasomatism: A new route for water to the deep Earth. Earth Planet Sci Lett 393:275–284. https://doi.org/10.1016/j.epsl.2014.03.001

Vogt K, Gerya T V. (2014) From oceanic plateaus to allochthonous terranes: Numerical modelling. Gondwana Res 25:494–508. https://doi.org/10.1016/j.gr.2012.11.002

Walsh EO, Hacker BR (2004) The fate of subducted continental margins: Two-stage exhumation of the high-pressure to ultrahigh-pressure Western Gneiss Region, Norway. J Metamorph Geol 22:671–687. https://doi.org/10.1111/j.1525-1314.2004.00541.x

Weber S, Bucher K (2015) An eclogite-bearing continental tectonic slice in the Zermatt-Saas high-pressure ophiolites at Trockener Steg (Zermatt, Swiss Western Alps). Lithos 232:336–359. https://doi.org/10.1016/j.lithos.2015.07.010

Weber S, Sandmann S, Miladinova I, et al (2015) Dating the initiation of Piemonte-Liguria Ocean subduction: Lu–Hf garnet chronometry of eclogites from the Theodul Glacier Unit (Zermatt-Saas zone, Switzerland). Swiss J Geosci 108:183–199. https://doi.org/10.1007/s00015-015-0180-5

White RW, Powell R, Holland TJB (2007) Progress relating to calculation of partial melting equilibria for metapelites. J Metamorph Geol 25:511–527. https://doi.org/10.1111/j.1525-1314.2007.00711.x

White RW, Powell R, Holland TJB, Worley B (2000) The effect of TiO2 and Fe2O3 on metapelitic assemblages at

greenschist and amphibolite facies conditions: Mineral equilibria calculations in the system K2O-FeO-MgO-Al2O3-SiO2-H2O-TiO2-Fe2O3. J Metamorph Geol 18:497–511. https://doi.org/10.1046/j.1525-1314.2000.00269.x

Whitney DL, Evans BW (2010) Abbreviations for names of rock-forming minerals. Am Mineral 95:185–187. https://doi.org/10.2138/am.2010.3371

Whitney DL, Teyssier C, Toraman E, et al (2011) Metamorphic and tectonic evolution of a structurally continuous blueschist-to-Barrovian terrane, Sivrihisar Massif, Turkey. J Metamorph Geol 29:193–212. https://doi.org/10.1111/j.1525-1314.2010.00915.x

Wiederkehr M, Bousquet R, Schmid SM, Berger A (2008) From subduction to collision: Thermal overprint of HP/LT meta-sediments in the north-eastern Lepontine Dome (Swiss Alps) and consequences regarding the tectono-metamorphic evolution of the Alpine orogenic wedge. Swiss J Geosci 101:. https://doi.org/10.1007/s00015-008-1289-6

Wilke FDH, O'Brien PJ, Altenberger U, et al (2010) Multi-stage reaction history in different eclogite types from the Pakistan Himalaya and implications for exhumation processes. Lithos 114:70–85. https://doi.org/10.1016/j.lithos.2009.07.015

Wolfe OM, Spear FS (2018) Determining the amount of overstepping required to nucleate garnet during Barrovian regional metamorphism, Connecticut Valley Synclinorium. J Metamorph Geol 36:79–94. https://doi.org/10.1111/jmg.12284

SUPPLEMENTARY MATERIAL

Supplementary Figures

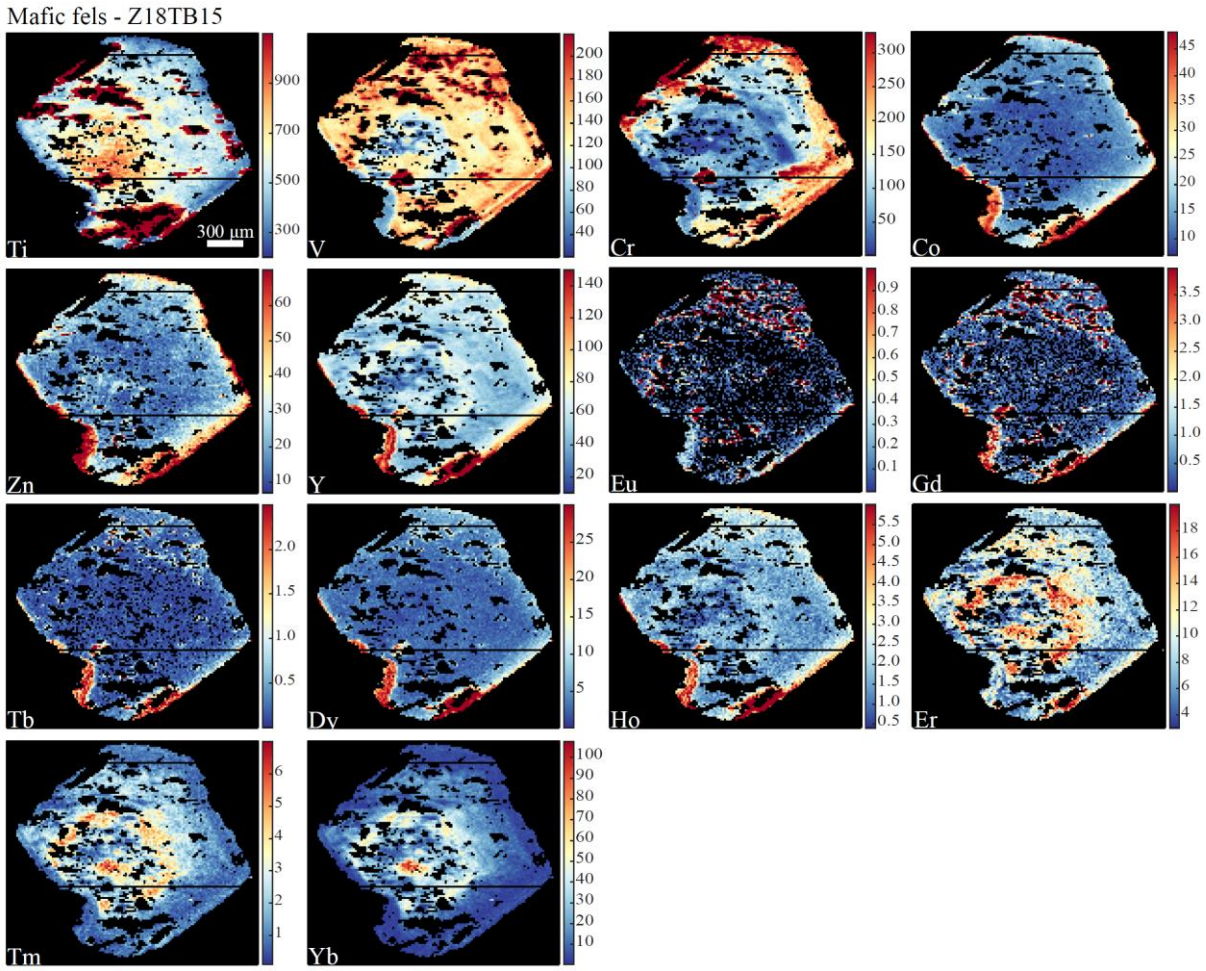

Figure S1: Quantified LA-ICP-MS compositional maps in garnets, all maps show µg/g abundance. Software: XMapTools (Lanari et al. 2014, 2019)***. Mafic fels sample Z18TB15.***

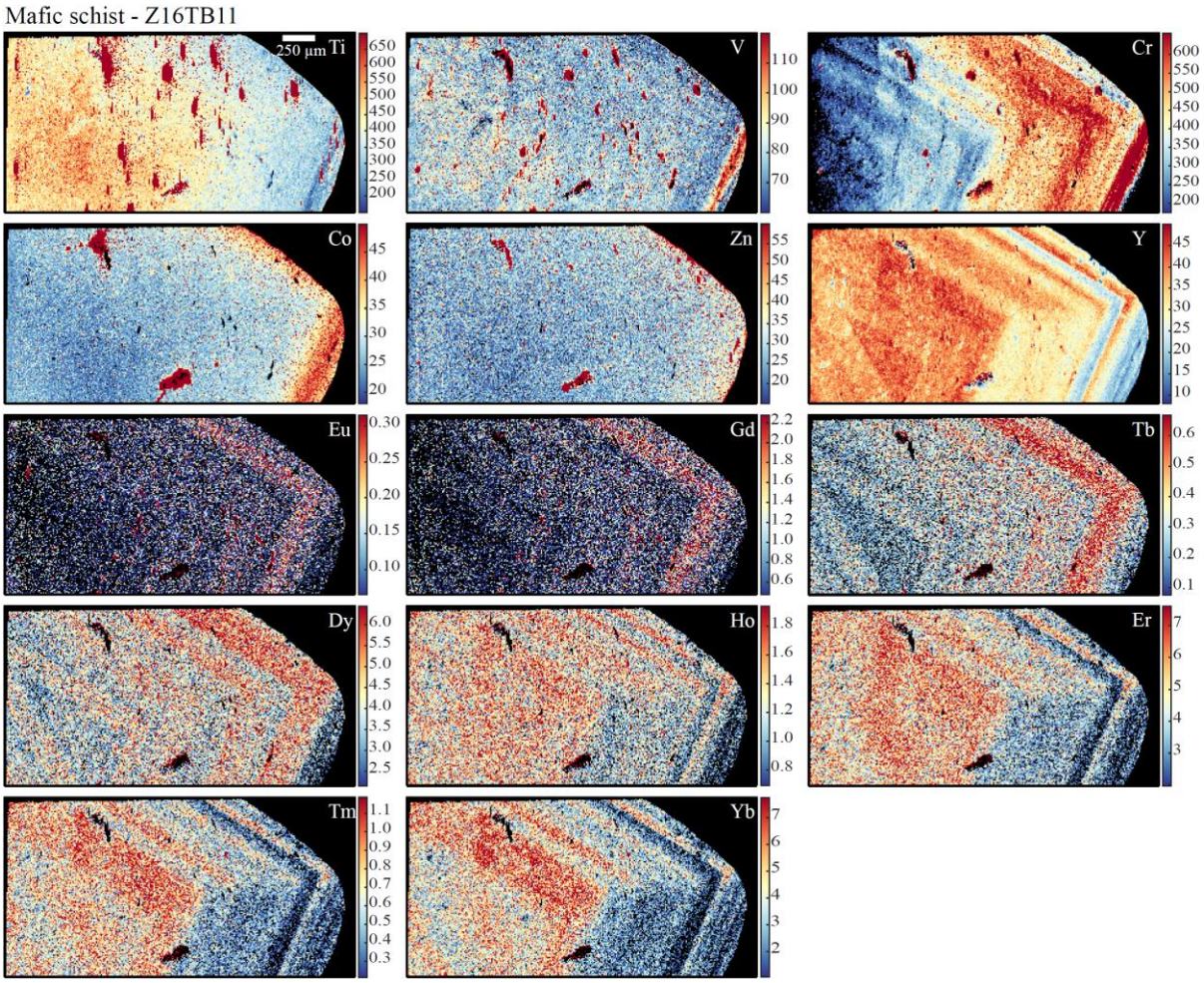

Figure S2: Quantified LA-ICP-MS compositional maps in garnets, all maps show µg/g abundance. Software: XMapTools (Lanari et al. 2014, 2019)***. Mafic schist sample Z16TB11.***

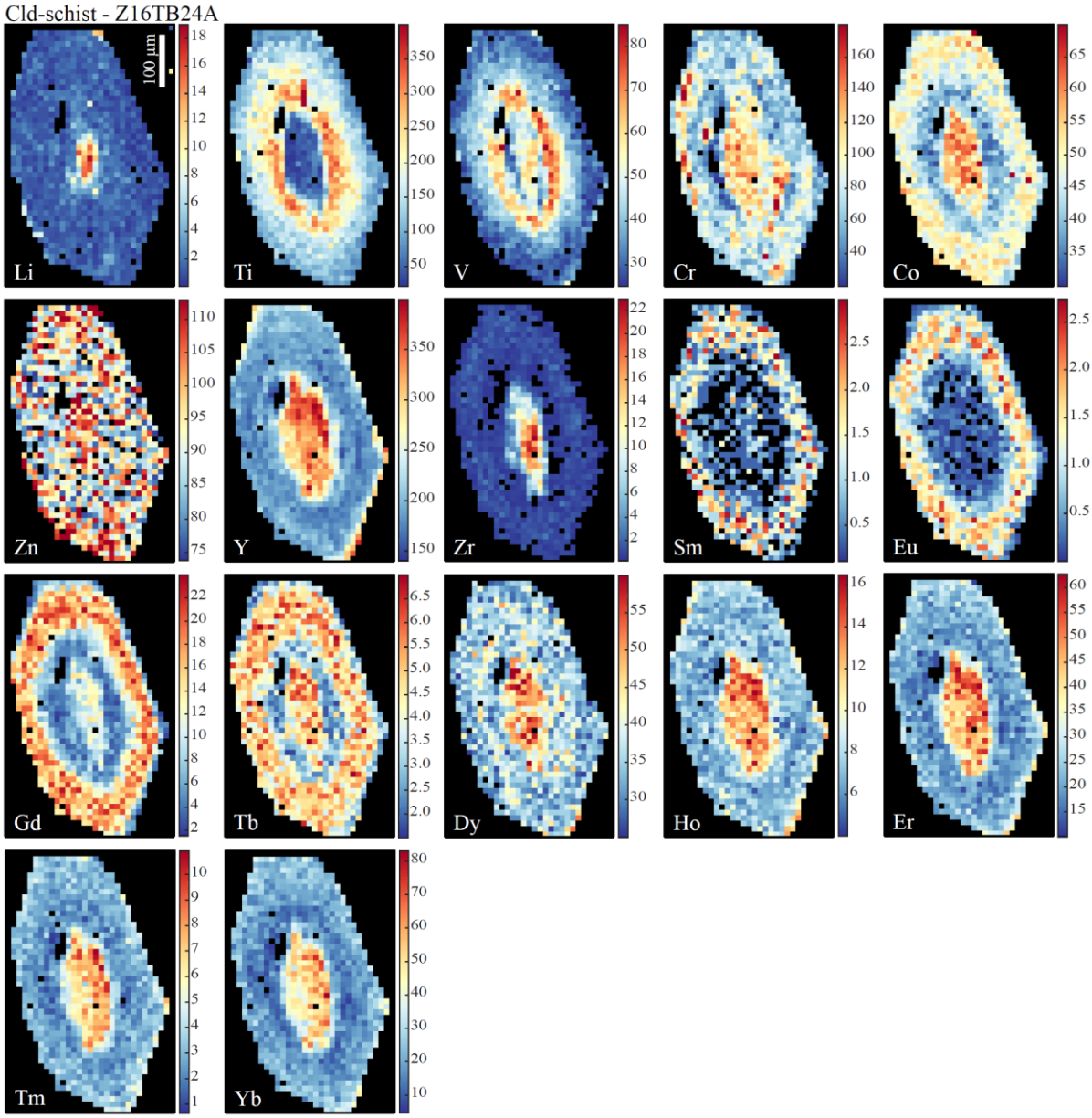

Figure S3: Quantified LA-ICP-MS compositional maps in garnets, all maps show µg/g abundance. Software: XMapTools (Lanari et al. 2014, 2019)***. Cld-schist sample Z16TB24A.***

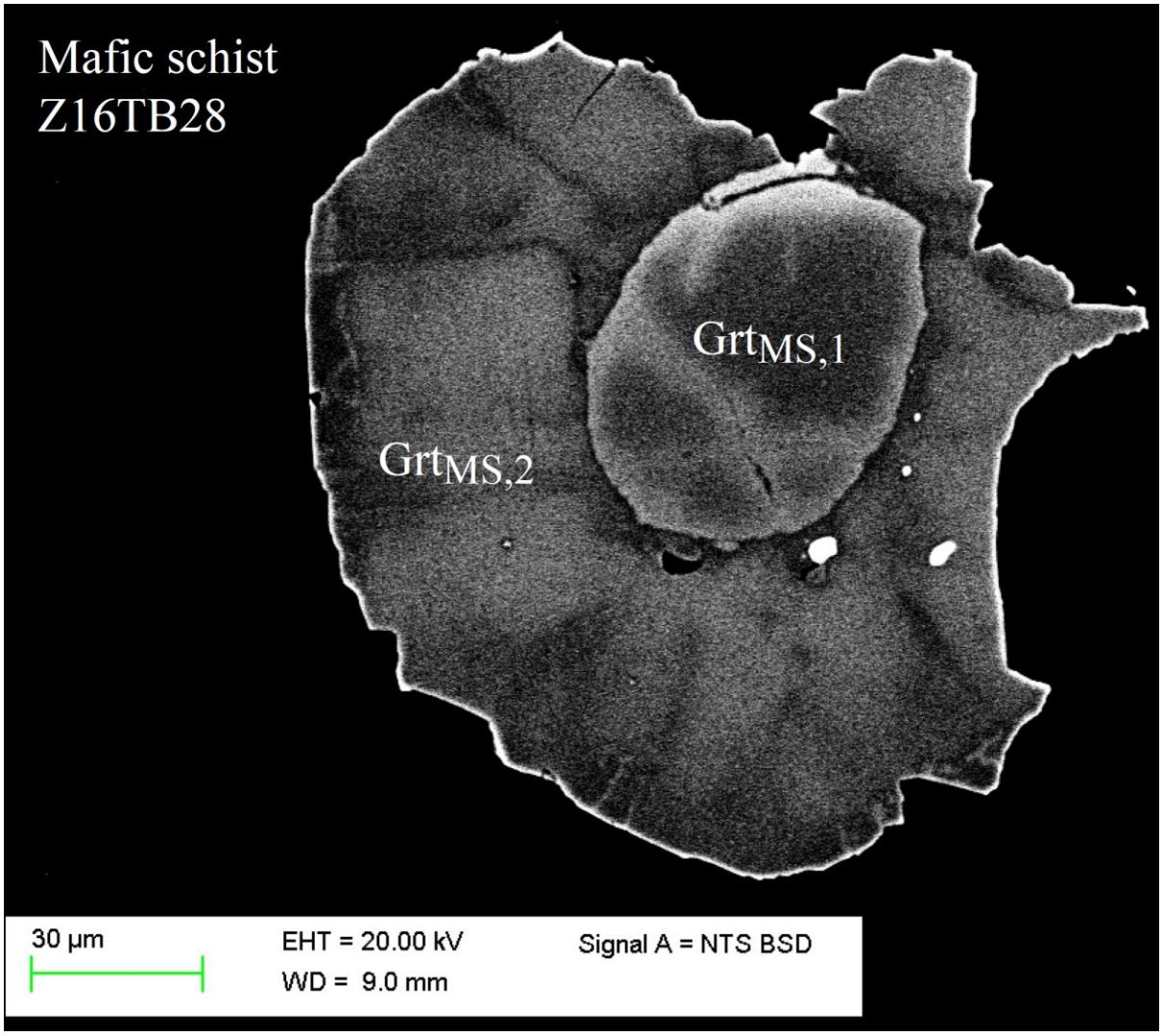

Figure S4: BSE image of small garnet with sharp chemical zoning in sample Z16TB28 (Mafic schist).

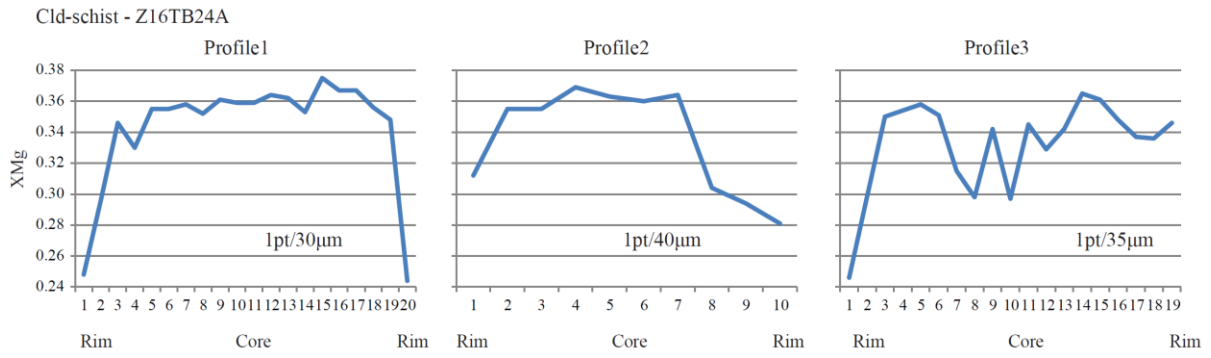

Figure S5: EPMA profile across chloritoid grains in sample Z16TB24A (Cld-schist).

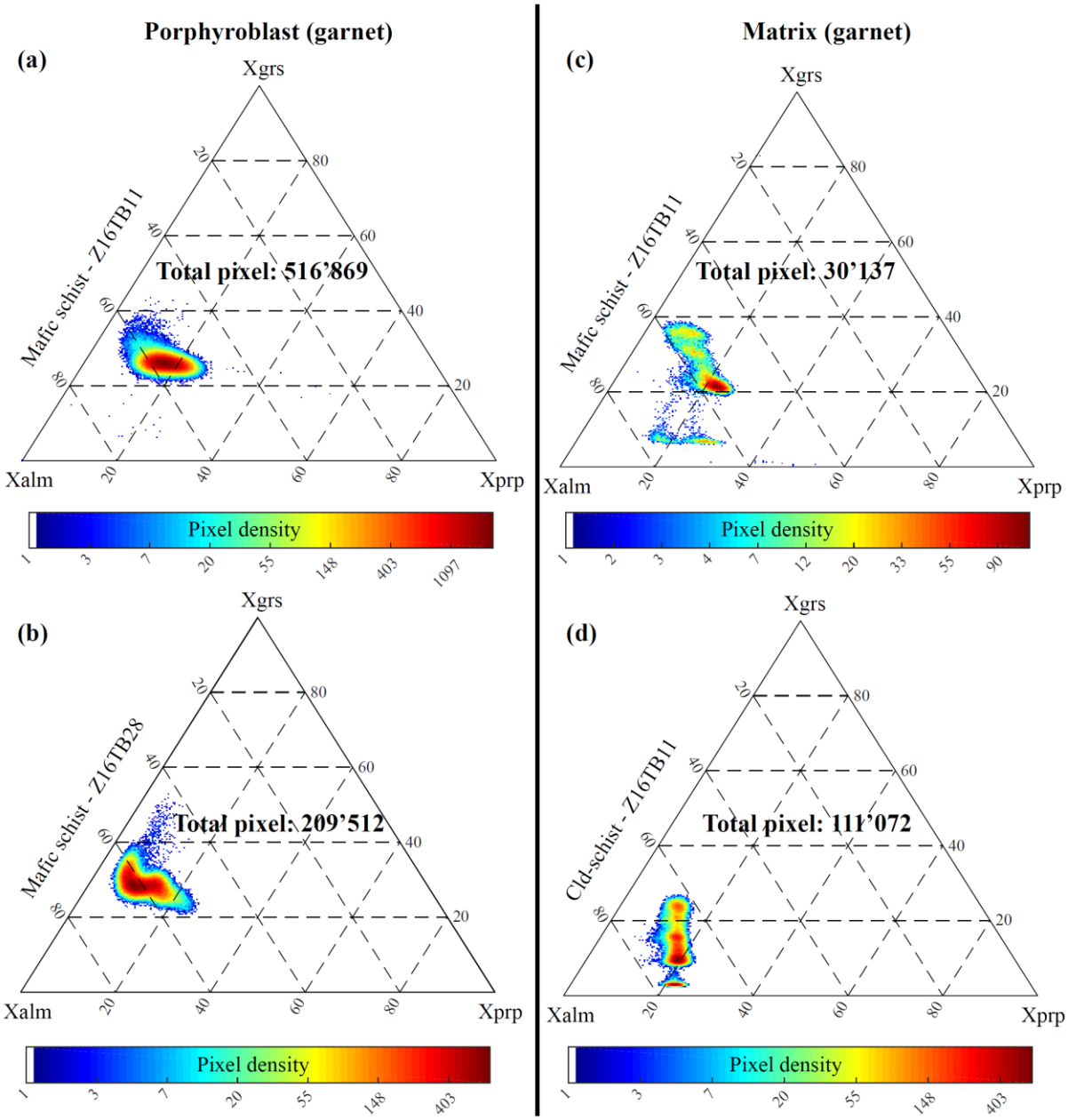

Figure S6: Ternary chemical diagram showing the range of garnet composition in Xgrs-Xalm-Xprp. Range of compositional data were exported from compositional maps using XMaptTools (Lanari et al. 2014, 2019)**.**

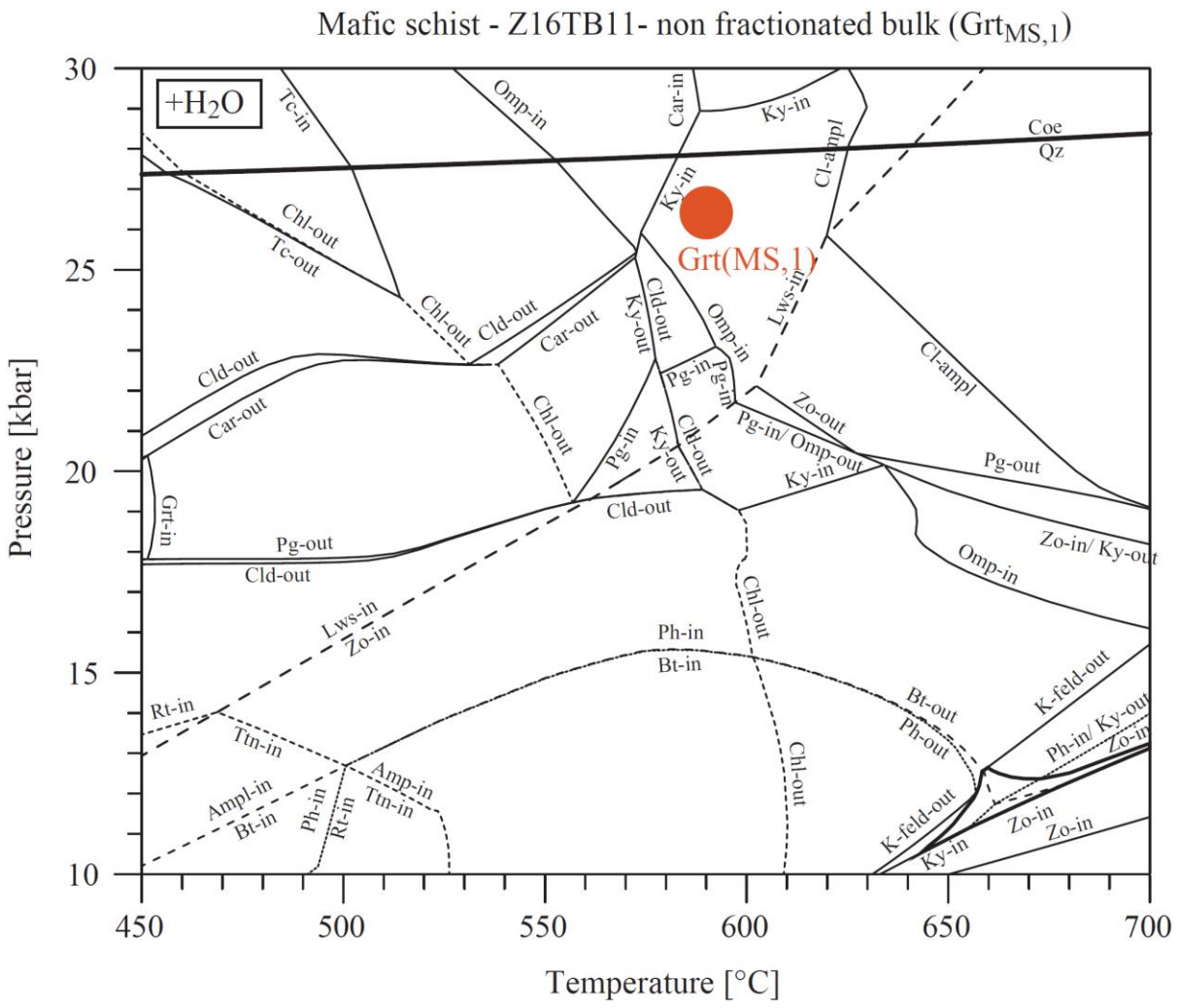

Figure S7: Pseudosection calculated with the software Theriak-Domino (De Capitani and Brown 1987; De Capitani and Petrakakis 2010)***. Bulk rock used is found in Table S6 ($GRT_{MS,1}$). Red dot corresponds to garnet P–T stable condition (Fig.4c, 10) obtained using GrtMod 1.6.2*** (Lanari et al. 2017)***, see Phase equilibria modelling for explanations. Water saturation was chosen as input parameter.***

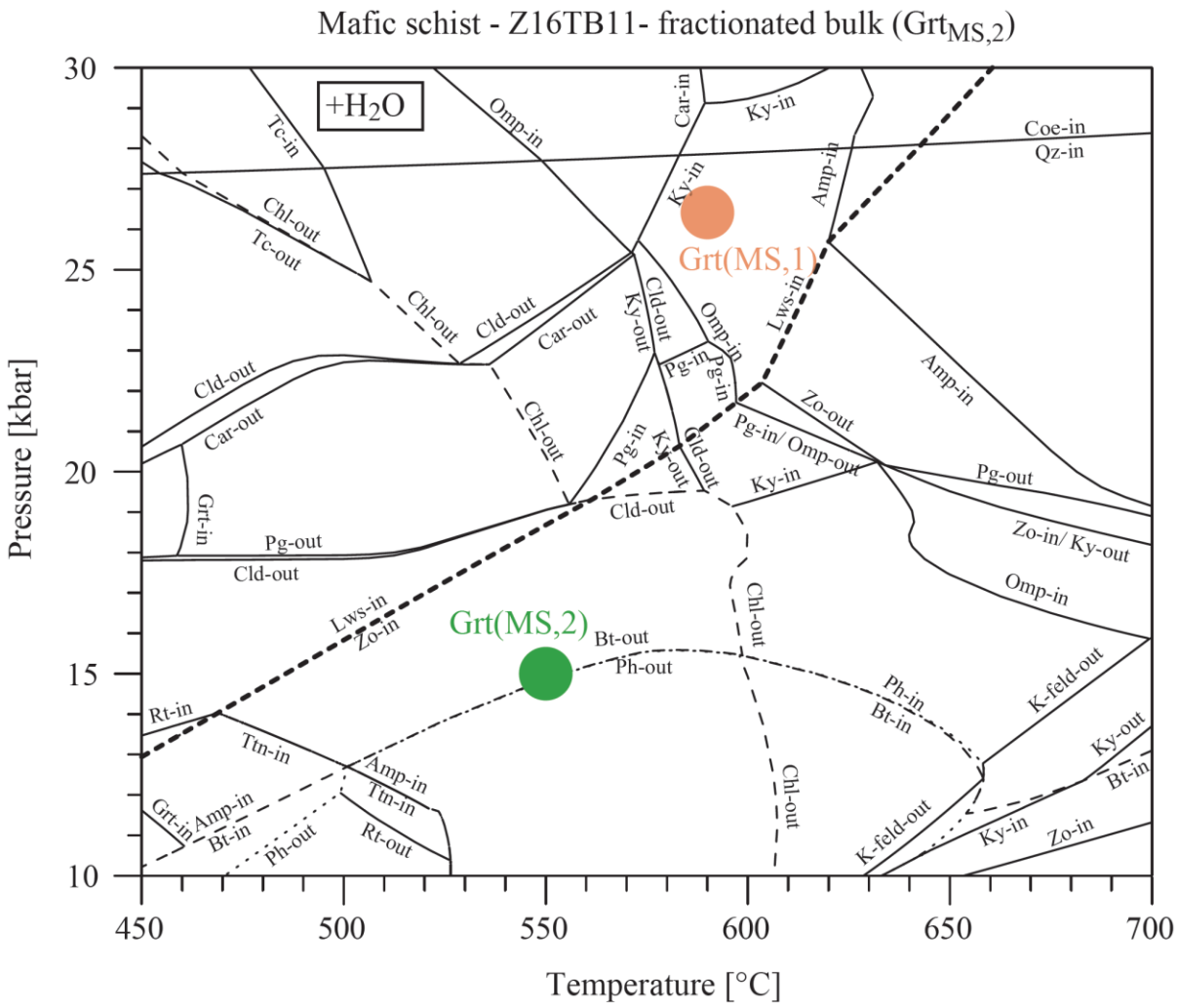

Figure S8: Pseudosection calculated with the software Theriak-Domino (De Capitani and Brown 1987; De Capitani and Petrakakis 2010)***. Bulk rock used is found in Table S6 ($GRT_{MS,2}$). Red and green dots correspond to successive garnet P–T stable conditions (Fig.4c, 4g, 10) obtained using GrtMod 1.6.2*** (Lanari et al. 2017)***, see Phase equilibria modelling for explanations. Water saturation was chosen as input parameter.***

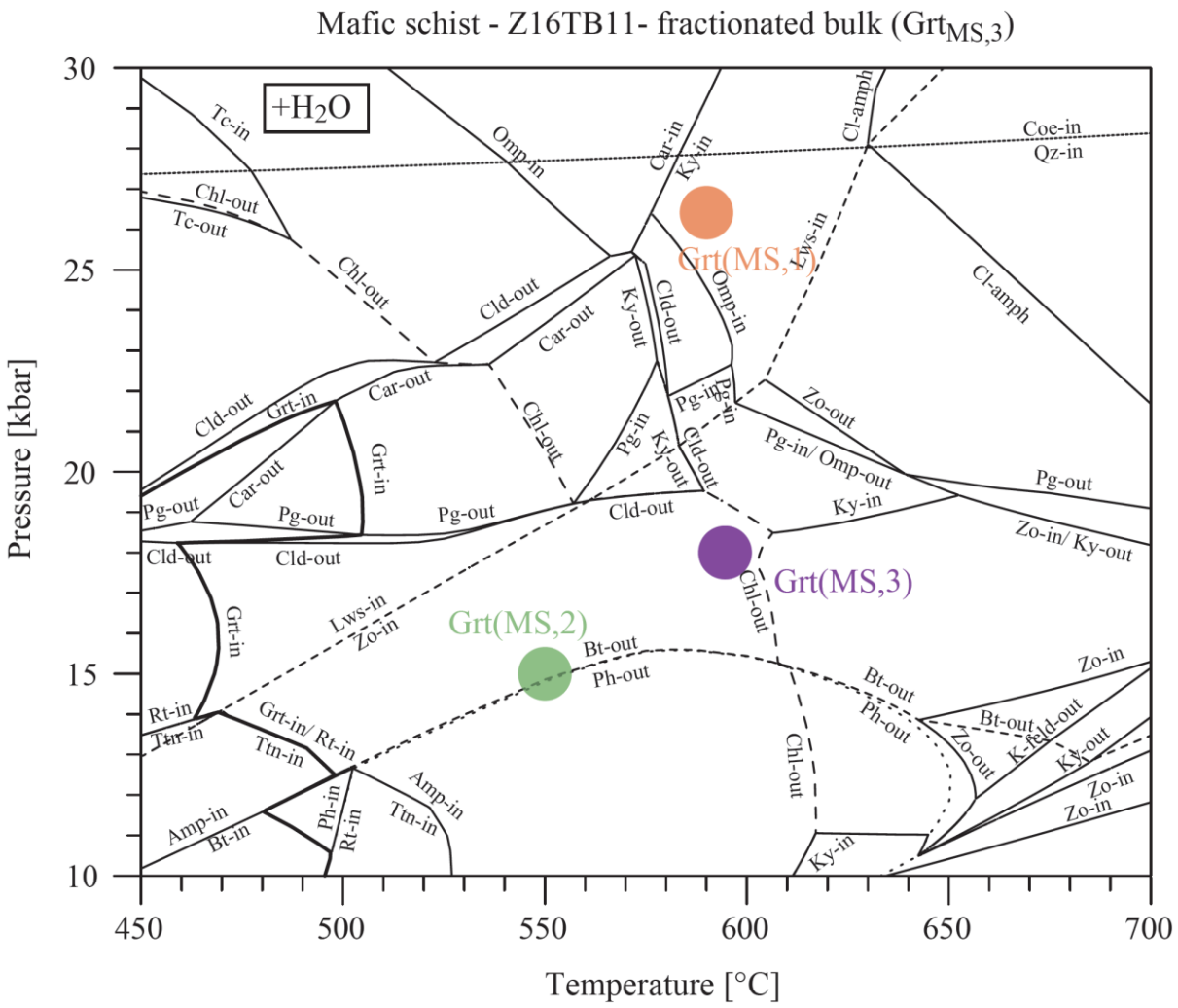

Figure S9: Pseudosection calculated with the software Theriak-Domino (De Capitani and Brown 1987; De Capitani and Petrakakis 2010)***. Bulk rock used is found in Table S6 ($GRT_{MS,3}$). Red, green and violet dots correspond to successive garnet P–T stable conditions (Fig.4c, 4g, 10) obtained using GrtMod 1.6.2*** (Lanari et al. 2017)***, see Phase equilibria modelling for explanations. Water saturation was chosen as input parameter.***

Mafic fels - Z18TB15
diameter: >500µm

Mafic fels - Z18TB15
diameter: 250 - 500µm

Mafic schist - Z16TB28
diameter: >500µm

Cld-schist - Z16TB24A
diameter: >500µm

Cld-schist - Z16TB24A
diameter: 250 - 500µm

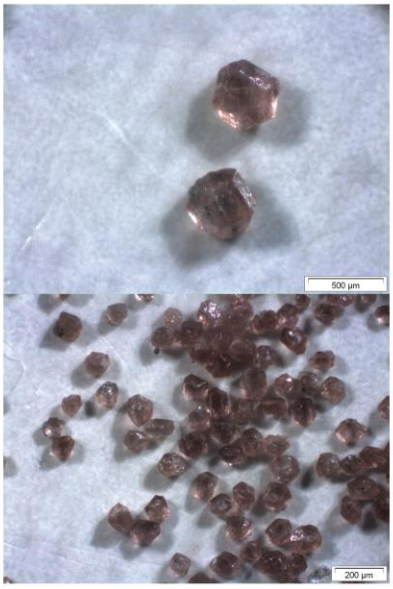

Figure S10: Pictures of garnet separates for Lu-Hf dating.

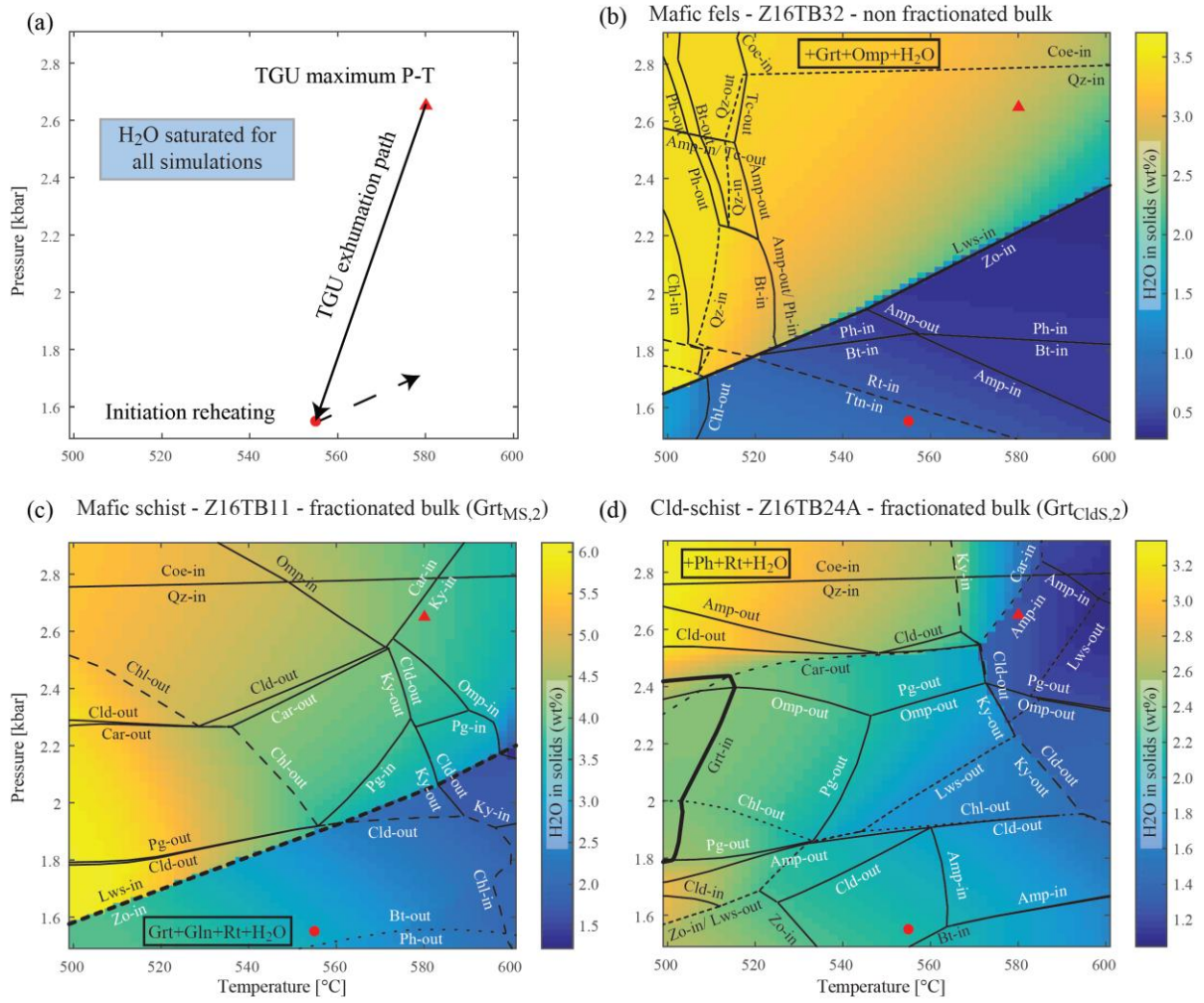

Figure S11: P-T diagrams presenting variation of H_2O in solids, superimposed pseudosections were calculated using software Theriak-Domino (De Capitani and Brown 1987; De Capitani and Petrakakis 2010)***. The triangle corresponds to TGU maximum P–T stable conditions and the circle corresponds to the P-T stable conditions prior to the re-heating stage. (a) TGU exhumation path is indicated (arrow) as a reminder of Figure 11a. (b) Metabasite, bulk rock used is non fractionated (Table S6, $Grt_{MB,1a}$). (c) Mafic schist, bulk rock used is fractionated (Table S6, $Grt_{MS,2}$). (d) Cld-schist, bulk rock used is fractionated (Table S6, $Grt_{CldS,2}$).***

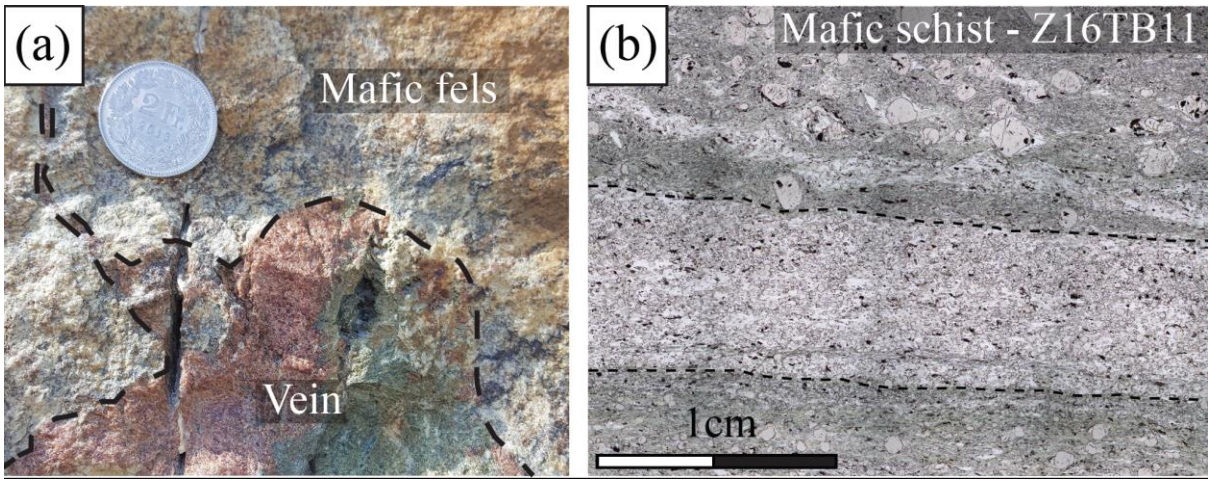

Figure S12 Outcrop pictures and scanned thin section images illustrating fluid-rock interaction in TGU. (a) Picture of veinlets with high-pressure assemblage (garnet-diopside) cross cutting the metabasites. (b) Picture of thin section (sample Z16TB11), where some schist layers contain abundant deformed clusters of garnet grains having sharp chemical zoning.

Supplementary Tables

All supplementary tables are stored on a CD in a folder labelled “SupplementaryTablesChapter2”.

Table S1: Garnet major element average composition.

Table S2: LA-ICP-MS trace element of garnet.

Table S3: K-white mica major element average composition.

Table S4: Chloritoid major element chemical composition.

Table S5: LA-ICP-MS trace element of rutile.

Table S6: Reactive bulk-rock chemistry evolution using GrtMode.

Table S7: LA-ICP-MS major and trace element bulk-rock analyses.

CHAPTER 3

Pervasive fluid-rock interaction in subducted oceanic crust revealed by oxygen isotope zoning in garnet

Thomas Bovay[1], Daniela Rubatto[1,2], Pierre Lanari[1]

[1]Institute of Geological Sciences, University of Bern, 3012 Bern, Switzerland

[2]Institut des Sciences de la Terre, University of Lausanne, 1015 Lausanne, Switzerland

KEYWORDS

Permeability, Garnet oxygen isotope composition; Pervasive fluid flow; Subduction; Fluid-rock interaction

In revision for *Contributions to Mineralogy and Petrology*

ABSTRACT

Dehydration reactions in the subducting slab liberate fluids causing major changes in rock density, volume and permeability. Although it is well known that the fluids can migrate and interact with the surrounding rocks, fluid pathways remain challenging to track and the consequences of fluid-rock interactions processes are often overlooked. In this study we investigate pervasive fluid-rock interaction in a sequence of schists and mafic felses exposed in the Theodul Glacier Unit (TGU), Western Alps. This unit is embedded within metaophiolites of the Zermatt Saas Zone and reached eclogite-facies conditions during Alpine convergence. Chemical mapping and in situ oxygen isotope analyses of garnet from the schists reveal a sharp chemical zoning between a xenomorphic core and a euhedral rim, associated to a drop of ~8 ‰ in $\delta^{18}O$. Thermodynamic and $\delta^{18}O$ models show that the large amount of low $\delta^{18}O$ H_2O required to change the reactive bulk $\delta^{18}O$ composition cannot be produced by dehydration of the mafic fels from the TGU only, and requires a large contribution of the surrounding serpentinites. The calculated time-integrated fluid flux across the TGU rocks is 1.1 x 10^5 cm^3/cm^2, which is above the open-system behaviour threshold and argues for pervasive fluid flow at high-pressure conditions. The transient rock volume variations caused by lawsonite breakdown is identified as a possible trigger for the pervasive fluid influx. The schist permeability at eclogite-facies conditions (~2 x 10^{-20} m^2) is comparable to the permeability determined experimentally for blueschist and serpentinites.

1. INTRODUCTION

Increase of pressure and temperature during prograde metamorphism along a subducting slab leads to a series of breakdown reactions involving hydrous phases (e.g. Schmidt and Poli, 2003) and is associated with major variation in rock density, rock volume and rock porosity. This process liberates varying amounts of free fluids (dominantly aqueous fluids) responsible for element transfer between crust and mantle in subduction zones. Fluids in turns play an important role in arc magmatism, geochemical cycles, energy budgets, mantle composition and seismicity. Studying the scale of fluid migration and the degree of fluid-rock interaction at depth provides information to quantify the fluid budget in the subducting slab environment (Sorensen and Barton 1987; Bebout 1991a; Philippot and Selverstone 1991; Selverstone et al. 1992; Nadeau et al. 1993; Spandler et al. 2011).

It has been demonstrated that large amounts of aqueous fluids in subduction zone can be generated by dehydration of mafic oceanic crust and associated hydrated oceanic lithospheric mantle (Ito et al. 1983; Peacock 1990; Ulmer and Trommsdorff 1995; Poli and Schmidt 2002; Spandler et al. 2003; Angiboust and Agard 2010). Aqueous fluids released from the lower layers of the subducting slab necessarily infiltrate upper layers of the subducting oceanic plate (Zack and John 2007) and eventually infiltrate the overriding mantle wedge. Propagation of fluids at depth may occur by interconnected vein networks and channelization (Miller and Cartwright 2000; Hacker et al. 2003; Miller et al. 2003; Zack and John 2007; John et al. 2008; Angiboust et al. 2014; Taetz et al. 2016) or by pervasive fluid flow (Bebout 1991b; Bebout and Barton 1993; Konrad-Schmolke et al. 2011). The fluid flow mechanisms may have different dynamics in the downgoing slab, at the slab mantle interface or in the hanging-wall mantle wedge (Konrad-Schmolke et al. 2011). A better understanding of the dynamics of fluid-rock interaction and the associated permeability is crucial to quantify fluid-driven mass transfer processes in subduction zones (Ingebritsen and Manning 1999; Manning and Ingebritsen 1999; Ingebritsen and Manning 2003, 2010; Konrad-Schmolke et al. 2011; Ganzhorn et al. 2019).

Stable isotopes are particularly suited to investigating the evolution of aqueous fluids in metamorphic terranes (e.g. Baumgartner and Valley, 2001). They have been successfully applied to constrain the origin of subduction fluids and to describe fluid-rock and fluid-rock-melt interaction in subducting slabs (e.g. Barnes et al., 2014; Barnicoat and Cartwright, 1997; Bebout and Barton, 1989; Putlitz et al., 2000; Sharp et al., 1993). Distinct rock types are each characterized by a limited range of bulk $\delta^{18}O$ values, and thus the $\delta^{18}O$ composition of the derived fluids (water) at equilibrium can be estimated at a given temperature. In refractive metamorphic minerals that are robust to successive re-equilibration, such as garnet, mineral-fluid interaction will results in intra-crystalline $\delta^{18}O$

variations when the reactive fluid is out of equilibrium with the bulk rock. Such variations in mineral oxygen isotope composition are a key tool to evaluate fluid-rock interaction with externally-derived fluids and its relative timing during pressure-temperature (*P*–*T*) evolutions (e.g. Errico et al., 2013; Gauthiez-Putallaz et al., 2016; Martin et al., 2014; Nadeau et al., 1993; Page et al., 2014; Putlitz et al., 2000; Rubatto and Angiboust, 2015; Russell et al., 2013; Page et al., 2019). Advances in thermodynamic modelling and underpinning experiments provide a detailed framework on fluid production and mineral $\delta^{18}O$ change in single rock types (Kohn 1993; Zheng 1993; Manning 2004; Kessel et al. 2005). Recent studies have enabled major improvement in numerical modelling of petrological and isotopic systems by coupling thermodynamic and $\delta^{18}O$ simulations (Vho et al. 2019, 2020a). With this approach, the effect of fluid interaction between multiple rock types of contrasting composition can be quantitatively evaluated along a given *P*–*T* metamorphic path, allowing monitoring of variables of interest such as fluid-rock ratios and $\delta^{18}O$ isotopic variations at the rock and mineral scale (Vho et al., 2020b).

Common dehydration reactions in metamorphic environments generate fluid and grain-scale porosity (Connolly 2010). Because the volume of fluid and minerals produced by devolatilizing reactions is greater than the volume of the mineral reactants, this pressurizes the porosity of the rigid host rock (Ferry 1994). As a consequence a micro-porous network forms, which permeability relies on the hydraulic connectivity among fluid-filled porosity produced by individual reaction nuclei (Miller et al. 2003; Zack and John 2007; Konrad-Schmolke et al. 2011). Even if fluids are poorly drained in deep environments (Connolly 2010), pervasive fluid flow will eventually set up in response to buoyancy forces and gradients in fluid pressure, where the interconnected porosity is sufficient to allow fluid motion (Oliver 1996; Ague 2003). The related fluid flux strongly depends on the rate of fluid production, on how the deformation accommodates the rock volume variation and on the drainage efficiency (Connolly 2010). Fluid gradients and associated permeabilities, which vary in time and space, must be effective across the length of the fluid-flow system (Oliver 1996; Ingebritsen and Manning 2010) and remain sustained over sufficient time to accommodate the variations recorded by the exhumed metamorphic rocks (Manning and Ingebritsen 1999), such as a shift in stable isotopes or variation in major and trace elements bulk composition. Thus, on short time scales, a transient rock permeability may reach values significantly in excess than those expected (Ingebritsen and Manning 2010) and initiation of fluid flow will start as a consequence of fluid pressure dissipation (Manning and Ingebritsen 1999).

The European Alps are a good laboratory to observe relicts of fluid-rock interaction processes, with occurrence of a broad variety of metamorphic rocks exhumed from a paleo subduction zone. We investigated an association of metasediments and mafic felses from the Theodul Glacier Unit,

embedded within the Zermatt Saas metaophiolite in the Western Alps. Both tectonic units reached eclogitic facies metamorphic conditions during Alpine convergence at ~45-50 Ma (Chapter 2; Duchêne et al. 1997; Rubatto et al. 1998; Lapen et al. 2003). Garnet chemical zoning and garnet $\delta^{18}O$ variation are used to infer the record of fluid-rock interaction along the TGU metamorphic *P–T* path. Thermodynamic and $\delta^{18}O$ isotope modelling provides quantitative information on fluid source, fluid-rock ratio, time integrated fluid flux and rock rheological variation. Modelling the variation in rock volume allows investigation of the origin of fluid transfer initiation and of rock permeabilities.

2. GEOLOGICAL AND TECTONIC SETTING

The Zermatt-Saas Zone (ZSZ) and the Theodul Glacier Unit (TGU) are two juxtaposed tectonic units located in the Western Alps (Fig. S1). They represent distinct fragments of the Mesozoic Piemont-Ligurian oceanic lithosphere, which were subducted below the Adriatic margin between circa 50 and 40 Ma during the Alpine orogeny (Chapter 2; Duchêne et al. 1997; Rubatto et al. 1998; Amato et al. 1999; Dal Piaz et al. 2001; Agard et al. 2009).

The ZSZ metaophiolite, which extends from Saas-Fee (Switzerland) in the north to the Aosta Valley (Italy) in the south, represents one of the largest and deepest known portion of exhumed oceanic lithosphere in the world (Bearth 1967; Dal Piaz and Ernst 1978; Reinecke 1998; Bucher et al. 2005; Angiboust et al. 2009). The unit preserved a dismembered ophiolitic sequence made of an association of serpentinites, metagabbros, metabasalts, marbles, schists, calcschists, meta-radiolarites and Mn-bearing metacherts (Bearth 1967; Dal Piaz 1979). The overall lithostratigraphy has slow spreading ridge affinity (Dilek and Furnes 2014) with an internal tectonic structure poorly constrained and highly variable (Angiboust and Agard 2010). The 150-500 m thick ophiolite slices are systematically underlain by a serpentinite body that is 500 m to several km thick (Angiboust and Agard 2010). The rocks have experienced eclogitic high pressure (HP) metamorphism at 23-25 kbar and 530-550 °C (Bearth 1967; Dal Piaz and Ernst 1978; Bucher et al. 2005; Angiboust et al. 2009), with small lenses showing typical ultra-HP mineral relicts corresponding to a pressure of 26-28 kbar (Reinecke 1991; Groppo et al. 2009). The metamorphic ages range between 50 and 40 Ma (Rubatto et al. 1998; Lapen et al. 2003; Dragovic et al. 2020). Retrogression during exhumation locally reflects rock re-equilibration under blueschist facies conditions at 15-16 kbar (Angiboust et al. 2009).

The TGU is located south of Zermatt in Switzerland (Fig. S1) and is a 2 km^2 and 100 m thick tectonic slice made of complex interlayering between mafic and felsic rocks interpreted as a volcanoclastic sequence. The main rock types are mafic fels, mafic schist, Cld-schist and Grt-schist. The TGU is now folded and fully embedded within the ZSZ. The complex garnet textures in the mafic schist reflect a multi-stage metamorphic history of the TGU, which is under debate. Bucher et al.

(2019, 2020) interpreted the TGU as a polymetamorphic continental slice based on thermodynamic modelling of garnet in the schists. In Chapter 2, Lu-Hf dating was conducted on garnet in the schists and mafic fels and obtained ages ranging from 48 to 50 Ma, which favoured a mono-metamorphic Alpine history. This age range corresponds to the metamorphic ages previously determined for ZSZ (Duchêne et al. 1997; Rubatto et al. 1998; Amato et al. 1999; Dal Piaz et al. 2001; Dragovic et al. 2020) and might represent the early stage of Piemont-Ligurian oceanic lithosphere subduction as suggested by Weber *et al.* (2015) and in Chapter 2. Thermodynamic modelling and Zr-in-rutile thermometry additionally show that TGU mafic fels and metasediments reached a common maximum metamorphic condition at 26.5 ± 1.5 kbar and 580 ± 15 °C (Chapter 2), which is similar to that reported for the ZSZ (Bearth 1967; Dal Piaz and Ernst 1978; Bucher et al. 2005; Angiboust et al. 2009). In the metasedimentary rocks, an external garnet rim with sharp chemical zoning was assigned to a reheating step during exhumation at ca. 15-17 kbar from 555 °C to 590 °C (Chapter 2).

3. SAMPLES

The three main lithologies of the TGU were investigated: mafic fels, mafic schist and the Cld-schist. The samples contain a rather typical assemblage for blueschist to eclogitic rocks and thus are not identified as metasomatic rocks with limited and/or unusual mineralogy. Veins within the mafic fels are represented by sample Z17TB04A and Z17TB05v (Table 1). Multiple samples were collected over the area to get a spectrum and broad representation of rock type variability within the tectonic unit (Table 1). These lithologies are described in more details in Chapter 2 and briefly summarized below.

Mafic felses outcrop either as large eclogitic bodies or as stretched mafic boudins that are embedded within the surrounding schists (Fig. 1a) and elongated parallel to the main foliation. The thickness of the mafic bodies varies from 1 to 10 m, whereas the mafic boudins have various thickness and elongations ranging from some centimetres to pluri-metres in size. Two end-members assemblages are observed: (1) garnet-omphacite-glaucophane-rutile-quartz-phengite (sample Z18TB15); (2) garnet-diopside-epidote-titanite-graphite, where epidote refers to the mineral group and is present either as zoisite-epidote (sample Z16TB32) or zoisite alone (sample Z17TB07, Z17TB05). Thermodynamic modelling has shown that zoisite-rich areas are produced through lawsonite breakdown reaction (Chapter 2). In both mafic fels assemblages, garnet crystals are mostly euhedral having a diameter between 0.2 and 1 cm. Some veinlets found in zoisite-rich mafic boudins (sample Z17TB04A, Z17TB05v). In some veins, a symmetrical continuous layer of euhedral garnet crystals can be observed at the contact with the host rock, whereas the inner part of the vein consists of diopside-amphibole-quartz-calcite (Fig. 1b). These minerals do not show any preferred

orientation. Amphibole with little quartz is often found around diopside, is suggested to be a retrogression product.

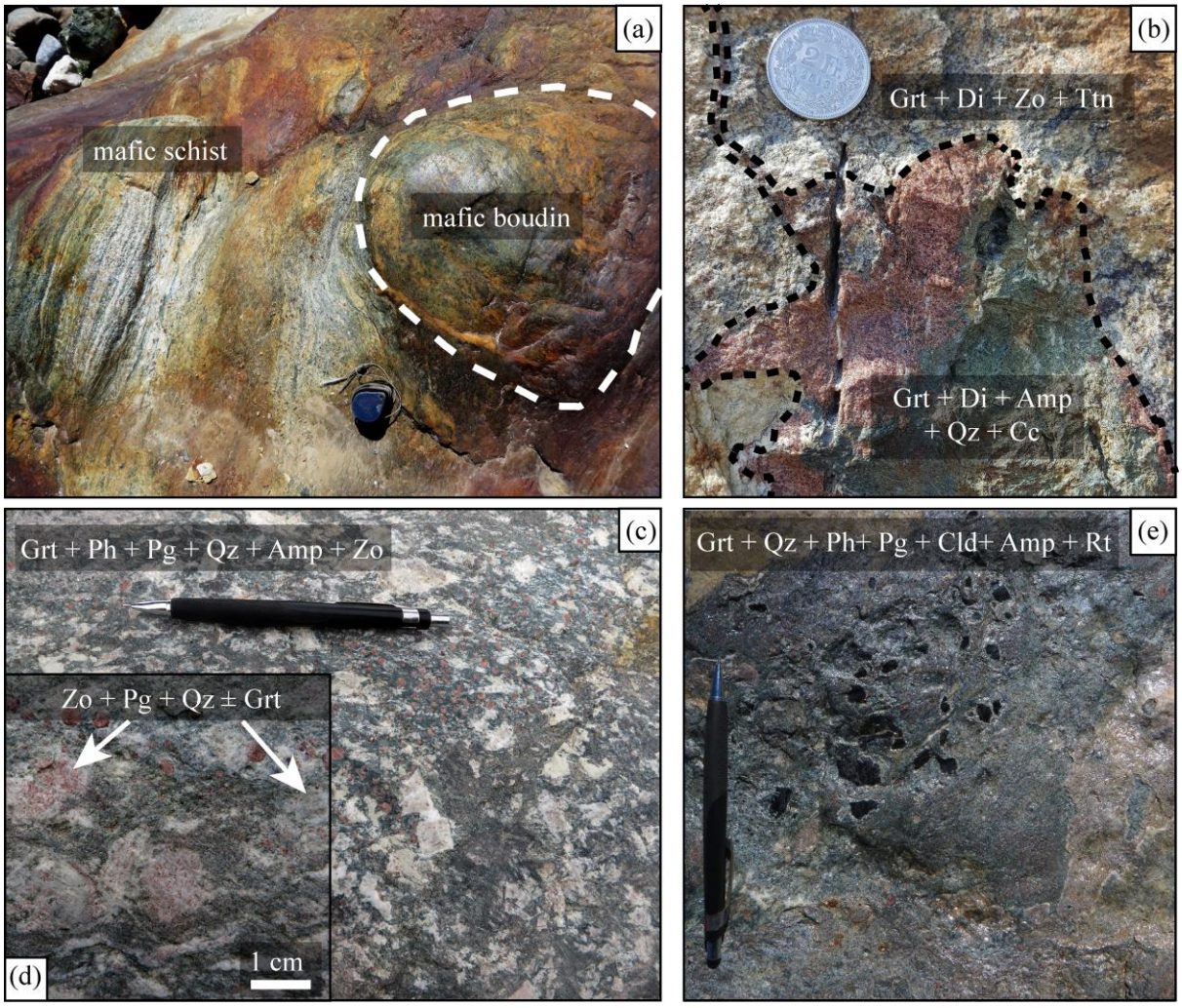

Figure 1: Field images of TGU lithologies. Mineral abbreviation are from Whitney and Evans (2010). (a) Mafic boudin wrapped by the foliation within mafic schist. The fine interlayering of the schist has various compositions (see text). (b) Vein within epidote-rich mafic fels. (c-d) Mafic schist with numerous relicts of lawsonite having the typical diamond shape. The detail (d) shows different types of lawsonite relict area, i.e. with and without garnet (see text). (e) Cld-schist with large flakes of chloritoid.

The mafic schist (sample Z16TB04, Z16TB11, Z16TB28) is banded and foliated, with layers that range from a few millimetres to a few metres in thickness (Fig. 1a). The common mineral assemblage is garnet-phengite-paragonite-quartz, whereas zoisite, chloritoid and amphibole complete this mineral association in various proportions. Chloritoid never exceeds 1-2 vol%, whereas garnet, zoisite and amphibole have highly variable abundance up to 70 vol%. Irregularly distributed lawsonite pseudomorphs (0 to 35 volume %) occur as milky euhedral diamonds of circa 0.5-2 cm in size, which are stretched along the main foliation (Fig. 1c). The pseudomorphs are filled with paragonite, zoisite and quartz, with rare garnet (Fig. 1d). Three main garnet populations were characterized. (i) Garnet clusters, composed of grains that are up to 200 µm in diameter. They are

either stretched along the main foliation or form continuous millimetre thick garnet-rich layers. (ii) Euhedral garnet grains, which size range between 200 and 700 µm in diameter. (iii) Euhedral garnet porphyroblasts with a typical diameter of 2 to 7 mm.

The Cld-schist shows a pervasive foliation and is primarily composed of quartz, phengite, paragonite, chloritoid, garnet, amphibole and rutile (sample Z16TB24A). Garnet grains are euhedral and equally distributed with an abundance of 20 vol%. The typical garnet diameter varies from 200 to 400 µm with episodic occurrences of atoll garnet.

Sample	Latitude	Longitude	Major phases	Minor phases	Description from
Mafic fels					
Z16TB32	45°58'9.66"N	7°42'42.84"E	Grt + Ep + Di + Amp	Qz + Ttn + Ap	Chapitre 2
Z17TB05	45°58'17.5"N	7°42'38.244"E	Grt + Di + Ep	Ttn + Gr + Py	Chapitre 3
Z17TB07	45°58'17.5"N	7°42'38.244"E	Grt + Di + Amp + Ep	Qz + Ttn + Cc + Chl	Chapitre 3
Z18TB15	45°58'20.9''N	7°42'34.8''E	Omp + Grt + Amp	Ep + Qz + Ph + Pg + Chl + Ap + Rt + Ttn	Chapitre 2
Mafic fels - vein					
Z17TB04A	45°58'17.5"N	7°42'38.244"E	Grt + Qz + Cc + Di + Amp	Chl	Chapitre 3
Z17TB05v	45°58'17.5"N	7°42'38.244"E	Grt + Di	Amp + Qz + Cc + Chl	Chapitre 3
Mafic schist					
Z16TB04	45°58'1.04"N	7°43'0.53"E	Grt + Ph + Pg + Chl + Amp	Ep + Rt + Ttn + Qz + Ab + Ap	Chapitre 3
Z16TB11	45°58'1.04"N	7°43'0.53"E	Grt + Qz + Ph + Pg + Amp + Ep	Chl + Ab + Rt + Ttn + Ap	Chapitre 2
Z16TB28	45°58'1.26"N	7°42'56.64"E	Grt + Ep + Chl + Qz + Ph	Ttn + Rt + Ab + Ap	Chapitre 2
Cld-schist					
Z16TB24A	45°57'54.72"N	7°43'4.62"E	Grt + Qz + Ph + Pg + Cld + Amp	Chl + Rt + Ttn	Chapitre 2

Ep = epidote group minerals.

Table 1: Sample list including geolocalisation and mineral assemblages.

4. ANALYTICAL METHODS

4.1. Electron probe micro-analysis and chemical mapping

Electron probe micro-analysis (EPMA) of garnet was performed using a JEOL JXA-8200 superprobe at the Institute of Geological Science, University of Bern. Spot analyses were performed using 15 keV accelerating voltage, 20 nA specimen current, and 40 s dwell time (10 s for each background after 20s on peak). Nine oxide components were obtained using synthetic and natural standards: almandine (SiO_2, Al_2O_3, FeO), albite (Na_2O), anorthite (CaO), orthoclase (K_2O), forsterite (MgO), ilmenite (TiO_2) and tephroite (MnO).

Quantitative compositional maps were generated from X-ray intensity maps using spot analyses acquired in the same area as internal standards. The X-ray maps were measured by WDS with 15 keV accelerating voltage and 100 nA specimen current, with various dwell time and resolutions. Nine elements (Si, Ti, Al, Fe, Mn, Mg, Na, Ca, K) were measured at the specific wavelength in two successive passes (with Na, Ca and K analyzed on the first scan). Compositional maps were processed using XMapTools 3.2.1 (Lanari et al. 2014, 2019). Representative compositions of each garnet and phengite growth zones were obtained by averaging pixels from manually selected

areas. The domains were chosen in a way to avoid any mixing between garnet generations and excluding mineral inclusions.

4.2. Oxygen isotopes

In situ oxygen isotope analysis of garnet was performed using a CAMECA SIMS 1280HR ion probe at the Institute of Earth Sciences, University of Lausanne. The analyses were carried out following the protocol detailed in Vho et al. (2020b) and using the primary standard UWG2 garnet ($\delta^{18}O$ = 5.80 ‰, Valley *et al.*, 1995). Count rates on the ^{16}O peak were between 1.2 and 2.0x10^9 counts per second. An off-line matrix bias correction based on the grossular and spessartine contents of garnet was applied using the equation given in (Vho et al. 2020c). In every session, the secondary garnet reference material GRS-JH2 (X_{grs} = 0.833 ± 0.008; Vho et al., 2020b) was analyzed to check the validity of the matrix bias calibration (Table S1). The $\delta^{18}O$ value obtained for the secondary reference material was systematically within the reference values reported in Vho et al. (2020b). The garnet chemical composition of each domain needed for matrix correction was taken from EPMA analyses acquired prior to SIMS analyses. The resulting matrix bias correction on the $\delta^{18}O$ of individual analyses ranges typically between 0.1 and 1.5 ‰, and is mainly or exclusively related to the grossular component. The internal uncertainty on individual oxygen isotopic analyses ranges between 0.14 and 0.30 ‰ (2σ), whereas the total uncertainty that includes the repeatability of the primary standard and the residuals on the matrix correction curve is 0.31 to 0.40 ‰ (2σ). Therefore, the final uncertainty on average values is forced to be no less than 0.3‰ to account for accuracy.

4.3. Forward modelling

Fluid-rock interaction during rock metamorphic history was investigated using the computer program PTLOOP (Vho et al. 2020a), which combines equilibrium thermodynamic calculations with oxygen isotopic fractionation modelling. The model performs successive Gibbs free energy minimizations computed using Theriak-Domino (De Capitani and Brown 1987; De Capitani and Petrakakis 2010) along a given *P*–*T* trajectory and calculates at each simulation step the oxygen isotopic fractionation between the mineral predicted to be stable. The model geometry was set to a two-rock stack with the possibility for any free fluid released by the underneath lithology to migrate and interact with the lithology situated above. As discussed in Vho et al (2020a), an additional external free fluid phase can be introduced in the lower lithology at any simulation step.

Oxygen isotopic variation among stable phases, bulk and free fluid was monitored using an internally-consistent database for oxygen isotope fractionation (Vho et al. 2019). Thermodynamic

modelling was based on the internally-consistent thermodynamic dataset of Holland and Powell (1998) and subsequent updates gathered in tc55. The chemical system was restricted to the system SiO_2-TiO_2-Al_2O_3-FeO-MnO-MgO-CaO-Na_2O-K_2O-H_2O-O_2. The following a-x relations for solid solutions phases were used: calcite-magnesite-dolomite (Holland and Powell 2003); feldspar (Holland and Powell 2003; Baldwin et al. 2005); spinel, biotite (White et al. 2007); epidote, cordierite, talc, staurolite, chlorite, carpholite and garnet (Holland and Powell 1998); clinopyroxene (Green et al. 2007); chloritoid (White et al. 2000); white mica (Coggon and Holland 2002); amphibole (Diener et al. 2007).

5. RESULTS

5.1. Garnet major element chemistry

The diverse TGU rock types contain garnet with a wide range of textures and chemical compositions. Some key garnet crystals from samples used in this study (mafic fels Z16TB32 and Z18TB15, mafic schist Z16TB11 and Cld-schist Z16TB24A) were already investigated for P-T modelling and geochronology in Chapter 2, yet additional grains and samples are considered here. Representative element maps are shown in Figure 2, 3 and 4. The end-member fractions of garnet for all samples and lithologies are summarized in Figure S2. Representative garnet compositions are presented in Table S2. Additional EPMA quantitative maps and BSE images are presented in the Figure S3, S4.

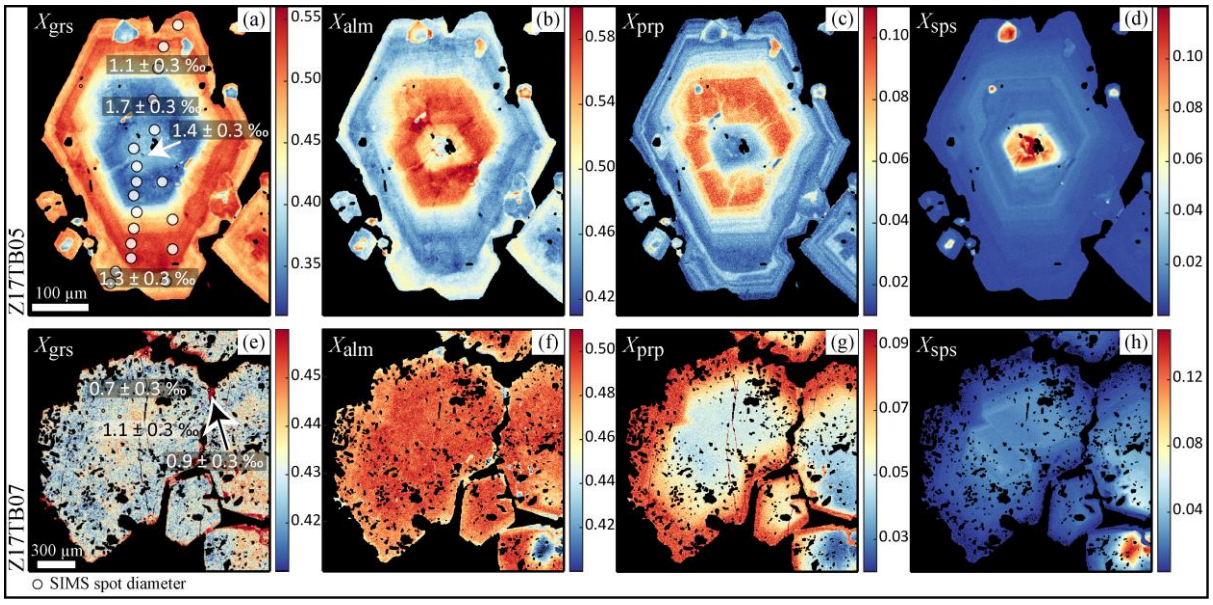

Figure 2: Representative compositional map of garnet from for the mafic fels samples showing garnet end-members (X_{grs}-X_{alm}-X_{prp}-X_{sps}), processed with XMapTools (Lanari et al. 2014, 2019). On the X_{grs} map, average garnet $\delta^{18}O$ values are superimposed with the location of SIMS spot analyses (white circles).

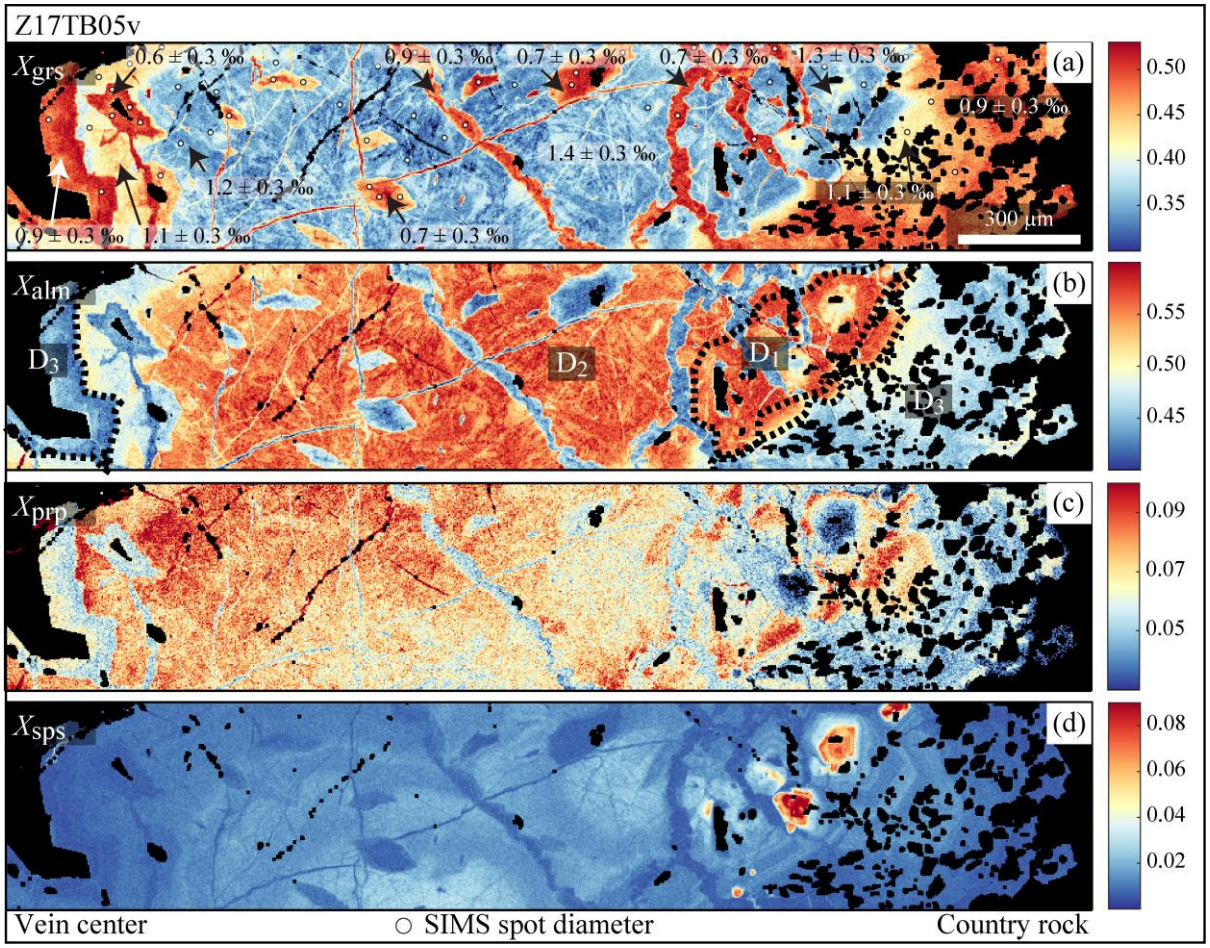

Figure 3: Representative compositional map of garnet from the vein showing garnet end-members (X_{grs}-X_{alm}-X_{prp}-X_{sps}). On X_{grs} map, average garnet $\delta^{18}O$ values are superimposed with SIMS spot analysis location (white circles).

Garnet cores from the mafic fels are systematically enriched in Mn varying from Sps_{14} (sample Z17TB07) up to Sps_{15} (sample Z18TB15). In samples Z16TB32, Z17TB05 and Z17TB07 three chemical domains can be recognised (Fig. 2). From core to mantle, both Fe and Mg concentrations (corresponding to X_{alm} and X_{prp} in Fig. 2) increase radially from the core towards the rim at the expenses of Ca (X_{grs}). A rather homogeneous garnet rim of maximum 150 µm thickness is marked by a decrease in Fe and Mg coupled with an increase in Ca compared to the inner domain. This transition between mantle and rim is discontinuous and can either be sharp or more gradual over a distance of 50 µm. In the core of garnet from mafic fels Z16TB32, zoisite inclusions are highlighted by diffuse Ca-rich halos (Fig. S4a,e). Major element zoning in sample Z18TB15 is similar to the previous samples except for Ca, which shows low Ca inner core, a mantle zone enriched in Ca and a low Ca rim. A discontinuous and distinct rim of 200–300 µm enriched in Mg and depleted in Mn, Fe and Ca is visible in part of the crystal (Fig. S4f-i).

Garnet crystals located at the contact between vein and metamafic boudin (samples Z17TB04A and Z17TB05v, Fig. 3) have more complex textures. The overall garnet chemical zoning

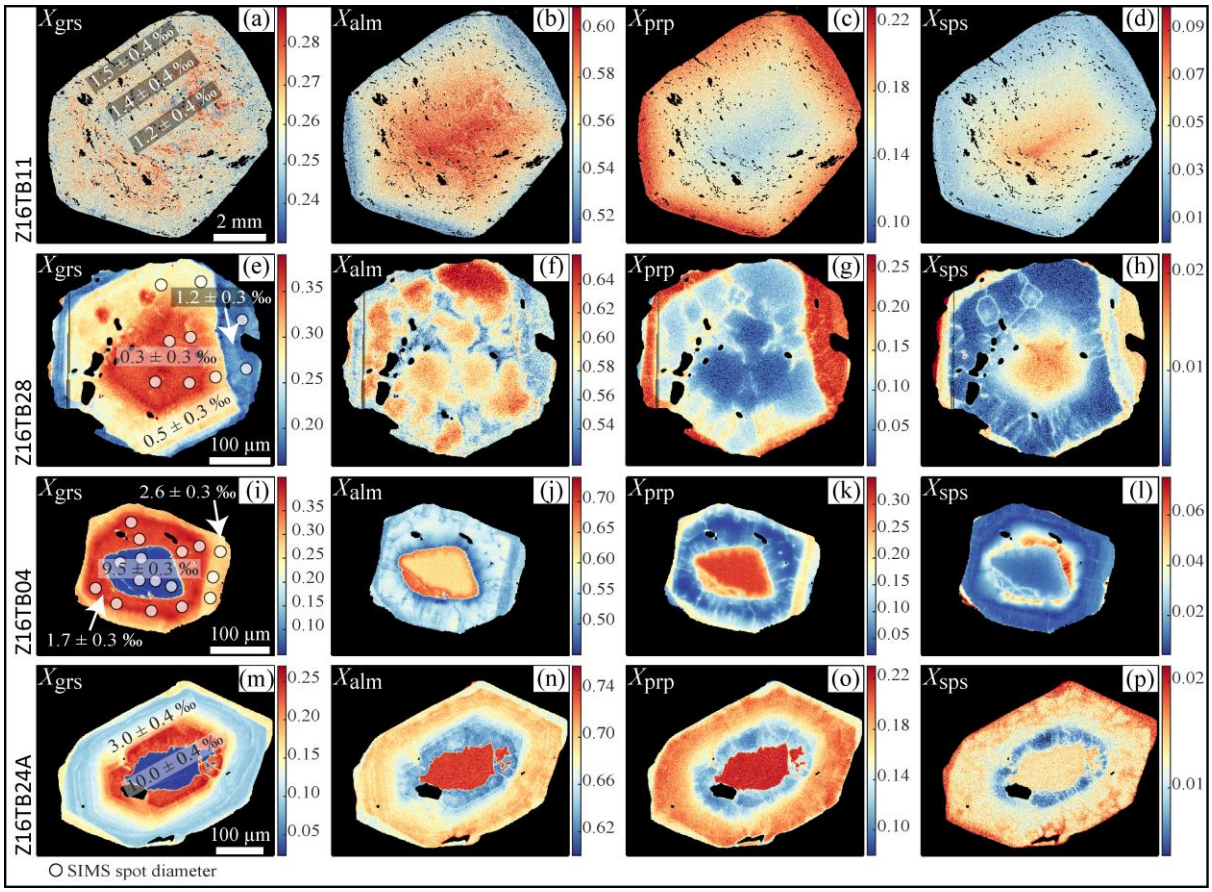

Figure 4: Representative compositional map of garnet from mafic schists (a-l) and the Cld-schist (m-p) showing garnet end-members (X_{grs}-X_{alm}-X_{prp}-X_{sps}). On X_{grs} map, average garnet $\delta^{18}O$ values are superimposed with SIMS spot analysis location (white circles). (a-d) sample Z16TB11, garnet porphyroblast. (e-h) sample Z16TB28, intermediate size garnet. (i-l) sample Z16TB04, small garnet. (m-p) sample Z16TB24A, garnet in the matrix.

variation from core to rim is comparable to garnet from the host rock (see above). Additionally, the first internal domain is characterized by Mn-rich areas with euhedral shape trailing parallel to the vein direction. This feature is probably reflecting loci of garnet nucleation localization at the time of vein formation (Hollister 1966). The domain D_1 (see Fig. 3b) is characterized by a rimward decrease in Mn and Ca, whereas Mg and Fe increase. Two garnet domains have symmetrically overgrown the first domain perpendicular to the vein direction. Compared to the first domain, in the second domain D_2, Fe decreases while Ca increases rimward. The last overgrowth corresponding to domain D_3 is wider on the host rock side and shows a dramatic increase in Ca coupled with a decrease in Mg, Fe and Mn. The transition between D_2 and D_3 is rather sharp, whereas Domains D_1 and D_2 are cross cut by discordant channels having the chemical composition of the garnet from D_3. They form a complex network or diamond-like shape islands (Fig. 3).

Garnet grains from the mafic schists (sample Z16TB04, Z16TB11 and Z16TB28) can be classified in three distinct types, which correlate with grain-size variation. Type I garnet consists of porphyroblasts having a diameter over 2 mm. These garnet have a continuous bell shape growth

zoning (Fig. 4a-d), where Fe, Ca and Mn contents decrease from core to rim at the expenses of Mg. Some garnet grains display irregularly distributed Ca-rich patchy areas ranging from 10 to 100 μm in size. Type II garnet forms grains with diameter between 200–700 μm (Fig. 4e-h). This garnet type shows a complex chemical zoning and has a highly variable texture with decoupling between major elements. Both Ca and Mn show similar zoning patterns with decreasing contents from core to rim. By contrast, Fe and Mg chemical zoning is more irregular and complex. A discordant and irregular rim of maximum 100 μm thickness is separated from the core by a sharp chemical transition over 1-3 μm. Compared to the garnet core, the rim is depleted in Ca and enriched in Mn and Mg. The chemical compositional range of this garnet type is similar to that of the garnet porphyroblasts (Fig. S2). Type III garnet consists of small grains (< 300 μm) and is characterised by a sharp (< 1 μm) and discordant core-rim texture (Fig. 4i-l). The xenomorphic core is enriched in Mg, Fe and Mn and depleted in Ca compared to the rim. Unequally distributed irregular Mn-rich zones occur along the contact within the garnet rim (Fig. 4l). The garnet rim has limited zoning with slight decreasing of Ca and Fe coupled with Mg increase. The core chemical composition ($Alm_{64-68}Prp_{23-27}Grs_{13-15}Sps_{1-3}$) of type III garnet is unique and is never observed for any type I and type II garnet (Fig. S2).

Garnet in the Cld-schist (sample Z16TB24a) has a zoning pattern and style that is similar to type III garnet in the mafic schist, with a discordant core-rim texture (Fig. 4m-p). Unlike the mafic schist, in the rim of this garnet Mn is depleted at the contact (compare Fig. 4l and 4p) and then increases outwards. The Mn zoning pattern of the mantle is cross cut by thin radial channel-like textures with rim composition. Additionally, a euhedral external rim of 15 μm thickness that is enriched in Ca and Mn and depleted in Fe and Mg is observed in the the Cld-schist garnet.

5.2. Oxygen isotope of garnet

The oxygen isotopic composition of garnet was measured in situ to identify variations in $\delta^{18}O$ associated to major element zoning. The results of $\delta^{18}O$ analysis are shown in Figure 5 plotted against X_{grs} garnet content as an indicator of chemical zoning. Individual oxygen isotopic measurements are presented in Table S1.

Garnet in the different mafic fels samples shows little variation in oxygen isotopic composition, without systematic zoning from core to rim, and consistently low $\delta^{18}O$ values (Fig. 2a,e). In the epidote-rich mafic fels sample Z16TB32, values of $\delta^{18}O$ are 0.9–2.3 ‰ in the core, 1.6–2.1 ‰ in the mantle and 1.2–2.9 ‰ in the rim. Similar $\delta^{18}O$ compositions were measured in the zoisite-rich mafic fels samples Z17TB05 and Z17TB07: values of $\delta^{18}O$ are 0.6–1.6 ‰ in the core, 0.3–1.8 ‰ in the mantle and 0.8–1.5 ‰ in the rim. Garnet in omphacite-bearing mafic fels sample Z18TB15 has $\delta^{18}O$ values of 0.9–1.2 ‰ in the core, 1.3–1.8 ‰ in the mantle, 1.2–1.4 ‰ in the rim

and 1.7–2.1 ‰ in the discontinuous rim. Within each sample, the range of $\delta^{18}O$ values for the garnet zones defined by major element zoning is overlapping.

Despite the complex chemical zoning, the $\delta^{18}O$ variations measured in the garnet from the vein within the mafic fels samples are small (Fig. 3a). In sample Z17TB04A the $\delta^{18}O$ ranges from 1.4 ± 0.4 ‰ in the core and mantle to 1.0 ± 0.4 ‰ in the rim and the discordant areas. Sample Z17TB05v displays comparable $\delta^{18}O$ values, where the core value of 1.4 ± 0.3 ‰ decreases to 0.9 ± 0.3 ‰ in both directions, i.e. toward the host rock and inner vein side. The cross-cutting domains show lower $\delta^{18}O$ values than the surrounding, but similar to the oxygen isotopic composition of the rim, with values ranging from 0.5 to 1.0 ‰. The extent of $\delta^{18}O$ value variation is in accordance with values of garnet from host rock (sample Z17TB05). In both samples, $\delta^{18}O$ values are similarly slightly decreasing from core to rim of around 0.4 ‰.

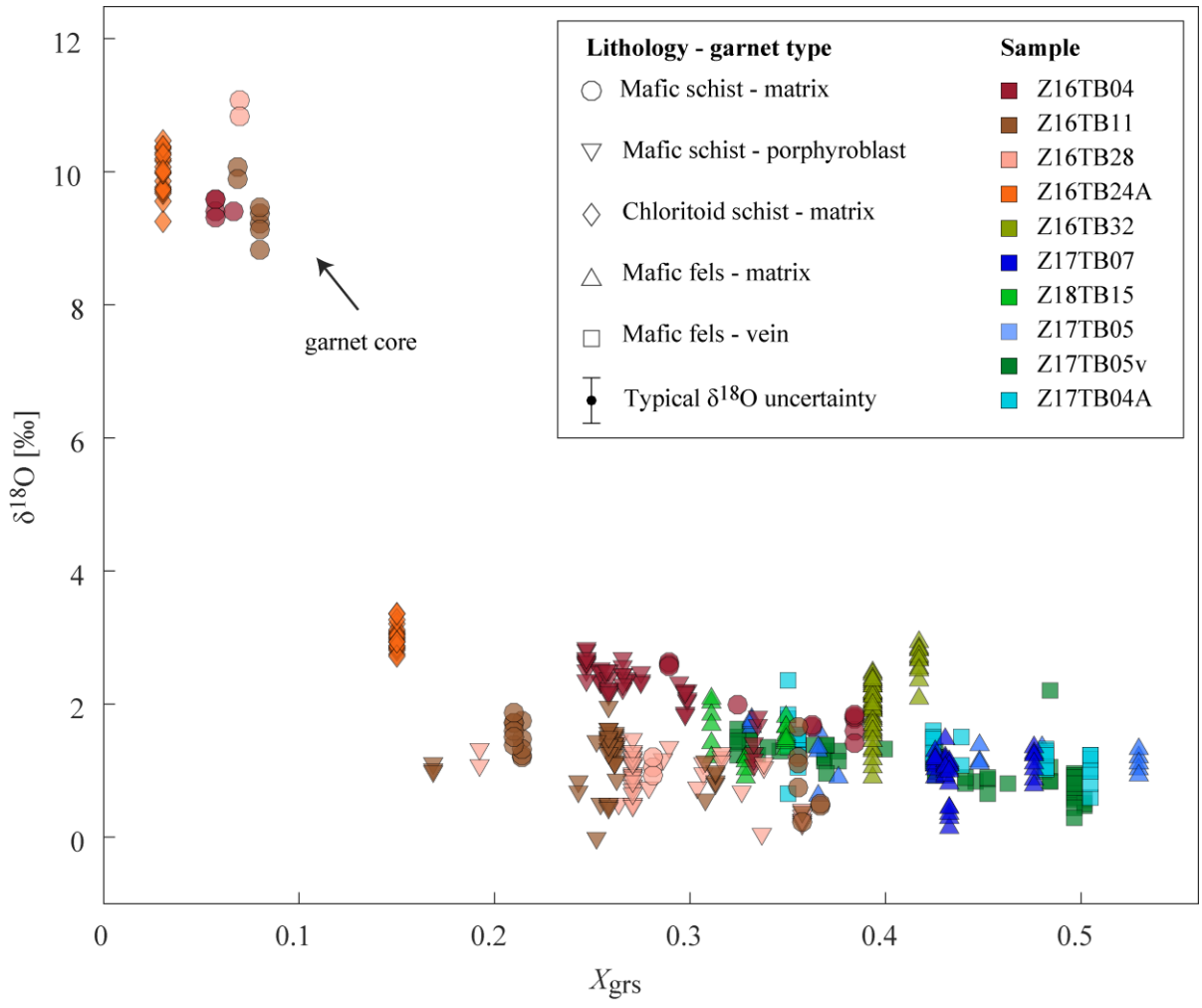

Figure 5: ***Binary diagram X_{grs} vs $\delta^{18}O$ for garnet. Garnet $\delta^{18}O$ composition was analyzed with SIMS. Garnet composition for matrix correction was taken from the chemical maps (see text). The uncertainty for X_{grs} is smaller than the symbol size, whereas the typical uncertainty for $\delta^{18}O$ is reported in the legend.***

The mafic schist is the most abundant lithology in the TGU and in every sample (Z16TB04, Z16TB11 and Z16TB28) the small garnet grains of type III show extreme oxygen isotope zoning from a high $\delta^{18}O$ core (8.8–11.1 ‰) to a low $\delta^{18}O$ rim (0.2–2.0 ‰). The step variation in $\delta^{18}O$ corresponds to the sharp chemical zoning defined by major elements (Fig. 4i-l). Within the rim itself, the Ca-rich inner part has slightly lower $\delta^{18}O$ values than the Mg-rich external part: from 1.7 ± 0.3 ‰ to 2.6 ± 0.3 ‰ in sample Z16TB04 and from 0.8 ± 0.3 ‰ to 1.5 ± 0.3 ‰ in sample Z16TB11. Type II garnet with intermediate size shows moderate $\delta^{18}O$ zoning with a slight $\delta^{18}O$ increase from core to rim (Fig. 4e), from 1.5 ± 0.3 ‰ to 2.3 ± 0.3 ‰ (Z16TB04), from 0.6 ± 0.3 ‰ to 1.0 ± 0.4 ‰ (Z16TB11) and from 0.2 ± 0.3 ‰ to 0.7 ± 0.3 ‰ (Z16TB28). The chemically discordant rim always shows equivalent $\delta^{18}O$ values to the adjacent rim within uncertainty, such as 2.0 ± 0.3 ‰ (Z16TB04), 1.0 ± 0.3 ‰ (Z16TB11) and 1.2 ± 0.3 ‰ (Z16TB28). Type I garnet porphyroblasts in every sample display homogeneous compositions from core to rim (Fig. 4a), with $\delta^{18}O$ values of 2.5 ± 0.3 ‰ (Z16TB04), 1.4 ± 0.4 ‰ (Z16TB11) and 1.0 ± 0.3 ‰ (Z16TB28). Garnet porphyroblasts and intermediate garnet grains rim have similar oxygen isotopic composition.

The $\delta^{18}O$ variation measured in garnet from the Cld-schist is considerable and comparable to what is observed in the mafic schist: a drop of about 7 ‰ from 10.0 ± 0.4 ‰ in the core to 3.0 ± 0.4 ‰ in the rim. Like garnet from the mafic schist (type III), the change in oxygen isotopic composition corresponds to the sharp chemical zoning (Fig. 4m-p).

6. DISCUSSION

6.1. Open system behavior and pervasive fluid flow during decompression

The *P*–*T* path followed by the TGU during Alpine subduction was constrained based on equilibrium thermodynamics (Fig. 6) (Chapter 2; Weber and Bucher 2015; Bucher et al. 2019). For the samples investigated here, the core of small garnet grains from the mafic schist (type III) and Cld-schist was modelled to be stable at 26.5 ± 1.5 kbar and 580 ± 15 °C, whereas the inner part of the rim is stable at 15.5 ± 1.0 kbar and 555 ± 10 °C (Chapter 2). The sharp chemical boundary between the high-pressure core and the moderate-pressure mantle corresponds to an equally sharp $\delta^{18}O$ drop of 7-9 ‰ from garnet core to rim. This sharp zoning is compatible with slow rates of oxygen intergranular diffusion (Vielzeuf et al. 2005; Page et al. 2019) and suggests that the original $\delta^{18}O$ composition of garnet core is preserved during exhumation and cooling. It has been demonstrated that, in a closed-system evolution over a temperature range of 150-200°C, dehydration reactions, fluid loss and mineral fractionation have only minor influence on the bulk rock $\delta^{18}O$ value (<1 ‰) and will not influence the $\delta^{18}O$ protolith signature (Kohn 1993; Vho et al. 2020a). Consequently, the magnitude of $\delta^{18}O$ variation observed in the small garnet grains can only be explained by ingress of

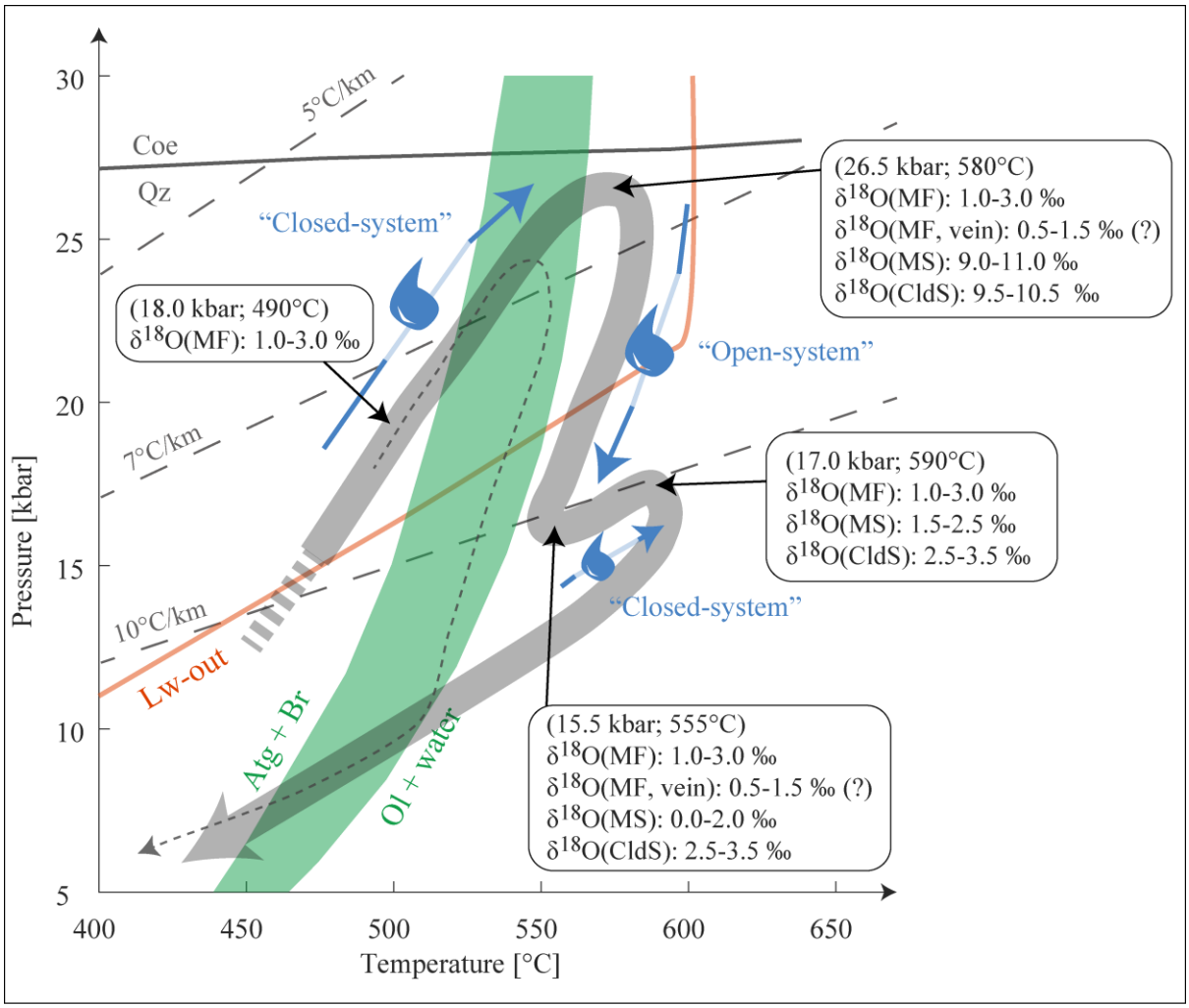

Figure 6: P–T–fluid path of the TGU modified from Chapter 2. Pressure-Temperature path of ZSZ is added as comparison (dashed lines; Angiboust et al., (2009)). The main steps of garnet growth according to Chapter 2 and corresponding $\delta^{18}O$ composition are specified. The $\delta^{18}O$ values are reported here as interval, because for each lithology one or multiple sample were analysed. Samples with (?) have a known $\delta^{18}O$ composition but unconstrained P-T growth conditions. The two potential external fluid sources are plotted: (1) Lawsonite-out reaction in mafic fels sample Z18TB15 simulated using Theriak-Domino (De Capitani and Brown 1987; De Capitani and Petrakakis 2010) assuming water saturation; (2) Atg+Br->Ol+water range from Johannes (1968). MS: mafic schist, MF: mafic fels, CldS: Cld-schist.

external fluids with low $\delta^{18}O$ values and in isotopic disequilibrium with the rock, during the TGU first decompression stage.

Garnet porphyroblasts found in the mafic schist are predicted to be stable during the reheating stage (from 15.5 ± 0.5 kbar and 555 ± 10 °C to 17.0 ± 1.0 kbar and 590 ± 15 °C, Fig. 6) that follows the initial decompression stage (Chapter 2). Both garnet porphyroblasts (type I) and intermediate garnet with complex textures (type II) display a homogeneous oxygen isotope composition. Their oxygen isotope signature is comparable to that of the rim of small garnet grains. This relative timing indicates that fluid-rock interaction associated to the drop in $\delta^{18}O$ occurred prior to the growth of the large garnet grains. Moreover, the small amount (~5 vol%) of relic high-$\delta^{18}O$

garnet core versus the widespread and high modal abundance (15-20 vol%) of the larger garnet grains suggest that the fluid at the origin of the $\delta^{18}O$ drop was pervasive and affected the entire tectonic unit. The mechanism that leads to the complex textures in the intermediate size garnet of type II is unclear (Fig. 4e-h), but it occurred after the ingress of low-$\delta^{18}O$ external fluid. The slight increase in $\delta^{18}O$ (0.3 – 0.9 ‰) from garnet core to rim in type II garnet could be attributed to the positive temperature variation during the reheating stage; a slight increase of ~0.1 ‰ in garnet is predicted with PTLOOP (Vho et al. 2020a).

In the mafic fels, garnet formed during the prograde and retrograde evolution of the TGU, and thus the outer rim was stable during the ingress of external fluid documented in the country rock schists (Fig. 6). Garnet from sample Z16TB32 recorded prograde (490 ± 10 °C and 17.5 ± 0.5 kbar) to peak pressure conditions (580 ± 10 °C and 26.5 ± 0.5 kbar), whereas garnet from sample Z18TB15 recorded both prograde (490 ± 10 °C and 17.5 ± 0.5 kbar) and the reheating stage occurring after the first decompression (590 ± 10 °C and 17.0 ± 0.5 kbar) (Chapter 2). All the garnet grains analyzed show similar $\delta^{18}O$ signature ranging between 1-3 ‰, indicating an unchanged $\delta^{18}O$ reactive bulk composition in the mafic fels throughout the entire TGU metamorphic history. The oxygen isotopic composition of the garnet from the mafic fels is equivalent to that of the garnet from the schists, excluding the core of the small garnet grains (type III). Because the prograde-to-peak garnet in the mafic fels already grew from a low $\delta^{18}O$ reactive bulk composition, it is impossible to track if this rock type also interacted with the low-$\delta^{18}O$ external fluid that affected the metasediments, despite the mafic fels exhibiting a hydrated assemblage with abundant epidote and amphibole.

Veins in metamorphic terrains are commonly interpreted as evidence for fluid flow along fractures, which develop when fluid pressure is close to lithostatic (Ferry 1994). The preserved anhydrous mineral paragenesis (garnet + diopside) observed in veins found within the TGU mafic boudin suggest vein formation during prograde metamorphism at eclogitic facies through devolatilization reactions (Schmidt and Poli 2003). The complex textures observed in garnet from the vein (Fig. 3) point to multiple episodes of garnet growth, associated to (hydro)fracturing and possibly dissolution-precipitation. Similar processes were documented in other high-pressure terranes (Angiboust et al. 2012; Giuntoli et al. 2018b, a; Rubatto et al. 2020; Vho et al. 2020b). Garnet likely grew in the presence of fluids but did not record significant variation of the reactive bulk $\delta^{18}O$ composition. This suggests that the fluids that fractured and partially dissolved the garnet in the vein were in (close) isotopic equilibrium with the rock. Subsequently, the formation of a hydrous retrograde assemblage, requiring more H_2O than available from the peak assemblage with amphibole and quartz around diopside, testifies to further rehydration during decompression.

6.2. Oxygen isotopic composition of the fluid-rock system and potential fluid sources

The reactive bulk oxygen isotopic composition of each sample can be reconstructed for a given temperature knowing the garnet $\delta^{18}O$ value, mineral modal abundances in equilibrium at temperature of garnet growth, and thermodynamic oxygen isotope fractionation factors among coexisting phases. Textural evidence combined with *P–T* data suggest, as discussed above, that the oxygen isotope shift in the mafic schist occurred during the first decompression stage. The original bulk rock $\delta^{18}O$ composition was thus calculated for each lithology at peak pressure conditions, before the ingress of external fluids (Table S3), using the software PTLOOP (Vho et al. 2020a) and the bulk rock compositions for major and minor elements (Table S4). The use of bulk rock chemistry for phase equilibrium modelling requires the assumption of minor or insignificant bulk chemical variations, outside water, during fluid-rock interaction (see discussion in Chapter 2). For the following calculations, a value of 1 ‰ is taken as average of the range of low $\delta^{18}O$ values measured in garnet from all rock types (0 to 3 ‰, Fig. 5).

An original bulk $\delta^{18}O$ composition of ~2 ‰ is calculated for the mafic fels in equilibrium with the measured garnet $\delta^{18}O$ of 1 ‰. Such low bulk $\delta^{18}O$ is below the MORB range (Taylor 1968; Muehlenbachs and Clayton 1972; Alt et al. 1986) but is typical for hydrothermally altered mafic oceanic crust (Cartwright and Barnicoat 1999; Miller et al. 2001; McCaig et al. 2007). Therefore, the relatively low bulk $\delta^{18}O$ values of the mafic fels could be ascribed to high-temperature seafloor alteration prior to Alpine metamorphism. A similar process affecting the schists would have equally decreased their original $\delta^{18}O$ of a few ‰ in the oceanic stage. For the mafic schist and Cld-schist, the calculated bulk $\delta^{18}O$ is ~11 ‰ based on the $\delta^{18}O$ of 9.5 ‰ of the garnet core. The bulk rock $\delta^{18}O$ composition of the schists corresponds to the lower side of the wide $\delta^{18}O$ range usually observed for metasediments and more specifically pelites (Rumble et al. 1982; Bebout and Barton 1989; Cartwright and Barnicoat 1999). On the other hand, a bulk rock with $\delta^{18}O$ of ~3 ‰ would be in equilibrium with in the low $\delta^{18}O$ garnet rim in the schists (Fig. S7, S8).

Similarly, the $\delta^{18}O$ value of the fluid in isotopic equilibrium with garnet at the time of fluid-rock interaction was calculated (Table S3), where fluid is considered as pure H_2O. Considering a temperature range of 580-555 °C, pure water with $\delta^{18}O$ of ~3.5 ‰ would be in equilibrium with the ~1 ‰ garnet rim from the schists (and coincidentally with the garnet from the mafic fels). This allows to conclude that the decrease in $\delta^{18}O$ in the schists was due to an external fluid with a $\delta^{18}O$ of ~3.5 ‰ or lower, as any partial equilibration with a fluid with lower $\delta^{18}O$ could produce the same garnet and bulk rock signature. The values for the corresponding reactive bulk rock composition and fluid in equilibrium with the garnet rim are the basis for reconstructing the potential fluid source and the fluid dynamics.

Fluid is commonly thought to be expelled during prograde metamorphism in subduction zones (Schmidt and Poli 2013), but it can also happen via retrograde dehydration reactions (Angiboust and Agard 2010). Slab material being exhumed towards the surface during retrogression, such as the TGU, is expected to interact with external fluid either expelled from structurally lower layers within the slab or from deeper down in the subduction system. Prior to subduction, TGU was a volcanoclastic sequence (Chapter 2; Bucher et al. 2020) and was stratigraphically the uppermost layer atop the magma-poor Piemont-Ligurian oceanic crust, now identified as the ZSZ metaophiolite. Considering the rock types involved and the geological relationships, the fluid that interacted with TGU rocks during early exhumation could be provided by two main mineral dehydration reactions (Fig. 6): (1) lawsonite-out within the TGU or ZSZ mafic rocks; (2) antigorite-out within the underlying hydrated ultramafic rocks (serpentinites) from the ZSZ. For these two scenarios, the reactions involved and the isotopic signature of the fluids are considered below.

(1a) Lawsonite-out dehydration reaction, in TGU. Lawsonite is a common metamorphic mineral at HP–LT conditions and contains 11.5 wt% H_2O in its structural formula, which makes it is one of the major water carriers in subduction zones (Schmidt and Poli 1998; Clarke et al. 2006). Preserved lawsonite is seldom observed in metaophiolites even though experimental work and modelling suggest that lawsonite eclogite should be an abundant rock type in oceanic subduction zones (Poli and Schmidt 1995; Clarke et al. 2006; Angiboust and Agard 2010). Instead, lawsonite is often retrogressed in epidote-rich aggregates during decompression and exhumation (Ernst and Dal Piaz 1978; Ballèvre et al. 2003; Angiboust and Agard 2010). Typical diamond shape relicts of lawsonite are commonly found in the TGU schists, but never in the mafic fels. However, this rock type contains various amounts (up to 70 vol% in sample Z17TB05) of epidote group minerals (Fig. 1b). Assuming water saturation and using the bulk rock chemistry presented in Table S4, a thermodynamic forward model of mafic fels at TGU maximum metamorphic conditions (580 °C, 26.5 kbar; Chapter 2) predicts lawsonite modal abundances between 9 vol% (sample Z18TB15) and 40 vol% (sample Z17TB05). During exhumation of the TGU, lawsonite breakdown reaction in the mafic fels (low $\delta^{18}O$ bulk) will release a H_2O fluid having the required $\delta^{18}O$ composition to change the bulk $\delta^{18}O$ in the TGU schists (see above).

(1b) Lawsonite-out dehydration reaction, in ZSZ. Lawsonite relicts have been described in the ZSZ metabasalts (Barnicoat and Cartwright 1995; Cartwright and Barnicoat 1999; Angiboust and Agard 2010) which have bulk rock $\delta^{18}O$ values from 4.4 to 9.2 ‰ (Barnicoat and Cartwright 1995; Cartwright and Barnicoat 1999). Such bulk rock compositions would produce fluids with even higher $\delta^{18}O$ values. As calculated above, the entering fluids in the TGU metasediments must have had a $\delta^{18}O$ value of 3.5‰ or lower. Therefore, the fluid released by lawsonite breakdown in the metabasic

rocks from the ZSZ during exhumation (Angiboust and Agard 2010) have a $\delta^{18}O$ values that is too high to be the fluid entering the TGU schists.

(2) Antigorite-out dehydration reaction. Subduction of serpentinized peridotite is the most efficient mechanism to carry water at depth (Scambelluri et al. 1995) and the most important dehydration reaction occurring in serpentinite is related to antigorite breakdown (Ulmer and Trommsdorff 1995; Schmidt and Poli 1998). Antigorite dehydration occurs through two subsequent dehydration reactions: (a) antigorite + brucite –> olivine + chlorite + water (Johannes 1968); (b) antigorite -> olivine + enstatite + water (Ulmer and Trommsdorff 1995; Padrón-Navarta et al. 2013). Reaction (a) occurs within the temperature range ~500-550 °C, which overlaps with the *P–T* history of the TGU (Fig. 6), whereas reaction (b) corresponds to the full antigorite breakdown that is predicted to occur at higher temperature (and pressure) in the downgoing slab. As a slow spreading setting, the Piemont-Ligurian oceanic lithosphere was harzburgitic and was largely hydrated at the ocean floor (Ernst and Dal Piaz 1978; Li et al. 2004; Dilek and Furnes 2011). Kempf et al. (2020) showed that harzburgite can contain from ~5 to 10 wt% brucite and reaction (a) would release between 3.4 and 7.2 wt% of water at 25 kbar. Literature data show that ultramafic rocks in the Alps have a wide range in $\delta^{18}O$, from 1 to 9 ‰ (Früh-Green et al. 1990, 2001; Cartwright and Barnicoat 1999; Miller et al. 2001). Serpentine-water $\delta^{18}O$ equilibrium calculations, using the fractionation factors of Vho et al. (2019), show that at 500 – 550 °C serpentine with a $\delta^{18}O$ of 2 ‰ is in equilibrium with water having a $\delta^{18}O$ value of 3.7 – 3.9 ‰. This value is comparable to the maximum $\delta^{18}O$ of the fluid entering the TGU metasediments (see above). Whereas there are no published values for the oxygen isotope composition of serpentinite adjacent to the TGU, serpentinites from Mellichen and Valtournanche, which are relatively near to the TGU, have bulk $\delta^{18}O$ values between 4.3 – 5.8 ‰ and 1.2 – 3.2 ‰, respectively (Cartwright and Barnicoat 1999). Serpentinites comparable to those outcropping in Valtournanche could thus represent a suitable source for fluid infiltrating the TGU rocks.

6.3. Quantitative fluid modelling

Modelling using the software PTLOOP (Vho et al. 2020a) was conducted in order to evaluate the validity of the two scenarios introduced above and results are shown in Table 2 and Figure S5, S6, S7, S8. A decompression *P–T* trajectory from 580 °C and 26.5 kbar to 555 °C and 15.5 kbar (Chapter 2) including 15 successive simulation steps was used. For each simulation step, the mineral paragenesis, $\delta^{18}O$ composition of stable phases, mass and $\delta^{18}O$ composition of excess fluid for the source rock are calculated. At every step of the simulation, the totality of free fluid predicted to be stable in the source rock is transferred to the overlying metasediment. After fluid influx, the mineral

paragenesis, $\delta^{18}O$ composition of stable phases, mass and $\delta^{18}O$ composition of excess fluid for the metasediment are calculated. Finally, the excess fluid from the metasediment is removed from the system before the next simulation step begins. Prior to run the simulation, the water content required for the observed paragenesis at maximum metamorphic condition was investigated. Pressure–temperature phase diagrams were calculated with associated pristine or fractionated bulk rock chemistry (Table S4), using the Theriak Domino software (De Capitani and Brown 1987; De Capitani and Petrakakis 2010). In every case, the best result was achieved with water saturation and this assumption was set as an input parameter in PTLOOP (Fig. S9a,d). The pervasive $\delta^{18}O$ resetting in the schists attests for fluid-rock interaction at the unit scale. The modelling is performed considering solely the mafic schist among the metasedimentary rock, because this is the main metasedimentary type observed within the TGU. For the simulation, the bulk rock chemistry of the mafic schist (Z16TB11) was adapted by fractionating 5 vol% of garnet core, considering that this garnet relict did not react at the peak stage (Table S4).

External fluid origin	Mafic schist (Z16TB11)	Mafic fels (Z18TB15)	Serpentinite 3.4 [wt%] water	Serpentinite 7.2 [wt%] water	Initial garnet $\delta^{18}O$ composition	Final garnet $\delta^{18}O$ composition	Fluid $\delta^{18}O$ composition	Time integrated fluid mass	Time integrated fluid flux
	[m]	[m]	[m]	[m]	[‰]	[‰]	[‰]	[kg]	[cm^3/cm^2]
Mafic fels (Z18TB15)	100*	10*	-	-	9.5	9.3	3.5	161	0
Mafic fels (Z18TB15)	100*	150000*	-	-	9.5	1.1	3.5	2419727	242701
Serpentinite	100*	-	11765	5556	9.5	1.1	3.5*	1100000*	110331

* are input parameters

Table 2: Input and output values from PTLOOP simulations to evaluate the fluid origin and reconstruct the time integrated fluid flux.

on top of 10 m of mafic fels. The thickness ratio between the mafic fels and the mafic schist was estimated based on field observations, where the lithologies have a subhorizontal stacking (Weber and Bucher 2015). The bulk chemical composition of mafic fels Z18TB15 was chosen because it is the most common type of mafic fels found in the TGU. Results (Table 2) show that water expelled from the mafic fels and infiltrating the mafic schist has a $\delta^{18}O$ signature of 3.5 ‰ for a total integrated mass of 161 kg of H_2O. This corresponds to a fluid rock mass ratio of ~5.8×10^{-4} assuming a rock density of 2,800 kg/m^3. Infiltration of this amount of fluid into the mafic schist produces only a minimal shift in garnet $\delta^{18}O$ composition from 9.5 ‰ to 9.3 ‰, which is not enough to match the observed shift. In order to achieve the garnet oxygen isotopic composition of ~1 ‰ (thus -8.5‰ shift), the mafic schist/mafic fels volume ratio has to be set to an unrealistic value of 1:1,500 (Table 2), which is not in line with the proportion of each rock type observed in either the TGU, or in the ZSZ. Therefore the mafic fels alone cannot produce enough fluid to explain the observed $\delta^{18}O$ shift.

The second scenario considers external fluid coming from the serpentinite (a rock column of 100 [m] x 1 [m] x 1 [m], row 3 in Table 2) and infiltrating directly the metasediment. This procedure allows an exact evaluation of the quantity of external fluid needed to shift garnet $\delta^{18}O$ composition from ~9.5 to 1 ‰, and the bulk rock accordingly. The external fluid $\delta^{18}O$ composition was set at 3.5 ‰, which is in isotopic equilibrium with the mafic fels and with the range of $\delta^{18}O$ measured in the Valtournanche serpentinites (Cartwright and Barnicoat 1999). The ingress of serpentinite-derived fluid was spread over several successive batches to simulate a limited continuous fluid flow. In order to produce the observed dramatic shift of -8.5 ‰ in garnet and bulk rock, 1.1 x 10^6 kg of H_2O from the serpentinite is required to enter the system (Table 2). This corresponds to a fluid-rock mass ratio of ~3.9 assuming a host rock density of 2800 kg/m^3. Given that serpentinite of the composition of the ZSZ release from 3.4 to 7.2 wt% water through the reaction antigorite + brucite –> olivine + chlorite + water (Kempf et al. 2020), a 5.6 to 11.8 km thick layer of hydrated ultramafic crust (density of 2750 kg/m^3) is required below the metasediments in order to produce the necessary amount of fluid. Hydration of the oceanic lithosphere commonly occurs in the first two kilometres, but partial hydration could reach greater depth of ~10 km, particularly in slow-spreading ridges (Schmidt and Poli 1998; Baumgartner and Valley 2001; Früh-Green et al. 2001; Angiboust and Agard 2010; Dilek and Furnes 2011). Additionally, the TGU is volumetrically small compared to the underlying oceanic lithosphere exposed in the ZSZ and serpentinite-derived fluids could be sourced from a larger area. Therefore, the serpentinite are identified as a suitable source for the fluids in terms of isotopic signature and availability.

6.4. Pervasive flow, time-integrated fluid flux, rock permeability

Channelized fluid-flow is regarded as the representative mechanism for intra-slab fluid flow (Miller et al. 2001; Scambelluri and Philippot 2001; Hermann et al. 2006; Zack and John 2007; Ague 2011; Spandler et al. 2011). However, in some parts of subducting slabs, important fluid release could be pervasive over large distances (Früh-Green et al. 1990; Oliver 1996; Scambelluri and Philippot 2001; Spandler et al. 2003; Vho et al. 2020b). This latter behaviour is favoured in units with monotonous rheology and permeability (Oliver 1996). In the TGU schists, the decrease in $\delta^{18}O$ from garnet cores at 9 – 11% to values that converge at 0 – 3‰ (Fig. 5) testify for pervasive fluid flow across a 2000 x 100 m tectonic unit during HP metamorphism. This is unlike the scenario proposed by studies that describe small-scale channelized fluid flow in veins and shear zones, whereas the country rock shows a “closed-system” behaviour (Zack and John 2007; John et al. 2012). The time-integrated fluid flux corresponds to the total amount of external fluid influx that passes across an area of interest during a given time interval (Ague 2003). Fluid channelization processes strongly

impact time-integrated fluid fluxes (Fig. 7). It has been proposed by Zack and John (2007) that at subarc depth, the time-integrated fluid flux of the H_2O escaping the subducting oceanic crust regarded as pervasive fluid flow is ~3.4 x 10^4 cm^3/cm^2. The effect of structural features that concentrate fluid flow, such as veins or ductile shear zones, will increase the time-integrated fluid flux of a factor 10 to 100 in these areas and consequently deprive the surrounding areas of fluid (Ague 2003; Zack and John 2007). However, quantification of time-integrated fluid-flux in subduction zone at the slab-mantle interface for open system associated to pervasive flow remains poorly documented. This is because open-system behaviour can only be traced in the rare cases where the fluid conduits or zones are preserved and exposed to the surface where they become accessible to investigation (Zack and John 2007); the TGU offers this rare opportunity.

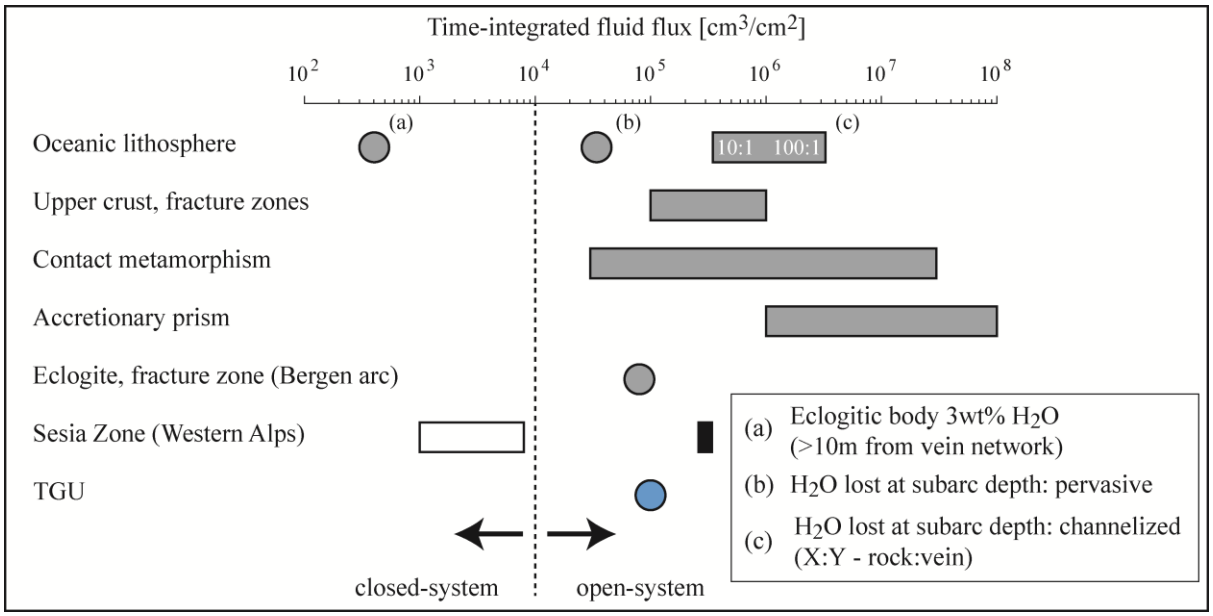

Figure 7: ***Time-integrated fluxes in different geological environment (modified from Zack and John, 2007). Circles represent punctual value, whereas rectangles represent range of analyses. The boundary between open and closed system is from Oliver (1996). Fluid fluxes for oceanic lithosphere (a) eclogitic body is from Zack and John (2007), (b) pervasive H_2O flow at subarc depth is deduced by Zack and John (2007) using data from Schmidt and Poli (1998), and (c) channelized H_2O flow at subarc depth is from Zack and John (2007), where flux intensity is inversely proportional to the vein density. Fluid fluxes for: upper crust is from Ferry and Gerdes (1998), for contact metamorphism is from Ague (2003), accretionary prism is from Ague (2003), eclogite fracture zone is from Philippot and Rumble (2000), and Sesia Zone: white rectangle is from Konrad-Schmolke et al. (2011), and black rectangle is from Vho et al. (2020b).***

be deduced from the total amount of fluid expelled from the serpentinite that interacted with the TGU (water density of ~10^3 kg/m^3) and corresponds to 1.1 x 10^5 cm^3/cm^2 (Table 2). This value represents a conservative estimate, because a fraction of the fluid could pass through the system without reacting with the rock (Zack and John 2007). This result is above the time-integrated fluid flux threshold value of 1 x 10^4 cm^3/cm^2 defining open-system behaviour (Ferry and Dipple 1991;

Dipple and Ferry 1992; Oliver 1996), beyond which a major tracer, like oxygen isotopes, is affected by infiltrating aqueous reactive fluid (Fig. 7).

The time integrate fluid flux in the TGU can be compared to values proposed for the high pressure continental unit of the Sesia Zone (Western Alps), which underwent a *P–T* evolution similar to the TGU (Compagnoni 1977; Gosso 1977) and was affected by pervasive rehydration during exhumation (Konrad-Schmolke et al. 2011). Time-integrated fluid flux calculated for the Sesia Zone by Konrad-Schmolke et al. (2011) are 1.5 – 7.5 x 10^3 cm^3/cm^2. Such values cannot be classified as open-system behavior according to the definition of Oliver (1996) and are comparable to the time-integrated fluid flux of dehydrated eclogites (5 x 10^2 – 5 x 10^3 cm^3/cm^2) situated away from channelization drainage (Zack and John 2007). By contrast, Vho et al. (2020b) calculated a time-integrated fluid flux for the Sesia Zone (1.7 – 2.2 x 10^5 cm^3/cm^2) that is above the threshold value for open-system behaviour. Likewise, systems such as fracture zones in eclogite (Philippot and Rumble 2000), upper crustal fracture zones (Ferry and Gerdes 1998), contact metamorphic aureoles and accretionary wedges (Ague 2003) typically have higher time-integrated fluid fluxes of >10^4 cm^3/cm^2. The above estimates suggest a diversity of fluid fluxes at the slab-mantle transition zone (Konrad-Schmolke et al. 2011).

Fluid migration can operate along significant distances in the subduction channel (John et al. 2012) and needs highly interconnected porosity to act efficiently (Ague 2003). Rock permeability is a critical hydrologic parameter, which determine the ability of a fluid to migrate through the rock (Manning and Ingebritsen 1999). Parameters taken in account to calculate rock permeability are mostly integrated with respect to time, because fluid-rock interaction take place throughout a discrete time window and must have been sufficient to accommodate fluid flow recorded by the exhumed metamorphic rocks (Manning and Ingebritsen 1999; Ague 2003). Rock permeability can be calculated as follow (Ingebritsen and Manning 1999; Manning and Ingebritsen 1999):

$$k = \frac{Q\mu}{\Delta t\ g\ (\rho_{rock} - \rho_{fluid})} \quad (1)$$

where Q is the time integrated fluid flux (m^3/m^2) (Table 2), μ is the fluid viscosity (~1 x 10^{-4} Pas at 550°C for water), Δt is the duration of fluid flow in seconds, g is the gravitational force equivalent (9.81 ms^{-2}), ρ_{rock} the rock density (2800 kgm^{-3} for metasediments), ρ_{fluid} the fluid density (997 kgm^{-3} for pure water). In the deep crust, the maximum fluid pressure are approximatively lithostatic and for vertical upwards fluid flow path the driving-force gradient is approximated by $g\cdot(\rho_{rock} - \rho_{fluid})$, which is the difference of the lithostatic pressure and hydrostatic pressure (Manning and Ingebritsen 1999; Ague 2003). In the case of the TGU, the duration of fluid-rock interaction is not well constrained, but most geochronological data for HP metamorphism in the ZSZ are within a few million years (e.g. Dragovic et al., 2020). Therefore, a time parameter Δt between 1 and 10 Ma was

considered: this leads to permeability variations of a factor 10, where longer duration will decrease the permeability (Fig. 8).

The calculated permeability of the TGU metasediment according to equation (1) is 2 x 10^{-20} m^2 for 10 Ma of external fluid influx and 2 x 10^{-19} m^2 for 1 Ma (Fig. 8). An alternative way to calculate permeability is using the empirical formula that relates permeability with depth: log k = -14-3.2 log(z), where z is the depth in kilometres (Manning and Ingebritsen 1999; Ingebritsen and Manning 2010). The permeability calculated with formula (1) for the TGU matches the empirical value at 60 km depth for the 10 Ma scenario, or at 30 km depth for the 1 Ma case (Fig 8). Simulations indicate that fluid-rock interaction in the TGU occured between 26.5 and 15.5 kbar. Using a typical continental crust rock density of 2800 kg/m^3 this corresponds to a depth range of 95 and 55 km depth and favours a scenario lasting at least 8 Ma (Fig. 8). The calculated permeability can be compared to data from experimental studies conducted at similar pressure (Fig. 8). Our result is higher than the impermeable zone set at a permeability below 10^{-21} m^2, but comparable to the permeability of blueschists and deformed antigorite serpentinite, whereas Atg-serpentinite and chlorite schist show lower permeabilities (Kawano et al. 2011; Ganzhorn et al. 2019). Moreover, petrographic and stable isotope data from Alpine ophiolite (Platta nappe) seem to indicate lower permeabilities in serpentinites over metasediment during Alpine metamorphism (Früh-Green et al. 1990). Contrasts in permeability are known to constrain fluid paths (Ague 2003; Connolly 2010). Similar to lower permeability in the mafic schist compared to the deformed serpentinite might have promoted direct fluid transfer from the serpentinites of the ZSZ to the metasediments of the TGU with respect to less permeable lithologies such as the mafic fels. This scenario does not exclude that higher flux fluxes occur in veins and shear zones, but rather indicates that significant fluid fluxes are pervasive throughout the HP mafic schists with sufficient permeability to accommodate the flow recorded by the exhumed metamorphic rocks (Manning and Ingebritsen 1999).

6.5. Fluid flow initiation

Volume variations caused by mineral reactions in the different lithologies of the TGU were investigated to assess fluid flow initiation from the serpentinite of the ZSZ towards the schists of the TGU. Rock volume variation in the TGU mafic fels sample Z18TB15 and mafic schist Z16TB11 was modelled using Theriak-Domino (De Capitani and Brown 1987; De Capitani and Petrakakis 2010). Water saturation is assumed at maximum metamorphic condition and free fluid is not allowed to exit the system. As no evidences of fluid-rock interaction were observed along the prograde path

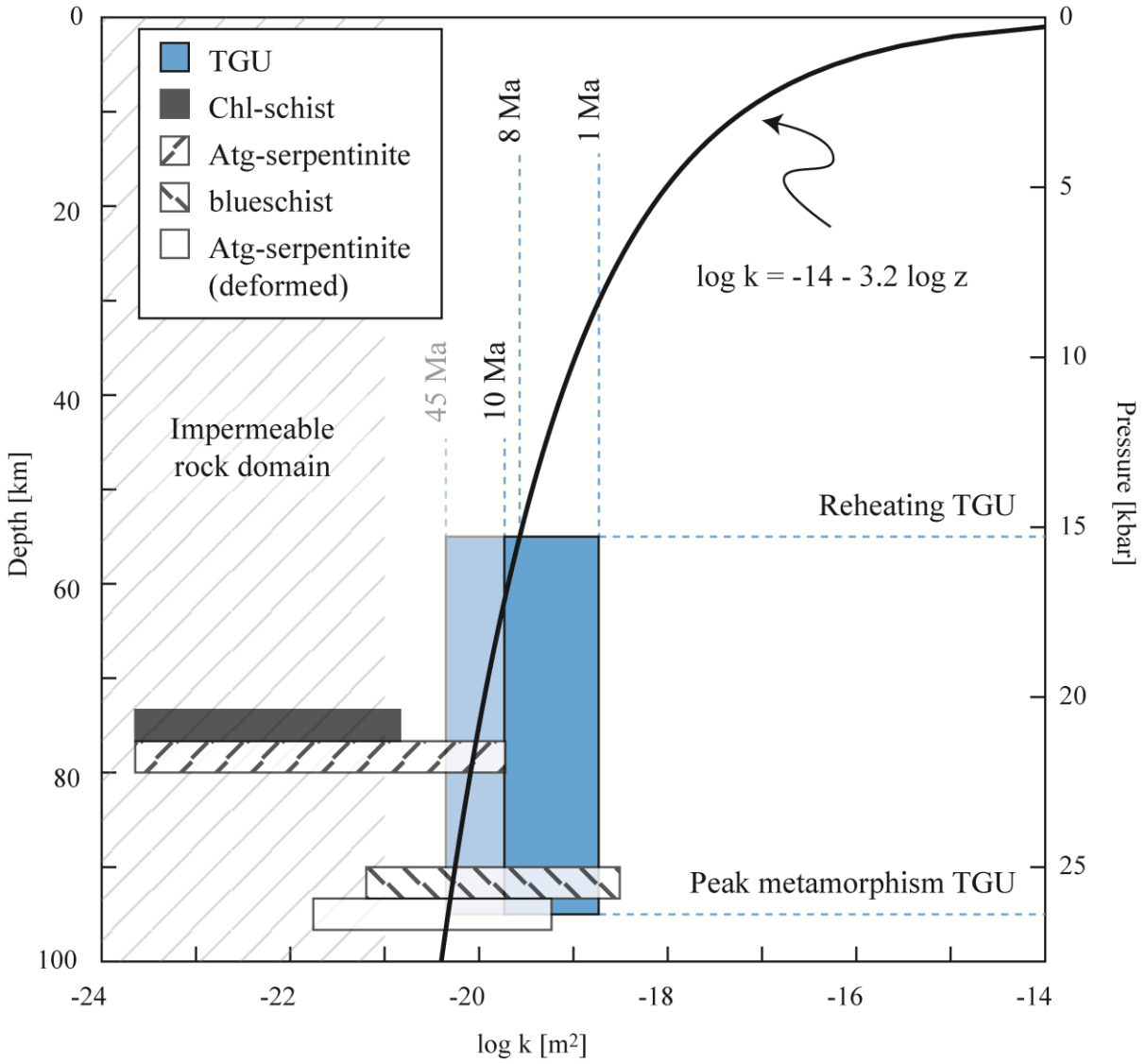

Figure 8: Evolution of permeability with depth compared to results for this study. Empirical formula (bold line) from Ingebritsen and Manning (1999). Grey shaded squares are different rock permeabilities from experiments on ultramafic rocks (Ganzhorn et al. 2019). Impermeable rock domain (hatched area) from Ganzhorn et al. (2019).

(Fig. 6), simulations were consequently focused on the early stage of decompression from 580 °C and 26.5 kbar to 555 °C and 15.5 kbar. We defined the cumulative rock volume variation as:

$$V_{cumulative,i} = \left(\frac{V_i - V_{i-1}}{V_0} + V_{cumulative,i-1}\right) \times 100, where\ V_{cumulative,0} = 0\ and\ i\ \in \mathbb{N} \quad (2)$$

Where *i* corresponds to a specific iteration step along the retrograde path and V_0 is the volume at maximum pressure taken as a reference. Results plotted against pressure show an overall absolute volume increase of ~4 % along the exhumation path for both lithologies (Fig. 9). Localized volume variations of various magnitude are associated to mineral reactions and occurs at different iterative steps (i.e. P and T) in each lithologies (Fig. 9a-d). Interestingly, negative volume variation in both rock types is associated to lawsonite dehydration reaction (Fig. 9, Fig. S9). Following the exhumation path, this reaction is predicted to occur first in the mafic fels at ~20.0 kbar and later on

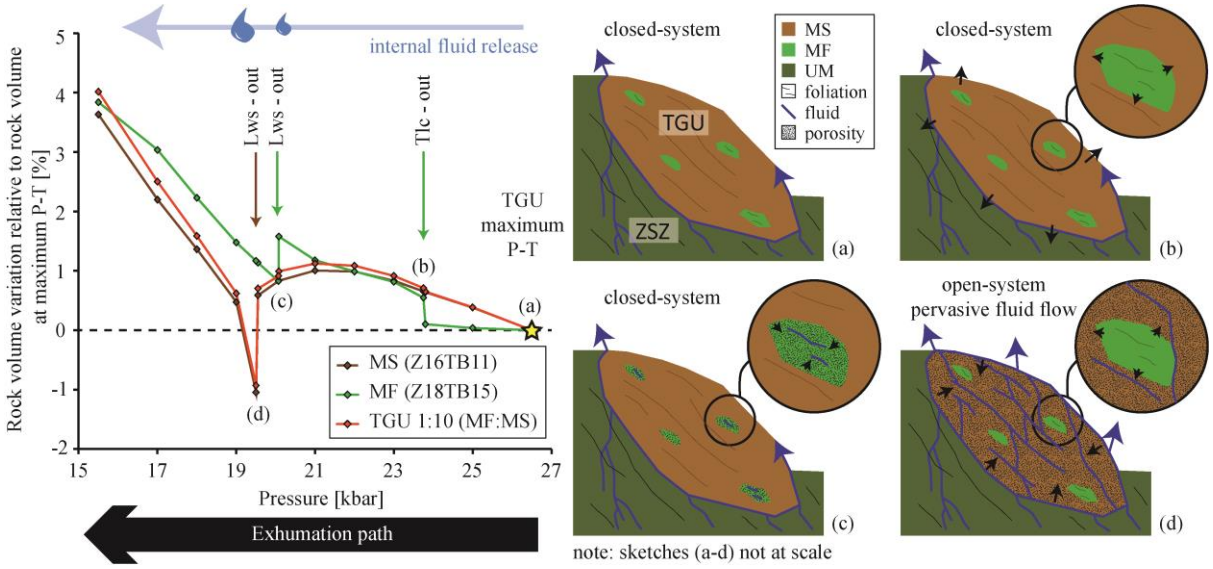

Figure 9: Cumulative volume variation for selected TGU rock types plotted along the TGU retrograde metamorphic path. Main volume variations are related to hydrous phases breakdown (see details in text). Sketches on the right (a-d) are a representation of the system at the point of hydrous phases breakdown during TGU exhumation. Sketches are not to scale and represent the volume (small black arrows) and porosity (textures) variation of the different lithologies from the TGU and the effect on fluid-rock interaction. Fluid flow is represented by blue lines with arrows indicating the direction of flow. MS: mafic schist, MF: mafic fels, UM: ultramafic.

in the mafic schist at ~19.5 kbar, where the rock volume variation is ~1 % in the mafic fels and ~2 % in the mafic schist, respectively. Mafic fels from the TGU are not in contact with the ZSZ (Fig. S1) and show no evidence for external fluid input. Consequently volume variations in the mafic fels will not perturb the overall fluid flow dynamic during fluid transfer between serpentinite and the schist. Moreover, field observations show that the numerous occurrences of mafic boudins within the schists are not interconnected. This discards the possibility of fluid infiltration within the TGU along structural features, such as lithological contacts or boudins necking (Fig. 9c) (Ague 2003).

The TGU is mainly composed of mafic schist, and its significant absolute volume variation is assumed to have a major impact on the fluid flow dynamic within the tectonic unit (Fig. 9d). Negative volume changes associated to mineral reactions are known as an efficient mechanism to develop transient micro-porosity (Rumble and Spear 1983; Oliver 1996; Balashov and Yardley 1998; Ague 2003). Such an event will create short-lived excess permeability needed to let external fluid coming-in and initiate fluid flow. Therefore lawsonite breakdown in the mafic fels is not a major fluid source in the $\delta^{18}O$ budget due to its negligible rock volume, but lawsonite breakdown in the schist is rather a key reaction for the onset of fluid flow from the serpentinites towards the TGU metasediments.

7. CONCLUSIONS

This study identifies the large amounts of low $\delta^{18}O$ fluid generated from antigorite + brucite breakdown reaction in the ZSZ serpentinites as the major origin for the external fluid that interacted pervasively with the schists of TGU during exhumation between 26.5 and 15.5 kbar in the subduction channel. TGU mafic fels rocks have no $\delta^{18}O$ evidence for an external fluid input and simulations show that they play only a minor role in the $\delta^{18}O$ budget of the TGU. Serpentinites from the ZSZ would have the right oxygen isotopic composition to produce the low $\delta^{18}O$ fluid that infiltrated the TGU rocks. In the mafic fels, the low bulk $\delta^{18}O$ signature of all garnet generations, including those grown during prograde metamorphism, suggests a pre-metamorphic lowering of the bulk rock $\delta^{18}O$, probably through seafloor alteration.

The time-integrated fluid flux calculated for fluid-rock interaction at HP in the TGU falls in the range of open-system behavior. In HP environments, such large fluid fluxes are usually attributed to channelized fluid-flow or fracture zone and seldom for pervasive fluid flow as that documented in the TGU. The calculated permeability for the TGU schist during fluid-rock interaction at depth is comparable to values from experimental and empirical studies. Transient rock volume variation associated to lawsonite-out reaction in the schist of the TGU are interpreted to have initiated fluid transfer between the TGU and the surrounding ultramafic rocks from the ZSZ.

ACKNOLEDGEMENTS

We are grateful to J. Hermann and E. Kempf for insightful discussion. We thank A.-S. Bouvier and G. Siron for their help with the laboratory work and A. Vho for expert guidance in oxygen isotope modelling.

BIBLIOGRAPHY

Agard P, Yamato P, Jolivet L, Burov E (2009) Exhumation of oceanic blueschists and eclogites in subduction zones: Timing and mechanisms. Earth-Science Rev 92:53–79. https://doi.org/10.1016/j.earscirev.2008.11.002

Ague JJ (2003) Fluid Flow in the Deep Crust. In: Treatise on Geochemistry. pp 195–228

Ague JJ (2011) Extreme channelization of fluid and the problem of element mobility during Barrovian metamorphism. Am Mineral 96:333–352. https://doi.org/10.2138/am.2011.3582

Alt JC, Muehlenbachs K, Honnorez J (1986) An oxygen isotopic profile through the upper kilometer of the oceanic crust, DSDP Hole 504B. Earth Planet Sci Lett 80:217–229. https://doi.org/10.1016/0012-821X(86)90106-8

Amato JM, Johnson CM, Baumgartner LP, Beard BL (1999) Rapid exhumation of the Zermatt-Saas ophiolite deduced from. Earth Planet Sci Lett 171:425–438

Angiboust S, Agard P (2010) Lithos Initial water budget : The key to detaching large volumes of eclogitized oceanic crust along the subduction channel ? LITHOS 120:453–474. https://doi.org/10.1016/j.lithos.2010.09.007

Angiboust S, Agard P, Jolivet L, Beyssac O (2009) The Zermatt-Saas ophiolite: The largest (60-km wide) and deepest (c. 70-80km) continuous slice of oceanic lithosphere detached from a subduction zone? Terra Nov. https://doi.org/10.1111/j.1365-3121.2009.00870.x

Angiboust S, Langdon R, Agard P, et al (2012) Eclogitization of the Monviso ophiolite (W. Alps) and implications on subduction dynamics. J Metamorph Geol 30:37–61. https://doi.org/10.1111/j.1525-1314.2011.00951.x

Angiboust S, Pettke T, De Hoog JCM, et al (2014) Channelized fluid flow and eclogite-facies metasomatism along the subduction shear zone. J Petrol 55:883–916. https://doi.org/10.1093/petrology/egu010

Balashov VN, Yardley BWD (1998) Modeling metamorphic fluid flow with reaction - compaction - permeability feedbacks. Am J Sci 298:441–470

Baldwin JA, Powell R, Brown M, et al (2005) Modelling of mineral equilibria in ultrahigh-temperature metamorphic rocks from the Anápolis-Itauçu Complex, central Brazil. J Metamorph Geol 23:511–531. https://doi.org/10.1111/j.1525-1314.2005.00591.x

Ballèvre M, Pitra P, Bohn M (2003) Lawsonite growth in the epidote blueschists from the Ile de Groix (Armorican Massif, France): A potential geobarometer. J Metamorph Geol 21:723–735. https://doi.org/10.1046/j.1525-1314.2003.00474.x

Barnes JD, Beltrando M, Lee CTA, et al (2014) Geochemistry of Alpine serpentinites from rifting to subduction: A view across paleogeographic domains and metamorphic grade. Chem Geol 389:29–47. https://doi.org/10.1016/j.chemgeo.2014.09.012

Barnicoat AC, Cartwright I (1997) The gabbro-eclogite transformation: An oxygen isotope and petrographic study of west Alpine ophiolites. J Metamorph Geol 15:93–104. https://doi.org/10.1111/j.1525-1314.1997.00058.x

Barnicoat AC, Cartwright I (1995) Focused fluid flow during subduction: Oxygen isotope data from high-

pressure ophiolites of the western Alps. Earth Planet Sci Lett 132:53–61. https://doi.org/10.1016/0012-821X(95)00040-J

Baumgartner LP, Valley JW (2001) Stable isotope transport and contact metamorphic fluid flow. Rev Mineral Geochemistry 43:414–467

Bearth P (1967) Die ophiolite der Zone von Zermatt-Saas Fee. Beiträge Geol Karte Schweitz 132:1–130

Bebout GE (1991a) Field-Based Evidence for Devolatilization in Subduction Zones: Implications for Arc Magmatism. Science (80-) 251:413–416

Bebout GE (1991b) Geometry and mechanisms of fluid flow at 15 to 45 kilometer depths in an early Cretaceous accretionary complex. Geophys Res Lett 18:923–926. https://doi.org/10.1017/CBO9781107415324.004

Bebout GE, Barton MD (1993) Metasomatism during subduction: products and possible paths in the Catalina Schist, California. Chem Geol 108:61–92. https://doi.org/10.1016/0009-2541(93)90318-D

Bebout GE, Barton MD (1989) Fluid flow and Metasomatism in a subduction zone hydrothermal system: Catalina Schist Terrane, California. Geology Vol. 17:976–980

Bucher K, Fazis Y, de Capitani C, Grapes R (2005) Blueschists, eclogites, and decompression assemblages of the Zermatt-Saas ophiolite: High-pressure metamorphism of subducted Tethys lithosphere. Am Mineral 90:821–835. https://doi.org/10.2138/am.2005.1718

Bucher K, Weisenberger TB, Klemm O, Weber S (2019) Decoding the complex internal chemical structure of garnet porphyroblasts from the Zermatt area, Western Alps. J Metamorph Geol 37:1151–1169. https://doi.org/10.1111/jmg.12506

Bucher K, Weisenberger TB, Weber S, et al (2020) The Theodul Glacier Unit, a slab of pre-Alpine rocks in the Alpine meta-ophiolite of Zermatt-Saas, Western Alps. Swiss J Geosci 113:1–22. https://doi.org/10.1186/s00015-020-00354-6

Cartwright I, Barnicoat AC (1999) Stable isotope geochemistry of Alpine ophiolites: A window to ocean-floor hydrothermal alteration and constraints on fluid-rock interaction during high-pressure metamorphism. Int J Earth Sci 88:219–235. https://doi.org/10.1007/s005310050261

Clarke GL, Powell R, Fitzherbert JA (2006) The lawsonite paradox: A comparison of field evidence and mineral equilibria modelling. J Metamorph Geol 24:715–725. https://doi.org/10.1111/j.1525-1314.2006.00664.x

Coggon R, Holland TJB (2002) Mixing properties of phengitic micas and revised garnet-phengite thermobarometers. J Metamorph Geol 20:683–696. https://doi.org/10.1046/j.1525-1314.2002.00395.x

Compagnoni R (1977) The Sesia-Lanzo Zone: high pressure-low temperature metamorphism in the Austroalpine continental margin. Rend della Soc Ital di Mineral e Petrol 33:335–374

Connolly JAD (2010) The mechanics of metamorphic fluid expulsion. Elements 6:165–172. https://doi.org/10.2113/gselements.6.3.165

Dal Piaz GV (1979) Manganiferous quartzitic schists of the piemonte ophiolite Nappe-in the Valsesia-valtournach arc, Italian Western Alps. Mem Sci Geol Gia Mom degli Ist Geol Miner dell Univ di Padova 24:

Dal Piaz GV, Cortiana G, Del Moro A, et al (2001) Tertiary age and paleostructural inferences of the eclogitic imprint in the Austroalpine outliers and zermatt-saas ophiolite, Western Alps. Int J Earth Sci 90:668–684.

https://doi.org/10.1007/s005310000177

Dal Piaz GV, Ernst WG (1978) Areal geology and petrology of eclogites and associated metabasites of the Piemonte ophiolite nappe, breuil-st. Jacques area, Italian Western Alps. Tectonophysics 51:99–126. https://doi.org/10.1016/0040-1951(78)90053-7

De Capitani C, Brown TH (1987) The computation of chemical equilibrium in complex systems containing non-ideal solutions. Geochim Cosmochim Acta 51:2639–2652

De Capitani C, Petrakakis K (2010) The computation of equilibrium assemblage diagrams with Theriak/Domino software. Am Mineral 95:1006–1016. https://doi.org/10.2138/am.2010.3354

Diener JFA, Powell R, White RW, Holland TJB (2007) A new thermodynamic model for clino- and orthoamphiboles in the system Na2O-CaO-FeO-MgO-Al2O3-SiO2 -H2O-O. J Metamorph Geol 25:631–656. https://doi.org/10.1111/j.1525-1314.2007.00720.x

Dilek Y, Furnes H (2014) Ophiolites and their origins. Elements 10:93–100. https://doi.org/10.2113/gselements.10.2.93

Dilek Y, Furnes H (2011) Ophiolite genesis and global tectonics: Geochemical and tectonic fingerprinting of ancient oceanic lithosphere. Bull Geol Soc Am 123:387–411. https://doi.org/10.1130/B30446.1

Dipple GM, Ferry JM (1992) Metasomatism and fluid flow in ductile fault zones. Contrib to Mineral Petrol 112:149–164. https://doi.org/10.1007/BF00310451

Dragovic B, Angiboust S, Tappa MJ (2020) Petrochronological close-up on the thermal structure of a paleo-subduction zone (W. Alps). Earth Planet Sci Lett 547:116446. https://doi.org/10.1016/j.epsl.2020.116446

Duchêne S, Blichert-Toft J, Luais B, et al (1997) The Lu-Hf dating of garnets and the ages of the Alpine high-pressure metamorphism. Nature 387:586–589. https://doi.org/10.1038/42446

Engi M, Giuntoli F, Lanari P, et al (2018) Pervasive Eclogitization Due to Brittle Deformation and Rehydration of Subducted Basement: Effects on Continental Recycling? Geochemistry, Geophys Geosystems 19:865–881. https://doi.org/10.1002/2017GC007215

Ernst WG, Dal Piaz GV (1978) Mineral parageneses of eclogitic rocks and related mafic schists of the Piemonte ophiolite nappe, Breuil-St. Jacques area, Italian Western Alps. Am Mineral 63:621–640

Errico JC, Barnes JD, Strickland A, Valley JW (2013) Oxygen isotope zoning in garnets from Franciscan eclogite blocks: Evidence for rock-buffered fluid interaction in the mantle wedge. Contrib to Mineral Petrol 166:1161–1176. https://doi.org/10.1007/s00410-013-0915-0

Ferry JM (1994) A historical review of metamorphic fluid flow. J Geophys Res 99:15487. https://doi.org/10.1029/94jb01147

Ferry JM, Dipple GM (1991) Fluid flow, mineral reactions, and metasomatism. Geology 19:211–214. https://doi.org/10.1130/0091-7613(1991)019<0211:FFMRAM>2.3.CO;2

Ferry JM, Gerdes ML (1998) Chemically reactive fluid flow during metamorphism. Annu Rev Earth Planet Sci 26:255–287. https://doi.org/10.1146/annurev.earth.26.1.255

Früh-Green GL, Scambelluri M, Vallis F (2001) O-H isotope ratios of high pressure ultramafic rocks: Implications for fluid sources and mobility in the subducted hydrous mantle. Contrib to Mineral Petrol 141:145–159. https://doi.org/10.1007/s004100000228

Früh-Green GL, Weissert H, Bernoulli D (1990) A multiple fluid history recorded in Alpine ophiolites. J Geol Soc London 147:959–970. https://doi.org/10.1144/gsjgs.147.6.0959

Ganzhorn AC, Pilorgé H, Reynard B (2019) Porosity of metamorphic rocks and fluid migration within subduction interfaces. Earth Planet Sci Lett 522:107–117. https://doi.org/10.1016/j.epsl.2019.06.030

Gauthiez-Putallaz L, Rubatto D, Hermann J (2016) Dating prograde fluid pulses during subduction by in situ U–Pb and oxygen isotope analysis. Contrib to Mineral Petrol 171:1–20. https://doi.org/10.1007/s00410-015-1226-4

Giuntoli F, Lanari P, Burn M, et al (2018a) Deeply subducted continental fragments - Part 2: Insight from petrochronology in the central Sesia Zone (western Italian Alps). Solid Earth 9:191–222. https://doi.org/10.5194/se-9-191-2018

Giuntoli F, Lanari P, Engi M (2018b) Deeply subducted continental fragments - Part 1: Fracturing, dissolution-precipitation, and diffusion processes recorded by garnet textures of the central Sesia Zone (western Italian Alps). Solid Earth 9:167–189. https://doi.org/10.5194/se-9-167-2018

Gosso G (1977) Metamorphic evolution and fold history in the Eclogitic Micaschists of the upper Gressoney Valley (Sesia-Lanzo Zone, Western Alps). Rend Soclietà Ital di Mineral e Pelrologia 33:389–407

Green E, Holland T, Powell R (2007) An order-disorder model for omphacitic pyroxenes in the system jadeite-diopside-hedenbergite-acmite, with applications to eclogitic rocks. Am Mineral 92:1181–1189. https://doi.org/10.2138/am.2007.2401

Groppo C, Beltrando M, Compagnoni R (2009) The P-T path of the ultra-high pressure Lago Di Cignana and adjoining high-pressure meta-ophiolitic units: Insights into the evolution of the subducting Tethyan slab. J Metamorph Geol 27:207–231. https://doi.org/10.1111/j.1525-1314.2009.00814.x

Hacker BR, Peacock SM, Abers GA, Holloway SD (2003) Subduction factory 2. Are intermediate-depth earthquakes in subducting slabs linked to metamorphic dehydration reactions? J Geophys Res Solid Earth 108:. https://doi.org/10.1029/2001jb001129

Hermann J, Spandler C, Hack A, Korsakov A V. (2006) Aqueous fluids and hydrous melts in high-pressure and ultra-high pressure rocks: Implications for element transfer in subduction zones. Lithos 92:399–417. https://doi.org/10.1016/j.lithos.2006.03.055

Holland T, Powell R (2003) Activity-compositions relations for phases in petrological calculations: An asymetric multicomponent formulation. Contrib to Mineral Petrol 145:492–501. https://doi.org/10.1007/s00410-003-0464-z

Holland TJB, Powell R (1998) An internally consistent thermodynamic data set for phases of petrological interest. J Metamorph Geol 16:309–343. https://doi.org/10.1111/j.1525-1314.1998.00140.x

Hollister LS (1966) Garnet Zoning : An Interpretation Based on the Rayleigh Fractionation Model. 154:1647–1651

Ingebritsen SE, Manning CE (2010) Permeability of the continental crust: Dynamic variations inferred from seismicity and metamorphism. Geofluids 10:193–205. https://doi.org/10.1111/j.1468-8123.2010.00278.x

Ingebritsen SE, Manning CE (1999) Geological implications of a permeability-depth curve for the continental

crust. Geology 27:1107–1110. https://doi.org/10.1130/0091-7613(1999)027<1107:GIOAPD>2.3.CO;2

Ingebritsen SE, Manning CE (2003) Implications of crustal permeability for fluid movement between terrestrial fluid reservoirs. J Geochemical Explor 78–79:1–6. https://doi.org/10.1016/S0375-6742(03)00037-2

Ito E, Harris DM, Anderson AT (1983) Alteration of oceanic crust and geologic cycling of chlorine and water. Geochim Cosmochim Acta 47:1613–1624. https://doi.org/10.1016/0016-7037(83)90188-6

Johannes W (1968) Experimental investigation of the reaction forsterite + H2O ⇌ serpentine + brucite. Contrib to Mineral Petrol 19:309–315. https://doi.org/10.1007/BF00389413

John T, Gussone N, Podladchikov YY, et al (2012) Volcanic arcs fed by rapid pulsed fluid flow through subducting slabs. Nat Geosci 5:489–492. https://doi.org/10.1038/ngeo1482

John T, Klemd R, Gao J, Garbe-Schönberg CD (2008) Trace-element mobilization in slabs due to non steady-state fluid-rock interaction: Constraints from an eclogite-facies transport vein in blueschist (Tianshan, China). Lithos 103:1–24. https://doi.org/10.1016/j.lithos.2007.09.005

Kawano S, Katayama I, Okazaki K (2011) Permeability anisotropy of serpentinite and fluid pathways in a subduction zone. Geology 39:939–942. https://doi.org/10.1130/G32173.1

Kempf ED, Hermann J, Reusser E, et al (2020) The role of the antigorite + brucite to olivine reaction in subducted serpentinites (Zermatt, Switzerland. Swiss J Geosci 1–36. https://doi.org/10.1186/s00015-020-00368-0

Kessel R, Schmidt MW, Ulmer P, Pettke T (2005) Trace element signature of subduction-zone fluids, melts and supercritical liquids at 120-180 km depth. Nature 437:724–727. https://doi.org/10.1038/nature03971

Kohn MJ (1993) Modeling of prograde mineral δ18O changes in metamorphic systems. Contrib to Mineral Petrol 113:249–261. https://doi.org/10.1007/BF00283232

Konrad-Schmolke M, O'Brien PJ, Zack T (2011) Fluid migration above a subducted slab-constraints on amount, pathways and major element mobility from partially overprinted eclogite-facies rocks (Sesia Zone, Western Alps). J Petrol 52:457–486. https://doi.org/10.1093/petrology/egq087

Lanari P, Vho A, Bovay T, et al (2019) Quantitative compositional mapping of mineral phases by electron probe micro-analyser. Geol Soc Spec Publ 478:39–63. https://doi.org/10.1144/SP478.4

Lanari P, Vidal O, De Andrade V, et al (2014) XMapTools: A MATLAB©-based program for electron microprobe X-ray image processing and geothermobarometry. Comput Geosci 62:227–240. https://doi.org/10.1016/j.cageo.2013.08.010

Lapen TJ, Johnson CM, Baumgartner LP, et al (2003) Burial rates during prograde metamorphism of an ultra-high-pressure terrane: An example from Lago di Cignana, western Alps, Italy. Earth Planet Sci Lett 215:57–72. https://doi.org/10.1016/S0012-821X(03)00455-2

Li XP, Rahn M, Bucher K (2004) Serpentinites of the Zermatt-Saas ophiolite complex and their texture evolution. J Metamorph Geol 22:159–177. https://doi.org/10.1111/j.1525-1314.2004.00503.x

Manning CE (2004) The chemistry of subduction-zone fluids. Earth Planet Sci Lett 223:1–16. https://doi.org/10.1016/j.epsl.2004.04.030

Manning CE, Ingebritsen SE (1999) Permeability of the continental crust: Implications of geothermal data and metamorphic systems. Rev Geophys 37:127–150. https://doi.org/10.1029/1998RG900002

Martin LAJ, Hermann J, Gauthiez-Putallaz L, et al (2014) Lawsonite geochemistry and stability - implication for trace element and water cycles in subduction zones. J Metamorph Geol 32:455–478. https://doi.org/10.1111/jmg.12093

McCaig AM, Cliff RA, Escartin J, et al (2007) Oceanic detachment faults focus very large volumes of black smoker fluids. Geology 35:935–938. https://doi.org/10.1130/G23657A.1

Miller JA, Cartwright I (2000) Distinguishing between seafloor alteration and fluid flow during subduction using stable isotope geochemistry: Examples from Tethyan ophiolites in the Western Alps. J Metamorph Geol. https://doi.org/10.1046/j.1525-1314.2000.00274.x

Miller JA, Cartwright I, Buick IS, Barnicoat AC (2001) An O-isotope profile through the HP-LT Corsican ophiolite, France and its implications for fluid flow during subduction. Chem Geol. https://doi.org/10.1016/S0009-2541(00)00428-9

Miller SA, Van der Zee W, Olgaard DL, Connolly JAD (2003) A fluid-pressure feedback model of dehydration reactions: Experiments, modelling, and application to subduction zones. Tectonophysics 370:241–251. https://doi.org/10.1016/S0040-1951(03)00189-6

Muehlenbachs K, Clayton RN (1972) Oxygen Isotope Studies of Fresh and Weathered Submarine Basalts. Can J Earth Sci 172:172–184

Nadeau S, Philippot P, Pineau F (1993) Fluid inclusion and mineral isotopic compositions (HCO) in eclogitic rocks as tracers of local fluid migration during high-pressure metamorphism. Earth Planet Sci Lett 114:431–448. https://doi.org/10.1016/0012-821X(93)90074-J

Oliver NHS (1996) Review and classification of structural controls on fluid flow during regional metamorphism. J Metamorph Geol 14:477–492. https://doi.org/10.1046/j.1525-1314.1996.00347.x

Padrón-Navarta JA, Sánchez-Vizcaíno VL, Hermann J, et al (2013) Tschermak's substitution in antigorite and consequences for phase relations and water liberation in high-grade serpentinites. Lithos 178:186–196. https://doi.org/10.1016/j.lithos.2013.02.001

Page FZ, Cameron EM, Flood CM, et al (2019) Extreme oxygen isotope zoning in garnet and zircon from a metachert block in mélange reveals metasomatism at the peak of subduction metamorphism. Geology 47:655–658. https://doi.org/10.1130/G46135.1

Page FZ, Essene EJ, Mukasa SB, Valley JW (2014) A garnet-zircon oxygen isotope record of subduction and exhumation fluids from the Franciscan complex, California. J Petrol 55:103–131. https://doi.org/10.1093/petrology/egt062

Peacock SM (1990) Fluid processes in subduction zones. Science (80-) 248:329–337. https://doi.org/10.1126/science.248.4953.329

Philippot P, Rumble D (2000) Fluid-rock interactions during high-pressure and ultrahigh-pressure metamorphism. Int Geol Rev 42:312–327. https://doi.org/10.1080/00206810009465085

Philippot P, Selverstone J (1991) Trace-element-rich brines in eclogitic veins: implications for fluid composition and transport during subduction. Contrib to Mineral Petrol 106:417–430. https://doi.org/10.1007/BF00321985

Poli S, Schmidt MW (1995) H2O transport and release in subduction zones: experimental constraints on

basaltic and andesitic systems. J Geophys Res 100:299–314. https://doi.org/10.1029/95jb01570

Poli S, Schmidt MW (2002) Petrology of Subducted Slabs. Annu Rev Earth Planet Sci 30:207–235. https://doi.org/10.1146/annurev.earth.30.091201.140550

Putlitz B, Matthews A, Valley JW (2000) Oxygen and hydrogen isotope study of high-pressure metagabbros and metabasalts (Cyclades, Greece): Implications for the subduction of oceanic crust. Contrib to Mineral Petrol 138:114–126. https://doi.org/10.1007/s004100050012

Reinecke T (1998) Prograde high- to ultrahigh-pressure metamorphism and exhumation of oceanic sediments at Lago di Cignana, Zermatt-Saas Zone, western Alps. Lithos 42:147–189. https://doi.org/10.1016/s0024-4937(97)00041-8

Reinecke T (1991) Very high-pressure metamorphism and uplift of coesit-bearing metasediments from the Zermatt-Saas zone, Western Alps. Eur J Mineral 3:7–17

Rubatto D, Angiboust S (2015) Oxygen isotope record of oceanic and high-pressure metasomatism: a P-T-time-fluid path for the Monviso eclogites (Italy). Contrib to Mineral Petrol. https://doi.org/10.1007/s00410-015-1198-4

Rubatto D, Burger M, Lanari P, et al (2020) Identification of growth mechanisms in metamorphic garnet by high-resolution trace element mapping with LA-ICP-TOFMS. Contrib to Mineral Petrol 175:1–19. https://doi.org/10.1007/s00410-020-01700-5

Rubatto D, Gebauer D, Fanning M (1998) Jurassic formation and Eocene subduction of the Zermatt-Saas-Fee ophiolites: Implications for the geodynamic evolution of the Central and Western Alps. Contrib to Mineral Petrol 132:269–287. https://doi.org/10.1007/s004100050421

Rubatto D, Hermann J (2003) Zircon formation during fluid circulation in eclogites (Monviso, Western Alps): Implications for Zr and Hf budget in subduction zones. Geochim Cosmochim Acta 67:2173–2187. https://doi.org/10.1016/S0016-7037(02)01321-2

Rumble D, Ferry JM, Hoering TC, Boucot AJ (1982) Fluid flow during metamorphism at the Beaver Brook fossil locality, New Hampshire. Am. J. Sci. 282:886–919

Rumble D, Spear FS (1983) Oxygen-isotope equilibration and permeability enhancement during regional metamorphism. J - Geol Soc 140:619–628

Russell AK, Kitajima K, Strickland A, et al (2013) Eclogite-facies fluid infiltration: Constraints from δ18O zoning in garnet. Contrib to Mineral Petrol 165:103–116. https://doi.org/10.1007/s00410-012-0794-9

Scambelluri M, Müntener O, Hermann J, et al (1995) Subduction of water into the mantle: history of an Alpine peridotite. Geology 23:459–462. https://doi.org/10.1130/0091-7613(1995)023<0459:SOWITM>2.3.CO;2

Scambelluri M, Philippot P (2001) Deep fluids in subduction zones. Lithos 55:213–227. https://doi.org/10.1016/S0024-4937(00)00046-3

Schmidt MW, Poli S (2003) Generation of Mobile Components during Subduction of Oceanic Crust. In: Treatise on Geochemistry. pp 567–591

Schmidt MW, Poli S (2013) Devolatilization During Subduction. In: Treatise on Geochemistry: Second Edition, 2nd edn. Elsevier Ltd., pp 669–701

Schmidt MW, Poli S (1998) Experimentally based water budgets for dehydrating slabs and consequences for

arc magma generation. Earth Planet Sci Lett 163:361–379. https://doi.org/10.1016/S0012-821X(98)00142-3

Selverstone J, Franz G, Thomas S, Getty S (1992) Fluid variability in 2 GPa eclogites as an indicator of fluid behavior during subduction. Contrib to Mineral Petrol 112:341–357. https://doi.org/10.1007/BF00310465

Sharp ZD, Essene EJ, Hunziker J-C (1993) Stable isotope geochemistry and phase equilibria of coesite-bearing whiteschists, Dora Maira Massif, western Alps. Contrib to Mineral Petrol 114:1–12. https://doi.org/10.1007/BF00307861

Sorensen SS, Barton MD (1987) Metasomatism and partial melting in a subduction complex: Catalina schist, southern California. Geology 15:115–118. https://doi.org/10.1130/0091-7613(1987)15<115:MAPMIA>2.0.CO;2

Spandler C, Hermann J, Arculus RJ, Mavrogenes J (2003) Redistribution of trace elements during prograde metamorphism from lawsonite blueschist to eclogite facies; implications for deep subduction-zone processes. Contrib to Mineral Petrol 146:205–222. https://doi.org/10.1007/s00410-003-0495-5

Spandler C, Pettke T, Rubatto D (2011) Internal and external fluid sources for eclogite-facies veins in the Monviso Meta-ophiolite, Western Alps: Implications for fluid flow in subduction zones. J Petrol 52:1207–1236. https://doi.org/10.1093/petrology/egr025

Taetz S, John T, Bröcker M, Spandler C (2016) Fluid–rock interaction and evolution of a high-pressure/low-temperature vein system in eclogite from New Caledonia: insights into intraslab fluid flow processes. Contrib to Mineral Petrol 171:. https://doi.org/10.1007/s00410-016-1295-z

Taylor HP (1968) The oxygen isotope geochemistry of igneous rocks. Contrib to Mineral Petrol 19:1–71. https://doi.org/10.1007/BF00371729

Ulmer P, Trommsdorff V (1995) Serpentine stability to mantle depths and subduction-related magmatism. Science (80-) 268:858–861. https://doi.org/10.1126/science.268.5212.858

Valley JW, Kitchen N, Kohn MJ, et al (1995) UWG-2, a garnet standard for oxygen isotope ratios: Strategies for high precision and accuracy with laser heating. Geochim Cosmochim Acta 59:5223–5231. https://doi.org/10.1016/0016-7037(95)00386-X

Vho A, Lanari P, Rubatto D (2019) An Internally-Consistent Database for Oxygen Isotope Fractionation Between Minerals. J Petrol 60:2101–2130. https://doi.org/10.1093/petrology/egaa001

Vho A, Lanari P, Rubatto D, Hermann J (2020a) Tracing fluid transfers in subduction zones: An integrated thermodynamic and δ18O fractionation modelling approach. Solid Earth 11:307–328. https://doi.org/10.5194/se-11-307-2020

Vho A, Rubatto D, Lanari P, et al (2020b) Crustal reworking and hydration: Insights from element zoning and oxygen isotopes of garnet in high-pressure rocks (Sesia Zone, Western Alps). Contrib to Mineral Petrol 1–28. https://doi.org/10.1007/s00410-020-01745-6

Vho A, Rubatto D, Putlitz B, Bouvier A-S (2020c) New Reference Materials and Assessment of Matrix Effects for SIMS Measurements of Oxygen Isotopes in Garnet. Geostand Geoanalytical Res 1–13. https://doi.org/10.1111/ggr.12324

Vielzeuf D, Champenois M, Valley JW, et al (2005) SIMS analyses of oxygen isotopes: Matrix effects in Fe-Mg-Ca garnets. Chem Geol 223:208–226. https://doi.org/10.1016/j.chemgeo.2005.07.008

Weber S, Bucher K (2015) An eclogite-bearing continental tectonic slice in the Zermatt-Saas high-pressure ophiolites at Trockener Steg (Zermatt, Swiss Western Alps). Lithos 232:336–359. https://doi.org/10.1016/j.lithos.2015.07.010

Weber S, Sandmann S, Miladinova I, et al (2015) Dating the initiation of Piemonte-Liguria Ocean subduction: Lu–Hf garnet chronometry of eclogites from the Theodul Glacier Unit (Zermatt-Saas zone, Switzerland). Swiss J Geosci 108:183–199. https://doi.org/10.1007/s00015-015-0180-5

White RW, Powell R, Holland TJB (2007) Progress relating to calculation of partial melting equilibria for metapelites. J Metamorph Geol 25:511–527. https://doi.org/10.1111/j.1525-1314.2007.00711.x

White RW, Powell R, Holland TJB, Worley B (2000) The effect of TiO2 and Fe2O3 on metapelitic assemblages at greenschist and amphibolite facies conditions: Mineral equilibria calculations in the system K2O-FeO-MgO-Al2O3-SiO2-H2O-TiO2-Fe2O3. J Metamorph Geol 18:497–511. https://doi.org/10.1046/j.1525-1314.2000.00269.x

Whitney DL, Evans BW (2010) Abbreviations for names of rock-forming minerals. Am Mineral 95:185–187. https://doi.org/10.2138/am.2010.3371

Zack T, John T (2007) An evaluation of reactive fluid flow and trace element mobility in subducting slabs. Chem Geol 239:199–216. https://doi.org/10.1016/j.chemgeo.2006.10.020

Zheng Y-F (1993) Calculation of oxygen isotope fractionation in anhydrous silicate minerals. Geochim Cosmochim Acta 57:1079–1091. https://doi.org/10.1016/0016-7037(93)90042-U

SUPPLEMENTARY MATERIAL

Supplementary Figures:

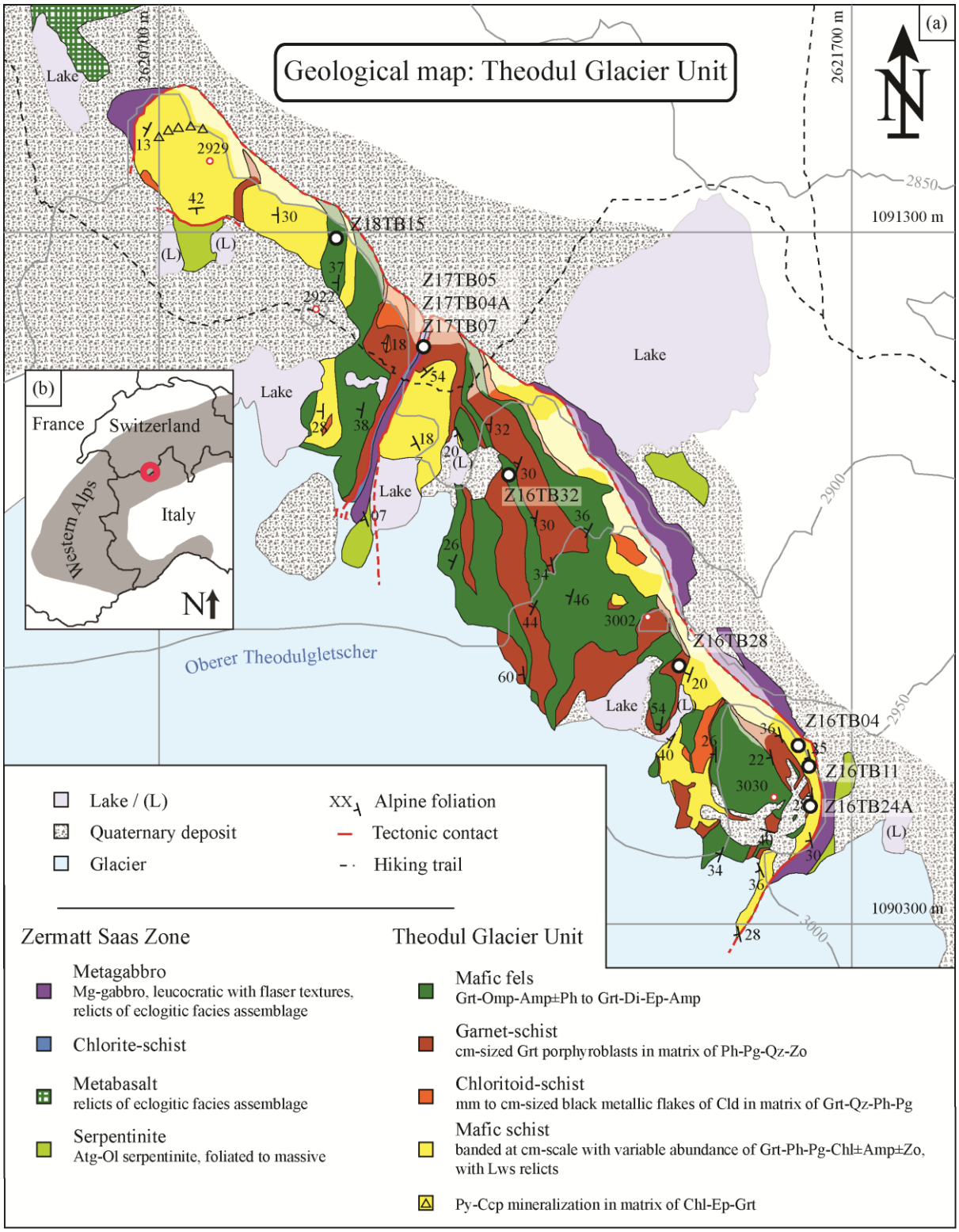

Figure S1: (a) Geological map of the Theodul Glacier Unit (TGU). White circles show sample location. (b) Geolocalisation of the TGU in the Western Alps.

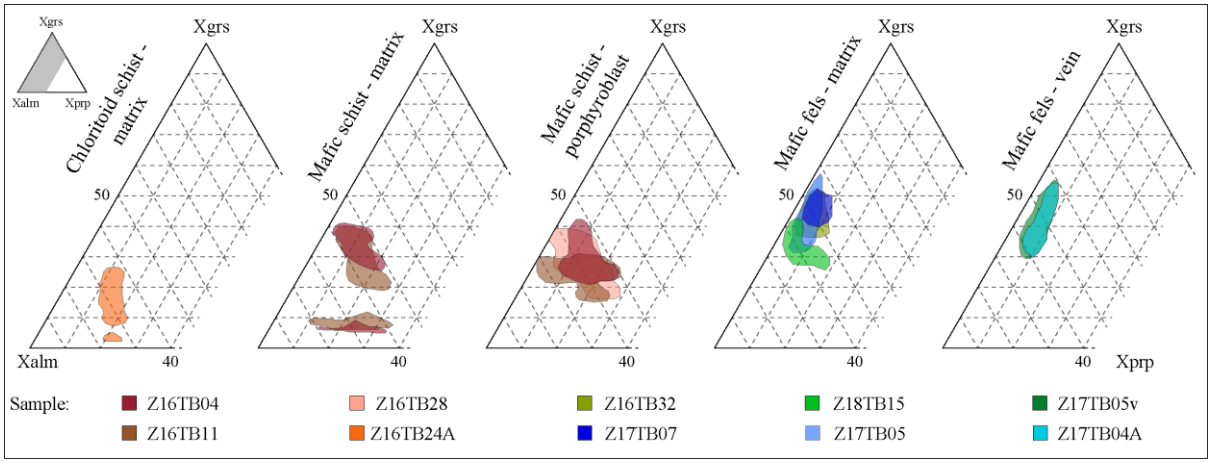

Figure S2: Summary of the garnet chemical composition from the different lithologies plotted in a X_{grs}-X_{alm}-X_{prp} ternary diagram. Composition areas are retrieved from EPMA maps processed with XMapTools (Lanari et al. 2014, 2019). Areas were drawn on the basis of: 51,412 points (mafic schist Z16TB04, matrix garnet); 107,392 points (mafic schist Z16TB11, matrix garnet); 111,072 points (mafic schist Z16TB11, matrix garnet); 527,573 points (mafic schist Z16TB04, matrix garnet); 654,074 points (mafic schist Z16TB11, matrix garnet); 363,395 points (mafic schist Z16TB28, matrix garnet); 148,036 points (mafic fels Z17TB05, matrix garnet); 239,905 points (mafic fels Z17TB07, matrix garnet); 238,334 points (mafic fels Z16TB32, matrix garnet); 184,997 points (mafic fels Z17TB04A, garnet in vein); 125,688 points (mafic fels Z17TB05v, garnet in vein).

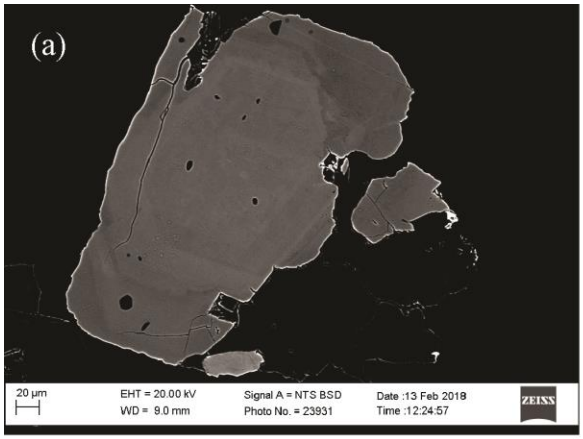

Z16TB32-crystalmountZ17TBgr1-zoneZ4-63

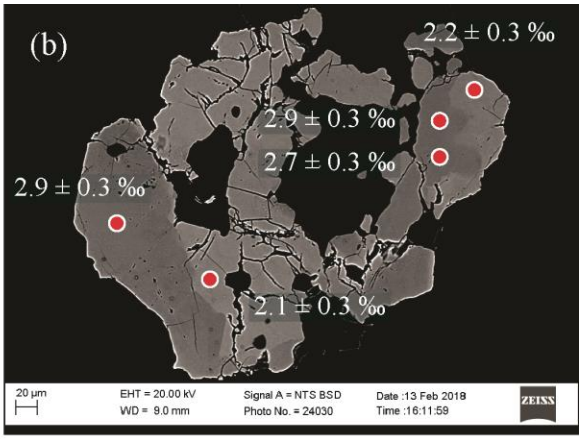

Z16TB32-crystalmountZ17TBgr1-zoneZ4-161

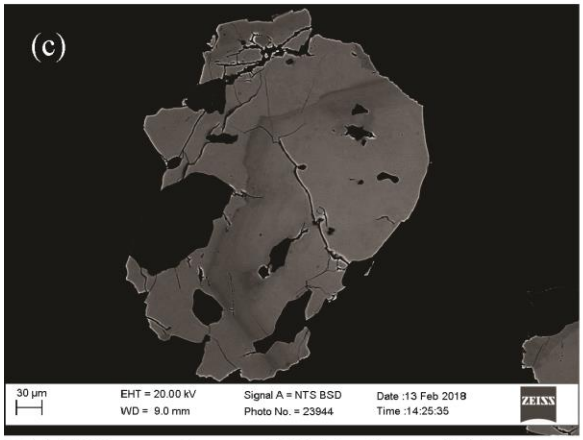

Z16TB32-crystalmountZ17TBgr1-zoneZ4-76

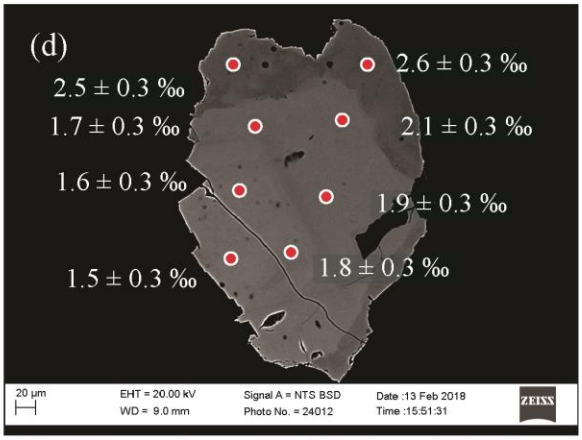

Z16TB32-crystalmountZ17TBgr1-zoneZ4-144

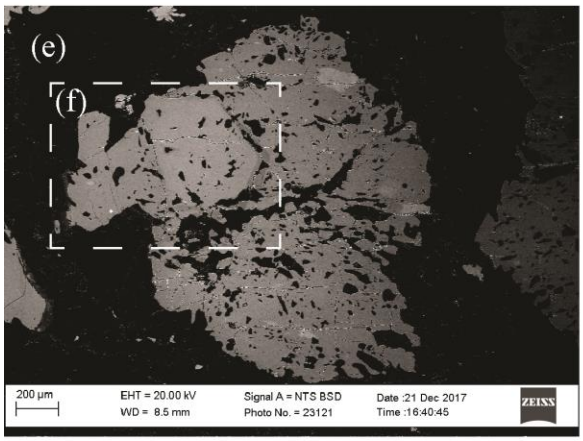

Z17TB07-16

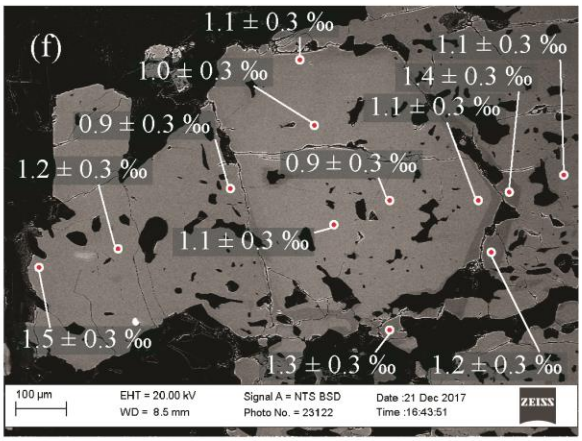

Z17TB07-16(Zoom)

● SIMS spot diameter

Figure S3: BSE images of garnet crystals from mafic fels samples Z16TB32 (a-d) and Z17TB07 (e-f) showing chemical zoning. Some of these crystals were analysed at the SIMS and show no systematic $\delta^{18}O$ zoning among grains with values ranging between 0.9 and 2.9 ‰ (Z16TB32) and between 0.3 to 1.5 ‰ (Z17TB07) (Fig. 5). Image (f) is a zoom of the part of figure (e) within the white rectangle.

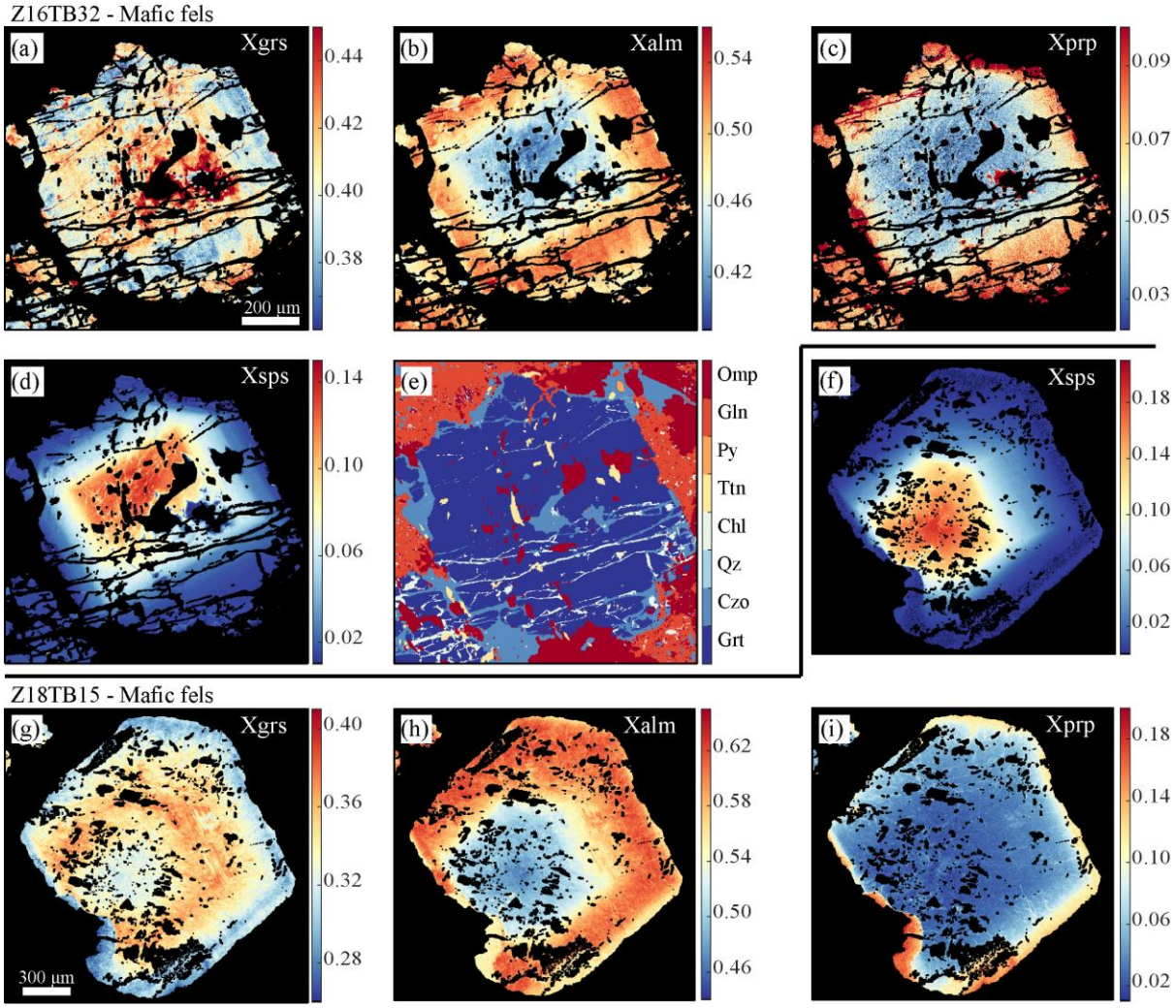

Figure S4: EPMA compositional maps of garnet crystals from mafic fels sample Z16TB32 (a-d) and Z18TB15 (f-i). (e) Phase repartition in the matrix and as inclusion in garnet in sample Z16TB32. Ca enrichment is visible around the clinozoisite inclusions at the centre of the grain (see Fig. S4a). EPMA maps were processed with XMapTools (Lanari et al. 2014, 2019). Mineral abbreviation are from Whitney and Evans (2010).

Figure S5 (next page): Outline of the three successive scenarios considered for the external fluid origin. (a) Discretization of the exhumation path with 15 successive iterations beginning at the maximum P-T conditions of TGU at 580 °C and 26.5 kbar, and ending at the beginning of the reheating stage at 555 °C and 15.5 kbar (Bovay et al. 2020). (b) Scenario 1: observed rock ratio between the mafic fels rock and the mafic schist. All the fluid produced by dehydration reactions in the mafic fels is transferred to the mafic schist. (c) Scenario 2: unrealistic rock ratio between the mafic fels rock and the mafic schist calculated in order to produce enough fluid to decrease garnet $\delta^{18}O$ value from 9.5 ‰ to 1 ‰ in the mafic schist. (d) Scenario 3: External fluid from the serpentinites from ZSZ with a constrained $\delta^{18}O$ composition directly infiltrates the mafic schist at specific simulation steps.

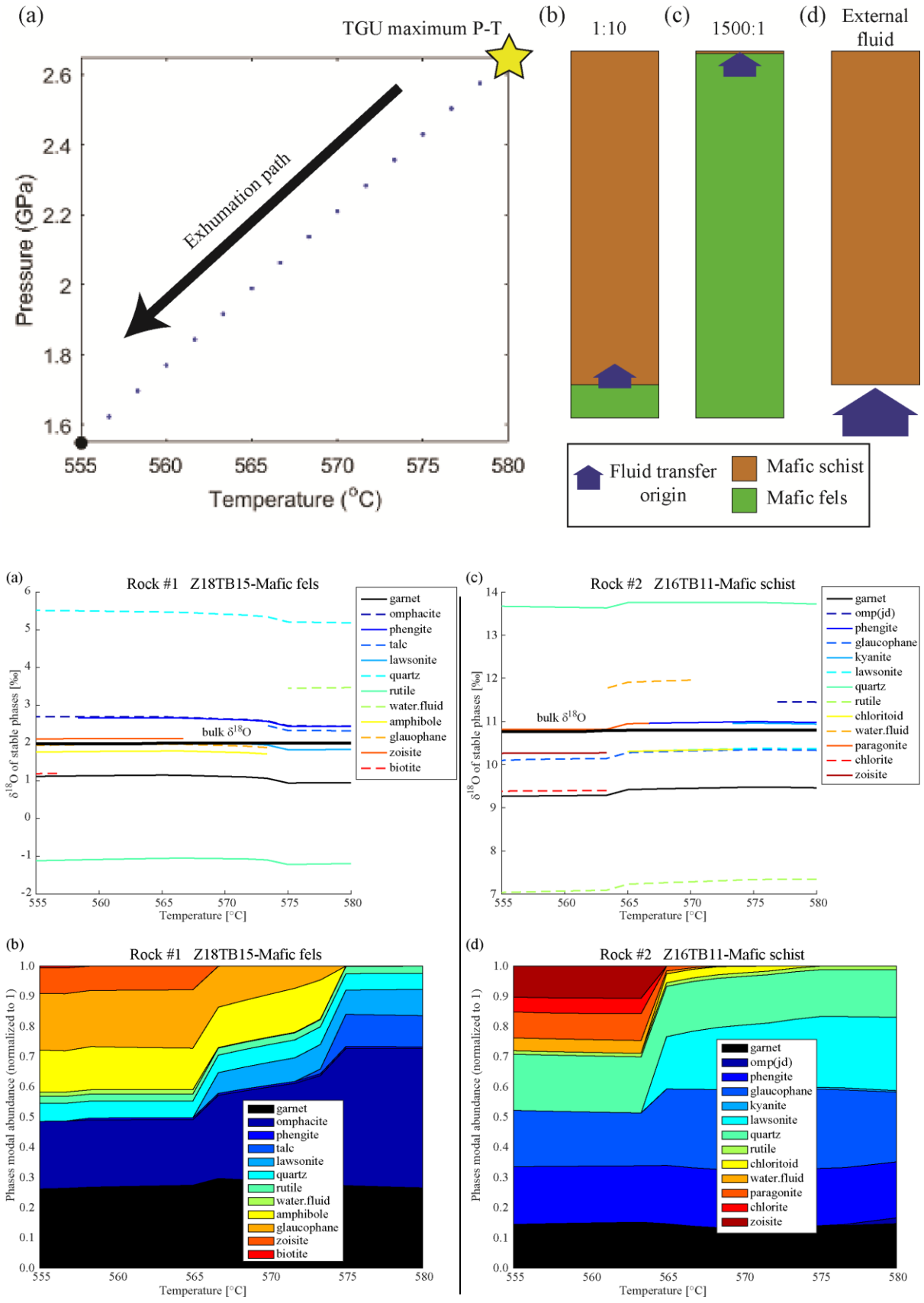

Figure S6: Output figures from PTLOOP (Vho et al. 2020) after scenario 1 (Fig. S5b), plotted against temperature for sample Z18TB15 (a-b) and sample Z16TB11 (c-d). All the water released from the mafic fels (Z18TB15) is transferred to the mafic schist (Z16TB11). All the water released from the mafic schist is removed from the system. (a,c) Evolution of $\delta^{18}O$ in the bulk and phases along the TGU exhumation P-T path. (b,d) Phases modal abundance in equilibrium (normalised to 1) along the TGU exhumation P-T path.

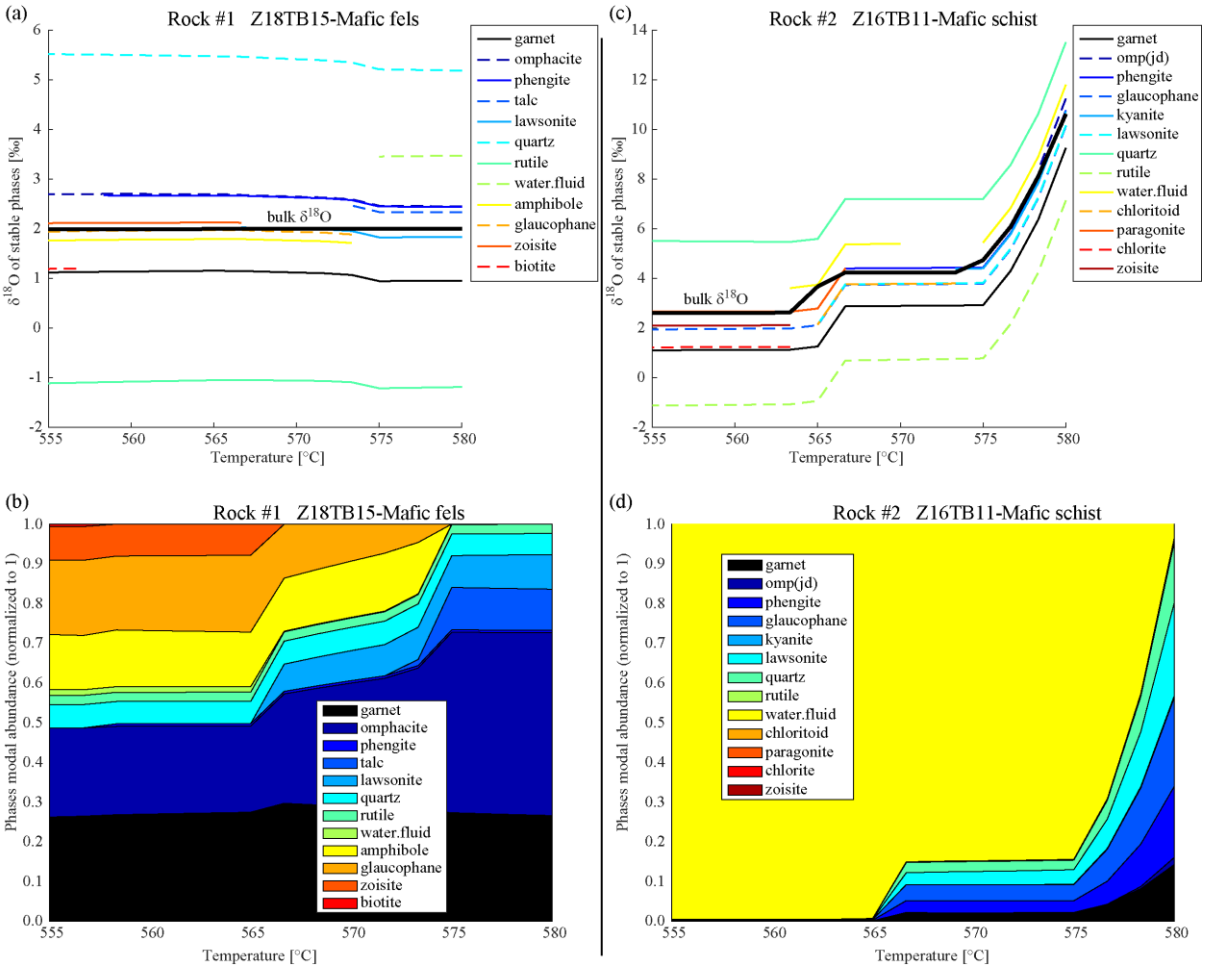

Figure S7: Output figures from PTLOOP (Vho et al. 2020) after scenario 2 (Fig. S5c), plotted against temperature for sample Z18TB15 (a-b) and sample Z16TB11 (c-d). All the water released from the mafic fels (Z18TB15) is transferred to the mafic schist (Z16TB11). All the water released from the mafic schist is removed from the system. (a,c) Evolution of $\delta^{18}O$ in the bulk and phases along the TGU exhumation P-T path. (b,d) Phases modal abundance in equilibrium (normalised to 1) along the TGU exhumation P-T path.

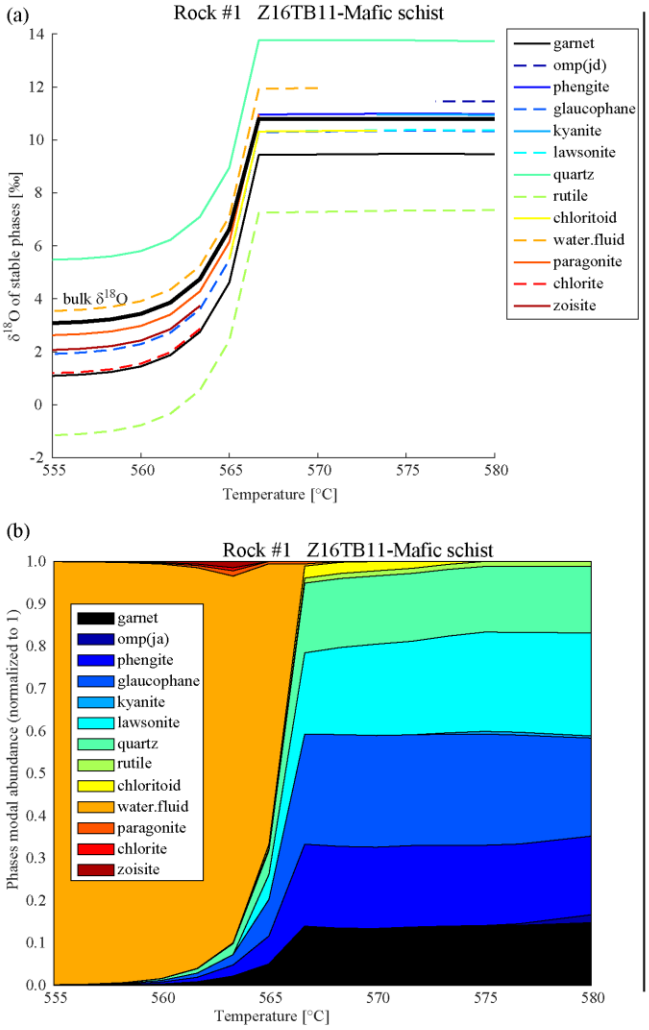

(c) Fluid-rock interaction Summary (Input PTLoop)

Pressure	Temperature	H2O-in	
		mass	d18O
[bar]	[°C]	[kg]	[‰]
26500	580	0	1
25733	578	0	1
24967	577	0	1
24200	576	0	1
23433	574	0	1
22667	573	0	1
21900	572	0	1
21133	570	0	1
20367	569	0	1
19600	568	200000	3.5
18833	566	150000	3.5
18067	565	150000	3.5
17300	564	150000	3.5
16533	562	150000	3.5
15767	561	150000	3.5
15500	555	150000	3.5

***Figure S8: Output figures from PTLOOP** (Vho et al. 2020) after scenario 3 (Fig. S5d), plotted against temperature for sample Z18TB11. All the water released from the mafic schist is removed from the system. (a) Evolution of $\delta^{18}O$ in the bulk and phases along the TGU exhumation P-T path. (b) Phases modal abundance in equilibrium (normalised to 1) along the TGU exhumation P-T path. (c) Mass of external fluid entering the system. Each line corresponds to a simulation step, with a specific pressure and temperature, at which a fixed amount of fluid (in kg) with a $\delta^{18}O$ of 3.5 ‰ is injected (see text for details).*

***Figure S9 (next page): P-T diagrams showing the variation of H_2O** in solids (a, d), volume of solids (b, e) and rock density (c, f). Pseudosections were calculated using the software Theriak-Domino (De Capitani and Brown 1987; De Capitani and Petrakakis 2010). Each column is specific to a sample: (a-c) Z16TB11 and (d-f) Z18TB15. The TGU exhumation path (arrow) is from Bovay et al. (2020) and is between the maximum P-T conditions (red triangle) and the P-T conditions prior to the reheating stage (red circle). Calculations were performed with bulk rock chemistry presented in Table S4 (modified bulk rock chemistry for sample Z16TB11, see text) and water saturation is set for TGU at maximum P-T conditions (Bovay et al. 2020) for both lithologies. Input parameters for Theriak-Domino (De Capitani and Brown 1987; De Capitani and Petrakakis 2010) are:*
Z16TB11 (modified):
SI(0.8444800)AL(0.3768806)FE(0.0993564)MN(0.0009274)MG(0.1069949)CA(0.0832722)NA(0.0649407)TI(0.0186249)K(0.0386342)H(0.424046)O(?)C(0)O(0)
Z18TB15:
SI(0.83541)AL(0.28325)FE(0.15129)MN(0.0021145)MG(0.18337)CA(0.1817)NA(0.097773)TI(0.036473)K(0.0012314)H(0.14863)O(?)C(0)O(0)

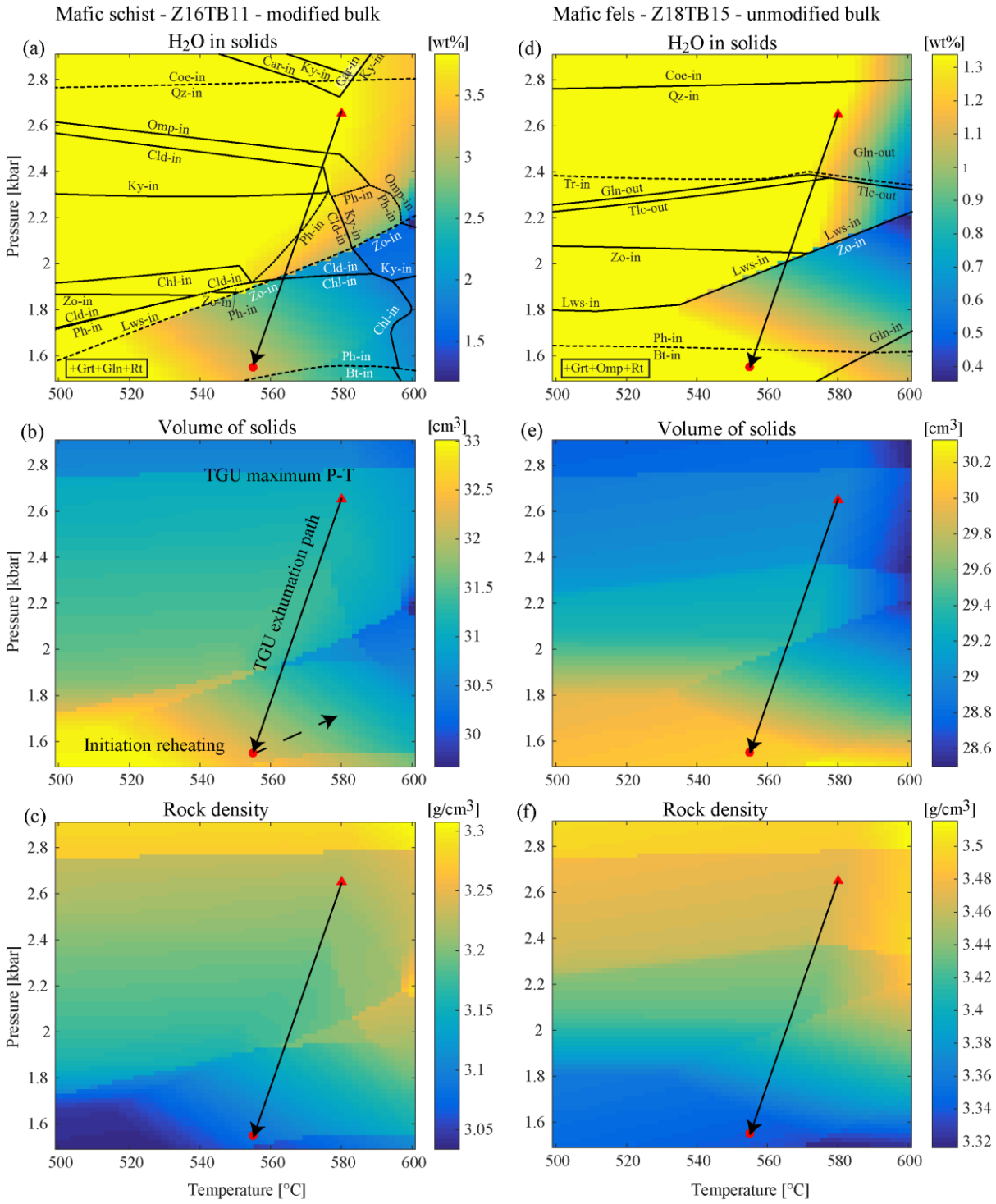

Note: H_2O saturated for both simulations at maximum P-T conditions

Supplementary Tables:

All supplementary tables are stored on a CD in a folder labelled “SupplementaryTablesChapter3”.

Table S1a-f: SIMS oxygen isotope analyses of garnet divided by analytical session.

Table S2a-c: Garnet major element composition for the three rock types.

Table S3: Input and output values from PTLOOP simulation to reconstruct the $\delta^{18}O$ of phases at specific temperature and pressure stages.

Table S4: Major element composition of bulk samples measured by LA-ICP-MS.

CHAPTER 4

Unresolved evolution of garnet porphyroblasts from the TGU

KEYWORDS

Phase equilibria; Quantitative compositional mapping; Lu-Hf garnet-whole rock geochronology; RSCM and Zr-in-rutile thermometry; Garnet oxygen isotope composition

ABSTRACT

Garnet porphyroblasts are particularly suited to investigate the metamorphic evolution of high-grade crustal rocks, because they can retain multiple microtextural and microchemical information. Additionally, garnet can be dated and it is resistant to re-equilibration, making it one of the best petrochronometers. All the rock types that compose the Theodul Glacier Unit contain garnet, but the cm-sized garnet porphyroblasts found in the Grt-schist have some peculiar features. Compared to the garnet from the other lithologies, these garnet porphyroblasts have a relict core domain with a unique texture and chemistry. On the other hand, the rest of the garnet (mantle and rim) as well as small garnet grains in the matrix have chemical and oxygen isotope zoning comparable to garnet from other samples. Lu-Hf geochronology of the porphyroblasts returns a Jurassic isochron date that is not found in any other sample and that questions the monometamorphic evolution of the unit deduced from multiple lines of evidence.

Combining geological, petrological and geochemical data, lead to three possible scenarios: (1) Gabbroic intrusion associated to the opening of the Piemont-Ligurian Ocean could have promoted garnet growth in the sedimentary pile either through contact metamorphism or hydrothermal activity. (2) Garnet growth associated to metamorphic sole formation produced through intra-oceanic subduction coupled with nascent oceanic opening in the Jurassic. (3) The Lu-Hf isochron is an errorchron.

1. INTRODUCTION

Metamorphic rocks commonly contain zoned minerals (Marmo et al. 2002), which chemical compositions are functions of temperature (*T*), pressure (*P*), the reactive bulk chemistry of the rock and the interstitial fluids, and time (*t*) (Wilbur and Ague 2006). As a consequence, the zoning pattern is commonly used by metamorphic petrologists to infer the pressure-temperature-time *P–T–t* evolution of the mineral host rock (e.g. Spear and Selverstone 1983; Airaghi et al. 2017), to constrain the timing and duration of single or polymetamorphic events (e.g. Rubatto et al. 1998; Sandmann et al. 2014) and to investigate crystal growth and transport mechanisms in metamorphic rocks (e.g. Daniel and Spear 1999; Spear and Daniel 2001). Depending on the different abilities of each mineral to re-equilibrate, the retrieved information provide discrete snapshots of the rock metamorphic history (Spear and Selverstone 1983). The study of porphyroblasts, such as garnet, is advantageous because they have higher probability to record multiple stages of the microtextural and microchemical evolution of the host sample (Ketcham and Carlson 2012).

Garnet occurs in a large variety of rock types with a wide span of chemical compositions ranging from ultramafic to felsic (Baxter et al. 2013). Stability and *P–T* growth conditions of garnet spans from ~300 to ~2000 °C and from atmospheric pressure to ~250 kbar (Baxter et al. 2013). Garnet zoning composition is dependent on *P–T* growth conditions (Daniel and Spear 1999; Tirone and Ganguly 2010), on the reactive bulk chemistry (Marmo et al. 2002; Lanari and Engi 2017) and on the water content in the system (Konrad-Schmolke et al. 2006). Because intracrystalline diffusion of divalent cation in garnet is slow at low to middle metamorphic temperatures (Carlson 2006; Vielzeuf et al. 2007; Caddick et al. 2010), mineral interior can be effectively isolated from chemical re-equilibration with the matrix during garnet growth (Spear 1988; Marmo et al. 2002). These features make garnet a robust mineral for thermobarometry. However, proper interpretation of the mineral archive requires good knowledge of the mechanisms and the kinetics involved during syn- and post-garnet growth (Ketcham and Carlson 2012).

Additional to major and trace element zoning, investigation of stable and radiogenic isotopes in garnet provides information on the environment of mineral growth and its absolute age. Stable isotope fractionation in mineral depends on temperature and the bulk oxygen composition of the host rock (Faure and Mensing 2005). Thus, oxygen isotope profiles across garnet mineral allow evaluating variations in temperature and fluid-rock interaction at the time of garnet growth. The preferential partitioning of heavy rare earth elements (HREE) in garnet, together with their slow diffusivity makes it a common minerals for Lu-Hf geochronology (e.g. Duchêne et al. 1997; Smit et al. 2013). The quality of the isochron (Scherer et al. 2001; Kelly et al. 2011; Sandmann et al. 2014) together with the trace element zoning (Konrad-Schmolke et al. 2008b) have to be thoroughly

evaluated for correct age interpretation. The combination of petrology and chronology methods on garnet make this mineral a favourite petrochronometer (Baxter et al. 2017).

Garnet porphyroblasts with complex internal zoning were investigated within the Grt-schist from the Theodul Glacier Unit (TGU). The large size of the garnet crystals posed a challenge and a multi-method approach at multi-scale was necessary. The external domains of the garnet porphyroblasts show similar chemical zoning and oxygen isotopic variation than garnet from other lithologies of the TGU (Chapter 2 and 3). However, the garnet core displays a unique texture and chemistry, and Lu-Hf geochronology returns a puzzling Jurassic date. These important discrepancies raise questions on the pre-Alpine history of the TGU.

2. GEOLOGICAL SETTINGS AND PETROLOGICAL DESCRIPTION

The TGU is a 2 km^2 metasedimentary volcaniclastic sequence embedded within the meta-ophiolites of the Zermatt-Saas Zone (ZSZ). A detailed filed description is provided in Chapter 1. Four main lithologies compose the TGU: mafic fels, Cld-schist, mafic schist and Grt-schist (Chapter 1). The latter typically show cm-sized garnet and often occurs close and/or around layers and boudins of mafic fels. The rock foliation is defined by the mineral assemblage quartz-phengite-paragonite-zoisite, with scarce relicts of amphibole (Table 1). The accessory phases in the rock are apatite, zircon, graphite, pyrite rutile and titanite, with rutile crystals stretched along the main foliation. Retrogression occurs locally and is marked by scarce poikilitic albite, chlorite that usually rims garnet and titanite wrapping rutile. Despite the low content of sulphides observed in the rock, active superficial weathering gives a typical rusty tint to the rock (Fig. 1a).

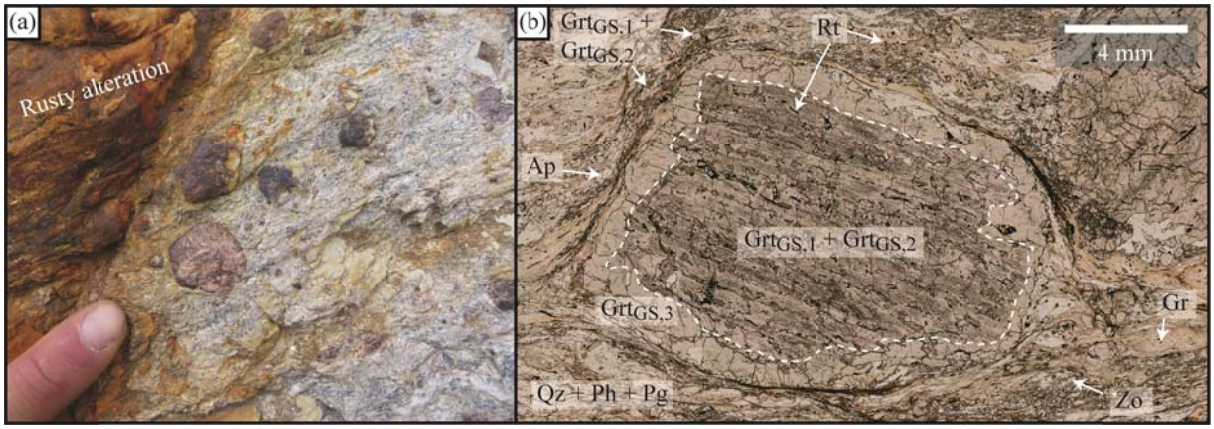

Figure 1: Grt-schist (a) outcrop photograph, and (b) sample microphotograph. Mineral abbreviations follow Whitney and Evans (2010).

Garnet has a bimodal size distribution and is characterized by the occurrence of spectacular cm-sized euhedral garnet porphyroblasts (Fig. 1). These garnets are highly fractured and are characterized by core-rim colour variation that is visible in hand specimen and thin section (Fig. 1b). The lighter thin rim is barren of inclusions, whereas the core is inclusion rich. Small rutile needles

aggregates aligned perpendicularly to the mineral growth direction are observed along the mineral core-rim transition. The minerals included in garnet are rutile, zircon, zoisite, quartz, chloritoid, graphite and pyrite. Their overall alignment is not necessarily parallel to the rock main foliation and the inclusion pattern varies from sample to sample. The rim of the garnet porphyroblasts is composed of numerous sub-crystals, forming a fractal front. The smaller garnets found in the matrix have a size ranging from few hundreds µm to mm in diameter and can be rounded or euhedral.

Sample	Latitude	Longitude	Lithology	Mineral assemblage	
				Major phases	Minor phases
Z16TB20	45°58'17''N	7°42'38''E	Grt-schist	Grt, Qz, Ph, Pg	Gr, Rt, Zo, Chl, Ap
Z16TB30A, B, C, D	45°58'04"N	7°42'53"E	Grt-schist	Single grain	-
Z16TB31, B	45°58'04"N	7°42'53"E	Grt-schist	Grt, Ph, Pg, Qz, Zo	Cld, Amp, Chl, Py, Rt, Ttn, Gr, Ap
Z17TB03A	45°58'17"N	7°42'38"E	Grt-schist	Grt, Ph, Pg, Qz	Zo, Rt, Ttn, Gr, Chl, Ap

Table 1: Sample list with geolocation and mineral assemblage.

3. ANALYTICAL METHODS

Details of methods for scanning electron microscopy, electron micro probe analysis, garnet equilibria modelling, Zr-in-rutile thermometry and Lu-Hf geochronology are reported in Chapter 2.

For *trace element analysis*, the general method are in Chapter 2. Specific parameters for the samples measured in this Chapter are: (1) For the garnet single point measurements, the accuracy on secondary standard was better than 10% for all elements. (2) Rutile was ablated on the Resonetics RESOlutionSE 193nm excimer laser system at 5 Hz and a fluence of 3 $J \cdot cm^{-2}$. Accuracy on secondary standard NIST 612 was within 10% for all elements but 20% for Zr. (3) For garnet trace element maps the laser was operated at a repetition rate of 10 Hz, a fluence of 7 $J \cdot cm^{-2}$ and a continuous scan speed of 22 µm/s, using a beam diameter of 16 µm. Line spacing was adapted accordingly to the beam diameter. A total of 38 elements were measured for a total sweep time of 0.47 s, where dwell times were 0.01 s for most masses with the exception of for LREE (from La to Gd = 0.02 s), and Hf (0.03 s).

For *oxygen isotope analysis*, the general method are in Chapter 3. For the garnet analysed in this Chapter, the matrix bias correction on the $\delta^{18}O$ of individual analyses ranges typically between -0.62 and 1.21 ‰, and is mainly or exclusively related to the grossular component. The internal uncertainty on individual oxygen isotopic analyses ranges between 0.11 and 0.32 ‰ (2σ), whereas the total uncertainty that includes the repeatability of the primary standard and the residuals on the matrix correction curve is 0.31 to 0.38 ‰ (2σ). Therefore, as in Chapter 3, the final uncertainty on average values is forced to be no less than 0.3‰ to account for accuracy.

The carbonaceous material was analysed by *Laser Raman spectroscopy* at the Institute of Geological Science (University of Bern) with a Horiba Jobin-Yvon LabRam HR-800 instrument consisting of an Olympus BX41 confocal microscope (x100 objective) attached to a 800 mm focal-

length spectrograph. A green Nd-YAG laser with wavelength of 532.12 nm, 1-3 µm beam diameter and a sample power of about 4-5 mW was used for signal excitation. Acquisition time was 20 to 120 s and Raman shift was measured from 1100 to 1800 cm^{-1} targeting the first order band occurrence of carbonaceous material (Beyssac et al. 2002). Raman spectra are highly sensitive to the orientation of carbonaceous material due to its strong structural anisotropy (Katagiri et al. 1988; Wang et al. 1989; Compagnini et al. 1997). In the investigated samples, carbonaceous material in the matrix is aligned along the rock foliation or included in garnet, therefore samples were cut perpendicular to the foliation. Due to the probability to create artificial crystallinity through thin section making and polishing (Pasteris 1989) all the analysis were performed below the surface of the thin section (Fig. 2). A minimum of 10 grains were analysed per sample and per textural position. Temperatures were calculated following the method described in Beyssac et al. (2002a), which is applicable within a temperature range of 330-650 °C. The absolute precision of the method is ±50 °C due to uncertainties in temperature data used for calibration (Beyssac et al. 2004). Peak position, band amplitude and band width was determined using the software PeakFit 3.0 with a Voigt area function.

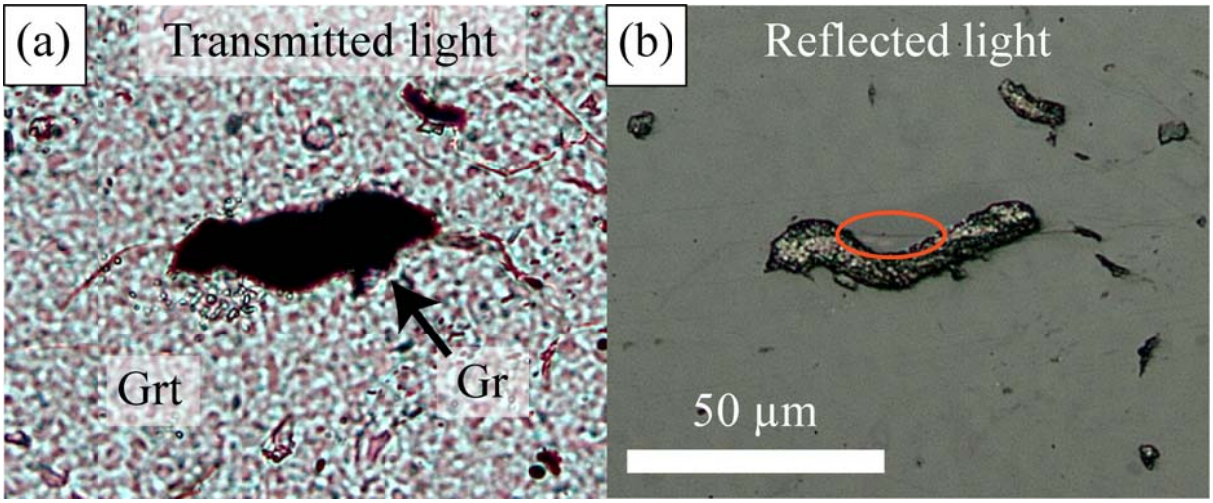

Figure 2: Microphotographs of carbonaceous material (CM) included in garnet in (a) transmitted light and (b) reflected light. The red circle indicates the part of the CM inclusion that is below the surface of the thin section and that was targeted for Raman spectroscopy of carbonaceous material (RSCM) measurement.

4. RESULTS

4.1. Garnet texture and chemistry

Elemental maps showing the major and trace element zoning in garnet of sample Z16TB31 and sample Z17TB03 are presented in Figure 3, 4, 5 and 6. The average major element composition of each domain is reported in Table S1 and the trace element analysis in Table S2.

In the garnet porphyroblasts, three domains are distinguished: a core $Grt_{GS,1}$ surrounded by a mantle $Grt_{GS,2}$ and a thin rim $Grt_{GS,3}$ (Fig. 3c,g). The two samples considered show undistinguishable major element compositional range for each garnet domain (Fig. 7a) and are consequently

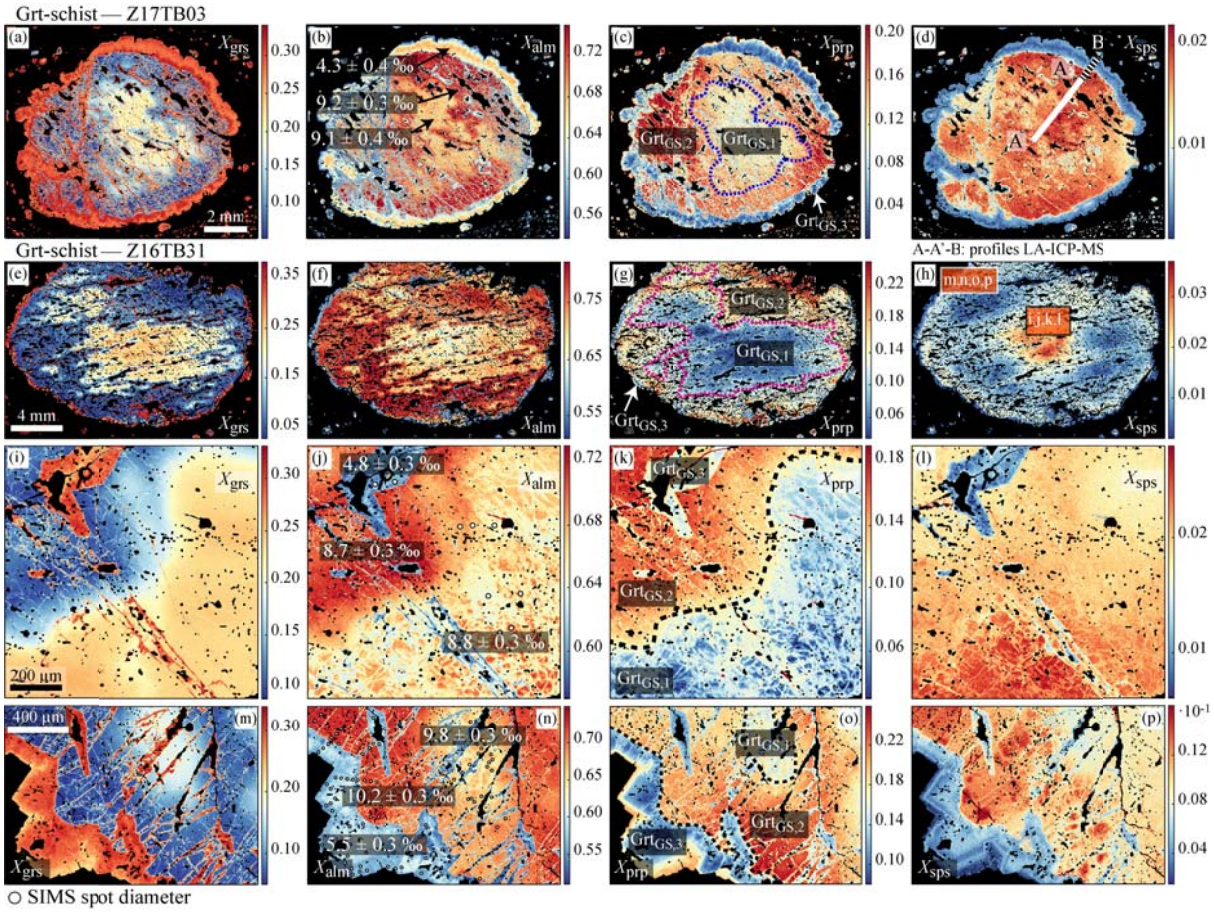

Figure 3: End-member compositional maps of garnet porphyroblasts from the Grt-schist sample Z17TB03 (a-d) and sample Z16B31(e-p). The maps in (i-l) and (m-p) are high-resolution map, which location is indicated on image (h). Average garnet $\delta^{18}O$ values are superimposed (b,j,n).

presented together. The garnet core $Grt_{GS,1}$ is enriched in grossular and almandine ($Alm_{65-70}Prp_{7-13}Grs_{18-24}Sps_{2-4}$), with a slight increase of Ca and Mn associated to a decrease of Fe and Mg outwards. In sample Z16TB31, two compositional groups within core region of $Grt_{GS,1}$ are visible in Fe and Mg but with homogeneous Ca (Fig. 3i-l). Island-type domains of 50-200 µm are Fe-rich and Mg-poor, surrounded by a Fe-poor and Mg-rich garnet matrix. The different domains within the core have sharp compositional contacts (<5 µm), and the transition between core $Grt_{GS,1}$ and mantle $Grt_{GS,2}$ is irregular with lobed shapes and island-type structures (Fig. 3a-h). The mantle $Grt_{GS,2}$ is depleted in Ca and enriched in Fe and Mg ($Alm_{70-76}Prp_{14-22}Grs_{4-10}Sps_{1-2}$) with respect to the core. The rim thickness ($Grt_{GS,3}$) varies irregularly from few microns to ~400 µm width. It is enriched in Ca and depleted in all other elements ($Alm_{54-60}Prp_{5-18}Grs_{23-38}Sps_{0.2-1}$) compared to the mantle $Grt_{GS,2}$. Within the rim, Ca concentration decreases outwards associated to an increase of Mg. In addition, rim $Grt_{GS,3}$ composition is also observed along irregular linear features (fractures) crosscutting both the core and the mantle (Fig. 3i-p). The transition from $Grt_{GS,3}$ to any of the previous garnet domain is sharp within less than 3 µm at maximum (limited by EPMA mapping resolution). The inclusion-free garnet described in the petrography (Fig. 1b) corresponds to the rim $Grt_{GS,3}$.

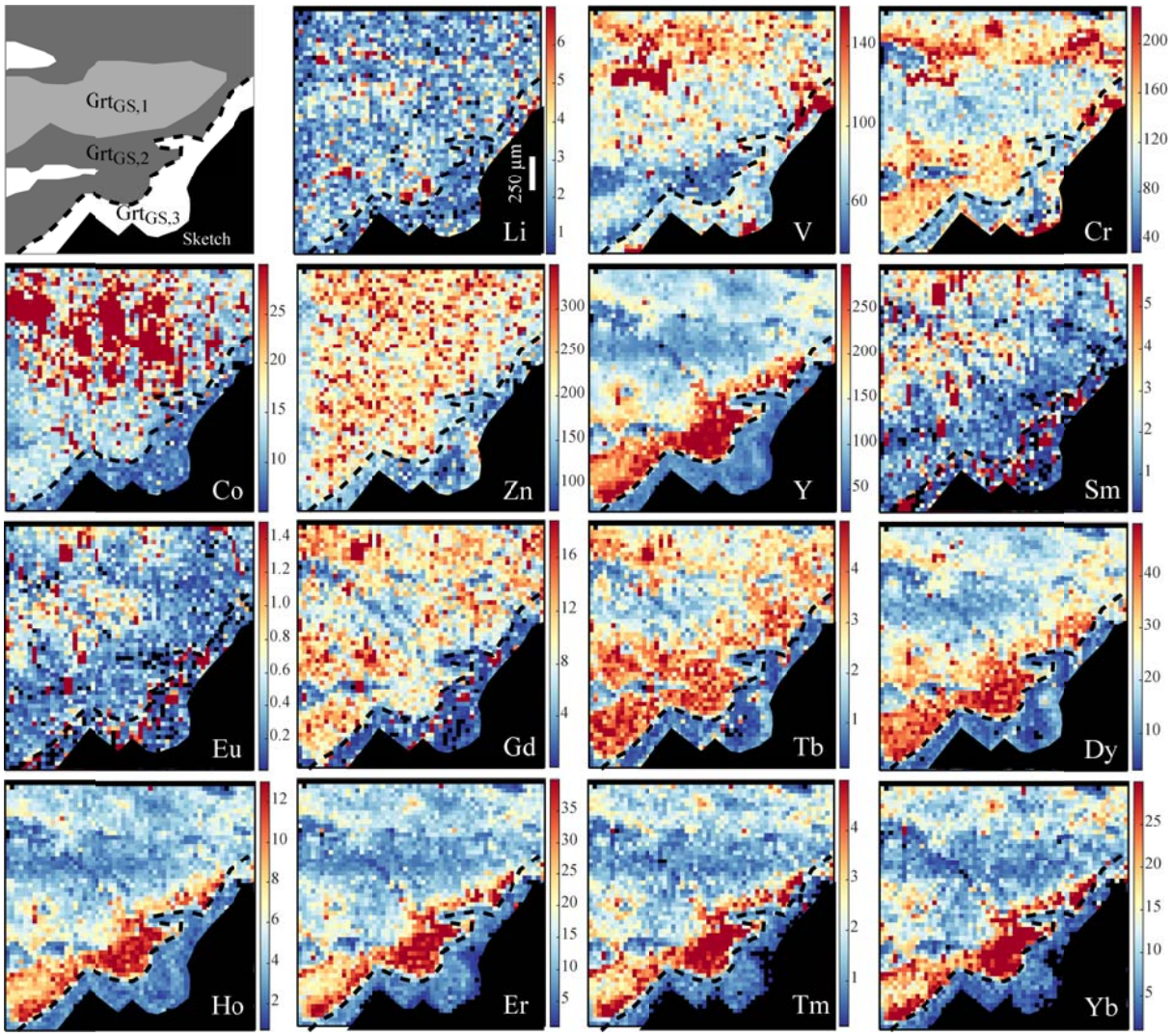

Figure 4: Trace element LA-ICP-MS compositional maps in garnet porphyroblast from sample Z16TB31. The area corresponds to Figure 3m-p, localized in Figure 3h. The sketch on the top left highlights the three different garnet domains.

In sample Z16TB31 trace element mapping (Fig. 4, 5a) was performed in the same area as the major element map shown in Figure 3i-l. The zoning reveals a sharp chemical transition between $Grt_{GS,2}$ and $Grt_{GS,3}$ coherent with the major element zoning. Notably the outer part of the mantle is the domain with the highest concentration in Y+HREE. Compared to the mantle ($Grt_{GS,2}$), the rim ($Grt_{GS,3}$) is depleted in Co, Zn, Y and MHREE and enriched in V, whereas Li and Cr show no evident zoning. The concentration of Y+HREE in the mantle domain increases outwards. The 16·11 µm^2 resolution of the map cannot resolve the complex imbrication of garnet domains in the mantle zone (Fig. 3i-l), as well as the small inclusions in the garnet (Fig. 1b). REE normalized pattern of sample Z17TB03 (Fig. 8a,b,c) show an increase in HREE from $Grt_{GS,1}$ to $Grt_{GS,2}$ and both domain show negative Eu anomaly. In the garnet core $Grt_{GS,1}$ Eu/Eu* (Eu/Eu*=$Eu_N/(Sm_N \cdot Gd_N)^{0.5}$) ranges between 0.3 to 0.7 and Gd_N/Lu_N (N= Chondrite normalized) between 0.3 and 0.6. In the mantle $Grt_{GS,2}$ the Eu/Eu* is more marked (0.2–0.3), whereas Gd_N/Lu_N varies between 0.2 and 1.2. The rim $Grt_{GS,3}$ has

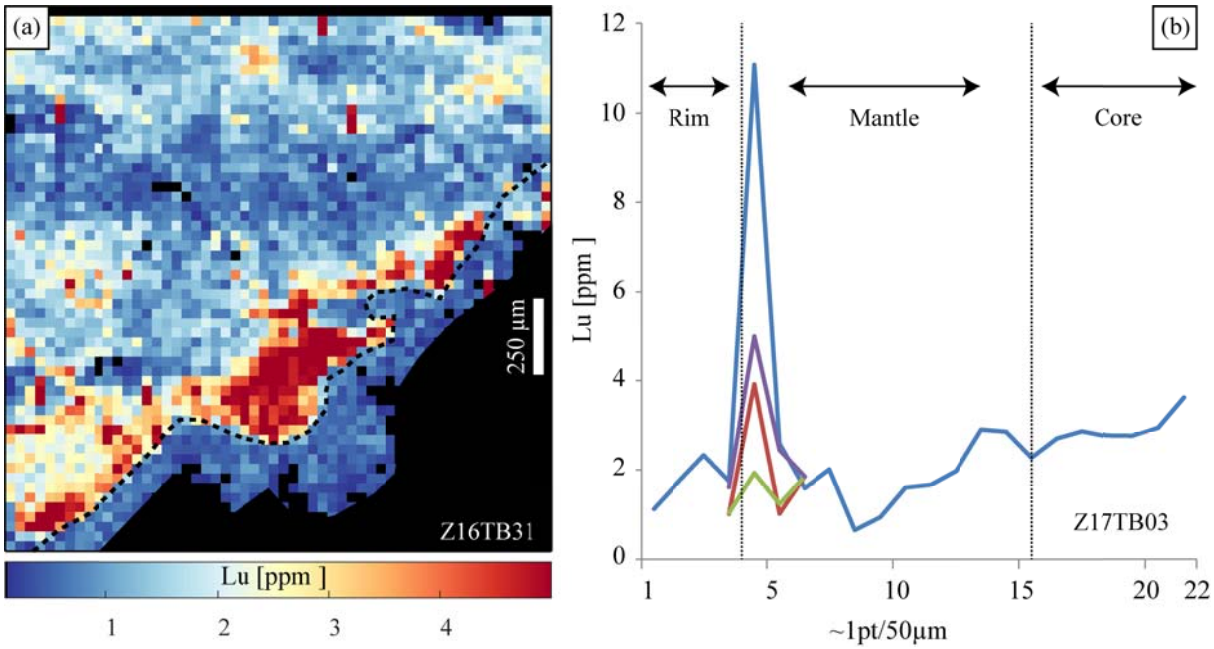

Figure 5: (a) Trace element LA-ICP-MS compositional maps of Lu in garnet from sample Z16TB31. The area corresponds to Figure 3m-p, localized on Figure 3h. (b) Trace element LA-ICP-MS compositional profiles of Lu in garnet from one grain of sample Z17TB03. This sample was dated by Lu-Hf.

lower HREE compared to the two other domains, with no Eu anomaly. The Eu/Eu* is averaged at ~0.9 and Gd_N/Lu_N at ~0.2. A profile across a garnet grain from sample Z17TB03 (Fig. 5b) shows a strong increase in Lu in the outer part of the mantle, similarly to what observed in sample Z16TB31 (Fig. 5a).

Only $Grt_{GS,2}$ and $Grt_{GS,3}$ compositions are observed in the small garnet grains distributed in the matrix (Fig. 7b), with two main types of zoning patterns: (1) breccia-like textures ($matrix_1$) with islets of $Grt_{GS,2}$ surrounded by a matrix of $Grt_{GS,3}$ (Fig. 6, 9); (2) regular zoning corresponding to the rim of the large porphyroblasts $Grt_{GS,3}$ ($matrix_2$, Fig. 9d). In the breccia-like garnet, the islets show xenomorphic to polygonal shape with sharp edges. Both Fe and Ca preserve weak concentric zoning

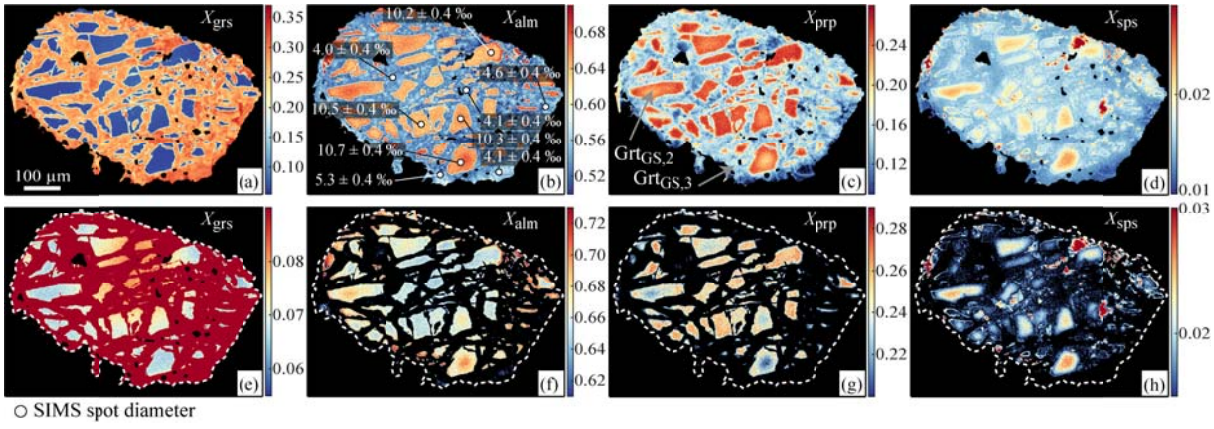

Figure 6: End-member compositional maps of matrix garnet from the Grt-schist sample Z16TB31. (b) Garnet $\delta^{18}O$ values are reported beside the SIMS spot analysis location (white circles). (e-h) The Because the contrasts for each end-member were adjusted to highlight zoning within the $Grt_{GS,2}$ domain, $Grt_{GS,3}$ appears black in (f-h).

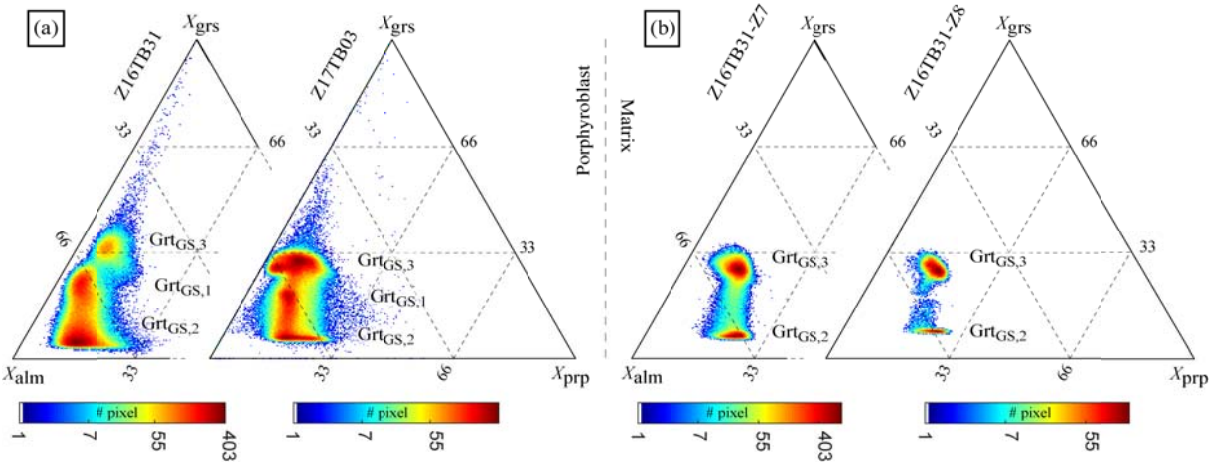

Figure 7: Ternary chemical diagram showing the range of garnet composition in X_{grs}-X_{alm}-X_{prp}. Composition areas are retrieved from EPMA maps processed with XMapTools (Lanari et al. 2014, 2019). (a) Areas were drawn on the basis of: 366,049 points (sample Z16TB31, Fig. 3e-h) and 445,827 points (sample Z17TB03, Fig. 3a-d). (b) Areas were drawn on the basis of: 230,731 points (sample Z16TB31-Z7, Fig. 6a-d) and 39,293 points (sample Z16TB31-Z8).

transition between the domain is sharp (<1 µm). BSE investigation revealed pyrite trailing around the islets of $Grt_{GS,2}$ enclosed in $Grt_{GS,3}$ (Fig. 9g,h). In sample Z17TB03, REE normalized pattern of breccia-like garnets reveal a factor 10 discrepancy between a HREE enriched core and HREE depleted rim. The core of these garnets ($matrix_1$) shows negative Europium anomaly (Eu/Eu* = 0.13) and Gd/Lu of ~0.4. As for the major element zoning, these REE variations are in agreement with the REE behaviour observed in the mantle and rim of the garnet porphyroblasts. BSE investigation of numerous $matrix_2$ garnet cut through the physical centre, never revealed islet with $matrix_1$ composition.

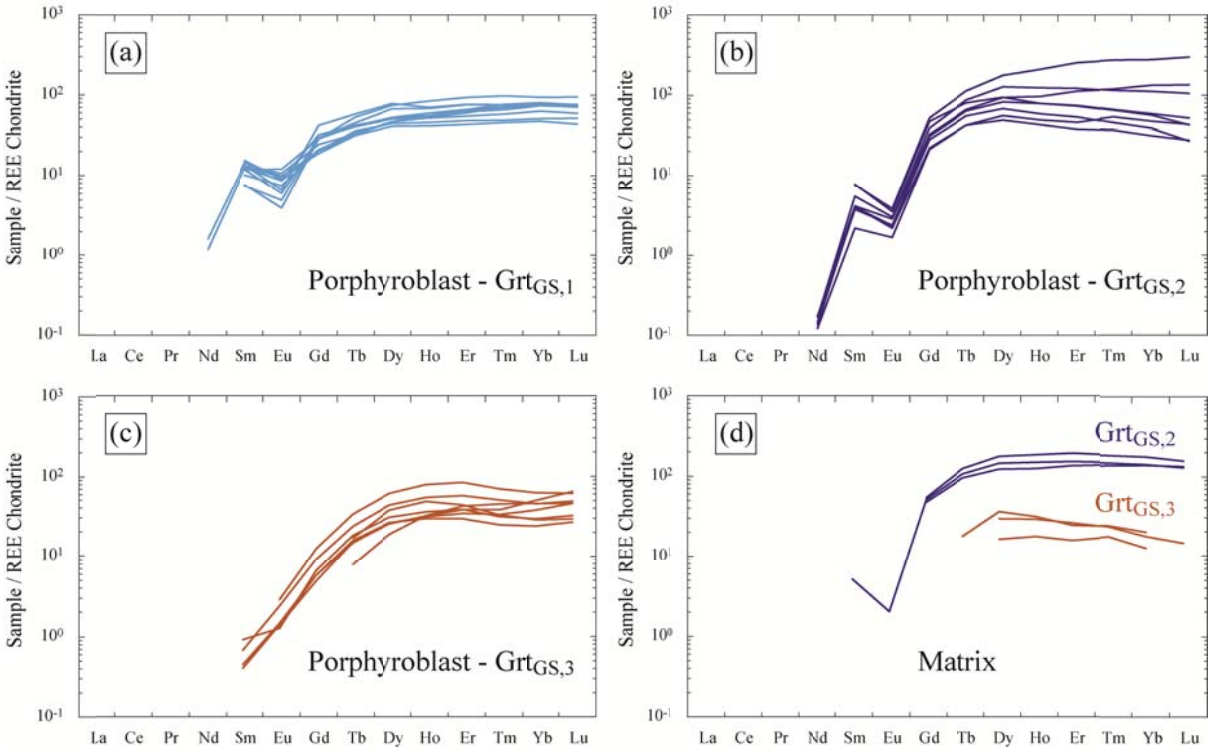

Figure 8: REE chondrite-normalized concentrations of garnet domains for sample Z17TB03. Normalization data: Taylor & McLennan (1985).

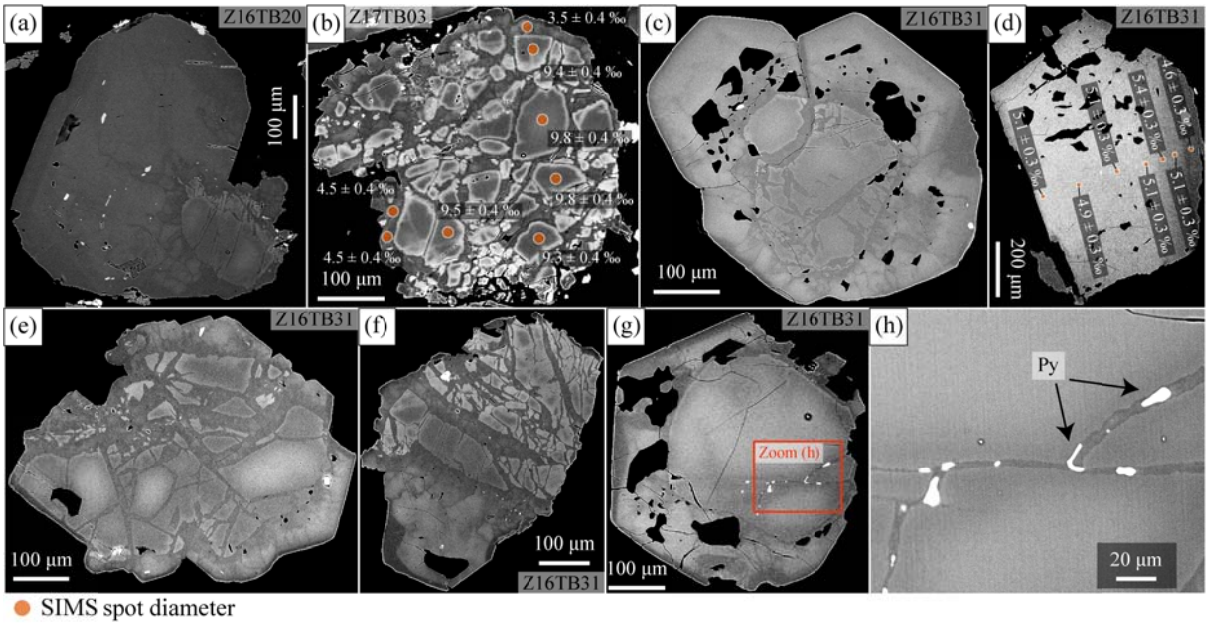

Figure 9: BSE images of matrix garnet crystals. Garnet $\delta^{18}O$ values are reported beside the SIMS spot analysis location (white circles). Image (h) is a zoom of the area in figure (g) indicated with the red rectangle. (h) Pyrite grains are distributed along the edges of $Grt_{GS,2}$ domain (see text).

4.2. Thermodynamic modelling on garnet

The *P–T* stability conditions of garnet formation in sample Z16TB31 were determined using the strategy outlined above, the results are shown in Figure 10. The high-resolution elemental maps (Fig. 3i-p: 1pixel = 2·2 µm^2) reveal small-scale chemical variations that are invisible in the overview map (Fig. 3e-h: 1pixel = 20·20 µm^2). The average chemical composition sampled in the overview map (Fig. 3e-h) for each representative chemical garnet domain (Fig. 3g, 6c, 10c) is presented in Table S1. The minor chemical zoning within $Grt_{GS,2}$ and $Grt_{GS,3}$ were probably controlled by sluggish kinetics rather than global chemical equilibrium and was therefore not considered. However, the core of the garnet porphyroblasts $Grt_{GS,1}$ exhibits complex patterns with spatial heterogeneities at the scale of 2-40 µm. These features suggest that equilibrium was not attained at this scale during growth or replacement of the core (Fig. i-l); consequently the *P–T* stability conditions for this growth stage cannot be determined using equilibrium thermodynamics. Two different initial bulk compositions were considered for modelling (Table S3): (1) the—pristine—bulk rock composition; (2) a reactive bulk composition, where 5 wt% (i.e. 3.75 vol%) of garnet with $Grt_{GS,1}$ composition was fractionated from the bulk rock composition.

In the simulations with an initial pristine bulk (Fig. 10a), the garnet mantle $Grt_{GS,2}$ is predicted to be stable at 548 ± 10 °C and 26.2 ± 2.0 kbar (TF: 0.002). The modelled mineral assemblage is Omp+Cld+Ph+Gln+Lws+Qz+Rt and contains 12.2 vol% of garnet. Simulation for the rim $Grt_{GS,3}$ is predicted to be stable at 549 ± 15 °C and 16.2 +0.5/-1.0 kbar (TF: 0.002). Previously formed garnet ($Grt_{GS,2}$) is slightly affected with a modelled 1.7 vol% resorption accompanied with up to 1.4 vol%

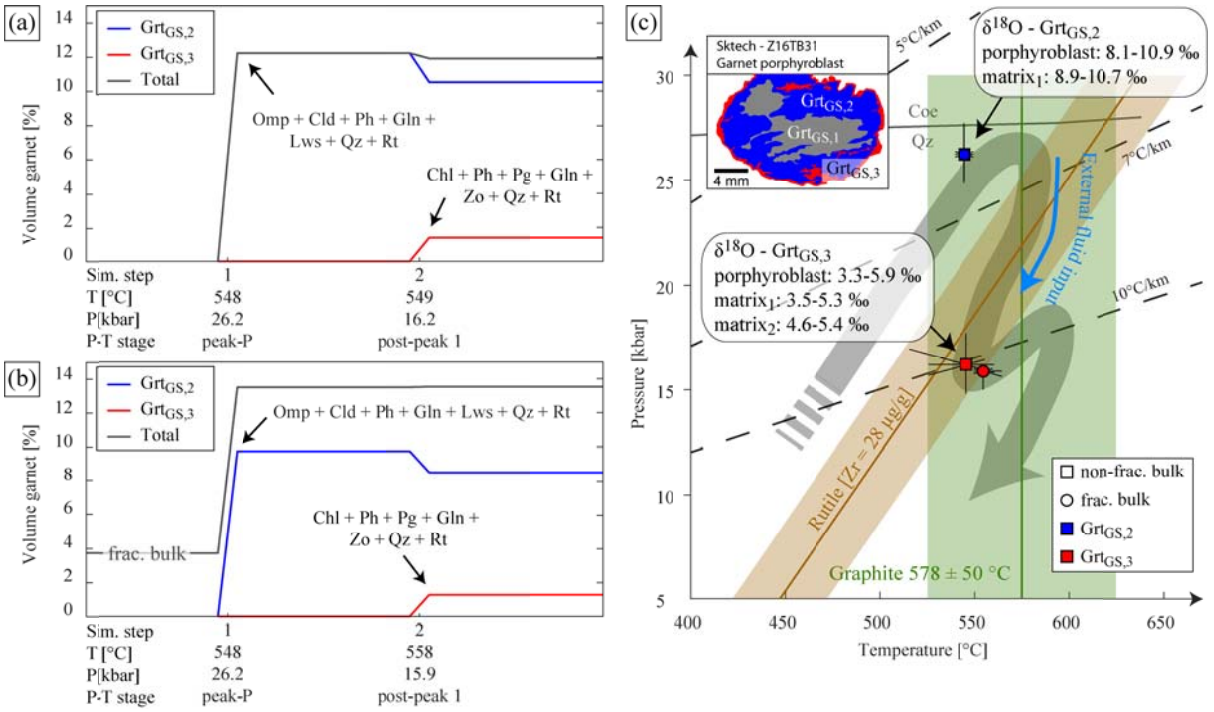

Figure 10: P–T conditions of garnet growth for two simulated scenarios (see text for details). (a,b) Garnet growth/resorption history obtained using GrtMod (Lanari et al. 2017). The volume fraction (in vol%) of each growth zone is plotted for each step. The curve labelled "Total" shows the evolution of the total amount of garnet in the system. The P–T conditions for each step of garnet growth are the optimal conditions determined by the model. The modelled mineral assemblage is indicated for each garnet growth step. (a) Non-fractionated bulk scenario. (b) Reactive bulk scenario, where 5 wt% (i.e. 3.75 vol%) of garnet with $Grt_{GS,1}$ composition was fractionated from the bulk rock composition (see text). (c) P–T path of the TGU from Chapter 2 with fluid rock-interaction event from Chapter 3. The thermobarometric results obtained for the different garnet domains (Grt-schist) are plotted as blue and red symbols. The sketch is based on the garnet of Figure 3e-h, where the three garnet domains are highlighted with a colour code. The ranges of $\delta^{18}O$ compositions measured on each garnet domain are indicated in the text boxes and reported as interval because multiple sample were analysed.

garnet fractionation of $Grt_{GS,3}$ (TF: 0.049). The overall modal abundance of garnet is 11.9 vol% and the modelled mineral assemblage is Chl+Ph+Pg+Gln+Zo+Qz+Rt. In the simulations with an initial modified bulk (Fig. 10b) a quantity of 3.75 vol% of garnet having $Grt_{GS,1}$ composition is fractionated in the system to obtain the first reactive bulk composition. The garnet mantle $Grt_{GS,2}$ is modelled stable at 548 ± 10 °C and 26.2 ± 2.0 kbar (TF: 0.002). The modelled mineral assemblage is Omp+Cld+Ph+Gln+Lws+Qz+Rt and contains 9.8 vol% of garnet with $Grt_{GS,2}$ composition and an total garnet modal abundance of 13.5 vol%. Simulation for the rim $Grt_{GS,3}$ indicate garnet formation at 558 +15/-30 °C and 16.2 ± 2.0 kbar (TF: 0.002). Previously formed garnet ($Grt_{GS,2}$) is slightly affected with 1.2 vol% resorption accompanied with up to 1.3 vol% garnet fractionation of $Grt_{GS,3}$ (TF: 0.049). The overall garnet modal abundance is 13.5 vol% and the modelled mineral assemblage is Chl+Ph+Pg+Gln+Zo+Qz+Rt.

The results for the two simulations are similar. This indicates that the low fraction of garnet core fractionation in model (2) does not significantly affect the *P–T* conditions of stability for the

successive garnet domains. This is expected for small volume of garnet fractionated (Marmo et al. 2002; Konrad-Schmolke et al. 2008a; Moynihan and Pattison 2013; Lanari and Engi 2017). By contrast, a relatively large volume of mantle needs to be fractionated to model the rim $Grt_{GS,3}$.

4.3. Thermometry of carbonaceous material

Carbonaceous material (CM) from three samples were investigated (sample Z16TB20, Z16TB30C and Z16TB31B) aiming to procure a first independent constrain on the temperature (Fig. 10c). The CM was either found as inclusion in the garnet porphyroblasts or in the matrix (Fig. 1b, Table 2). The uncertainty on the temperature for each area investigated, i.e. either inclusion in garnet or matrix, is reported as standard deviation. For the CM measured as inclusion in the garnet, calculated temperatures by Raman spectroscopy of carbonaceous material (RSCM) are respectively 578 ± 19°C (sample Z16TB20), 571 ± 28°C (sample Z16TB30C) and 564 ± 24°C (sample Z16TB31B). The estimated temperatures for the CM found in the matrix are 536 ± 36°C (sample Z16TB20) and 575 ± 9°C (Z16TB31B). These results show a homogeneous CM crystallinity within uncertainty across all samples, and between CM included in garnet and CM from the matrix in sample Z16TB20 and Z16TB31B.

Sample	N spectra	N Grains	R2		T [°C]	
			Average	SD	Average	Error
Garnet						
Z16TB20	84	13	0.14	0.04	578	50
Z16TB30	27	10	0.16	0.06	571	50
Z16TB31	42	16	0.17	0.05	564	50
Matrix						
Z16TB20	29	10	0.24	0.08	536	50
Z16TB31	24	11	0.15	0.02	575	50

Standard deviation (SD)

Table 2: Temperature calculations from Raman spectroscopy of carbonaceous material.

4.4. Zr-in-rutile thermometry

Among the studied samples (sample Z16TB30A, Z16TB30B, Z16TB30D), rutile grains range in size from few microns to 100 µm and are either located within the matrix along the foliation or as inclusion in the garnet porphyroblasts (Fig. 1b). Analysed grains were carefully selected avoiding possible contamination by inclusions and, for the minerals included in garnet, avoiding proximity with fractures. Analyses (Table S4) were screened for contamination from inclusions based on high Si, Na, Al, Mn, Fe, Y, Sn, Hf and Zr contents. Rutile was found as inclusion in every chemical domain of the garnet porphyroblasts and shows a homogeneous Zr concentration irrespective to the

inclusion position (Table 3). The average concentration of Zr in rutile included in garnet is between 30 ± 5 and 26 ± 4 µg/g in the three samples, whereas grains from the matrix show an average of 27 ± 2 µg/g.

Lithology	Sample	N	Zr-Rutile [µg/g]				Pressure [kbar]	Pressure correction [°C]	Zr-in-Rutile T [°C]			
			Min	Max	Average	SD			Min	Max	Average	Error
Inclusion in garnet												
Grt-schist	Z16TB30A	6	27	38	30	5	27	124	605	625	610	25
Grt-schist	Z16TB30B	4	22	29	26	3	27	124	594	610	603	25
Grt-schist	Z16TB30D	16	18	37	26	4	27	124	585	623	603	25
Matrix												
Grt-schist	Z16TB30B	2	25	28	27	2	27	124	602	607	605	25

Number of grain analyzed (N), Minimum (Min), Maximum (Max), Standard Deviation (SD)

Table 3: Average Zr concentration in rutile and Zr-in-rutile thermometry calculation after Ferry and Watson (2007).

Zr-in-rutile thermometry was calculated assuming a pressure of 26.5 kbar according to results of the thermodynamic simulation (Fig. 10c). Averaged temperature (Table 3) for rutile found as inclusion in garnet are 610 ± 25 °C for sample Z16TB30A, 603 ± 25 °C for sample Z16TB30B, and 603 ± 25 °C for sample Z16TB30D. The rutile grains analysed in the matrix yield an average temperature of 605 ± 25 °C (sample Z16T30B). These results show homogeneous temperature of rutile crystallization among the sample considered.

4.5. Oxygen isotope of garnet

The oxygen isotopic composition of garnet was measured in situ to identify variations in $\delta^{18}O$ associated to major element zoning in two samples (sample Z16TB31 and Z17TB03). The results of $\delta^{18}O$ analysis are shown in Figure 11 and plotted against X_{grs} garnet content as an indicator of chemical zoning. Individual oxygen isotopic measurements are presented in Table S5. Despite the complex chemical zoning observed in the core and the mantle of the garnet porphyroblasts, the $\delta^{18}O$ variations are minor in the two analysed samples (Fig. 3b,j,n). The core has an average composition of 9.2 ± 0.3 ‰ in sample Z16TB31 and 9.1 ± 0.4 ‰ in sample Z17TB03, whereas the averaged mantle value is 9.8 ± 0.3 ‰ in sample Z16TB31 and 9.2 ± 0.3 ‰ in sample Z17TB03. The sharp chemical transition between mantle and rim is coupled to a strong decrease in $\delta^{18}O$ of ~5 ‰ (Fig. 3b,n), where the rim has an average composition of 5.3 ± 0.3 ‰ and 4.3 ± 0.4 ‰ in sample Z16TB31 and Z17TB03 respectively. The fractures across the core and mantle that are filled with rim $Grt_{GS,3}$ composition show a low $\delta^{18}O$ value similar to that of the rim, with an averaged value of 5.5 ± 0.3 ‰ in Z16TB31 and 4.4 ± 0.4 ‰ in Z17TB03.

Comparable $\delta^{18}O$ variation are observed in the breccia-like $matrix_1$ garnet with a significant drop in $\delta^{18}O$ of ~5 ‰ between the brecciated islets having $Grt_{GS,2}$ composition (10.1 ± 0.3 ‰ in Z16TB31 and 9.6 ± 0.4 ‰ in Z17TB03) and the surrounding matrix with $Grt_{GS,3}$ composition (4.7 ± 0.3

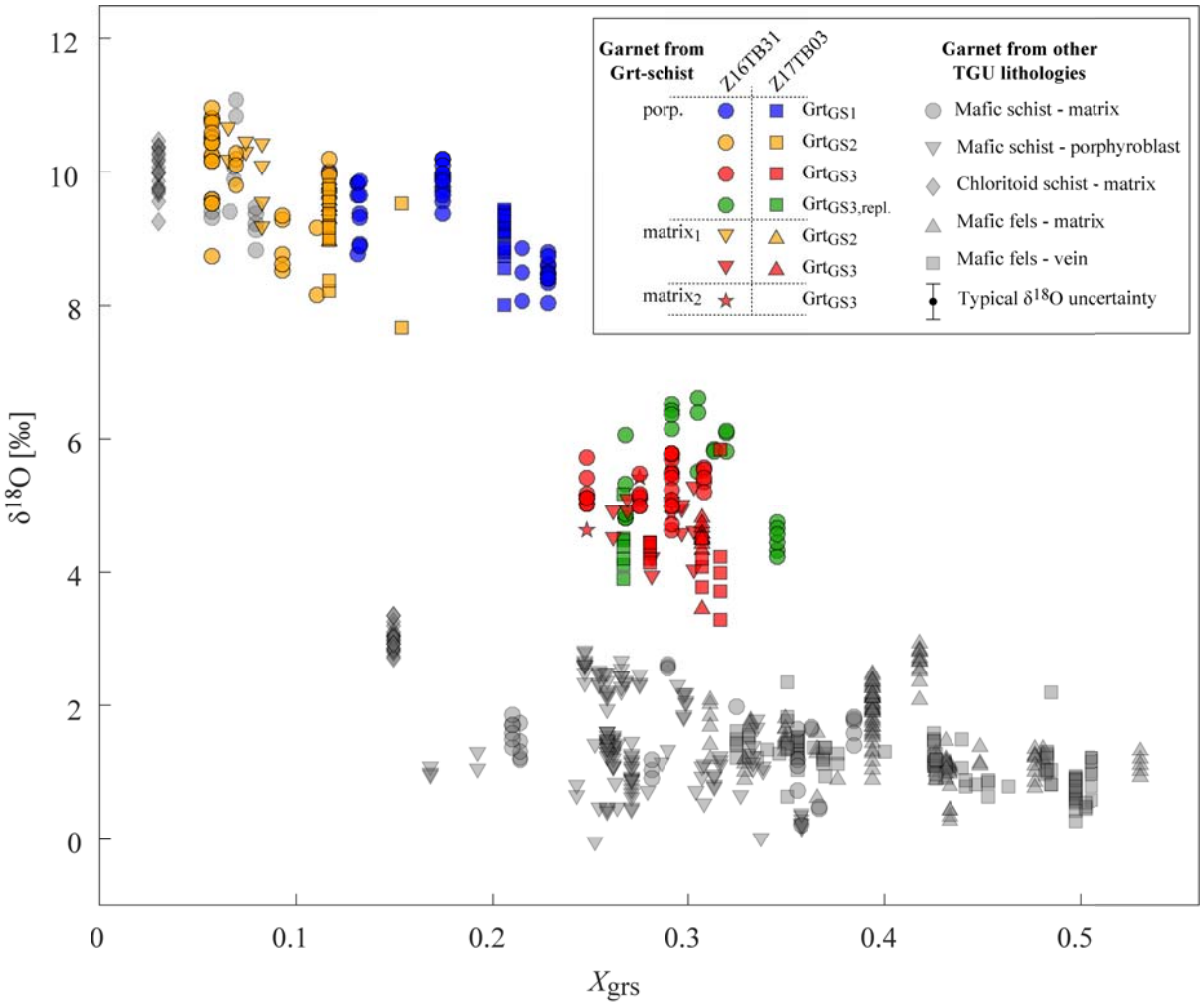

Figure 11: Binary diagram X_{grs} vs $\delta^{18}O$ for garnet analysed in situ. Garnet composition for matrix correction was taken from the chemical maps (see text). The uncertainty for X_{grs} is smaller than the symbol size, whereas the typical uncertainty for $\delta^{18}O$ is reported in the legend.

‰ in sample Z16TB31 and 4.5 ± 0.4 ‰ in sample Z17TB03). The chemically homogeneous matrix$_2$ garnets (Fig. 9d) show a low $\delta^{18}O$ average value of 5.0 ± 0.3 ‰ (sample Z16TB31), similar to the low $\delta^{18}O$ value of the rim from the garnet porphyroblasts and matrix of matrix$_1$ garnets.

The significant decrease in $\delta^{18}O$ from garnet core+mantle (Grt$_{GS,1}$ + Grt$_{GS,2}$) to rim is observed in both the garnet porphyroblast and the matrix$_1$ garnet. The lower $\delta^{18}O$ values always correspond to the chemical domain Grt$_{GS,3}$.

4.6. Lu-Hf garnet geochronology

The garnet porphyroblasts from sample Z17TB03 were dated because the cm-sized grains were optically the least altered and mostly free of matrix material sticking to the exterior of the grain rim. High quality mineral separates were obtained by hammering a cm-sized garnet porphyroblast previously embedded within parafilm. After grain size reduction, two groups were established based on the colour of the garnet fragment (Fig. 12a,b,c,d) and carefully prepared under

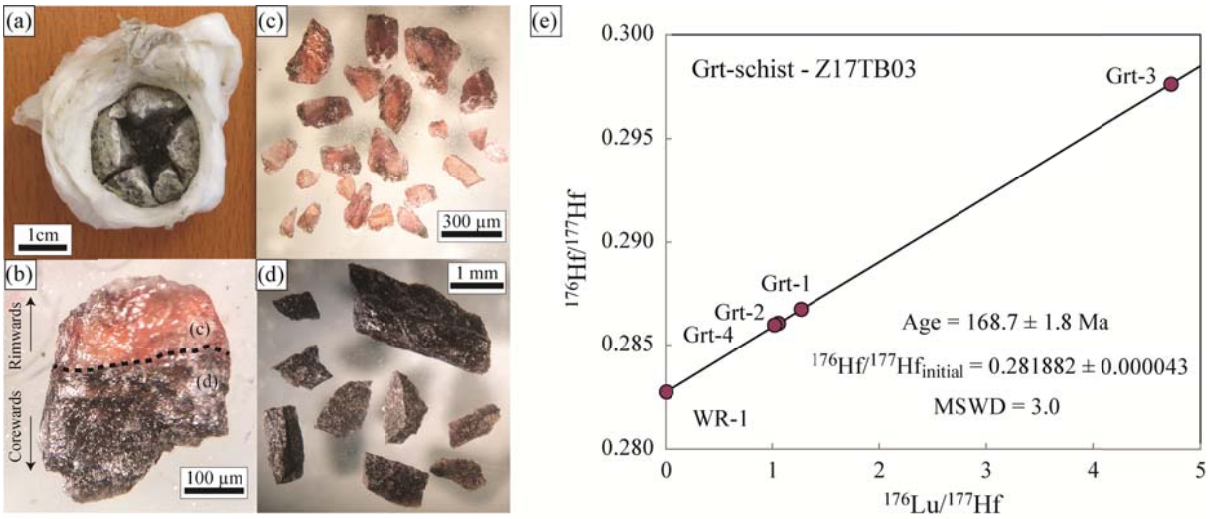

Figure 12: Lu-Hf dating of sample Z17TB03 (a) Garnet porphyroblast with radial cracks after hammering. Prior to fracturing, the sample was embedded in parafilm. (b) Colour change in the garnet fragments is expected to indicate core-rim transition (see text). (c-d) Garnet fragments used for Lu-Hf dating. (e) Lu-Hf isochron. The uncertainties on individual points are smaller than the symbols.

a binocular microscope. The core-mantle of the garnet shows a dark purple tint, whereas the rim is rather light pink and translucent. These colour variations are probably associated to the transition between the inclusion-rich core/mantle and the inclusion-poor rim (Fig. 1b), coupled with strong garnet chemical zoning (Fig. 3). It was impossible to differentiate core and mantle mineral fragments. Three core-mantle fractions and one rim fraction were considered for the analysis (Table 4). The analyses yielded a Lu-Hf age of 168.7 ± 1.8 Ma (mean square weighted deviation (MSWD) = 3.0; Figure 12e). The relative standard deviation returned extremely good precision of ±0.5 % RSD.

	Concentration		Isotope ratios				Final data			
Sample fraction	Lu [ppm]	Hf [ppm]	$^{176}Lu/^{177}Hf$	2SD	$^{176}Hf/^{177}Hf$	2SD	Lu-Hf age (Ma)	MSWD	$^{176}Hf/^{177}Hf_{initial}$	2SD
Grt-schist - Z17TB03										
Grt-1	0.7570	0.08430	1.27300	0.003000	0.285904	0.000040				
Grt-2	0.7240	0.09686	1.05900	0.003000	0.285229	0.000043				
Grt-3	3.364	0.10000	4.73100	0.012000	0.296772	0.000041				
Grt-4	0.8480	0.11700	1.02300	0.003000	0.285141	0.000026				
WR-1	0.5100	8.2730	0.008817	0.000022	0.281897	0.000018				
					All analyses included:		168.7 ± 1.8	3.0	0.281882	0.000043

Standard deviation (SD)

Table 4: Lu-Hf isotope data and apparent age.

5. DISCUSSION

5.1. Similarity and discrepancy with other samples of the TGU

Equilibrium thermodynamics applied to garnet, white mica and chloritoid from different lithologies of the TGU constrained the Alpine metamorphic *P–T* path shown in Figure 10c (see details in Chapter 2). The *P–T* conditions of stability for the $Grt_{GS,2}$ domain of garnet from the Grt-schist, i.e. core of the $matrix_2$ garnet and the mantle of the garnet porphyroblasts, are in good agreement with the peak-*P* stage determined at 26.5 ± 1.5 kbar and 580 ± 15 °C. The garnet rim ($Grt_{GS,3}$) *P–T* stability conditions matches with the subsequent first isothermal decompression stage of the TGU at 15.5 ±

1.0 kbar and 555 ± 15 °C. The observed mineral assemblage in the matrix matches with the prediction of the simulation for the last stage. Relicts of peak-*P* mineral assemblage predicted by equilibrium thermodynamic, such as chloritoid, were observed as inclusion in garnet. The successive reheating stage of ~30 °C is not recorded in the garnet from the Grt-schist, probably because the simulations performed in this study focused on first-order major element zoning, particularly within the rim domain. As observed in the garnet with discontinuous chemical zoning of both the mafic schist and the Cld-schist, the core of the matrix$_1$ garnet crystals is predicted stable at peak-*P* stage, whereas the rim recorded the first isothermal decompression stage (Chap. 2). Moreover, the detected variation in normalized REE pattern is as well observed in the garnet from the Grt-schist (Fig. 8), where the sharp chemical transition rimwards is marked by the disappearance of the Eu anomaly and a lowering in HREE concentration. These features were either interpreted as an inheritance from the bulk rock composition or to element partition coefficient among phases present in the stable assemblage at the time of garnet growth (Chap. 2).

Two independent constraints on temperature were attempted by RSCM and Zr-in-rutile thermometry. The calculation of Zr-in-rutile thermometry is pressure dependant (Ferry and Watson 2007). Our calculation was performed assuming peak-*P* condition (26.5 ± 1.5 kbar), but the rutile could have crystallized during the prograde path at lower pressure (Chap. 2). Consequently, the calculated average temperature of 605 ± 25 °C, which is similar for rutile included in garnet and rutile in the matrix, is to be considered as maximum estimates for the prograde to peak-*P* path. The graphitization process is irreversible and is strongly dependant on temperature variation, where the degree of crystallinity of carbonaceous material testifies the maximum temperature underwent by the system (Beyssac et al. 2002). Therefore, the temperature of 578 ± 50 °C from the RSCM thermometry is taken as the maximum temperature reached by the Grt-schist. There is no indication that any of the rutile and CM was derived from detrital inputs. Instead, for both Zr-in-rutile and RSCM thermometry there is no notable difference between the estimates for inclusions in garnet and grains in the matrix, confirming that the high-pressure evolution of the TGU unit was within a short temperature interval of less than 50–150°C. The RSCM temperatures for the TGU samples are within uncertainty of those obtained for the ZSZ (Negro et al. 2013) and the Monviso ophiolites (Angiboust et al. 2012), which confirms that TGU and ZSZ underwent at least the same maximum metamorphic temperatures during Alpine deformation.

The similarities between the garnet in the Grt-schist and garnet from other TGU samples go beyond the *P*–*T* stability conditions. It was shown in Chapter 3 that the sharp chemical zoning between garnet core and rim in the other types of schists was coupled to a significant drop in oxygen isotope of several per mill, which is also observed in the garnet from the Grt-schist. Even if the drop

is slightly less pronounced in the garnet from the Grt-schist (~5 ‰) than in the one detected garnet in the mafic shist and the Cld-schist (~8 ‰), the magnitude of the isotopic modification is sufficient to invoke fluid-rock interaction with an open system behaviour (Kohn 1993; Vho et al. 2020). This oxygen isotopic variation confirms that scenario proposed in Chapter 3 that the TGU was pervasively affected by external fluids with low $\delta^{18}O$ value, most probably coming from the underlying serpentinites, during early decompression (Chap. 3). In the garnet breccia-like garnet of Grt-schist, trails of small sulphides are observed around the relict core islets and their formation could be related to externally derived or internally remobilized fluids.

In summary, the compositional and oxygen isotopic zoning, as well as the Alpine *P–T* evolution of the Grt-schist is comparable to that of other samples from the TGU story discussed in the previous chapters. However, two features of the garnet from the Grt-schist relate to a possible pre-Alpine geological evolution of the TGU. Firstly, the garnet prophyroblasts in the Grt-schist contains a core domain ($Grt_{GS,1}$) that is unique to this lithology (Fig. 7a). Indeed, garnet that presents a sharp chemical zoning between core and rim in the other type of shists have a $Grt_{GS,2}$ core composition that corresponds to the mantle of the garnet porphyroblasts (Chap. 2, 3). Secondly and more notably, the Lu-Hf date for the Grt-schist is unexpected and different from any previous age result from zircon (U-Pb) and garnet (Lu-Hf) in the TGU.

5.2. Garnet porphyroblasts core domain

The relicts core domains in the garnet porphyroblasts ($Grt_{GS,1}$) suggests that the original diameter of this garnet generation was already relatively large prior to $Grt_{GS,2}$ growth (Fig. 3a-h,m-p). In the core domain ($Grt_{GS,1}$) the Fe content of the islets is comparable to the one of the mantle domain ($Grt_{GS,2}$), whereas the matrix surrounding the islets has a lower Fe content. This observation indicates that different events may have contributed to the development of the internal complex zoning in the inner part of the garnet porphyroblasts. Within $Grt_{GS,1}$ domains, sharp chemical zoning is observed for Mn, Mg and Fe, whereas Ca is the only element showing no zoning. Intracrystalline cation diffusivity is strongly dependant on temperature (Caddick et al. 2010) and Ca is expected to have the lowest diffusion coefficient among divalent cation in garnet (Schwandt et al. 1996; Carlson 2006; Perchuk et al. 2009; Li et al. 2018). This favours the hypothesis that $Grt_{GS,2}$ formed through a replacement process, rather than being the product of partial volume diffusion relaxation between two chemically different domains. In the latter case, post-growth intracrystalline diffusion would most probably have affected the sharp chemical zoning in $Grt_{GS,1}$, which is not observed and improbable considering that the maximum temperature of ~600 °C and that intergranular diffusion is sluggish at these temperatures (Dodson 1973; Caddick et al. 2010). The alleged replacement of

$Grt_{GS,1}$ by $Grt_{GS,2}$ occurred at peak-*P* condition and affected at least the four major divalent cations (Ca, Fe, Mg and Mn). The mechanisms of this replacement may resemble what reported by previous studies (Erambert and Austrheim 1993; Kurz et al. 1998; Zack et al. 2002; Pollok et al. 2008; Putnis 2009; Putnis and Austrheim 2010; Putnis and John 2010; Ague and Axler 2016; Rubatto et al. 2020), but remain here poorly constrained and would deserve further investigation.

In the garnet porphyroblasts, the average $\delta^{18}O$ value of the core $Grt_{GS,1}$ is similar to that of the mantle $Grt_{GS,2}$ (Fig. 11). There is no specific constrain on the temperature for that garnet domain ($Grt_{GS,1}$) stability. However, the temperature estimate retrieved from rutile inclusion in garnet (605 ± 25 °C), assuming that the latter were not re-equilibrated, and from RSCM thermometry (578 ± 50 °C) are relevant for the garnet core (Fig. 10c). In this temperature range, the oxygen isotopic signature of a garnet growing in a closed-system at equilibrium will not vary more than ~1 ‰ (Fig. 13). This implies that the bulk $\delta^{18}O$ signature of the Grt-schist didn't change between the growth of the garnet core ($Grt_{GS,1}$) and that of the mantle ($Grt_{GS,2}$). Moreover, the bulk $\delta^{18}O$ composition of the Grt-schist retro-calculated from the measured garnet core+mantle $\delta^{18}O$ composition (see Chap. 3) is ~11 ‰ (Fig. 13). As proposed for the other type of schists in the TGU (Chap. 3), compared to pelitic rocks this bulk $\delta^{18}O$ is on the lower end of the typical detrital material bulk $\delta^{18}O$ range (Rumble et al. 1982; Bebout and Barton 1989; Cartwright and Barnicoat 1999) and must have been acquired before or at

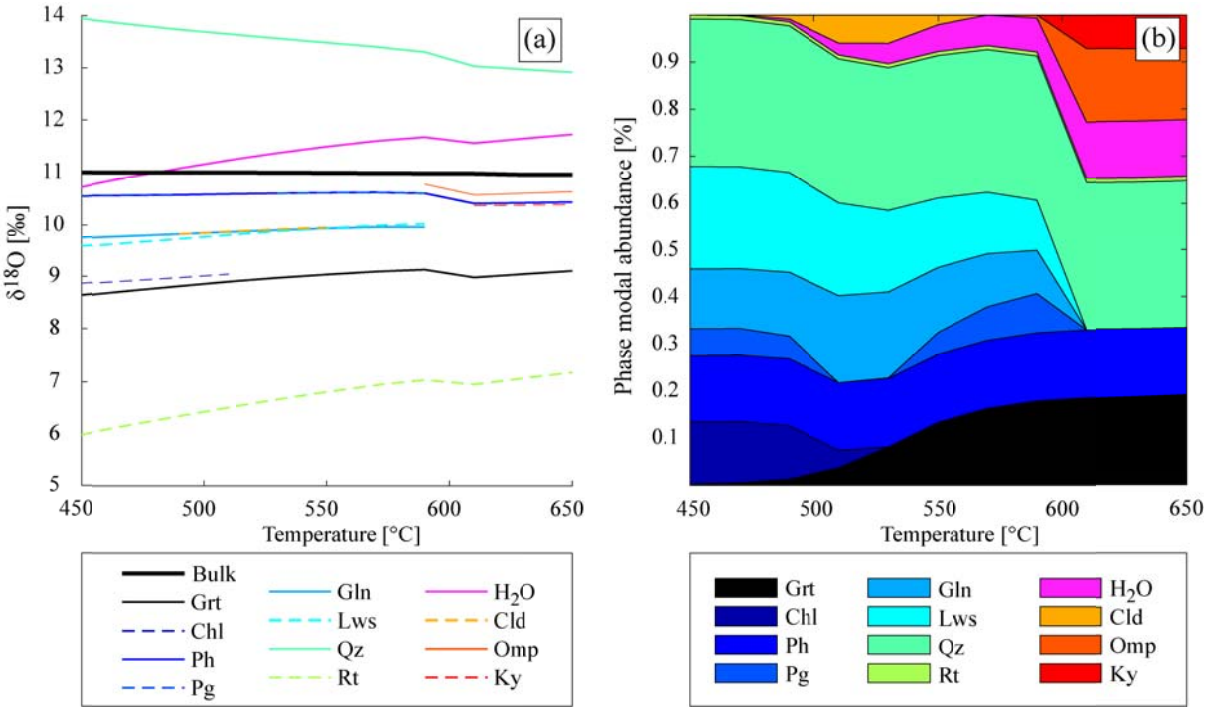

Figure 13: Output figures from PTLOOP (Vho et al. 2020) for sample Z16TB31 plotted against temperature. All the water released from the Grt-schist is removed from the system at each simulation step. Simulation was performed from 15 kbar and 450 °C, to 25 kbar and 650 °C, with 15 iterations (see text). (a) Evolution of $\delta^{18}O$ in the bulk and phases along the P–T path. (b) Phases modal abundance in equilibrium (normalised to 1) along the P–T path.

the inset of garnet growth ($Grt_{GS,1}$). The rather low bulk oxygen isotopic composition is in line with high-temperature seafloor alteration (Cartwright and Barnicoat 1999; Miller et al. 2001; McCaig et al. 2007) prior to Alpine metamorphism.

5.3. Critical assessment of the Lu-Hf date

The apparent Jurassic age of 168.7 ± 1.8 Ma is the first of this kind ever recorded by garnet in the Alps. Jurassic ages in the Alpine Pennine zone and within the meta-ophiolites, solely correspond to the crystallization of mafic oceanic magmas (Borsi et al. 1996; Bill et al. 1997; Rubatto et al. 1998). The quality of the isochron with high and variable $^{176}Lu/^{177}Hf$ and low MSWD support a significant age rather than inheritance or mixing of different age components. Yet, because of its uniqueness in the Alpine record, this result has to be cautiously evaluated.

The spread in $^{176}Lu/^{177}Hf$ (Fig. 12e) is in the typical range for garnet and allows speculating on the garnet domains sampled by each aliquot, especially the aliquot labelled “Grt-3”. Based on the light colour of the garnet fragments (Fig. 12b,c), the Grt-3 aliquot was sampled as rim, but surprisingly it has the highest $^{176}Lu/^{177}Hf$ value. The Lu concentration is a proxy for $^{176}Lu/^{177}Hf$ ratio where a higher ratio corresponds to high Lu concentration, as observed on Table 4. The Lu profile across a garnet porphyroblasts form this sample (Figure 5b) shows significant increase in Lu concentration in the outer part of the mantle domain. The same Lu enrichment in the mantle is also highlighted by the trace element map of garnet from sample Z16TB31 (Fig. 5a). The rim has a lower Lu average concentration compared to both the core and the mantle of the garnet porphyroblasts and is thus not expected to have a higher $^{176}Lu/^{177}Hf$ (Fig. 5b). Consequently, the high ratio measured for “Grt-3” is interpreted to have an important signal contribution from the outer mantle domain. This implies that: (1) the rim domain was not sampled alone; (2) garnet coloration alone is not a valid criteria to identify rim domains; (3) most likely, all the aliquots processed consist of mixed material with unconstrained modal abundance of each garnet domain; and (4) the complex Lu zoning revealed by trace element mapping argues for strong contribution of core and mantle domain to the Lu budget.

Zircon is the main Hf carrier in a rock (Scherer et al. 2000) and one has to consider its potential influence on the bulk rock as an inherited component. It was shown in Chapter 1 that every type of TGU lithology contained detrital zircons with similar Permian age and more specifically Grt-schist (sample Z16TB31) contained detrital zircons with minimum concordant rim age of 279.2 ± 5.2 Ma. Permian, or older zircon in sample Z17TB03 could have therefore influenced the $^{176}Lu/^{177}Hf$ and $^{176}Hf/^{177}Hf$ of the measured whole rock by lowering each of the two ratio (Scherer et al. 2000). The extrapolated initial $(^{176}Hf/^{177}Hf)_i$ value calculated with or without whole rock are similar within

uncertainty, they yield 0.281874 ± 0.000016 and 0.281902 ± 0.000043 respectively. This means that the isochron calculated on the basis of the garnet aliquots only is not influenced by the whole rock and that the inherited zircon observed in the matrix don't have a major influence on the Hf budget of the whole rock. This further implies that garnet equilibrated with a reservoir of Hf that was isotopically identical to that containing the detrital zircon, which could potentially be explained by two scenarios. On one hand, some of the zircons randomly dissolved into the matrix from which garnet crystallized. On the other hand, garnet might not have isotopically equilibrated with Hf contained in zircon, but there was too little time for this reservoir to develop a significant less radiogenic signature than the matrix garnet actually did equilibrate with.

Lu-Hf systematics of garnet that undergoes successive growth and/or resorption events can be perturbated, which could consequently affect the quality of the isochron (Herwartz et al. 2011; Kelly et al. 2011; Sandmann et al. 2014). In the absence of inclusion, the mechanisms suspected to perturbate the $^{176}Lu/^{177}Hf$ and $^{176}Hf/^{177}Hf$ of the garnet are multiple. (1) Mixing of garnet generations of different age, by which the resulting date will be younger than the older metamorphic event, and older than the younger metamorphic event (Sandmann et al. 2014). (2) Garnet resorption that favours Lu retro-enrichment in the garnet, whereas released Hf is preferentially incorporated into zircon and rutile. The Hf loss would lead to younger apparent ages of the garnet (Kelly et al. 2011; Sandmann et al. 2014). (3) Thermal re-equilibration of the Lu-Hf isotopic system will produce an apparent age that is younger than the growth age (Sandmann et al. 2014). Due to the complexity of the internal zoning in the garnet porphyroblast of sample Z17TB03 it is difficult to evaluate if and by which extent these mechanisms may have affected the Lu–Hf system. The seemly high quality of the isochron (Fig. 12e) favours a coherent Lu-Hf systematic among the different garnet aliquots and that the original Lu-Hf systematic was preserved. Further analyses of Lu–Hf in this sample have been hampered by the COVID-19 situation and the shutdown of the laboratory at the University of British Columbia; they are planned for 2021.

5.4. Possible origin of the garnet porphyroblasts

Several scenarios are proposed for the origin of the garnet within the Grt-schist considering the fact that the Lu-Hf age is either meaningful or incorrect. Each scenario requires further investigations to validate the origin of the garnet porphyroblast origin.

Option 1: Jurassic hydrothermal/contact garnet. Chapter 1 interpreted the TGU as a volcanoclastic sequence deposited in the Piemonte Ligurian ocean. In the Western Alps, gabbro intrusions that mark oceanic crust formation in the ZSZ are dated at 164.0 ± 2.7 and 163.5 ± 2.8 Ma in Mellichen and Allalin respectively (Rubatto et al. 1998) and at 166.7 ± 2.8 Ma at Trockener Steg

(Chap. 1). Similarly, recrystallization of zircon found in orthogneiss from the polymetamorphic Etirol-Levaz continental basement slice was attributed to magmatic activity at ca. 166-150 Ma (Beltrando et al. 2010). Thus, if the Lu-Hf age of the garnet porphyroblast is correct, garnet formation within the TGU sedimentation domain occurred in an extensional setting associated to oceanic crust formation. No significant population of zircon from the different lithologies of the TGU has a Jurassic age (Chap. 1). Regardless, thermal gradient within the oceanic crust induced by magmatic intrusions is considered as a mechanism that could have promoted garnet growth, even at relatively low temperature, either through hydrothermal circulation and metasomatism (Gutzmer et al. 2001; Bach and Klein 2009) or contact metamorphism (Loomis 1972).

Option 2: Jurassic metamorphic sole. Intra-oceanic subduction can develop along both transform fault and ridge-parallel detachment fault, the latter being typically observed in slow-spreading ridge environment (Dewey and Casey 2011; Maffione et al. 2015). Remnants of subduction initiation are known as metamorphic soles (Hacker 1990), which form within the first 1-2 My of subduction (Stern et al. 2012; Dewey and Casey 2013). They are made of an association of high-grade metamorphosed basalts and pelagic sediments originated from the upper crustal material of the downgoing slab (Wakabayashi and Dilek 2000; Jolivet et al. 2003). Their metamorphic history follow a first burial step and a successive partial exhumation, where they are progressively stacked below the overlying undeformed oceanic lithospheric hanging-wall (Agard et al. 2016). The overlying oceanic lithosphere (Dilek and Furnes 2011, 2014) is either MORB-type (Nicolas et al. 2000) or supra-subduction zone-type (Stern and Bloomer 1992; van Hinsbergen et al. 2015). Jurassic metamorphic soles have been already documented in Alpine ophiolites such as in the Cyclades (Saccani and Photiades 2004; Gartzos et al. 2009) and in the Dinarides (Pamić et al. 2002; Gaggero et al. 2009), but have never been proposed for the Western Alps. The close age relationships between the Lu-Hf of garnet porphyroblast from the Grt-schist (TGU) and the zircon intrusion age from the metagabbro in the ZSZ (Chap. 1; Rubatto et al. 1998) could indicate synchronous oceanic crust formation and garnet growth in the Grt-schist. The growth of garnet porphyroblast ($Grt_{GS,1}$) could be explained by metamorphic sole formation during an early stage of localized intra-oceanic subduction in the Piemont-Ligurian ocean. The temperature inferred by RSCM and Zr-in-rutile thermometry is in the lower end of the temperature range usually observed in metamorphic sole (see references in Agard et al. 2016).

Option 3: Mixing age. The single whole rock-garnet Lu-Hf isochron from one sample may not be geologically meaningful (see section 5.3). The domain of the garnet porphyroblast that is the best constrained in *P*–*T* is $Grt_{GS,3}$, which grew after peak-*P* and prior to reheating. This is because the reactive bulk rock used for equilibrium thermodynamic simulation is most likely representative of

the bulk at the time of $Grt_{GS,3}$ growth. Due to the complex chemical zoning of the interior domains of the garnet porphyroblast ($Grt_{GS,1}$ and $Grt_{GS,2}$), it is complicated to evaluate to which extent these domains represent primary element and isotopic composition. The Lu-Hf date could represent a mixing between Alpine garnet (as dated in other samples) and older growth event(s) in garnet or associated inclusions, which coincidentally form a nearly perfect isochron.

In the two first scenarios, the core of the garnet porphyroblasts ($Grt_{GS,1}$) would be largely inherited from a Jurassic stage, as opposed to the other lithologies that did not preserve this pre-Alpine stage. Notably, the Lu budget of the garnet porphyroblasts in the Grt-schist is dominated by the mantle domain ($Grt_{GS,2}$), which, according to *P*–*T* modelling, is stable at 26.5 ± 1.5 kbar and 580 ± 15 °C. These pressure conditions are hard to reconcile with hydrothermal circulation, contact metamorphism or metamorphic sole formation. However, it was shown that the original diameter of the core ($Grt_{GS,1}$) in the garnet porphyroblasts was close to, or even bigger than, the actual external limit of the $Grt_{GS,2}$ domain (Fig. 3a-h,m-p). Moreover, it was proposed that heterogeneous overprinting of $Grt_{GS,1}$ by $Grt_{GS,2}$ was possibly achieved by replacement at high–*P*. If we assume that the Lu-Hf garnet Jurassic age and the *P*–*T* modelling of the mantle ($Grt_{GS,2}$) are both correct, a process of selective replacement (Rubatto et al. 2020) could fit to the proposed scenarios. In such a fortuitous case, the Lu-Hf systematics of $Grt_{GS,1}$ would be preserved and garnet *P*–*T* equilibrium conditions calculated for the mantle ($Grt_{GS,2}$) would be representative of the Alpine high–*P* stage. Unfortunately, the possibility to verify this hypothesis is very limited due to the Alpine overprint. Further Lu–Hf analyses of an additional sample will potentially clarify these options.

6. CONCLUSIONS

The Grt-schist from the TGU is an enigmatic lithology that hosts garnet with a bimodal size distribution. These two garnet populations are made on one side of spectacular cm-sized euhedral garnet porphyroblasts and on the other side of smaller garnets spread in the matrix. The compositional and oxygen isotopic zoning, as well as the Alpine *P*–*T* evolution of this garnet type presents similarities with the story deduced from samples that belongs to other lithologies of the TGU. However, the garnet porphyroblasts from the Grt-schist present two singularities that are only observed within this lithology. This garnet shows a core with a unique complex zoning and an intriguing Jurassic Lu-Hf whole rock-garnet isochron. This latter feature, if confirmed by further analysis, could question the monometamorphic evolution of the tectonic unit.

ACKNOWLEDGMENTS

I am grateful to D. Rubatto for the constructive discussion and the thorough revision of the Chapter. I thank P. Lanari for productive discussion and help with GrtMod. I'm grateful to J. Hermann, T. Ewing and A. Bisch for insightful discussion. I thank F. Piccoli and T. Pettke for their expert guidance with the LA-ICP-MS. I thank L. Diamond and L. Aeschwanden for their assistance with Raman spectrometry. I thank M. Smit for productive discussion and expert guidance with the laboratory work for Lu-Hf analysis. I thank J. Cutts and L. Tual for their help with the laboratory work for Lu-Hf analysis.

BIBLIOGRAPHY

Agard P, Yamato P, Soret M, et al (2016) Plate interface rheological switches during subduction infancy: Control on slab penetration and metamorphic sole formation. Earth Planet Sci Lett 451:208–220. https://doi.org/10.1016/j.epsl.2016.06.054

Ague JJ, Axler JA (2016) Interface coupled dissolution-reprecipitation in garnet from subducted granulites and ultrahigh-pressure rocks revealed by phosphorous, sodium, and titanium zonation. Am Mineral 101:1696–1699. https://doi.org/10.2138/am-2016-5707

Airaghi L, Lanari P, de Sigoyer J, Guillot S (2017) Microstructural vs compositional preservation and pseudomorphic replacement of muscovite in deformed metapelites from the Longmen Shan (Sichuan, China). Lithos 282–283:262–280. https://doi.org/10.1016/j.lithos.2017.03.013

Angiboust S, Langdon R, Agard P, et al (2012) Eclogitization of the Monviso ophiolite (W. Alps) and implications on subduction dynamics. J Metamorph Geol 30:37–61. https://doi.org/10.1111/j.1525-1314.2011.00951.x

Bach W, Klein F (2009) The petrology of seafloor rodingites: Insights from geochemical reaction path modeling. Lithos 112:103–117. https://doi.org/10.1016/j.lithos.2008.10.022

Baxter EF, Caddick MJ, Ague JJ (2013) Garnet: Common mineral, uncommonly useful. Elements 9:415–419. https://doi.org/10.2113/gselements.9.6.415

Baxter EF, Caddick MJ, Dragovic B (2017) Garnet: A Rock-Forming Mineral Petrochronometer. Rev Mineral Geochemistry 83:469–533. https://doi.org/10.2138/rmg.2017.83.15

Bebout GE, Barton MD (1989) Fluid flow and Metasomatism in a subduction zone hydrothermal system: Catalina Schist Terrane, California. Geology Vol. 17:976–980

Beltrando M, Rubatto D, Manatschal G (2010) From passive margins to orogens: The link between ocean-continent transition zones and (ultra)high-pressure metamorphism. Geology 38:559–562. https://doi.org/10.1130/G30768.1

Beyssac O, Bollinger L, Avouac JP, Goffé B (2004) Thermal metamorphism in the lesser Himalaya of Nepal determined from Raman spectroscopy of carbonaceous material. Earth Planet Sci Lett 225:233–241. https://doi.org/10.1016/j.epsl.2004.05.023

Beyssac O, Goffé B, Chopin C, Rouzaud JN (2002) Raman spectra of carbonaceous material in metasediments: A new geothermometer. J Metamorph Geol 20:859–871. https://doi.org/10.1046/j.1525-1314.2002.00408.x

Bill M, Bussy F, Cosca M, et al (1997) High-precision U-Pb and 40Ar/ 39Ar dating of an Alpine ophiolite (Gets nappe, French Alps). Eclogae Geol Helv 90:43–54. https://doi.org/10.5169/seals-168144

Borsi L, Schärer U, Gaggero L, Crispini L (1996) Age, origin and geodynamic significance of plagiogranites in lherzolites and gabbros of the Piedmont-Ligurian ocean basin. Earth Planet Sci Lett 140:227–241. https://doi.org/10.1016/0012-821X(96)00034-9

Caddick MJ, Konopásek J, Thompson AB (2010) Preservation of garnet growth zoning and the duration of prograde metamorphism. J Petrol 51:2327–2347. https://doi.org/10.1093/petrology/egq059

Carlson WD (2006) Rates of Fe, Mg, Mn, and Ca diffusion in garnet. Am Mineral 91:1–11.

https://doi.org/10.2138/am.2006.2043

Cartwright I, Barnicoat AC (1999) Stable isotope geochemistry of Alpine ophiolites: A window to ocean-floor hydrothermal alteration and constraints on fluid-rock interaction during high-pressure metamorphism. Int J Earth Sci 88:219–235. https://doi.org/10.1007/s005310050261

Compagnini G, Puglisi O, Foti G (1997) Raman spectra of virgin and damaged graphite edge planes. Carbon N Y 35:1793–1797. https://doi.org/10.1016/S0008-6223(97)00141-3

Daniel CG, Spear FS (1999) The clustered nucleation and growth processes of garnet in regional metamorphic rocks from north-west Connecticut, USA. J Metamorph Geol 17:503–520. https://doi.org/10.1046/j.1525-1314.1999.00200.x

Dewey JF, Casey JF (2011) The Origin of Obducted Large-Slab Ophiolite Complexes. Front Earth Sci 431–444. https://doi.org/10.1007/978-3-540-88558-0

Dewey JF, Casey JF (2013) The sole of an ophiolite: The Ordovician Bay of Islands Complex, Newfoundland. J Geol Soc London 170:715–722. https://doi.org/10.1144/jgs2013-017

Dilek Y, Furnes H (2014) Ophiolites and their origins. Elements 10:93–100. https://doi.org/10.2113/gselements.10.2.93

Dilek Y, Furnes H (2011) Ophiolite genesis and global tectonics: Geochemical and tectonic fingerprinting of ancient oceanic lithosphere. Bull Geol Soc Am 123:387–411. https://doi.org/10.1130/B30446.1

Dodson MH (1973) Closure temperature in cooling geochronological and petrological systems. Contrib to Mineral Petrol 40:259–274. https://doi.org/10.1007/BF00373790

Duchêne S, Blichert-Toft J, Luais B, et al (1997) The Lu-Hf dating of garnets and the ages of the Alpine high-pressure metamorphism. Nature 387:586–589. https://doi.org/10.1038/42446

Erambert M, Austrheim H (1993) The effect of fluid and deformation on zoning and inclusion patterns in poly-metamorphic garnets. Contrib to Mineral Petrol 115:204–214. https://doi.org/10.1007/BF00321220

Faure G, Mensing TM (2005) Isotopes principles and applications

Ferry JM, Watson EB (2007) New thermodynamic models and revised calibrations for the Ti-in-zircon and Zr-in-rutile thermometers. Contrib to Mineral Petrol 154:429–437. https://doi.org/10.1007/s00410-007-0201-0

Gaggero L, Marroni M, Pandolfi L, Buzzi L (2009) Modeling the oceanic lithosphere obduction : Constraints from the metamorphic sole of Mirdita ophiolites (northern Albania). Ofioliti 34:17–42. https://doi.org/10.4454/ofioliti.v34i1.376

Gartzos E, Dietrich VJ, Migiros G, et al (2009) The origin of amphibolites from metamorphic soles beneath the ultramafic ophiolites in Evia and Lesvos (Greece) and their geotectonic implication. Lithos 108:224–242. https://doi.org/10.1016/j.lithos.2008.09.013

Gutzmer J, Pack A, Lüders V, et al (2001) Formation of jasper and andradite during low-temperature hydrothermal seafloor metamorphism, Ongeluk Formation, South Africa. Contrib to Mineral Petrol 142:27–42. https://doi.org/10.1007/s004100100270

Hacker BR (1990) Simulation of the metamorphic and deformational history of the metamorphic sole of the Oman ophiolite. J Geophys Res 95:4895–4907. https://doi.org/10.1029/JB095iB04p04895

Herwartz D, Nagel TJ, Münker C, et al (2011) Tracing two orogenic cycles in one eclogite sample by Lu-Hf garnet chronometry. Nat Geosci 4:178–183. https://doi.org/10.1038/ngeo1060

Jolivet L, Faccenna C, Goffé B, et al (2003) Subduction tectonics and exhumation of high-pressure metamorphic rocks in the Mediterranean orogens. Am J Sci 303:353–409. https://doi.org/10.2475/ajs.303.5.353

Katagiri G, Ishida H, Ishitani A (1988) Raman spectra of graphite edge planes. Carbon N Y 26:565–571. https://doi.org/10.1016/0008-6223(88)90157-1

Kelly ED, Carlson WD, Connelly JN (2011) Implications of garnet resorption for the Lu-Hf garnet geochronometer: An example from the contact aureole of the Makhavinekh Lake Pluton, Labrador. J Metamorph Geol 29:901–916. https://doi.org/10.1111/j.1525-1314.2011.00946.x

Ketcham RA, Carlson WD (2012) Numerical simulation of diffusion-controlled nucleation and growth of porphyroblasts. J Metamorph Geol 30:489–512. https://doi.org/10.1111/j.1525-1314.2012.00978.x

Kohn MJ (1993) Modeling of prograde mineral δ18O changes in metamorphic systems. Contrib to Mineral Petrol 113:249–261. https://doi.org/10.1007/BF00283232

Konrad-Schmolke M, Babist J, Handy MR, O'Brien PJ (2006) The physico-chemical properties of a subducted slab from garnet zonation patterns (Sesia Zone, Western Alps). J Petrol 47:2123–2148. https://doi.org/10.1093/petrology/egl039

Konrad-Schmolke M, O'Brien PJ, de Capitani C, Carswell DA (2008a) Garnet growth at high- and ultra-high pressure conditions and the effect of element fractionation on mineral modes and composition. Lithos 103:309–332. https://doi.org/10.1016/j.lithos.2007.10.007

Konrad-Schmolke M, Zack T, O'Brien PJ, Jacob DE (2008b) Combined thermodynamic and rare earth element modelling of garnet growth during subduction: Examples from ultrahigh-pressure eclogite of the Western Gneiss Region, Norway. Earth Planet Sci Lett 272:488–498. https://doi.org/10.1016/j.epsl.2008.05.018

Kurz W, Neubauer F, Dachs E (1998) Eclogite meso- and microfabrics: implications for the burial and exhumation history of eclogites in the Tauern Window (Eastern Alps) from P - T - d paths. Tectonophysics 285:183–209

Lanari P, Engi M (2017) Local Bulk Composition Effects on Metamorphic Mineral Assemblages. Rev Mineral Geochemistry 83:55–102. https://doi.org/10.2138/rmg.2017.83.3

Lanari P, Giuntoli F, Loury C, et al (2017) An inverse modeling approach to obtain P–T conditions of metamorphic stages involving garnet growth and resorption. Eur J Mineral 29:181–199. https://doi.org/10.1127/ejm/2017/0029-2597

Lanari P, Vho A, Bovay T, et al (2019) Quantitative compositional mapping of mineral phases by electron probe micro-analyser. Geol Soc Spec Publ 478:39–63. https://doi.org/10.1144/SP478.4

Lanari P, Vidal O, De Andrade V, et al (2014) XMapTools: A MATLAB©-based program for electron microprobe X-ray image processing and geothermobarometry. Comput Geosci 62:227–240. https://doi.org/10.1016/j.cageo.2013.08.010

Li B, Ge J, Zhang B (2018) Diffusion in garnet: a review. Acta Geochim 37:19–31. https://doi.org/10.1007/s11631-017-0187-x

Loomis TP (1972) Contact Metamorphism of Pelitic Rock by the Ronda Ultramafic Intrusion, Southern Spain. Geol Soc Am Bull 83:2449–2474

Maffione M, Thieulot C, van Hinsbergen DJJ, et al (2015) Dynamics of intraoceanic subduction initiation: 1. Oceanic detachment fault inversion and the formation of supra-subduction zone ophiolites. Geochemistry Geophys Geosystems 16:1753–1770. https://doi.org/10.1002/2014GC005684.Key

Marmo BA, Clarke GL, Powell R (2002) Fractionation of bulk rock composition due to porphyroblast growth: Effects on eclogite facies mineral equilibria, Pam Peninsula, New Caledonia. J Metamorph Geol 20:151–165. https://doi.org/10.1046/j.0263-4929.2001.00346.x

McCaig AM, Cliff RA, Escartin J, et al (2007) Oceanic detachment faults focus very large volumes of black smoker fluids. Geology 35:935–938. https://doi.org/10.1130/G23657A.1

Miller JA, Cartwright I, Buick IS, Barnicoat AC (2001) An O-isotope profile through the HP-LT Corsican ophiolite, France and its implications for fluid flow during subduction. Chem Geol 178:43–69. https://doi.org/10.1016/S0009-2541(00)00428-9

Moynihan DP, Pattison DRM (2013) An automated method for the calculation of P-T paths from garnet zoning, with application to metapelitic schist from the Kootenay Arc, British Columbia, Canada. J Metamorph Geol 31:525–548. https://doi.org/10.1111/jmg.12032

Negro F, Bousquet R, Vils F, et al (2013) Thermal structure and metamorphic evolution of the Piemont-Ligurian metasediments in the northern Western Alps. Swiss J Geosci 106:63–78. https://doi.org/10.1007/s00015-013-0119-7

Nicolas A, Bouldier F, Ildefonse B, Ball E (2000) Accretion of Oman and United Arab Emirates ophiolite - Discussion of a new structural map. Mar Geophys Res 21:147–180. https://doi.org/10.1023/A:1026769727917

Pamić J, Tomljenović B, Balen D (2002) Geodynamic and petrogenetic evolution of Alpine ophiolites from the central and NW Dinarides: An overview. Lithos 65:113–142. https://doi.org/10.1016/S0024-4937(02)00162-7

Pasteris JD (1989) In situ analysis in geological thin-sections by laser Raman microprobe spectroscopy: A cautionary note. Appl Spectrosc 43:567–570. https://doi.org/10.1366/0003702894202878

Perchuk AL, Burchard M, Schertl HP, et al (2009) Diffusion of divalent cations in garnet: Multi-couple experiments. Contrib to Mineral Petrol 157:573–592. https://doi.org/10.1007/s00410-008-0353-6

Pollok K, Lloyd GE, Austrheim H, Putnis A (2008) Complex replacement patterns in garnets from Bergen Arcs eclogites: A combined EBSD and analytical TEM study. Chemie der Erde 68:177–191. https://doi.org/10.1016/j.chemer.2007.12.002

Putnis A (2009) Mineral replacement reactions. Rev Mineral Geochemistry 70:87–124. https://doi.org/10.2138/rmg.2009.70.3

Putnis A, Austrheim H (2010) Fluid-induced processes: Metasomatism and metamorphism. Geofluids 10:254–269. https://doi.org/10.1111/j.1468-8123.2010.00285.x

Putnis A, John T (2010) Replacement processes in the earth's crust. Elements 6:159–164. https://doi.org/10.2113/gselements.6.3.159

Rubatto D, Burger M, Lanari P, et al (2020) Identification of growth mechanisms in metamorphic garnet by high-resolution trace element mapping with LA-ICP-TOFMS. Contrib to Mineral Petrol 175:1–19. https://doi.org/10.1007/s00410-020-01700-5

Rubatto D, Gebauer D, Fanning M (1998) Jurassic formation and Eocene subduction of the Zermatt-Saas-Fee ophiolites: Implications for the geodynamic evolution of the Central and Western Alps. Contrib to Mineral Petrol 132:269–287. https://doi.org/10.1007/s004100050421

Rumble D, Ferry JM, Hoering TC, Boucot AJ (1982) Fluid flow during metamorphism at the Beaver Brook fossil locality, New Hampshire. Am. J. Sci. 282:886–919

Saccani E, Photiades A (2004) Mid-ocean ridge and supra-subduction affinities in the Pindos ophiolites (Greece): Implications for magma genesis in a forearc setting. Lithos 73:229–253. https://doi.org/10.1016/j.lithos.2003.12.002

Sandmann S, Nagel TJ, Herwartz D, et al (2014) Lu–Hf garnet systematics of a polymetamorphic basement unit: new evidence for coherent exhumation of the Adula Nappe (Central Alps) from eclogite-facies conditions. Contrib to Mineral Petrol 168:1–21. https://doi.org/10.1007/s00410-014-1075-6

Scherer EE, Cameron KL, Blichert-Toft J (2000) Lu-Hf garnet geochronology: Closure temperature relative to the Sm-Nd system and the effects of trace mineral inclusions. Geochim Cosmochim Acta 64:3413–3432. https://doi.org/10.1016/S0016-7037(00)00440-3

Scherer EE, Münker C, Mezger K (2001) Calibration of the Lutetium-Hafnium Clock. Science (80-) 293:683–688

Schwandt CS, Cygan RT, Westrich HR (1996) Ca self-diffusion in grossular garnet. Am Mineral 81:448–451. https://doi.org/10.2138/am-1996-3-418

Smit MA, Scherer EE, Mezger K (2013) Lu-Hf and Sm-Nd garnet geochronology: Chronometric closure and implications for dating petrological processes. Earth Planet Sci Lett 381:222–233. https://doi.org/10.1016/j.epsl.2013.08.046

Spear FS (1988) Metamorphic fractional crystallization and internal metasomatism by diffusional homogenization of zoned garnets. Contrib to Mineral Petrol 99:507–517. https://doi.org/10.1007/BF00371941

Spear FS, Daniel CG (2001) Diffusion control of garnet growth, Harpswell Neck, Maine USA. J Metamorph Geol 19:179–195. https://doi.org/10.1046/j.0263-4929.2000.00306.x

Spear FS, Selverstone J (1983) Quantitative P-T paths from zoned minerals: Theory and tectonic applications. Contrib to Mineral Petrol 83:348–357. https://doi.org/10.1007/BF00371203

Stern RJ, Bloomer SH (1992) Subduction zone infancy: examples from the Eocene Izu-Bonin-Mariana and Jurassic California arcs. Geol Soc Am Bull 104:1621–1636. https://doi.org/10.1130/0016-7606(1992)104<1621:SZIEFT>2.3.CO;2

Stern RJ, Reagan M, Ishizuka O, et al (2012) To understand subduction initiation, study forearc crust: To understand forearc crust, study ophiolites. Lithosphere 4:469–483. https://doi.org/10.1130/L183.1

Taylor SR, McLennan SM (1985) The continental crust: Its composition and evolution

Tirone M, Ganguly J (2010) Garnet compositions as recorders of P-T-t history of metamorphic rocks. Gondwana Res 18:138–146. https://doi.org/10.1016/j.gr.2009.12.010

van Hinsbergen DJJ, Peters K, Maffione M, et al (2015) Dynamics of intraoceanic subduction initiation: 2. Suprasubduction zone ophiolite formation and metamorphic sole exhumation in context of absolute plate motions. Geochemistry Geophys Geosystems 16:1771–1785. https://doi.org/10.1002/2014GC005684.Key

Vho A, Lanari P, Rubatto D, Hermann J (2020) Tracing fluid transfers in subduction zones: An integrated thermodynamic and δ18O fractionation modelling approach. Solid Earth 11:307–328. https://doi.org/10.5194/se-11-307-2020

Vielzeuf D, Baronnet A, Perchuk AL, et al (2007) Calcium diffusivity in alumino-silicate garnets: An experimental and ATEM study. Contrib to Mineral Petrol 154:153–170. https://doi.org/10.1007/s00410-007-0184-x

Wakabayashi J, Dilek Y (2000) Spatial and temporal relationships between ophiolites and their metamorphic soles: A test of models of forearc ophiolite genesis. Spec Pap Geol Soc Am 349:53–64. https://doi.org/10.1130/0-8137-2349-3.53

Wang A, Dhamenincourt P, Dubessy J, et al (1989) Characterization of graphite alteration in an uranium deposit by micro-Raman spectroscopy, X-ray diffraction, transmission electron microscopy and scanning electron microscopy. Carbon N Y 27:209–218. https://doi.org/10.1016/0008-6223(89)90125-5

Whitney DL, Evans BW (2010) Abbreviations for names of rock-forming minerals. Am Mineral 95:185–187. https://doi.org/10.2138/am.2010.3371

Wilbur DE, Ague JJ (2006) Chemical disequilibrium during garnet growth: Monte Carlo simulations of natural crystal morphologies. Geology 34:689–692. https://doi.org/10.1130/G22483.1

Zack T, Foley SF, Rivers T (2002) Equilibrium and disequilibrium trace element partitioning in hydrous eclogites (Trescolmen, Central Alps). J Petrol 43:1947–1974. https://doi.org/10.1093/petrology/43.10.1947

SUPPLEMENTARY MATERIAL

Table S1 : Garnet major element average composition for each growth domain (EPMA).

Table S2 : LA-ICP-MS analyses of garnet.

Table S3 : Bulk rock chemistry used at each simulation step with GrtMode.

Table S4 : LA-ICP-MS analyses of rutile.

Table S5 : SIMS oxygen isotope analyses of garnet.

ACKNOLEDGEMENTS

First, I want to thank Daniela Rubatto for having provided me the great opportunity to work on this project. Thank you, Daniela, for sharing your passion for science, for your optimism, and guiding me through these four years of research. I'm very grateful for the confidence you have in me, for always leaving your door open for all my questions, for the countless advices, and for your patience. I still don't know where you hide all this energy, but it might somehow be contagious and greatly helped me to move forward.

Further, I want to thank Pierre Lanari, because you were there since my beginning in Bern. I really appreciate your calm and your optimism. I'm thankful for all the inputs you brought for my research and for the discovery of the thermodynamic modelling world. I thank you for the countless hours that we spent together at the EPMA and the confidence you put in me in helping you to handle this lab.

I want to thank the Petrology group, for its great atmosphere. It is a very positive environment out of which I beneficiated very insightful discussions and lab collaborations. I specifically want to thank Jörg Hermann for your in-depth inputs along these four years, that helped me a lot to look at my data differently. I want to thank the LA-ICP-MS specialists Thomas Pettke and Francesca Piccoli, for providing easy access to the lab and high-quality assistance. I thank Daniel Peters for the hours in the preparation lab to teach me the PPP process making.

The University of Bern is full of enthusiastic peolpe, always ready to give a hand and share their knowledge. I thank Lukas Aschwanden and Larryn Diamond who helped me to improve my skills with the Raman. I warmly thank the Workshop team Stephan Brechbühl and Thomas Aebi for their excellent work and help with the sample preparation. I thank Julia Krbanjevic, Christopher Pichler and Priska Bähler for the interlab coordination. I thank the administration team Sarah Antenen and Marina Beutler for their efficient work.

I thank Matthijs Smit who accepted to host me in his lab in Vancouver for showing me how to perform the lab work for Lu-Hf geochronology. I thank you for your spontaneous involvement in my work and the fruitful discussion that greatly improved my research. I want to thank the UBC team for the warm welcome and the time in and out the university, with a special thought to Lorraine and Jamie.

I want to make a special dedication to the ex-pizza team at University of Bern: Florian and Om, always ready for a breath of fresh air and fun at lunch time. I want to thank my office mates Elias, Julien and Alice with whom I could share multiple fieldtrips, fieldwork and nitrogen filling sessions. I want to thank the climbing team Sandro, Anne, Camille, Marius, Chloé and Michi for the relaxing boulder sessions in- and outside.

This thesis was a lot of work, but would have been much harder without a bunch of people who were always present outside the university bubble. My buddies from Lausanne, i.e. the unconditional Paleo team (Choco, Fred, Djo, Caro, Loulou, Djey, Gaëlle, Fano, Chrigu, Dave and Carole) and the Apoils (Vadimovic, Sarah, Sophie, Véro, Aurel, Jérém), thank you for your support. The A gauche climbing team in Zürich (Marius, Jess, Leo, Quim, Michal and Luzi) provided me what I needed to de-stress during hard times.

I warmly thank my family, my parents Simone and Claude, my brother Martin and his plus one Varinia, my grandmother Rosy, for your endless support and love.

This work was quite an adventure, especially the last year, which combined the writing of the Thesis and the pandemic. Coming through this path would not have been possible without the presence of the ONE person. Lena I'm so thankful for what you're giving me and what we're living together. "I never knew anyone, So one of a kind, until the night I seen her eyes,…" (Tarrus Riley)

Declaration of consent

on the basis of Article 18 of the PromR Phil.-nat. 19

Name/First Name:

Registration Number:

Study program:

Bachelor ☐ Master ☐ Dissertation ☐

Title of the thesis:

Supervisor:

I declare herewith that this thesis is my own work and that I have not used any sources other than those stated. I have indicated the adoption of quotations as well as thoughts taken from other authors as such in the thesis. I am aware that the Senate pursuant to Article 36 paragraph 1 litera r of the University Act of September 5th, 1996 and Article 69 of the University Statute of June 7th, 2011 is authorized to revoke the doctoral degree awarded on the basis of this thesis.
For the purposes of evaluation and verification of compliance with the declaration of originality and the regulations governing plagiarism, I hereby grant the University of Bern the right to process my personal data and to perform the acts of use this requires, in particular, to reproduce the written thesis and to store it permanently in a database, and to use said database, or to make said database available, to enable comparison with theses submitted by others.

Place/Date

Signature